Nonlinear forcing, response and damping of Oscillating Water Columns

Emma Patricia Bangun

Imperial College London

Department of Civil Engineering
Imperial College London

Thesis submitted for the degree of Doctor of Philosophy

To my loving family,

Declaration of originality

All the work presented in this thesis is that of the author. Any work or contributions made by others is referenced appropriately.

Copyright declaration

Abstract

This thesis improves the physical understanding of a dynamically responding offshore Oscillating Water Column (OWC) of a fixed and cylindrical type. The study concerns the analytical models of the linear potential flows and the numerical simulations of the fully nonlinear viscous flows of OWCs undergoing different excitation mechanisms and conditions.

Of particular interest in this research are the physical origin and the significance of nonlinearities in the forces acting on a water column. The vortex shedding at the lowermost end of an OWC has a marked influence on the forcing caused by wave excitation at the resonant and a higher frequency. On the other hand, the free-surface nonlinearity has a negligible effect on this force. Furthermore, an evaluation of the hydrodynamic and the air forces demonstrates the diminishing role of the vortex shedding as the amplitude of the response (or motion) of a water column increases.

The vortex shedding and the nonlinear inertial forcing are responsible for any nonlinear characteristics of the internal water surface elevation within an OWC. The former causes the progressively decreasing response amplitude operator and progressively varying phase difference of the water elevation, while the latter provokes the response asymmetry.

The hydrodynamic coefficients crucially depend on the amplitude of the water column motion, the mouth shape, and the dimensions of an OWC. When flow separation occurs, the added-mass coefficient progressively increases with the amplitude. It is consistent with the departures from linear radiation theory when considering the radiated wave elevation near an OWC with a sharp-edged mouth.

Formation of the vortex that primarily contributes to the nonlinear damping coefficient most significantly reduces the response at the resonant frequency. This role of vortex formation is more pronounced under a high- than a low-frequency excitation. These insights and the dominance of the flow driven by the water column (in relative comparison to the wave flow) explain the applicability of the hydrodynamic coefficients evaluated from a forced oscillation test to predict a wave-induced response.

Acknowledgements

First and foremost, I would like to thank my supervisor, Professor Chris Swan, for his guidance and encouragement during this Phd study. His invaluable advice and constructive criticism have significantly improved the quality of my research work and built my skills as a scientific researcher. I wish to continue applying his approach in undertaking research work and in writing scientific papers in the future.

It is also my wish to express my gratitude to the Directorate General of Higher Education of Indonesia for providing me with the financial support.

I am especially grateful to my examiners, Professor Graham Hughes and Professor Deborah Greaves, for their comments and advice on my thesis.

The research students in the basement offices have been very helpful throughout these years. My thanks go to Elena and Johanna for the friendship and discussions that we spent when I was stuck with my work. I also have to thank Vishnu and Rakheeb for lending me your hard drives, and Erwan who had kindly helped me dealing with Open Foam simulations. I am indebted to Rebecca and Sarah for making the process of my study as smooth as possible.

My parents, Dharma Bangun and Risnawaty Sinulingga, have been a very strong pillar of support during this journey. Thank you papa and mama for your love and guidance. Especially to mama, your dedication in everything you do has been an inspiration for me to pursue this Phd study.

Finally, I am forever grateful to my husband, Terang Meliala, for your sacrifice, patience and willingness to share my aspiration. I praise the Lord Jesus Christ for your steadfast love. I cannot forget to mention my daughter, Eirene Meliala, who has patiently accompanied me especially during the writing-up stage. Your cheerfulness has never failed to brighten up my day.

Contents

List of figures

List of tables

1
Introduction

1.1 Motivation

The idea of converting wave energy into a useful energy resource through the installation of a marine structure has long been considered. This is not surprising given the fact that ocean waves carry a substantial proportion of their energy at the ocean surface. Indeed, the concept of wave energy extraction was initially conceived around 1885 by J. M. Courtney when he invented a whistling buoy as a navigational aid. Later in 1947, a similiar idea was introduced by Yoshio Masuda, a Japanese naval commander, who tested a self-powered navigational Light-buoy in the sea. His design consisted of a surface-piercing floater and a vertical tube. This formed an air chamber, that was open to the atmosphere through an upper passage, where an impulse turbine was installed. The lower inlet of the tube was submerged and open to the water, thereby trapping a water column that oscillated in response to the wave excitations. Initially, his small-scale buoy device was only able to light a 60-watt bulb and to drive a flasher unit. Nowadays, his concept, also known as an Oscillating Water Column (OWC), has been adapted for higher-rated power extractions, ranging from 30kW to 2.5MW in full-scale design (Heath, 2011).

Over the past few decades, numerous designs for OWCs have been proposed. For example, the concept of an OWC being integrated into a breakwater or a shore-protection structure has been studied from field experiments. A caisson breakwater that extracts wave-energy rated at 60kW was constructed in Sakata Port, Japan

(Takahasi et al., 1992) and a multi-chamber OWC with the power rate at 320 kW was built in Mutriku Port, Spain (Torre-Enciso et al., 2009, Heath, 2011). Research investigations into the efficiencies of such devices based upon small-scale experimental models also indicate the potential of capturing wave energy (Thiruvenkatasamy & Neelamani, 1997, Tseng et al., 2000, Boccotti, 2007, 2012, He et al., 2016). The shoreline protection and the shared construction cost are considered as the additional benefits, especially at coastlines with relatively low wave-energy potential. In the northern hemisphere, designs of isolated and shore-connected OWCs have even reached the stage of full-scale model testing. An OWC plant in Norway (Falcão, 2010), the Pico Plant in Portugal (Falcão, 2000), and LIMPET in Scotland (Heath et al., 2001) are examples of nearshore (full-scale) devices. A picture of the Pico OWC plant integrated into a natural gully is shown in Figure 1.1(A). The air mass in the pneumatic chamber, shown schematically in Figure 1.1(B), flows into or out of an upper passage as an incident wave approaches the water column. This consequently drives the Wells turbine inside the passage. The turbine power is then converted into the electrical power rated at 400 kW (Falcão, 2000).

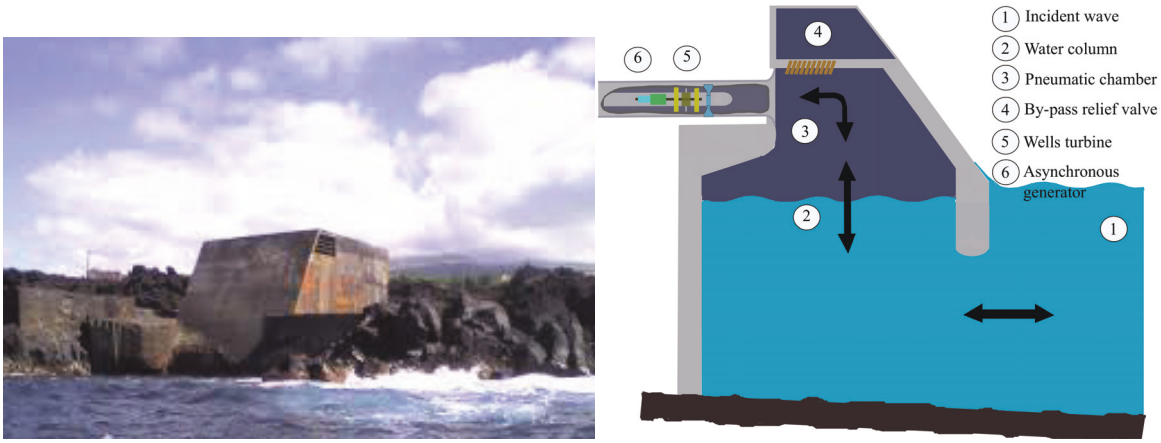

(A) (B)

Figure 1.1: (A) The Pico OWC integrated into a natural gully in Azores, Portugal and (B) the corresponding cross-section representing the plant's primary components (Aqua-RET, 2008).

The full-scale breakwater-integrated and shore-connected OWC plants have been shown capable of extracting wave energy in real sea-states. However, problems associated with the dissipative effects of seabed friction and the occurence of wave breaking due to shoaling effects in the nearshore area are among several critical factors reducing operational performance. Moreover, there is a growing concern over

the potential noise pollution from such plants. While the consequences of underwater noise pollution are inconclusive, the airborne noise is produced within the audible range for humans and may potentially affect the nearby populations (De Moura et al., 2010). In parallel, the UK government has made an ambitious plan to achieve a target of net-zero CO_2 emissions by 2050 (UKERC, 2019). The proportion of the electricity supply derived from renewable energies in the UK was low during the initial years of conception. Nevertheless, it had grown to thirty-three percent by 2018. In fact, renewable energies produced the majority of UK electricity for the first time in the following year (CarbonBrief, 2019). To date, the target of net-zero CO_2 emissions is, however, far from achievable. This fact, together with the challenges of shore-connected OWC devices highlighted above, explain the urgent need to further explore renewable energy sources, including the potential of deep water wave energy.

From the perspective of design maturity, offshore OWC Wave Energy Converterters (WECs) are still at a very early stage of commercialisation. For instance, the Ocean Energy Buoy, a 1:4 scaled model of the Backward-Bent-Duct-Buoy (BBDB) type OWC located in the Galway Bay of Ireland, completed the first three stages of model testing in 2011 (Heath, 2011). The Spar Buoy, an axisymmetric OWC that consists of a relatively long and submerged vertical tail tube, has been designed as wave-powered navigation buoys (Falcão, 2010). However, no large-scale energy production based upon a full-scale prototype has been reported. One major challenge is to produce the wave energy at a cost that can compete economically in the global energy market. To achieve this requires, at the very least, a significant effort to optimise the power output. This must be coupled with a firm understanding of the behaviour of the device, including the response in actual sea conditions. This, in turn, requires an in-depth understanding of the physical mechanisms that are responsible for instigating the response behaviour, as well as the physical parameters that govern the response characteristics.

In pursuit of the aforementioned goal, the dynamic response of the water column inside the device has to be reliably estimated. This involves modelling the hydrodynamic force and wave-excitation force, taking due account of all the nonlinearities that play a role in the response. In particular, when operating in a resonant state, where most of the power will be generated, the effects of flow separation and vortex shedding must be addressed. Force quantification must take into account this non-

linear flow behaviour, as well as other physical effects. With the inclusion of all the relevant forces, realistic dynamic responses of the water column can then be achieved and understood. Furthermore, analysing the flow field is an essential first step in providing physically grounded evidence that supports an improved understanding of the response behaviour.

Of the many geometrical configurations of offshore OWC being investigated, devices with cylindrical geometries have thus far received rather less attention. This trend is probably explained by the research outline in Evans & Porter (1997). The optimal capture width for a cylindrical OWC is generally lower than that of a bottom-standing OWC (Evans & Porter, 1995). However, when developed in combination with offshore wind energy, and after accounting for the fact that it is independent of wave direction, harnessing offshore wave energy using a cylindrical body may still be promising. Moreover, it provides the perfect test case to consider the role of nonlinear factors including flow separation and nonlinear free-surface effects, from a fundamental perspective. For these reasons, a study of cylindrical OWCs is worth pursuing to advance our knowledge of the offshore wave energy field. Cylindrical offshore OWC will thus be the focus of the present study.

1.2 Engineering significance

In offshore engineering design, Morison's equation has been extensively used to model the hydrodynamic loading on a slender, cylindrical body (Keulegan & Carpenter, 1958, Sarpkaya, 1975, Chakrabarti et al., 1976, Sarpkaya, 1977). The implementation of this equation necessitates information concerning some experimentally-calibrated loading coefficients. For each given coefficient, the loading is then described as a function of the instantaneous velocity and acceleration of the incident (un-disturbed) fluid flow. Consequently, the accuracy of the loading calculation is critically dependent on these hydrodynamic/loading coefficients. As such, the extent to which the coefficients closely represent the actual flow condition becomes very important.

In the context of an OWC, understanding the flow behaviour represented by the coefficients, over the full range of flow conditions, is necessary to estimate the dynamic response of the water column. In fact, all of the physical processes governing the body response need to be fully considered. This includes the scattered and

radiated waves around the structure, as well as the vortex shedding at the base of the OWC. To date, determination of the loading coefficients is largely based upon knowledge of the hydrodynamic forces acting on equipment commonly used in the offshore Oil & Gas industry (Babarit et al., 2012). Furthermore, to ensure that any calculations are relevant to full-scale conditions, a full range of length scales needs to be considered. In effect, research outcomes based upon lab-scaled data should assist in the reliable prediction of the water column response of a full-scale OWC.

In order to evaluate the flow behaviour over a broad range of flow conditions, the mechanisms responsible for the excitation of the water column motion need to be widely varied. One approach is to dynamically fluctuate the air pressure above the water column in the absence of incident waves; this is referred to as forced excitation. A second approach is to incorporate a pressure fluctuation at the open-ended inlet through a wave excitation. In traditional hydrodynamic theory, the hydrodynamic properties obtained from the two excitations are assumed to be comparable; the flow field from a forced excitation co-existing with the wave field around a fixed body. As a result, they can be linearly superposed to estimate the wave-induced response. This is a widely accepted approach in the design of many offshore structures (Himeno, 1981, Faltinsen, 1999). However, for a non-rigid body such as an OWC, the evaluation of this approach may not be straightforward since the wave-excitation force cannot be immediately estimated by considering a fixed water column. Specifically, the nonlinear forces resulting from the interaction of the waves and the vortex shedding at the bottom inlet may not be adequately represented by the incident wave pressure. Clarification as to the validity of the linear superposition approach is of fundamental importance and will be addressed within this thesis.

1.3 Thesis contribution

The overall contribution of this thesis is to provide an improved physical understanding of a dynamically responding OWC. The research analysis involves modelling an OWC under two different excitation mechanisms, a forced oscillation and a wave induced excitation; both undertaken in the absence of a power-take-off (PTO). In seeking to achieve this overall goal, individual aspects of the study will address:

1. The numerical modelling of OWCs with varying geometries. In each case, the

model will undergo free decay, forced oscillation and regular wave excitation,

2. The description of the water particle kinematics defining the rotational flow fields that arise due to varying excitation mechanisms,

3. Characterisation of the wave fields around an OWC; key points being the influence of vortex shedding and the validity of linear radiation theory,

4. Identifying the physical origin and significance of all nonlinearities in the forcing and motion of water columns,

5. Assessing the hydrodynamic coefficients appropriate to a practical range of flow conditions,

6. Fundamental guidance as to the importance of any vortex formation and motion in defining the response behaviour of a water column,

7. The applicability of forced oscillation tests and the validity of the principle of linear superposition.

In undertaking this work, it is important to note that a number of simplifications have been applied. These particularly relate to the absence of a PTO mechanism, the use of prescribed forcing, the assumption of air incompressibility and the reduced scale of the OWCs under investigation. The present work focuses on understanding the influence of the various sources of nonlinearity on the response behaviour and the excitation forces that act. As such, the work provides fundamental insights into the behaviour of an OWC.

A flow chart describing the various aspects of the investigation is presented in Figure 1.2. This also highlights the linkage between the chapters. As a first step, the physical sources of nonlinearity contributing to the radiated wave field, the response (or motion) and the forces acting on a water column are considered. These potential sources of nonlinearity are associated with the vortex shedding, free-surface nonlinearity and large excursion of the water column. In order to establish their effects, OWCs with a variety of dimensions undergoing different excitation mechanisms are analytically modelled using linear potential theory and numerically simulated in a viscous flow. These methods for evaluating and modelling an OWC are indicated by

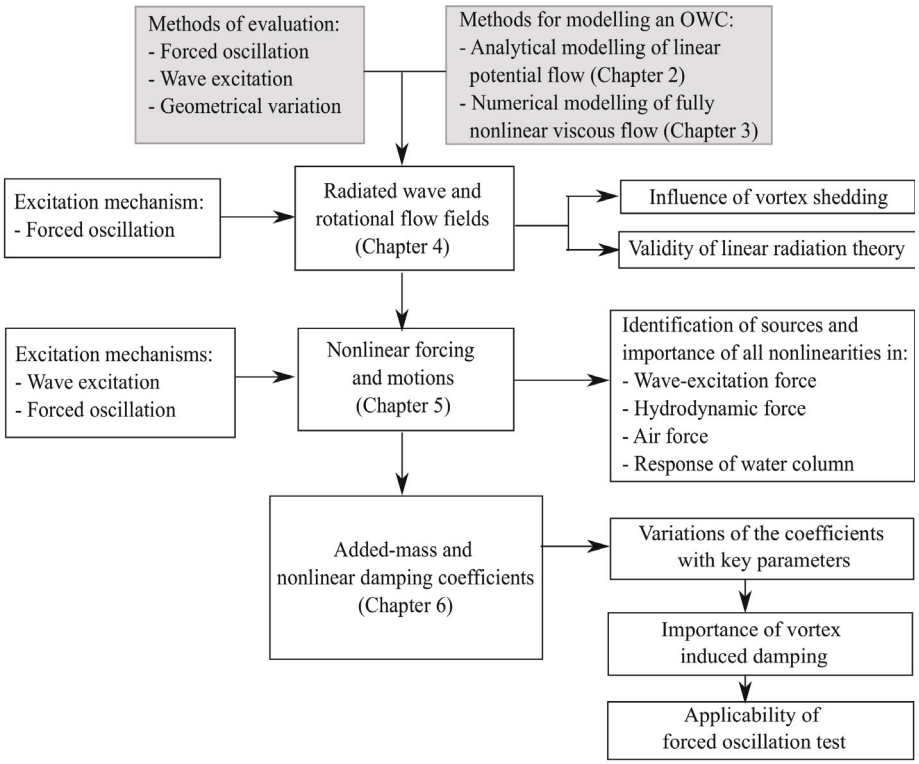

Figure 1.2: Flow chart describing the various aspects of the investigation [□] and the methods for modelling and evaluating an OWC [■].

the grey rectangles on Figure 1.2. The other rectangles represent specific aspects of the investigation and the methods implemented.

The next stage evaluates the nonlinearities in the radiated wave fields around an OWC. This requires an analysis of the rotational flow fields generated by forced oscillations. The aim, at this stage, is to understand the influence of vortex shedding on the radiated wave fields and the validity of linear radiation theory. The following step analyses the nonlinearities in the forces acting on and the motions of the water column. The forces considered are the wave-excitation force, the hydrodynamic and the air forces. Within this analysis, both forced oscillation and wave excitation problems are explored. The overall purpose of this work is to understand the sources and importance of all the nonlinearities arising.

Following on, the hydrodynamic coefficients appropriate to an OWC undergoing forced oscillations are evaluated; the purpose being to understand their variation with key parameters. The description of the rotational flow field, established (in Chapters 4 and 5), will help explain these variations. Based upon these results, the

importance of vortex induced damping on the response behaviour and the applicability of these coefficients to wave-excitation problems will be evaluated. With an improved understanding of the relevant nonlinear effects and their significance, guidance as to how best to develop the appropriate time-domain modelling of an OWC is provided. Building upon this work, the relevance of linear potential theory and the principle of linear superposition will be established.

1.4 Thesis overview

As indicated by Figure 1.2, the thesis which follows is divided into six chapters:

Chapter 2 provides the hydrodynamic theory describing the loads acting on slender structures. It addresses the key physical parameters and geometrical effects. The implementation of Morison's equation and its extended forms for load estimations on cylindrical structures is critically reviewed. A linear analytical solution to the OWC problem is provided and a critical assessment of existing numerical and experimental models of OWCs are discussed. The rigid-body dynamics of a fixed OWC based upon the principle of linear superposition is also described.

Chapter 3 presents the numerical model of an OWC developed within the present study. This implements a volume of fluid method, based upon the open source Computational Fluid Dynamics (CFD) code, Open Foam. Most importantly, this chapter provides the validation and convergence studies for various applications. This comprises simulations and boundary conditions of three-dimensional OWCs that experience freely decaying displacements, forced oscillations, as well as regular wave excitations. Additional proof of the method is provided using established test cases. These include regular wave modelling and wave interactions with plate structures.

Chapter 4 investigates the characteristics of the radiated waves in the near- and far-fields. The effect of vortex shedding on these wave fields is evaluated. For this purpose, an analytical solution of the wave field around an OWC is implemented and compared with the numerically predicted wave fields from the developed model. Furthermore, methods for quantifying the kinematic properties of flow fields are described. Lastly, the validity of the linear radiation damping is critically evaluated.

Chapter 5 provides evidence of nonlinearities in the forcing and in the motions

of water columns. The physical cause of these nonlinearities are investigated by comparing the responses subjected to different excitation mechanisms. Furthermore, differing mouth shapes or geometries are compared to reveal vortex effects on the nonlinearity. To understand nonlinear free-surface effects on the forces and response, the depth-inline pressure distributions over the cylinder drafts are evaluated. These are shown to be particularly informative. Finally, the physical significance of the nonlinear factors is investigated.

Chapter 6 discusses the behaviour of the hydrodynamic coefficients over a broad range of governing parameters. Based upon these research findings, the relative importance of vortex formation and motion as the nonlinear damping force in an OWC is evaluated. The applicability of the linear superposition theory is then investigated by comparing the hydrodynamic properties of OWCs under the two different excitation mechanisms.

Chapter 7 provides a summary of the work undertaken and discusses the principal findings. It also provides suggestions for future work.

2
Background

2.1 Chapter overview

This chapter reviews the critical issues relating to modelling of dynamically responding OWCs. It begins with an overview of a fluid loading analysis of two contrasting geometrical shapes involving circular cylinders and sharp edges. Section 2.2 reviews the implementation of Morison's equation when modelling the fluid loading on slender circular and sharp-edged cylinders. Within this review, the key parameters determining the fluid loading regimes are carefully described.

The next two sections concentrate on modelling OWCs in potential and viscous flows. Section 2.3 provides a review of the linear potential solutions from earlier studies, the governing equation and the boundary conditions appropriate to these models. The linear analytical model adopted within this thesis is also described. In addition, Sections 2.4 and 2.5 review the nonlinear potential flow models and the nonlinear viscous flow models applied for OWCs, respectively. The latter involves the physical experiments and numerical simulations in a real fluid flow. Critical issues that have yet to be fully explored and that require further investigations are highlighted therein. Following on, the time-domain modelling of dynamically responding OWCs is described in Section 2.6. Finally, concluding comments are provided in Section 2.7 to summarise the aspects that require evaluation given the goals outlined in Chapter 1 and the background theories in this chapter.

2.2 Overview of fluid loading analysis

The prediction of the wave loading on a cylindrical body is often related to the diffraction parameter. This dimensionless number is defined by D/λ; where D is the dimension of the body and λ the incident wave length. In effect, it determines whether the incident wave "feels" the body and will thus be disturbed; the latter taking the form of a scattered wave field. For a slender body ($D/\lambda < 0.2$), the geometrical dimension is sufficiently small that the wave field experiences little or no disturbance, except for the development of a local wake.

Most cylindrical OWCs designed to operate in offshore waves are slender body structures. In fact, it was suggested by Newman (1974) and Evans & Porter (1995, 1997) that the cross-sectional dimension of an OWC be determined to ensure a Helmholtz (piston) mode being the predominant motion mode of the water column rather than a higher-order mode; an example of the latter being a sloshing motion. Such a geometrical condition would ensure that the water column achieves a larger response and uniform displacement. This is usually attained by defining an OWC to have a relatively small diameter that lies within the slender body region, and a length consistent with a deep water draft.

For flows around a slender body, the fluid loading is traditionally predicted using Morison's equation (Morison et al., 1950). Although the present study does not seek to further our understanding of the drag or inertia forces acting on such a body, Morison's equation is relevant to the implementation of the hydrodynamic force model appropriate to an OWC. As such, it will be reviewed herein. Furthermore, the mathematical formulations and, particularly, the variations of the force coefficients with key parameters will be considered in detail.

2.2.1 Morison's equation

In fluid dynamics, Morison's equation is a semi-empirical equation for the in-line force on a fixed or moving body in a fluid flow. In the present study, the equation will be used in a rather different context, hence the wider considerations discussed below. Within Morison's equation, the fluid loading is decomposed into two force components; an inertia force and a drag force. The inertia force, expressed as a function that is in phase with the local flow acceleration $\dot{u}$, is assumed to be due to

acceleration of the fluid in inviscid and attached flow around a body. This component of the load is commonly referred to as the potential flow force. In contrast, the drag force is assumed to be force proportional to the square of the instantaneous flow velocity, u. This represents the contribution due to viscous effects and flow separation; the latter commonly referred to as the vortex force. These two force components are assumed linearly independent and simply added to give the total in-line force. For a fixed body in an oscillatory flow, the Morison's force per unit length is defined by:

$$F(t) = F_{inertia}(t) + F_{drag}(t), \tag{2.1}$$

$$F(t) = \rho C_M \frac{\pi}{4} D^2 \dot{u}(t) + \frac{1}{2} \rho C_D D u(t) |u(t)|, \tag{2.2}$$

where C_M is the inertia coefficient, C_D the drag coefficient, ρ the fluid density and D is the cylinder diameter.

2.2.2 Physical parameters

Extensive experimental work has sought to determine the drag and inertia coefficients for cylinders over the last few decades. These studies established a clear dependence on certain physical parameters. For a smooth cylinder in an oscillatory flow, the coefficients are commonly presented as a function of the Reynolds number $Re\,(= uD/\nu)$, the Keulegan-Carpenter number $KC\,(= uT/D)$ or viscous-frequency parameter $\beta\,(= D^2/\nu T)$ (Sarpkaya, 1975, 1977, 1986, Bearman et al., 1985). Within these parameters, u denotes the velocity, T the period of oscillation, ν the kinematic viscosity and D a characteristic length-scale defined by the cylinder diameter. From a physical point of view, the Re number denotes the relative importance of the viscous force over the inertial force, while the KC number indicates the importance of flow separation. The β number represents the ratio of Re over KC numbers.

Using Equation (2.2), one can deduce the dominance of each force component from the phase shift between the in-line force and the flow velocity. The relative dominance of one force component establishes the flow condition as being either inertia-dominated, drag-dominated, or a combination of the two. This characterisation can be estimated from a plot of the force-velocity phase shift as a function of the KC number. A relatively small phase shift indicates a smaller ratio of the inertial

force over the drag force; the former component being less dominant than the latter. The exact upper limit of KC that characterises the dominance of the inertial force for a circular cylinder in an oscillatory flow, will differ due to the flow dependence on the Re number. However, generally speaking, the flow is either inertia or drag dominated when KC is respectively defined by:

$$0 < KC < 5, \text{ for inertia-dominated flow} \tag{2.3}$$

$$KC > 20, \text{ for drag-dominated flow.} \tag{2.4}$$

For very small KC numbers, a potential flow is assumed; the C_D values being set to zero. However, the laboratory data does not suggest this. Sarpkaya (1986) conducted experimental studies involving circular cylinders and compared measured data with the analytical solution provided by Stokes (1851). On the basis of Sarpkaya's (1986) experimental results, it is clear that at small KC numbers, when the flow is expected to lie within the inertia-dominated regime, the C_D values are substantially larger than expected. In fact, comparisons between the analytical Stokes' (1851) solution and the experimental data in Figure 2.1 show good agreement at extremely small KC numbers. The agreement is because the assumptions defining the flow by which the analytical solution has been derived, meet the actual flow conditions; the flow being unseparated, stable and laminar. This explains why zero C_D values at very small KC numbers do not arise. Specifically, the shear stress associated with surface friction applies on a wall boundary in a viscous flow.

The validity of the Stokes' (1851) solution does not, however, cover the full range of KC numbers. Figure 2.1 also shows that the experimental data describing C_D deviates from the analytical Stokes' (1851) solution when $KC > 0.7$. This relates to the first occurence of vortical instabilities; the force induced by the flow separation becoming more important than the viscous surface friction. Importantly, the C_D coefficient increases sharply when the flow begins to shed vortices. In the current figure, this occurs for $KC > 2$. As the KC number increases, the importance of the drag force becomes progressively more significant. This is consistent with the fluid loading regime defined in Equation (2.4).

In other Re number regimes, the dependence on the physical parameters will differ. For example, in a subcritical flow condition, the variations of the force coefficients are largely determined by the KC number (Sarpkaya, 1975). This means that

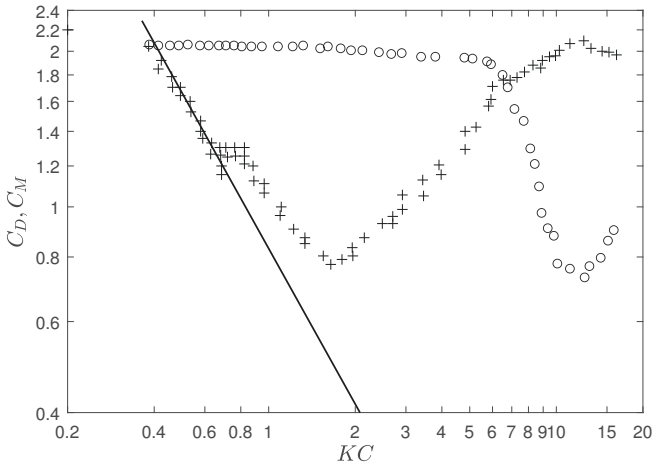

Figure 2.1: Drag C_D [+] and inertia C_M [○] coefficients for a fixed circular cylinder in planar oscillatory flows with varying KC numbers at $\beta = 1035$; the analytical Stokes' (1851) solution defined by [——] and all data in the figure taken from Sarpkaya (1986).

for a small-scaled structure, commonly studied in a physical model test, the flow may be solely varied based upon the KC number. However, if the flow is at a critical or transcritical Reynolds number, the force coefficients will be dependent on both the Re and KC numbers (Sarpkaya, 1977). This leads to important scaling effects; the force coefficients depending on the Re number. This is particularly important when calculating the loads on full-scale structures.

The dependence of the force coefficient on both the Re and KC numbers highlights the importance of the flow behaviour. Most importantly, it is possible to infer the loading regimes within which the different force components dominate. This, in turn, helps to evaluate which force component will critically affect the dynamic response of a moving structure. In considering the design of an OWC for offshore wave energy generation, the loading regime will most likely involve both drag and inertia loading. In considering this, it is important to highlight that vortex shedding does not only occur as the flow separates from the upstream and downstream surfaces of cylinder. Vortices may also form and shed at the open-ended mouth of the OWC. As a result, depending on the mouth shape, the drag-dominated flow regime may exist at a lower KC number for a certain range of Re numbers. In the case of an OWC with a streamlined mouth shape, the definition of the fluid loading regimes may be similar to those given for a circular cylinder. However, for an OWC with a straight and sharp mouth, also referred to as a sharp-edged OWC hereafter, significant vortex

shedding may be produced at its lower end. As a result, the fluid loading regime has the potential to be very different. Following a similar line of argument, one would expect the force coefficients appropriate to sharp-edged cylinders and their dependence on the Re and KC numbers to be very different. A review of work related to these effects is given in the following section.

2.2.3 Geometrical shape effects

The local cross-sectional shape of a body has a strong influence on the flow behaviour and hence the variations of the force coefficients and their dependence on the physical parameters. Keulegan & Carpenter (1958) confirmed the insensitivity of flows past a flat plate to the variation in the Re numbers. The Re number dependence of the associated loading coefficients is markedly reduced relative to those associated with circular cylinders. However, they showed that for a plate oriented normal to an oscillatory flow, the flow is strikingly influenced by the KC number. In general, the drag coefficients appropriate to bodies with sharp-edged geometries, are large at small KC numbers and have an asymptotic value at large KC numbers. Evidence of this has been reported in Bearman et al. (1984, 1985), Hamel-Derouich (1991) and Vengatesan et al. (2000). The large coefficients are associated with the fact that flow separation consistently occurs even at small KC numbers. For instance, the onset of vortex shedding occurs at $KC = 0.2$ for flows past a square cylinder with $\beta = \mathrm{O}(10^4)$(Troesch & Kim, 1991). In contrast, the corresponding KC number is defined by $KC = 3$ for flows past circular cylinders under relatively similar β conditions (Sarpkaya, 1986, Troesch & Kim, 1991). As a result, the range within which the flow is dominated by the drag force will be extended to relatively smaller KC numbers when compared to the corresponding range for a circular cylinder.

For a sharp-edged geometry, the characteristic length-scale appropriate to a KC number is defined by the geometric dimension that is normal to the encountering flow velocity (Bearman et al., 1985). An illustration of this variable is shown in Figure 2.2(A); a longitudinal axis parallel to the characteristic length is also indicated. The importance of this length on C_D values has been confirmed in Tanaka et al. (1983), Bearman et al. (1985) and Hamel-Derouich (1991). Tanaka et al. (1983) showed that reducing this length decreased the value of C_D. His study further confirmed the effect of flow orientation or angle of attack. As depicted in Figure 2.2(B), this

angle is defined by the difference between the longitudinal axis and the flow velocity direction. The drag forcing is markedly reduced if the velocity direction is parallel to the longitudinal axis. In other words, the value of C_D decreases if the encountering flow has a zero angle of attack with respect to the longitudinal axis that defines the characteristic length of a sharp-edged geometry.

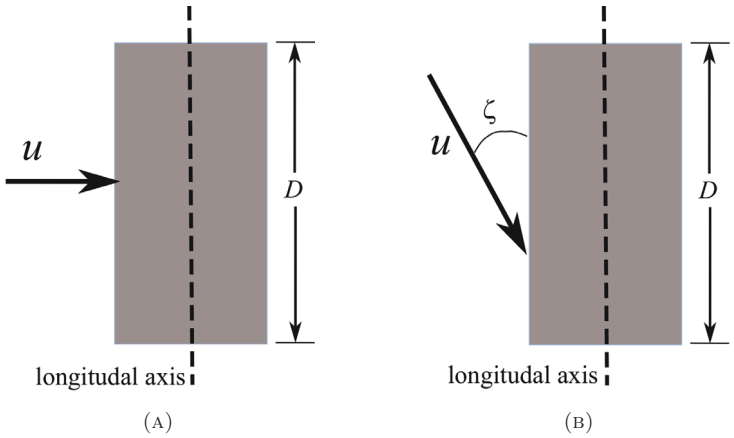

Figure 2.2: Illustration of a sharp-edged geometry with a characteristic length-scale D encountered by a flow velocity u that acts (A) normal to the longitudinal axis and (B) at an angle of attack, ζ, relative to this axis.

Based upon those aforementioned studies, two things are notable when analysing the fluid loading of an OWC. First, the criterion for drag or inertial flow dominance should be based upon the flow separation at the open-ended mouth of the OWC. For a sharp-edged OWC, the fluid loading at the draft is very likely to be affected by vortices even at a small KC number. Second, the vortex shedding at the mouth of the OWC may primarily be dictated by the vertical velocity induced by the oscillating water column. This speculation is suggested by the study of the vortex ring generated during the ejection of fluid out of a circular tube. In this latter flow problem, the fluid displacement within the tube relative to the cylinder diameter is an important parameter defining the vortex ring formation (Gharib et al., 1998). The horizontal velocity of the fluid outside the tube less significantly contributes to the vortex formation at the tube entrance. The study defines the diameter and the vertical velocity of the water column as the characteristic length-scale and characteristic flow velocity, respectively. This definition is consistent with the explanation of the flow orientation noted above. Importantly, it may be reasonable to consider the vertical velocity determined from the oscillation of the water column as the characteristic velocity in a wave-excitation problem.

2.3 Linear potential theory for an OWC

2.3.1 Analytical models

An OWC consists of a water column and air volume inside an enclosing chamber. A piece of turbo machinery that functions to take off the power output, is placed inside an upper passage above the water column free-surface (see Figure 1.1(b)). To understand the complex flow behaviour within an OWC, early researchers have put significant effort into deriving linear analytical models. Within these models, fluid problems are simplified by making assumptions to derive efficient and powerful analytical models. First, the fluid is assumed to be incompressible, irrotational and inviscid. As a result, a potential flow can thus be defined in the fluid domain.

Another consideration is to treat the (oscillating) water column as a body that has certain degrees of freedom. When considering only a heave mode (a simple piston motion), the internal free-surface relating to the water column is assumed to move uniformly. As such, the pressure distribution on this free surface is considered uniform. This approach was adopted in the analytical models developed by Evans & Porter (1995, 1997).

A deformable internal free-surface condition has also been considered by earlier researchers. In this case, the pressure variations accross the internal free-surface need to be taken into account. Evans (1982) considered varying pressure distributions on the internal free-surface within a fixed body, while Falnes & McIver (1985) modelled both varying pressure distributions and oscillating bodies.

2.3.2 Governing equation and boundary conditions

The following description explains the equations that govern a linear potential flow in a linear analytical model. The boundary conditions appropriate to a computational flow domain are also discussed. In considering the focus of the present study, a truncated and hollow cylinder with an infinitesimally thin wall-thickness inside a wave tank of constant water depth h, is depicted in Figure 2.3. The cylinder of draft B and radius b consists of a circular wall that encloses a water column with an internal free-surface S_i.

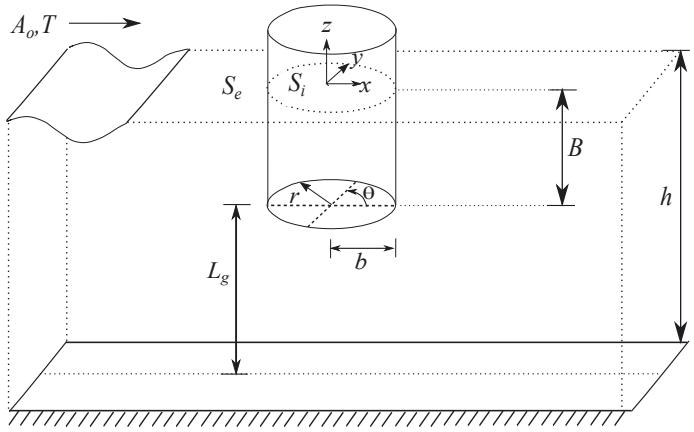

Figure 2.3: Schematic view of a cylindrical OWC inside a wave tank

Within the present study, two potential flow problems relevant to an OWC are modelled. These are described as follows:

(1) **A pure radiation potential flow.** In this problem, no incident waves are approaching the column; the initial conditions are described by a still water condition. Instead, the water column is excited by an oscillating air pressure p of a period T that acts uniformly on the internal free-surface S_i. The air volume above the internal free-surface is fully closed by a rigid wall.

(2) **A scattering potential flow.** In this case, the water column is excited by an incident wave of amplitude A_o and period T. The internal free-surface S_i is exposed to the local atmosphere; the oscillating air pressure p being zero.

In any potential flow problem, the water column inside the cylinder is assumed to be rigid and the internal free-surface non-deformable. Therefore, the horizontal pressure variation on the internal free-surface S_i is negligible. The atmospheric pressure p_a is constant on the external free-surface S_e outside the water column.

In the framework of linear wave theory, a velocity potential exists in any potential flow problem and satisfies the following equations:

$$\nabla^2\Phi = 0, \text{ in the fluid} \tag{2.5}$$

$$\Phi_n = 0, \text{ on solid boundaries} \tag{2.6}$$

where the suffix n denotes the normal derivative (to the boundary). On the linearised

free-surface, the boundary conditions satisfy:

$$g\eta - \frac{\partial \Phi}{\partial t} = \begin{cases} (p_a + p)/\rho, \text{ on } S_i \\ p_a/\rho, \text{ on } S_e \end{cases} \tag{2.7}$$

where $\eta(x, z, t)$ is the surface elevation and is related to the velocity potential through a kinematic boundary condition given by

$$\frac{\partial \eta}{\partial t} = \frac{\partial \Phi}{\partial z}. \tag{2.8}$$

If the motion is assumed to vary harmonically with time, t, the unknown variables Φ, p and η can be represented as functions of ωt as follows:

$$\Phi(x, y, z, t) = Re\left[\phi(x, y, z)\, e^{-i\omega t}\right], \tag{2.9}$$

$$p(t) = Re\left[P_o e^{-i\omega t}\right], \tag{2.10}$$

$$\eta(x, y, z, t) = Re\left[\eta(x, y, z)\, e^{-i\omega t}\right], \tag{2.11}$$

where $\omega = 2\pi/T$ is the angular frequency, T the period of oscillation and P_o is the amplitude of air pressure.

Combining Equations (2.5)-(2.8) produces a boundary-value problem expressed in terms of the time-independent velocity potential ϕ that satisfies these conditions:

$$\nabla^2 \phi = 0, \text{ in the fluid} \tag{2.12}$$

$$\phi_n = 0, \text{ on solid boundaries} \tag{2.13}$$

$$K\phi + \frac{\partial \phi}{\partial z} = \begin{cases} -i\omega P_o/\rho g, \text{ on } S_i \\ 0, \text{ on } S_e \end{cases} \tag{2.14}$$

where $K = \omega^2/g$ and the atmospheric pressure p_a has been set to zero. The potential solution for an OWC subjected to the air pressure and the incident wave is decomposed into two components; the scattered and radiated potentials defined by

$$\phi = \phi^S - \frac{i\omega P_o}{\rho g}\phi^R. \tag{2.15}$$

The scattered potential, ϕ^S, represents the flow excited by the incident wave in the

absence of oscillating air pressure. This potential also includes the flow solely driven by the incident wave. In contrast, the radiated potential, ϕ^R, describes the flow due to the oscillating air pressure on the internal free-surface in the absence of an incident wave. The total potential in a pure radiation potential flow can be written only in terms of ϕ^R. Equation (2.14) may thus be re-expressed by

$$K\phi^R + \frac{\partial \phi^R}{\partial z} = \begin{cases} 1, \text{ on } S_i \\ 0, \text{ on } S_e. \end{cases} \tag{2.16}$$

Linear analytical solutions to problems involving a cylindrical OWC in the presence or in the absence of an incident wave excitation have been proposed in Evans & Porter (1997). In their model, a velocity potential describing the boundary-value problem in a cylindrical coordinate system (r, θ, z) is defined as $\Phi(r, \theta, z, t) = \phi(r, \theta, z)\, e^{-i\omega t}$. A variable separation procedure, $\phi(r, \theta, z) = \phi_n(r, \theta)\, \psi_n(z)$, that requires the definition of a depth-dependent eigenfunction $\psi_n(z)$, is employed. Within the present study, the radiated and scattered potential flow solutions proposed by Evans & Porter (1997) will be adopted and described in the sections that follow.

2.3.3 A linear analytical model: wave radiation

To define this potential solution, the fluid domain is divided into two regions. The inner domain is defined by the fluid volume inside a virtual cylinder of radius b and draft that extends to the tank bottom h. The outer domain consists of the volume outside this virtual cylinder. The definition of the radiated velocity potential, ϕ^R, in terms of a general expansion is based upon this domain decomposition:

$$\phi^R(r, z) = \alpha_0^R H_0(kr)\, \psi_0(z) + \sum_{n=1}^{\infty} \alpha_n^R K_0(k_n r)\, \psi_n(z), \text{ for } r \geq b \tag{2.17}$$

$$\phi^R(r, z) = \beta_0^R J_0(kr)\, \psi_0(z) + \sum_{n=1}^{\infty} \beta_n^R I_0(k_n r)\, \psi_n(z) + K^{-1}, \text{ for } r \leq b. \tag{2.18}$$

Within the outer solution, $r \geq b$, the first term represents the outgoing radiated wave and the infinite series represents the exponentially decaying modes. In these equations, J_0, H_0, I_0, and K_0 are the Bessel and Hankel functions of the first kind and the modified Bessel functions of the first kind and second kind, respectively. All are of order 0; the suffix 0 of all these functions is given to indicate the independency

of the radiated potential on angular variation.

The depth-dependent eigenfunctions, ψ_0 and ψ_n, are associated with the wave numbers of the progressive and standing modes, k and k_n, respectively. The former is determined from the dispersion relationship, while the latter is quantified from the positive real roots of $K + k_n \tan k_n h = 0$. Furthermore, α_0^R, β_0^R, α_n^R and β_n^R are coefficients defining the radiation potential problem, based upon a solution of the boundary conditions. Further description of the derivation of the integral equation and the implementation of a Galerkin approximation to solve the problem are provided in Appendix A.

Having established a convergent solution to the radiated potential problem, the internal surface elevation (the response) and external surface elevation (the radiated wave) around an OWC may be quantified. In parallel, the hydrodynamic properties of the OWC subjected to an air pressure oscillation may also be evaluated by using this solution. It is well known that these properties are related to the hydrodynamic force that can be approximated by inertia and damping terms (Wehausen, 1971). This force quantification requires the evaluation of the added-mass and radiation damping coefficients using the radiated potential at the internal free-surface.

Figure 2.4 presents the hydrodynamic coefficients as functions of frequency and cylinder radius. The relative draft B/h is held constant, while the relative radius b/h is varied. Within this figure, the added mass, A_m, is normalised by the average mass of the water column, and the radiation damping coefficient, B_m, is normalised by the average volume of the water column. The added-mass coefficient, $A_m/\rho A_c B$, is shown to be relatively invariant over most of the frequency range, but significantly dependent on the radius. In contrast, the dimensionless radiation damping coefficient, $B_m/\rho A_c B\omega$, is clearly a function of both geometry and frequency. Moreover, the curves of $B_m/A_c B$ show the more pronounced coefficient at frequencies below the theoretical natural frequency ($\omega^2 B/g = 1$). This arises due to the added mass.

The radiated wave elevation at radial locations from the outer wall of the OWC may be quantified directly from the radiated potential using the linearised dynamic free-surface boundary condition. Alternatively, the radiated wave elevation in the far-field, η^e, may be estimated from the radiation damping coefficient. This approach is based upon the relationship between the linear wave power and the power loss that arises from wave radiation. It is shown in Appendix B that these approaches are

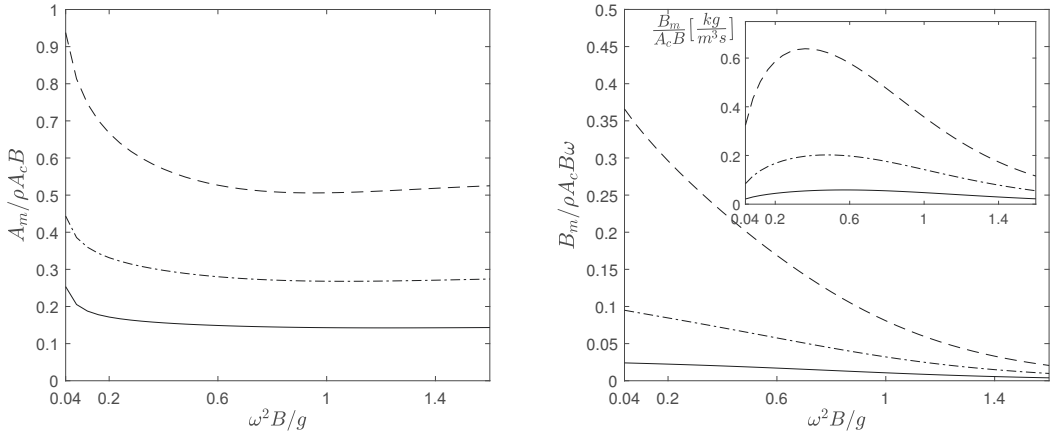

(A) (B)

FIGURE 2.4: (A) Added mass A_m and (B) radiation damping coefficient B_m plotted for varying $\omega^2 B/g$ in the case of $B/h = \frac{1}{2}$ for a cylinder radius of $b/h : \frac{1}{8}[\text{——}]$, $\frac{1}{4}$ $[\text{— · —}]$ and $\frac{1}{2}$ $[\text{— —}]$.

in good agreement. Furthermore, the radiation damping coefficients obtained from WAMIT (WAMIT, 2013) were employed to estimate the radiated wave elevations. These computed elevations also compare well with the present analytical solution (again, see Appendix B). The agreement between these solutions confirm that the analytical radiation solution has been correctly implemented.

2.3.4 A linear analytical model: wave scattering

The scattering potential flow problem can be solved using a similar approach. One substantial difference between the two solutions is the inclusion of the so-called azimuthal mode q. This seeks to incorporate the angular dependence of the wave scattering in the presence of an incident wave. The scattered potential ϕ^S, constructed using general expansion terms, is given by:

$$\phi^S(r,\theta,z) = \sum_{q=0}^{\infty} \epsilon_q i^q cosq\theta \Big[\Big(J_q(kr) + \alpha^S_{q,0} H_q(kr) \Big) \psi_0(z) + \sum_{n=1}^{\infty} \alpha^S_{q,n} K_q(k_n r)\, \psi_n(z) \Big], \quad \text{for } r \geq b \tag{2.19}$$

$$\phi^S(r,\theta,z) = \sum_{q=0}^{\infty} \epsilon_q i^q cosq\theta \Big[\beta^S_{q,0} J_q(kr)\, \psi_0(z) + \sum_{n=1}^{\infty} \beta^S_{q,n} I_q(k_n r)\, \psi_n(z) \Big] \text{ for } r \leq b. \tag{2.20}$$

Within these solutions, $\epsilon_0 = 1$ and $\epsilon_q = 2$, for $q \geq 1$. For the outer region, $r \geq b$, $\alpha^S_{q,0}$ represents the amplitudes of the outgoing progressive wave mode, and the terms arising within the series expansion over n express the exponentially decaying modes. Likewise, $\beta^S_{q,0}$ denotes the amplitudes of the standing wave modes inside the cylinder ($r \leq b$). Furthermore, the first term of the scattered potential inside the square bracket for the outer region represents the incident potential ϕ^I associated with the incident wave. The remaining terms of this potential represent the superposition of the wave field due to the oscillating water column and the disturbed wave field as a result of the cylinder existence in the fluid domain.

Further details concerning the derivation of the integral equation and the implementation of the Galerkin approximation are provided in Appendix C. To verify the present implementation of the analytic wave scattering model, comparisons of the Response Amplitude Operator (RAO) and the phase of this response are shown in Appendix C. Once again, these comparisons involve the results predicted from WAMIT simulations, the existing data presented in Evans & Porter (1997) and the present analytical model. The good agreement shown between these results confirms the successful implementation of the linear potential flow solution.

The far-field amplitude associated with the scattering potential $\alpha^S_{q,0}$ may be estimated by ignoring the exponentially decaying terms in the scattering potential function for $r > b$. Moreover, the Hankel function for large argument can be approximated analytically. Adopting these simplifications, the scattered potential can be expressed as follows:

$$\phi^S \sim R^S(\theta) \left(\frac{2}{\pi kr}\right)^{1/2} e^{ikr - i\pi/4} \psi_0(z), \tag{2.21}$$

where $R^S(\theta)$ is defined by the following expression:

$$R^S(\theta) = \sum_{q=0}^{\infty} \epsilon_q \alpha^S_{q,0} \cos q\theta, \tag{2.22}$$

$$\text{and} \quad \alpha^S_{q,0} = \frac{-\gamma_q J'_q(kb)}{\gamma_q H'_q(kb) + 2iA^S_q}, \tag{2.23}$$

$$A^S_q = \int_{L_g} u^S_q(z)\, \psi_0(z)\, dz, \tag{2.24}$$

$$\gamma_q = \pi kbkhJ'_q(kb). \tag{2.25}$$

Having estimated the modulus of the far-field scattered wave amplitude, $\mid R^S(\theta) \mid$, from Equation (2.22), the results are presented in Figure 2.5. This also provides a comparison with the corresponding results relating to a bottom-mounted cylinder predicted using the analytical solution of Mei (1983). In both cases, four incident wave frequencies are considered; the waves propagating in a wave tank with a one-metre water depth. Within this figure, the dashed and solid lines correspond to the modulus $R^S(\theta)$ around the bottom-mounted cylinder and the OWC with the B/h value set to 1/2, respectively. In all cases, the modulus in an angular direction is indicated by the distance between the line and the origin O. This data effectively highlights the wave frequencies at which the wave reflection is larger than the wave transmission and the excitation condition when the wave radiation is most pronounced.

In Figure 2.5, the scattered wave fields around the bottom-mounted cylinder are as expected; the trends being interpreted from the modulus quantity. With the increasing wave frequencies, the amplitudes of waves scattered upstream increase. This is a direct result of the D/λ ratio discussed earlier; the largest scattered wave occuring in the highest frequency (Figure 2.5(D)).

In the case of the OWC, the scattered wave pattern can be substantially affected by the amplified oscillation of the water column. This is particularly evident when the incident wave is either of a low frequency or a resonant frequency. At the low wave frequency of $\omega^2 B/g = 0.5$, for instance, the transmitted wave elevation behind the cylinder exceeds the reflected wave elevation in front of the cylinder (Figures 2.5(A)). In this case, the radiated wave reduces the reflected wave, whereas the former wave component adds to the transmitted wave. This reduction and amplification of the superposed waves become more evident as the water column experiences a larger amplitude of response. Overall, the transmitted waves are larger than the reflected for low frequencies (Figures 2.5(A) and (B)). Under the resonant condition, when $\omega^2 B/g = 0.875$, the theoretical amplification of the water column is extremely large. As a result, a radial pattern that resembles a wave radiation exists around the OWC (Figure 2.5(C)). This clearly indicates that the influence of the water column is at its most significant in this state. Conversely, in the frequency range of $\omega^2 B/g \geq 1$, the scattered wave pattern associated with the OWC resembles that around the bottom-mounted cylinder. In this case, the water column effect (denoted by the

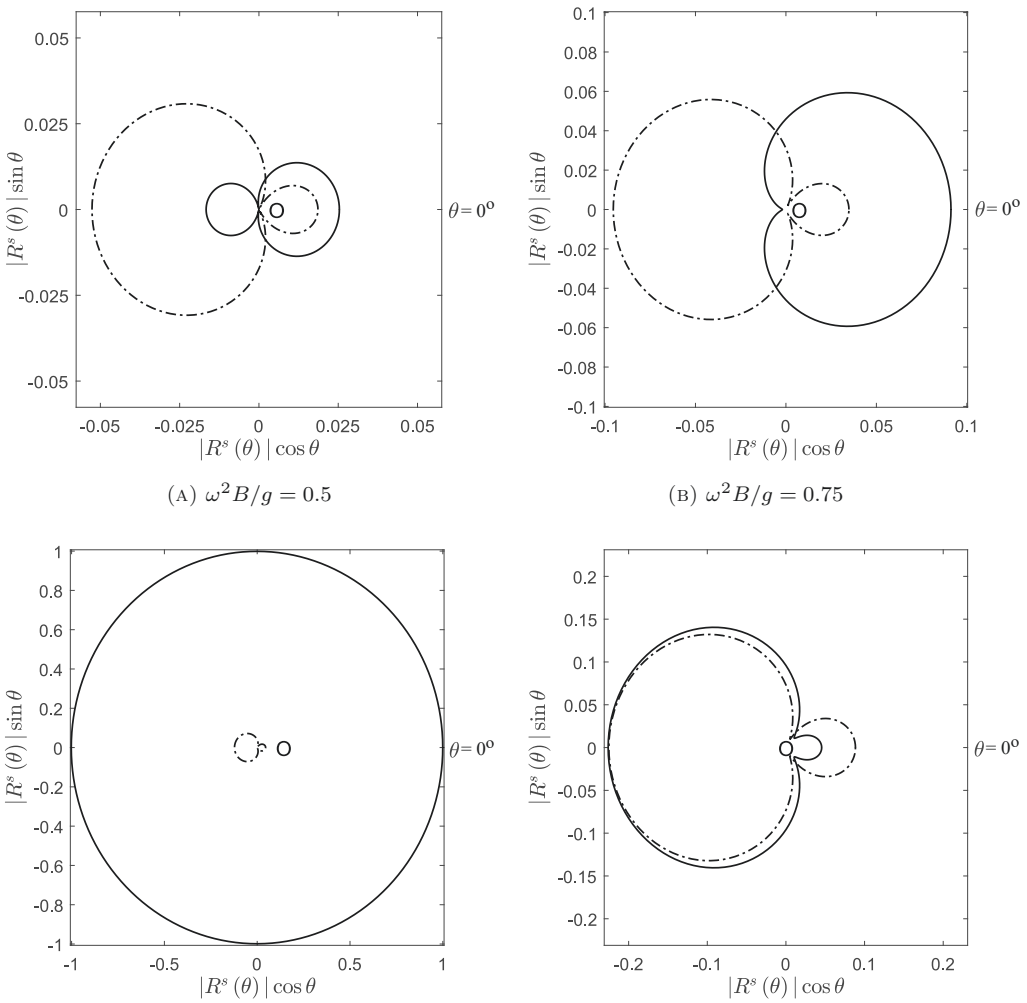

(A) $\omega^2 B/g = 0.5$

(B) $\omega^2 B/g = 0.75$

(C) $\omega^2 B/g = 0.875$

(D) $\omega^2 B/g = 1.25$

FIGURE 2.5: The modulus of the far-field scattered wave amplitudes $\mid R^S(\theta) \mid$ around a cylindrical OWC of radius $r/h = 1/8$ and draft $B/h = 1/2$ [——] compared to that around a bottom-mounted cylinder [— · —]; the incident waves with varying frequencies $\omega^2 B/g$ propagating from $\theta = \pi$.

difference between the lines) is small. This is consistent with its fact that in this high frequency regime, the incident wave does not excite the water column highly; the *RAO* indicated in Figure C.2(A) of Appendix C being small.

2.3.5 Numerical models

In an analytical model, the boundary conditions are defined specifically to solve the problem under investigation. An analytical solution is thus (usually) only applicable to a simple geometrical shape. When modelling a more complex geometry, a Boundary Element Method (BEM) may be utilised as an alternative numerical

model to solve a boundary-value problem. Unlike the analytical model, the BEM solves a Boundary Integral Equation (BIE) on the boundaries of a computational domain. The domain is discretised into a number of discrete panels on which a constant or higher-order velocity potential is defined; the former known as a constant panel method (CPM) and the latter referred to as Higher-order Boundary Element Method (HOBEM). A set of linear algebraic equations relating the unknown velocity potentials to some source terms is derived when implementing the BIE and the boundary conditions on each panel. By solving these equations through an iterative solver, the velocity potential of each panel on the computational boundaries may be estimated.

The BEM has been employed to numerically model an OWC in a linear potential flow using commercial or open-source wave-analysis programmes. These include WAMIT (Lee & Newman, 1996, Delaure & Lewis, 2003), AQUADYN (Brito-Melo et al., 1999) and NEMOH (Babarit & Delhommeau, 2015). The governing equation and boundary conditions are identical to those described in Section 2.3.2; the flow assumptions remain unchanged. In undertaking such calculations, the above noted studies highlight the need to have an adequate number of discrete panels to achieve a convergent result. This finding is unsurprising; the CPM was adopted in their studies and this method depends significantly on the panel number (Bai & Eatock Taylor, 2006).

An alternative numerical approach is based upon a finite element method (FEM). In this method, the computational domain is discretised into a finite number of elements. The velocity potential on each element is approximated by the sum of products of the velocity potential and shape function at a finite number of nodes. The number of computational nodes is thus higher than that in a BEM, yet the global coefficient matrix is symmetric and sparse (Davidson & Costello, 2020). As such, the computational storage is less costly and the matrix can be solved with reduced CPU time. A study by Nader et al. (2012) has implemented an FEM to model arrays of cylindrical OWCs.

2.4 OWC modelling in fully nonlinear potential flow

In a linear potential model, the free-surface boundary conditions are approximated at the mean free-surface. This contrasts with a fully nonlinear potential flow model in which the dynamic and kinematic free-surface boundary conditions are imposed on the instantaneous free-surface. Such models are usually developed in a time-domain simulation. For a two-dimensional modelling approach, Koo & Kim (2010) used an acceleration potential method to calculate the time-derivative of the velocity potential. In contrast, Ning et al. (2015) and Wang et al. (2018) employed a HOBEM in their OWC models.

To control the moving free-surface boundaries, a mixed Eulerian-Lagrangian (MEL) approach and a high-order Runge-Kutta (typically fourth-order) time-integration scheme were adopted in all these cited studies. The MEL approach necessitates that any node on the free-surface boundaries move along with the water particle velocities on these boundaries; the direction of travel not being limited to a single direction. The fully nonlinear dynamic and kinematic free-surface boundary conditions on the internal free-surface in a Lagrangian frame are expressed respectively as follows:

$$\frac{\partial \Phi}{\partial t} = -g\eta + \frac{1}{2}|\nabla\Phi|^2 - \frac{p}{\rho} - \mu_2 \frac{\partial \Phi}{\partial z}, \tag{2.26}$$

$$\frac{\partial \eta}{\partial t} = \nabla\Phi, \tag{2.27}$$

where p is again the air pressure above the internal free-surface. To incorporate dissipative forces, Koo & Kim (2010), Ning et al. (2015) and Wang et al. (2018) added another term involving a damping coefficient μ_2. The value was estimated by tuning the numerically predicted *RAO* with existing experimental or numerical results. Taken together these studies indicate the importance of the viscous effect. The importance of the additional damping coefficient raises questions concerning the appropriateness of all but the simplest (linear) potential flow solutions.

2.5 OWC modelling in fully nonlinear viscous flow

2.5.1 Physical experiments

There have been a small number of earlier studies concerning the significance of vortex shedding in OWCs. These studies were undertaken experimentally, typically involving simple models. For example, Knott & Flower (1979) utilised two submerged parallel-sided plates. These plates were of finite height, extending from the tank bottom to a certain height below the mean free-surface. The energy loss, quantified using the reflected and transmitted wave amplitudes, was estimated to be 5% of the incident wave energy. The wave steepness in the experiment was small, suggesting that wave breaking was not significant. As a result, it was concluded that vortex shedding was the physical cause.

With advances in flow visualisation, Knott & Mackley (1980) were able to reveal the marked contribution of vortex shedding in dissipating the energy stored in an oscillating water column. The enclosing wall was a surface-piercing tube of a finite draft. The tube had a straight-ended and sharp-edged or a bell-shaped mouth with a finite radius of curvature. The water column, as illustrated in Figures 2.6(A) and (B), was initially displaced above the still water level (SWL) in an initially stagnant water tank. The water column was then released and gradually decayed over a sequence of oscillations until it became completely still. In this so-called "decay test", the flow field was visualised by seeding the water with fine polyethylene particles. The water was illuminated by an optical system appropriate for the photography. The formation of a vortex ring was observed during both an upward and downward displacement of the water column inside the straight and sharp-edged tube. The first downward displacement gave the strongest, most evident, vortex motion.

The effect of the tube mouth shape was investigated and shown to be significant. Specifically, it was found that the energy stored in the water column inside the straight and sharp-edged tube was significantly dissipated. However, a marked decrease of energy loss occured if the mouth shape was replaced with a streamlined shape. Following on, the relationship between the shed vortex ring and the decaying water column amplitude was evaluated. This was undertaken by comparing (quantitatively) the energy loss with the kinetic energy bounded in a vortex ring. The kinetic energy was estimated based upon the size of the vortex ring generated

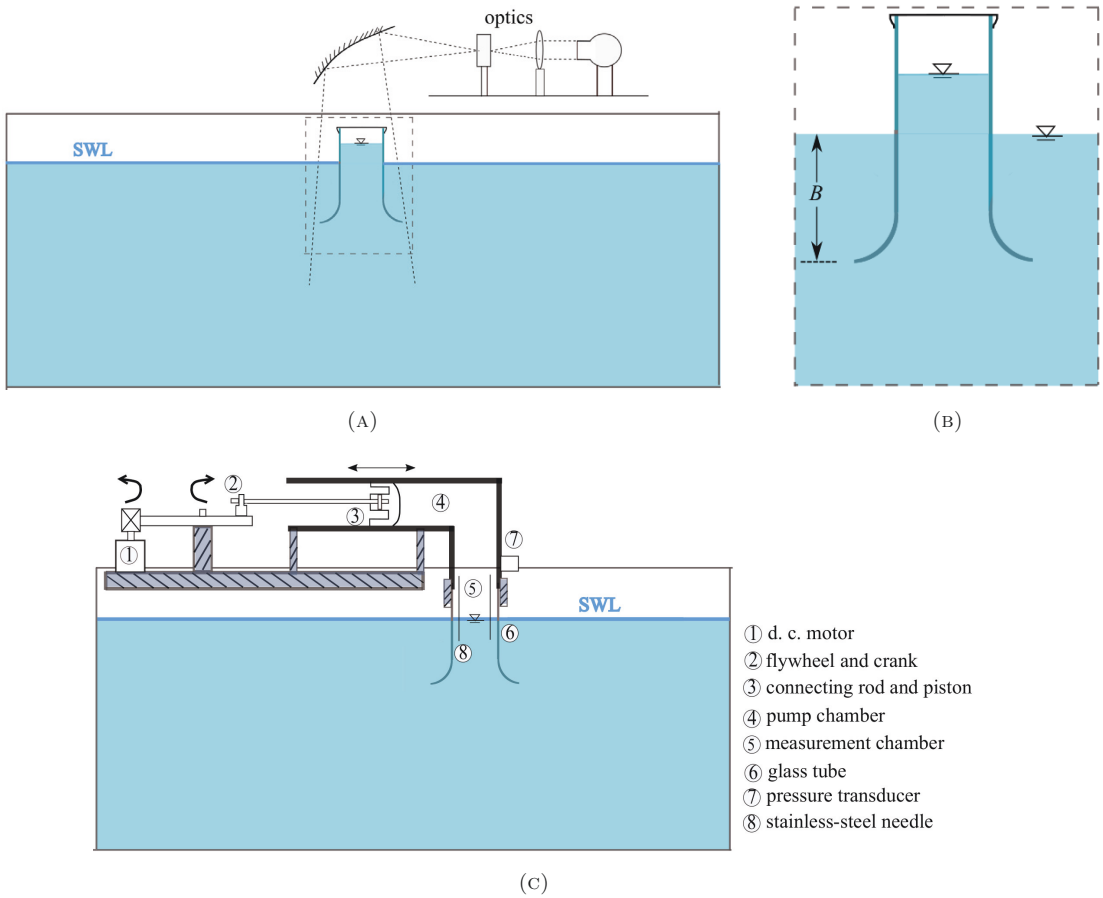

FIGURE 2.6: Schematic descriptions of: (A) an intially-displaced water column in a decay test (B) a close-up view of (A), and (C) a water column subjected to a forced oscillation test. These figures were redrawn from Knott & Mackley (1980) and Knott & Flower (1980).

from the first decay. These comparisons suggest that the major damping mechanism within the freely decaying water column was associated with the vortex ring formation. The decay rate was found to be dependent on the amplitude of the water column. A mathematical formula based upon the drag force in Morison's equation was expressed to represent this nonlinear damping force.

In Knott & Flower (1980)'s experiment, the water column inside a cylindrical tube was forced to heave by a sinusoidally displaced piston. This was located above the water column. The experimental setup is schematically depicted in Figure 2.6(C). A piston was displaced by a crank shaft connected to a heavy flywheel and driven by a small d.c. motor. The air volume in the pump chamber acted as a stiff spring. The water column thus moved rigidly in accordance with the displacement of the piston. In effect, the power transferred from the motor provided the water column the necessary amount of energy to oscillate steadily. In this so-called "forced oscillation

test", the displacement of the water column and its frequency of oscillation were measured by using two stainless-steel needles. These needles, as shown in Figure 2.6(C), were placed inside the tube and projecting into the internal free-surface. To measure the air pressure in the pump chamber, a pressure transducer was placed at a certain height above the free-surface. The product of this measured pressure and the free-surface velocity gave an estimation of the amount of power required to displace the water column.

Knott & Flower (1980) analysed the minimum amplitude of oscillation at which the vortex shedding began to play a damping role. This analysis was undertaken by showing a relation between the power and the free-surface velocity. For a straight-ended and sharp-edged tube, the flow separation occured immediately, even with a small amplitude displacement. The identification of a minimum amplitude was thus not straightforward; the nonlinear damping due to vortex shedding consistently outweighing the radiation damping. In contrast, the minimum amplitude markedly increased with the radius of curvature of a streamlined mouth. With the introduction of a streamlined mouth, the vortex shedding only acts as the primary damping mechanism at large amplitudes of oscillation. In considering the importance of the vortex induced damping in general, a broader range of test conditions are required. In particular, investigations should be undertaken to understand the role of varying cylinder diameter and oscillation frequency. In undertaking these steps, it is expected that the dependence of the damping on key parameters may be understood and ultimately, the dynamic response of an OWC under the various flow conditions may be fully comprehended.

In seeking to understand the operation of an OWC, related work concerning the so-called gap flow inside a moonpool is also relevant. This is justified because a moonpool, also known as a vertical well in the context of a drilling ship, is defined by a similar set of forces applied to the control volume surrounding the gap fluid (effectively water column). Aalbers (1984) experimentally studied the response of a cylindrical moonpool. Within this study, a variety of test arrangements were considered. This include moonpools that were freely decaying, forced to oscillate in still water, and excited by incident waves. In the first case, the experimental setup was similar to the physical experiments in Knott & Mackley (1980).

Aalbers (1984) estimated the nonlinear damping coefficients from the decay tests,

while the other hydrodynamic coefficients (added-mass and radiation damping coefficients) were simply predicted from a linear potential solution. Unfortunately, the applicability of these coefficients to simulate the responses of the moonpool undergoing the forced oscillations are invalid, particularly where high frequencies were addressed. Indeed, the over-estimation of the simulated response may indicate a higher level of damping associated with the vortex shedding in these cases. Interestingly, the deviation may have also been due (in part) to inconsistencies in the water column amplitudes and oscillation frequencies prescribed for the two test cases: the forced oscillation and decay tests. In contrast, the wave-excitation tests are more encouraging. However, Aalbers (1984) provides little by way of justification for using a decay test to estimate the damping and a potential solution to predict the added mass when the goal is to predict a wave-induced response.

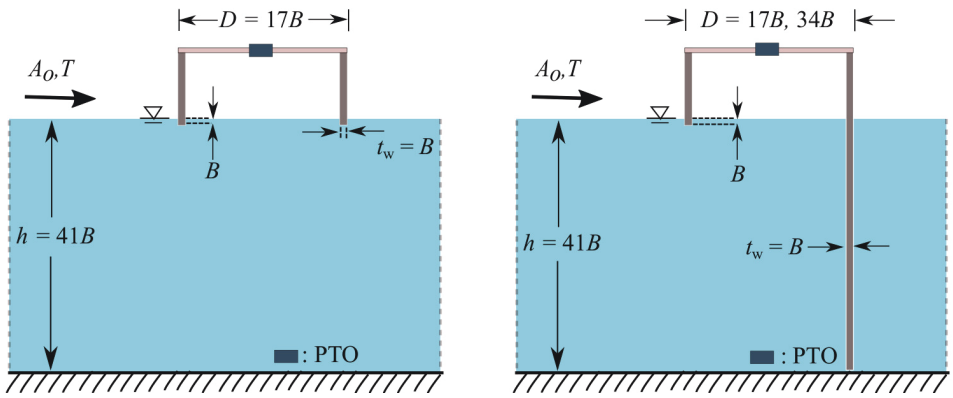

FIGURE 2.7: Schematic figures of (A) a symmetrical detached and (B) an asymmetrical bottom-standing OWC that undergoes wave excitation in the experimental study by Sarmento (1992)

The significance of vortex shedding on the response of a water column to incident waves has also been reported in the experimental studies by Sykes et al. (2008) and Wang & Falzarano (2017). In both cases, their models involved hollow cylindrical structures. The dynamic magnification factors of the responses (RAOs) were significantly under-estimated by the linear potential solutions at or near the resonant condition. An experimental model of an OWC is, however, more representative when it incorporates a power-take-off (PTO) system. This is typically undertaken by modelling the relationship between the pressure drop and the discharge of the air flow through the turbine; the former being the difference between the air pressure in the chamber and the atmospheric pressure. The characteristics of the modelled turbine

is set according to the intended nature of the PTO. A porous membrane or an orifice may be utilised to model a linear or nonlinear PTO, respectively. This was implemented in Sarmento (1992) to investigate the energy loss associated with the water column in a regular wave test. His experiment involved two slightly-immersed OWC types: (i) a symmetrical and detached double-plate structure, and (ii) an asymmetrical double-plate with its rear plate extended to the tank bottom. These models are depicted in Figures 2.7(A) and (B), respectively. At first, the amount of energy absorption was estimated based upon the measured air pressure p and air discharge q; the air assumed to be incompressible. As such, the air velocity was assumed equal to the internal free-surface velocity. In this case, the power ratio, ε, available for extraction was determined by:

$$\varepsilon = \frac{1}{P_i}\frac{1}{wT}\int_0^T p\,(t)\,q\,(t)\,dt, \tag{2.28}$$

where T is the incident wave period, w the tank width and P_i the incident wave power; the last variable estimated from Equation (B.4). This power ratio ε, also referred to as the hydrodynamic efficiency, is clearly dependent on the air discharge q, air pressure p, and the phase difference of these two variables.

Finally, the energy loss coefficient, C_l, was deduced from the ratios of the reflected and transmitted wave heights, H_r and H_t, relative to the incident wave height, H_i. Adopting these definitions, C_l is defined by

$$C_l = 1 - \left[(C_r)^2 + (C_t)^2\right] - \varepsilon, \tag{2.29}$$

$$\text{where } C_r = \frac{H_r}{H_i} \text{ and } C_t = \frac{H_t}{H_i}, \tag{2.30}$$

with C_r and C_t representing the reflection and transmission coefficients, respectively. At a wave steepness of $A_o k \leq 0.05$, the energy loss coefficients C_l were less than 20% and 10% in a symmetrical and asymmetrical OWC device, respectively. These were based upon comparisons with the theoretical result (Sarmento & Falcao, 1985).

In response to these earlier studies, Morris-Thomas MT & Thiagarajan (2006) studied the hydrodynamic efficiencies of an asymmetrical and bottom-standing OWC with various front plate shapes, wall-thickness and draft conditions. The experimental model was similar to the OWC type shown in Figure 2.7(B), except that the front-plate draft B was relatively deep lying in the range of $0.16 \leq B/h \leq 0.25$.

Furthermore, a relatively wide range of wave steepness at $0.01 \leq A_o k \leq 0.22$ was considered. Within this model, an orifice was implemented at the top enclosing wall of the OWC to model a nonlinear PTO.

Some notable findings given by Morris-Thomas MT & Thiagarajan (2006) are discussed as follows:

(i) The frequency-dependent hydrodynamic efficiencies were smaller than the analytically predicted values (Evans & Porter, 1995); the maximum percentage of reduction being 30%.

(ii) The wall thickness only moderately affects the hydrodynamic efficiencies in the high frequency range. In contrast, the draft has considerably more influence over a similar frequency range.

(iii) The measured natural frequency is reduced relative to the analytically predicted value.

(iv) The end shape (a sharp or semicircular end) of the front plate had an insignificant effect on the hydrodynamic efficiencies across a broad range of wave frequencies.

The first suggests that the incident wave steepness and plate draft do indeed affect the amount of energy loss. This is supported by the second result and a direct comparison with the earlier findings of Sarmento (1992); the latter estimating the efficiency reduction to be of the order of 10%. The third result has implications for the change in the excitation condition within the water column. As such, the response of the water column may be significantly modified due to vortex sheddding, and implementations of linear potential theory and linear superposition theory may thus be inappropriate. Unfortunately, these experimental studies did not study these aspects, but focused on the overall effect of vortex shedding on the efficiency. Furthermore, the fourth result may be associated with the state when flow separation becomes less sensitive to a local cross-sectional shape, provided that a certain KC number is exceeded. A similar finding has been reported by Bearman et al. (1985) for oscillatory flows past sharp-edged plates with various cross-sectional shapes; the measured drag coefficients for all the shapes varying similarly with the KC number. However, direct evidence of the damping coefficients and energy loss associated with

the shapes considered in Morris-Thomas MT & Thiagarajan (2006), is not provided. Consequently, futher interpretation is not possible.

2.5.2 Numerical calculations

Although a physical model presents the actual physics, subject to any scaling inaccuracies, it can be challenging to record multiple different physical quantities in an experimental study. For example, simultaneously recording the response of the water column, pressure and the velocity fields in an experimental model can be overwhelming. In contrast, a high-fidelity numerical solver can capture all the important physics from a single numerical viscous flow modelling, particularly the water particle kinematics. Specifically, a sequence of measuring activities, multiple measurement devices and complex image post-processing are not necessary. At present, the majority of numerical models of OWCs in a viscous flow has been limited to two-dimensional problems. Notable examples include the pioneering work by Şentürk & Özdamar (2011) and Zhang et al. (2012). While some fully three-dimensional numerical studies of detached or bottom-standing OWCs with rectangular cross-sections have also been undertaken, the interpretation (and generality) of the results arising is limited.

The numerical viscous flow modelling of OWCs have been developed using both commercial and open-source viscous solvers. For example, a two-phase level set method was employed in an in-house solver (Zhang et al., 2012) and in an open-source hydrodynamics programme, REEF3D (Kamath et al., 2015), to model a bottom-standing OWC. Furthermore, a volume fluid of method (VOF) was implemented in a commercial programme FLUENT to model a geometrically similar OWC in Luo et al. (2014) and a detached OWC in Şentürk & Özdamar (2011). The interface-capturing method (appropriate to VOF) supported in an open-source IHFOAM viscous solver was also utilised to capture the internal surface elevation of a detached and box-shaped OWC model in Iturrioz et al. (2014, 2015). Similarly, the VOF method developed in the STAR–CCM+ viscous solver was used to investigate the energy losses in a bottom-standing and detached OWC (Elhanafi et al., 2016, 2017a).

In most cases, validation of the models were undertaken by comparing the hydrodynamic efficiencies, the air pressures and velocities as well as the internal surface elevations. Furthermore, an interpretation of the hydrodynamic efficiencies esti-

mated from these quantities is based upon the description of the flow fields. For example, Kamath et al. (2015) observed the vortex shedding at the bottom tip of the front plate of a bottom-standing OWC and showed that the change in the phase shift between the air pressure and air velocity was related to the vortices. Iturrioz et al. (2015) also showed the vorticity fields near the bottom edges of a detached OWC and further argued that the energy loss was associated with these vorticity fields. Following on, the influence of incident wave length and wave height on the vortex generation was interpretated from qualitative descriptions of the flow fields in Elhanafi et al. (2017a,b).

Although these numerical models of OWCs have advanced our understanding, complementing the earlier experimental models, they are not directly relevant to the present study. The explanation for this lies in two parts:

(i) The wave scattering (diffraction) around a box, or the wave reflection and transmission by a rectangular section, can be very different to the problem involving a cylindrical body. This was first discussed in Section 2.5.1.

(ii) The vortex shedding at the mouth of an OWC will markedly differ. Kamath et al. (2015) found that a single vortex was generated at the front plate of a bottom-standing OWC during the displacement of the water column, while Iturrioz et al. (2015) and Elhanafi et al. (2017b) observed that two vortices were formed in the case of a detached OWC.

The points noted above may indicate the following considerations:

(i) The interaction between wave and an OWC affects the hydrodynamic efficiency. For instance, the theoretical optimal hydrodynamic efficiencies of a symmetrical and asymmetrical OWC in a two-dimensional problem are 0.5 and 1.0, respectively (Sarmento & Falcao, 1985, Sarmento, 1992), and

(ii) The damping coefficients arising from vortex may not be identical due to the incomparable strength and behaviour of vortices.

More fundamentally, the nonlinearities arising in the description of an OWC have received very little attention. This is surprising given the fact that nonlinearities are clearly evident in the above noted studies. For example, high-frequency content and asymmetrical records are observed in the time-varying air velocity and air pressure

in a pneumatic chamber (Zhang et al., 2012, Iturrioz et al., 2015, Kamath et al., 2015, Elhanafi et al., 2017a). Moreover, the surface elevations inside an OWC also exhibit nonlinearities (Zhang et al., 2012, Kamath et al., 2015). These nonlinearities are important for two reasons:

(i) The air pressure and motion (response) of a water column, as well as their relative phase shift, determine the hydrodynamic efficiency, and

(ii) A good understanding of these nonlinearities is required to develop an appropriate time-domain modelling of an OWC.

Given the points noted above, it is necessary to understand the physical origins of the nonlinear characteristics. This includes the high-frequency content, asymmetrical shape and nonlinear dependence on the incident wave. This inevitably involves an investigation of how force affects the motions based upon forcing mechanisms appropriate to an OWC. However, it remains a real challenge to identify whether a nonlinear characteristic arises from the free-surface nonlinearity or vortex shedding. This is, in part, because the viscous flow solvers implemented thus far couple all these effects in a single model. To address this issue, an alternative viscous flow model needs to be proposed.

The present study seeks to understand the nonlinear forcing and motions of a detached and cylindrical OWC. Given the fundamental nature of this work, the incorporation of a PTO system into the numerical modelling of an OWC may obscure the relation between vortices and nonlinear forces and motions; an increase in the damping arising from a PTO reducing the response yet magnifying the air pressure. As a result, it was decided to exclude a PTO damping in the viscous flow model. While this undoubtedly detracts from the practical application of the work, it allows the work to focus on the other sources of nonlinearity. Nevertheless, it is important to note that the range of geometrical dimensions in the present study is based upon typical cylindrical OWCs in intermediate and deep water conditions (Knott & Flower, 1980, Knott & Mackley, 1980, Gomes et al., 2012).

2.6 Modelling the rigid-body dynamics of an OWC

This section explains the present implementation of the time-domain modelling of an OWC. Two excitation mechanisms are adopted to drive the oscillation of the water

column. The first, indicated in Figure 2.8(A)(i), is driven by a regular wave excitation and the second, indicated in Figure 2.8(A)(ii), is driven by a forced excitation. In both cases, the water column is inside a cylindrical wall. For the wave excitation problem, the cylinder has a top end exposed to the local atmosphere. The pressure induced by an incident wave of amplitude A_o and period T determines the pressure P_b, that acts perpendicularly on the bottom cross-sectional area A_c. This pressure is shown to have an asymmetrical distribution in Figure 2.8(A)(i).

For the forced excitation model, the internal surface elevation is fully closed by a solid wall placed above the free surface. The wall movement is prescribed to mimic a moving piston as described in Knott & Flower (1980). As a result, a non-zero air pressure p with a uniform distribution acts on the free surface to respond to the prescribed wall movement. This, in turn, produces an axisymmetric pressure distribution P_b at the bottom inlet as shown in Figure 2.8(A)(ii).

In response to the applied forces, the water column oscillates to balance the net force. A schematic showing the dynamic system of the water column and its cartesian coordinate system of $X_i = (x_1, x_2, x_3)$ is illustrated in Figure 2.8(B). The water column has a control volume of Ω. On Figure 2.8(B), this volume is indicated by the grey rectangle and bounded by a top surface, S_t, and a bottom surface, S_b. Taking the upward direction as positive, the unit outward normal vector on S_t is +1, and on S_b is -1.

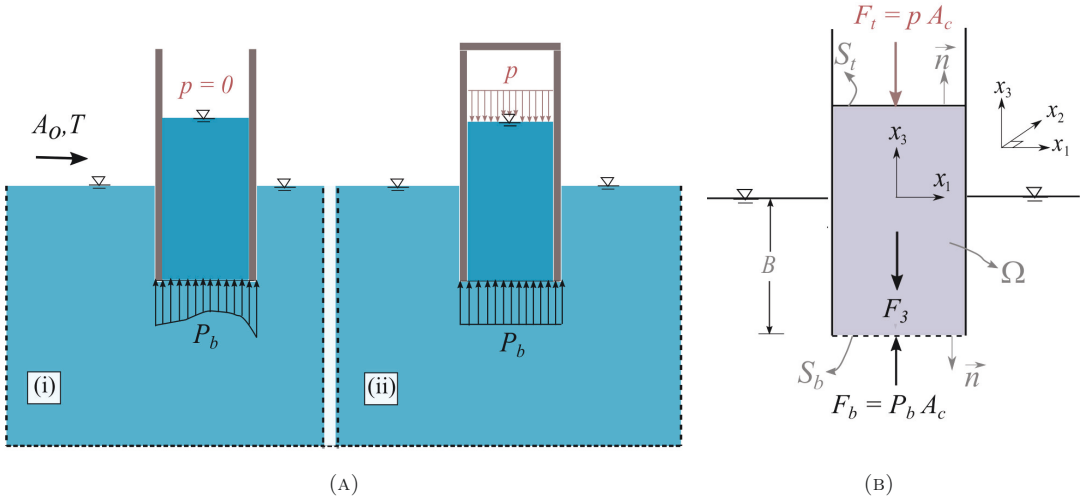

(A) (B)

Figure 2.8: Schematic figures showing (A) pressure distributions that act on the top and bottom areas of the enclosed water column undergoing (i) a wave excitation and (ii) a forced excitation and (B) the dynamic system of the water column and its coordinate system.

A mathematical model to predict the response of the water column subject to an excitation force is presented as follows. In all excitation problems, the water column is treated as a rigid body. As such, a piston mode is considered to be the only relevant dynamic model. In this case, the internal free-surface and the water particles in the water column are therefore assumed to move in unison. The convective acceleration term can thus be canceled out. This leaves only the unsteady term of the time derivative. In the cartesian coordinate system, momentum conservation is represented by:

$$\frac{\partial}{\partial t}\int_{\Omega}\rho u_3\, d\Omega = -\int_{S_b} P_b n_3 dS + pA_c - F_3, \tag{2.31}$$

where F_3 is the body force, P_b and p are respectively the pressures on the bottom and above the internal free-surface. The first term of the right hand side of Equation (2.31) is approximated using the Bernoulli equation and given as:

$$\int_{S_b} P_b n_3 dS = \int_{S_b}\rho\frac{\partial\Phi}{\partial t}n_3 dS + \int_{S_b}\frac{1}{2}\rho u_3^2 n_3 dS - \int_{S_b}\rho g B n_3 dS, \tag{2.32}$$

where B is the draft. Combining Equations (2.31) and (2.32) gives

$$\frac{\partial}{\partial t}\int_{\Omega}\rho u_3 d\Omega + \int_{S_b}\rho\frac{\partial\Phi}{\partial t}n_3 dS + \int_{S_b}\frac{1}{2}\rho u_3^2 n_3 dS = \int_{S_b}\rho g B n_3 dS + pA_c - \rho g\Omega. \tag{2.33}$$

In the absence of an incident wave, the potential flow in a forced oscillation is only associated with a radiated velocity potential. Therefore, the time-derivative of this velocity potential in Equation (2.33) may be expressed as a summation of an added-mass force and wave-radiation damping force as follows:

$$\int_{S_b}\rho\frac{\partial\Phi}{\partial t}n_3 dS = A_m\ddot{x}_3 + b_1 A_c\dot{x}_3. \tag{2.34}$$

This equation applies to the forced oscillation case illustrated in Figure 2.8(A)(ii). A_m is again the added mass and b_1 is the wave-radiation damping coefficient per unit cross-sectional area of the water column A_c; the coefficient being related to the former notation of radiation damping B_m in Section 2.3.3 by $B_m = b_1 A_c$. Substituting for the instantaneous volume of water in the column $\Omega(t) = A_c(B + x_3(t))$, the added-mass and wave-radiation damping forces of Equation (2.34) into Equation (2.33)

produces a mathematical form of the dynamic system of water column:

$$\{\rho A_c(B + x_3) + A_m\}\ddot{x_3} + b_1 A_c \dot{x_3} + \rho g A_c x_3 + \frac{1}{2}\rho A_c \dot{x}_3^2 = pA_c. \tag{2.35}$$

If an equivalent power loss P_l due to a nonlinear damping force is expressed as:

$$P_l = \frac{1}{2} b_2 \rho A_c \dot{x}_3^2 |\dot{x}_3|, \tag{2.36}$$

then b_2 denotes a nonlinear damping coefficient that may arise either from vortex shedding or surface friction or both. The absolute notation adopted in Equation (2.36) is to correctly identify the dependence of this damping on the velocity direction.

Dividing Equation (2.36) by the velocity $\dot{x}_3$ generates the formula of a nonlinear damping force. To take this damping into account, the nonlinear damping force is added to the mathematical form of the dynamic system of water column given in Equation (2.35). This produces a complete mathematical formulation of the dynamic system of an OWC undergoing a forced oscillation.

$$\begin{aligned}\left[\rho A_c(B + x_3) + A_m\right] \ddot{x}_3(t) + b_1 A_c \dot{x}_3(t) + \frac{1}{2} b_2 \rho A_c \dot{x}_3(t)|\dot{x}_3(t)| \\ + \rho g A_c x_3(t) + \frac{1}{2}\rho A_c \dot{x}_3^2 = F_t\,(t)\,,\end{aligned} \tag{2.37}$$

where $\frac{1}{2}\rho A_c \dot{x}_3^2$ is the second-order excitation force, and F_t is the excitation force given by pA_c. It should be noted herein that a forced excitation may be undertaken either by prescribing the water column displacement, which is similar to the moving piston wall, or by defining the air pressure oscillation. In the following chapters, the former will be referred to as a forced water column test and the latter as a forced air pressure test. For both cases, the time-domain OWC modelling expressed in Equation (2.37) may be applied.

The mathematical formulation noted above will be used in the subsequent chapters for two research objectives. First, the physical significance of the nonlinearity sources that contribute to the forcing and motions in a forced oscillation model will be investigated in Chapter 5. Second, the nonlinear dependence of the added mass A_m and the nonlinear damping coefficient b_2 on the key parameters will be evaluated in Chapter 6. In both analyses, the mathematical formulation expressed in Equa-

tion (2.37) will be adopted. Prior to the second analysis, it is necessary to evaluate the validity of the linear radiation theory and the justification for using the linear potential solution to estimate the radiation damping coefficient b_1. This requires an investigation of the radiated wave field around the OWC, which will be explained in Chapter 4.

In the presence of an incident wave, the time-derivative of velocity potential in Equation (2.33) is associated with an incident Φ^I, diffracted Φ^D and radiated potential Φ^R. The derivative term of the superposed potential Φ may be written as:

$$\int_{S_b} \rho \frac{\partial \Phi}{\partial t} n_3 dS = \int_{S_b} \rho \left(\frac{\partial \Phi^I}{\partial t} + \frac{\partial \Phi^D}{\partial t} + \frac{\partial \Phi^R}{\partial t} \right) n_3 dS, \tag{2.38}$$

$$= \int_{S_b} \rho \left(\frac{\partial \Phi^I}{\partial t} + \frac{\partial \Phi^D}{\partial t} \right) n_3 dS + A_m \ddot{x}_3 + b_1 A_c \dot{x}_3. \tag{2.39}$$

Substituting Equation (2.39) into Equations (2.32) and (2.31) and incorporating the power loss due to a nonlinear damping force (as described previously), produces a mathematical formulation of the dynamic system of an OWC subjected to a wave excitation.

$$\begin{aligned} \left[\rho A_c (B + x_3) + A_m\right] \ddot{x}_3(t) + b_1 A_c \dot{x}_3(t) + \frac{1}{2} b_2 \rho A_c \dot{x}_3(t) |\dot{x}_3(t)| \\ + \rho g A_c x_3(t) + \frac{1}{2} \rho A_c \dot{x}_3^2 = F_{ext}(t), \end{aligned} \tag{2.40}$$

where p is known to be zero in this wave excitation case, as indicated in Figure 2.8(A)(ii). The diffracted potential Φ^D is essentially the difference between the scattered potential and the incident and radiated potential. For a slender body, the diffracted potential can be assumed to be negligible as explained previously.

Furthermore, the wave-excitation force, $F_{ext} = -\int_{S_b} \rho \left(\frac{\partial \Phi^I}{\partial t} + \frac{\partial \Phi^D}{\partial t} \right) n_3 dS$, is the summation of the contributions from the incident and diffracted waves. To estimate the incident wave-excitation force, the incident potential Φ^I may be evaluated analytically using the Stokes 5^{th}-order theory (Fenton, 1985). The nonlinear contributions to this excitation force F_{ext} may also arise from the nonlinear wave-structure interaction and vortex shedding. Within the present study, these two sources and its significance will be investigated in Chapter 5. Finally, the applicability of the added mass and the nonlinear damping coefficient evaluated from a forced oscillation test to the problem of a wave excitation, will be evaluated in Chapter 6. This will be

undertaken by implementing the mathematical formulation given in Equation (2.40).

2.7 Concluding remarks

Having identified the critical issues concerning the fluid loading and the dynamic responses of the different types of OWCs, the aspects that require further evaluation in each subsequent chapter are summarised as follows:

(1) Chapter 3: The capability of the viscous flow solver that will be implemented to model cylindrical OWCs and relevant problems of fluid dynamics.

(2) Chapter 4:

   (i) The characterisation of the radiated wave fields around the OWCs,

   (ii) The description of the water particle kinematics defining the rotational flow fields that arise due to forced excitations, and

   (iii) The validity of linear radiation theory and linear potential solution in a viscous flow.

(3) Chapter 5:

   (i) The physical origins of the nonlinear characteristics in the motions and forces applied to the OWCs under forced excitations and regular wave excitations, and

   (ii) The significance of these nonlinearity sources in the motions and forces.

(4) Chapter 6:

   (i) The added-mass and nonlinear damping coefficients for the OWCs,

   (ii) The effect of vortex damping on the responses of the water columns, and

   (iii) The applicability of the hydrodynamic coefficients computed from forced oscillation tests to the prediction of the responses due to wave excitations.

3

Model description and validation

3.1 Chapter overview

Evaluating the accuracy of a numerical model is a crucial task; the quality of any physical interpretations depending critically on it. With this in mind, validations against all relevant and existing experimental results have to be carried out. Within the present study, several numerical models of OWCs using a viscous flow solver were built to investigate the fluid dynamics below the internal and external free-surfaces. This chapter aims to evaluate the following topics:

1. The capability of the implemented viscous flow solver to model the fluid dynamics under investigation, identifying possible causes of discrepancies,

2. The key numerical aspects required to achieve good accuracy, and

3. An initial physical interpretation of the simulation results.

The present study utilises Open Foam (Version 2.3.0) as the viscous flow solver. This is an open-source software for CFD written in the C++ programming language. Overall, the validation studies in this chapter can be divided into four parts. The first two validation studies described in Sections 3.2 and 3.3, address numerical simulations of OWCs undergoing freely damped (decay) oscillations and forced sinusoidal excitations, respectively. These numerical models are set in a three-dimensional system for which a grid independence study is presented. In Section 3.4.1, calculation

are presented to evaluate the capabilities of Open Foam to model wave generation and to investigate the accuracy of the numerical schemes implemented within the models. In undertaking this work, comparisons against analytical wave theories are presented. Having identified the preferred numerical schemes, an energy balance analysis is undertaken to assess the reliability of the numerical models in capturing the physics underpinning a fluid-structure interaction problem. In this regard, validations of surface waves interacting with a single plate and bi-plate structure in a two-dimensional wave tank are given in Section 3.4.2. Finally, the capability of the viscous solver to estimate important physical quantities in a three-dimensional OWC is addressed in Section 3.5.

3.2 Numerical modelling of freely damped oscillations

3.2.1 Geometry and boundary conditions

As stated in Chapter 1, a PTO model is not incorporated in the OWC system evaluated in the present study. Therefore, a surface-piercing hollow structure is numerically modelled to represent an OWC. A schematic view of the numerical domain and the setup of the OWC is provided in Figure 3.1. This includes: (A) an isometric view of the entire domain, (B) a plan view of the resonant fluid chamber and (C) a cross-sectional view of the domain. The cylindrical fluid chamber is defined by a fixed draft B, an internal radius b (or diameter $D = 2b$), and a wall thickness t_w. This structure is placed within a cylindrical numerical test tank of water depth h and radius R_f. The polar coordinate system in this domain is defined by (r, θ, z); the origin of (r, θ) is placed on the centre line of the OWC, and z is defined as positive in the upward direction with $z = 0$ located at the still water level (SWL). The initial height of the displaced water column in a Decay Test (DT) is denoted by η_o^i, also measured from the SWL.

Given the problem definition, the numerical domain shown in Figure 3.1 is discretised and solved using the open-source finite volume solver Open Foam. Details of Open Foam's numerical implementation are widely available; a clear example provided in Greenshields (2015). To complement this, a brief summary is given in

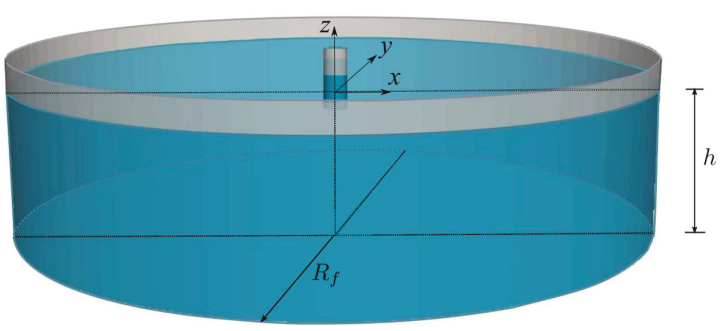

(A) Isometric view

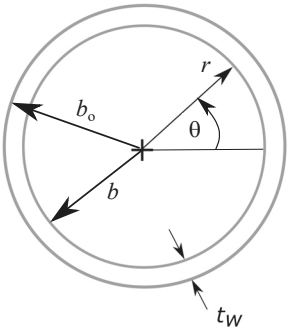

(B) Plan view of OWC wall

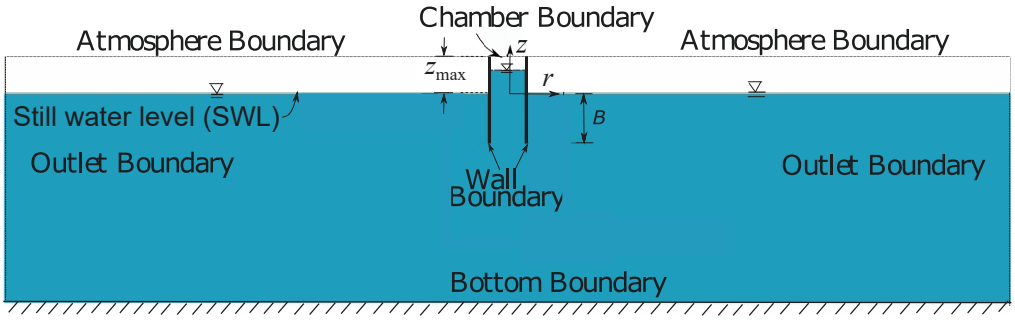

(C) Cross-sectional view of computational domain

Figure 3.1: Schematic of numerical domain

Appendix D. In the present case, a computational domain that includes both the water and the air domain is required. For such a multiphase problem, Open Foam provides a *Volume of Fluid* interface capturing method. Within this method, the kinematic and dynamic free-surface boundary conditions are not solved at the instantaneous free-surface. Instead, the domain boundary of the free atmosphere is located at a predetermined height ($z = z_{\max}$) above the SWL. As a result, the atmosphere boundary is stationary. The surface-piercing hollow cylinder is also stationary and so is the wall boundary. On this basis, all the boundaries enclosing the computational domain are stationary. An Eulerian-based mesh can therefore be used for the purpose of the numerical computation. The multiphase problem solver *interFoam*, supported in Open Foam, is implemented to model the free-surface displacement in a DT.

A schematic of the boundary conditions imposed on the numerical domain is shown in Figure 3.1(C). The corresponding mathematical conditions that stipulate the physical behaviour of the fluid on these boundaries are given in Table 3.1, and are expressed in terms of the pressure p, velocity $\boldsymbol{u}$, volume fraction α, and outward

normal $\boldsymbol{n}$. The volume fraction α describes whether the numerical cell is entirely filled with water ($\alpha = 1$), air ($\alpha = 0$), or represents the location of the interface if $0 < \alpha < 1$. By solving the governing Navier-Stokes equations subject to the boundary conditions in an iterative manner, the field variables p, $\boldsymbol{u}$ and α can be obtained.

Within the present numerical setup, two types of boundaries exist. The first describes a 'water-solid' interface and applies on the impermeable bed Γ_B, the OWC's wall surface Γ_w and the reflective outlet boundary Γ_O. On these solid boundaries, the conditions given in Table 3.1 are imposed as follows:

(a) zero gradient in the volume fraction at the wall,

(b) no normal flow into the wall,

(c) zero pressure gradient at the wall.

In addition, a no-slip condition is also imposed at each of these boundaries.

The second type of boundary describes an 'air-atmosphere' type boundary. This applies to the atmosphere boundary Γ_{FS} and the chamber boundary Γ_C; the latter boundary being labelled with (DT) for a Decay Test in Table 3.1. The volume fraction at these boundaries is imposed as follows. During an inflow ($\boldsymbol{u} \cdot \boldsymbol{n} < 0$), the volume fraction at this boundary is set to zero. During an outflow ($\boldsymbol{u} \cdot \boldsymbol{n} > 0$), the volume fraction is set to zero gradient. This type of condition ensures that any 'splash' of fluid occurring during an outflow is accounted for. This is in line with standard modelling definitions. In the context of the present work, no 'splash' or disintegration of any free surface is observed, and the distinction between the inflow and the outflow cycles is believed to be of little practical importance. Furthermore, the velocity gradient at the 'air-atmosphere' boundaries is set to zero along with zero pressure.

Given the symmetry of the problem under consideration, the flow inside the water column and at the water column mouth may be assumed radially symmetric. As a result, only one quarter of the numerical domain is solved to maximise computational efficiency; the cut computational boundaries defined by symmetry slip conditions.

Table 3.1: Boundary conditions implemented in the numerical models of a freely damped or Decay Test (DT), Forced Water Column Test (FWCT) and a Forced Air Pressure Test (FAPT).

Boundary type	Imposed on	(a) Volume fraction	(b) Velocity	(c) Pressure
Water-solid	$\Gamma_w, \Gamma_B, \Gamma_O$	$\boldsymbol{\nabla}\alpha \cdot \boldsymbol{n} = 0$	$\boldsymbol{u} \cdot \boldsymbol{n} = 0$	$\boldsymbol{\nabla}p \cdot \boldsymbol{n} = 0$
Air-Atmosphere	Γ_{FS}	$\alpha = 0,$	$\boldsymbol{\nabla}u \cdot \boldsymbol{n} = 0$	$p = 0$
		if $\boldsymbol{u} \cdot \boldsymbol{n} < 0$		
Chamber	Γ_C	and		
DT :		$\boldsymbol{\nabla}\alpha \cdot \boldsymbol{n} = 0$,	$\boldsymbol{\nabla}u \cdot \boldsymbol{n} = 0$	$p = 0$
FWCT, prescribed η_o^i :		if $\boldsymbol{u} \cdot \boldsymbol{n} > 0$	$(\boldsymbol{u} - \boldsymbol{u}_c) \cdot \boldsymbol{n} = 0$	$\boldsymbol{\nabla}p \cdot \boldsymbol{n} = 0$
FAPT, prescribed P_o :			$\boldsymbol{\nabla}u \cdot \boldsymbol{n} = 0$	$p = -P_o \sin\omega_f t$

3.2.2 Mouth shape configurations

For the purpose of the DT, the water column was initially displaced to a prescribed elevation, η_o^i, above the SWL. At the initial time, this displaced water column experiences an acceleration due to gravity, with no other external forcing being applied. A very similar test was undertaken experimentally by Knott & Mackley (1980). To enable a direct comparison to the latter experimental data, the geometry of the water column was defined to be identical to their experimental setup; all relevant dimensions being given in Table 3.2. Furthermore, the initial height of the displaced water column was also chosen to match Knott & Mackley (1980). This leads to three distinct cases for the free-decay comparisons: (I) $\eta_o^i/D = 0.27$, (II) $\eta_o^i/D = 0.54$ and (III) $\eta_o^i/D = 0.73$. The overall extent of the cylindrical test tank was chosen to ensure that the DT can be observed without contamination from spurious wave reflections at the outlet boundaries. Specifically, a domain radius of $R_f/\lambda_n = 4$ was found sufficiently large for this purpose, where λ_n is the wavelength corresponding to the theoretical natural period of the water column, $T_n = 2\pi\sqrt{B/g}$. This wavelength is computed as $\lambda_n = 2\pi/k$, where k is the solution to the dispersion equation $\omega_n^2 = gk \tanh kh$, with $\omega_n = 2\pi/T_n$ and g the acceleration due to gravity.

Three different mouth shape configurations were investigated. The first is a straight and sharp-edged (SE) mouth as described by Knott & Mackley (1980). In contrast, the second configuration has a curved mouth which radiates out similarly

Table 3.2: Geometrical parameters of the computational domain in various tests.

Parameter name	Dimensionless parameter	Parameter value
Inner diameter of wall	D/B	0.64
Wall thickness	t_w/D	0.043
Water column draft	B/h	0.11
Radius of NWT	R_f/λ_n	4

to a flared glass. This specific configuration will be hereafter referred to as a bell-shaped (BS) mouth and it has a lip radius of $r_l = 0.5D$. The third configuration is a semicircular-ended (SC) mouth and will be investigated in Chapters 5 and 6. A schematic showing cross-sectional views of these mouth shapes and their dimensions of wall thickness is given in Figure 3.2.

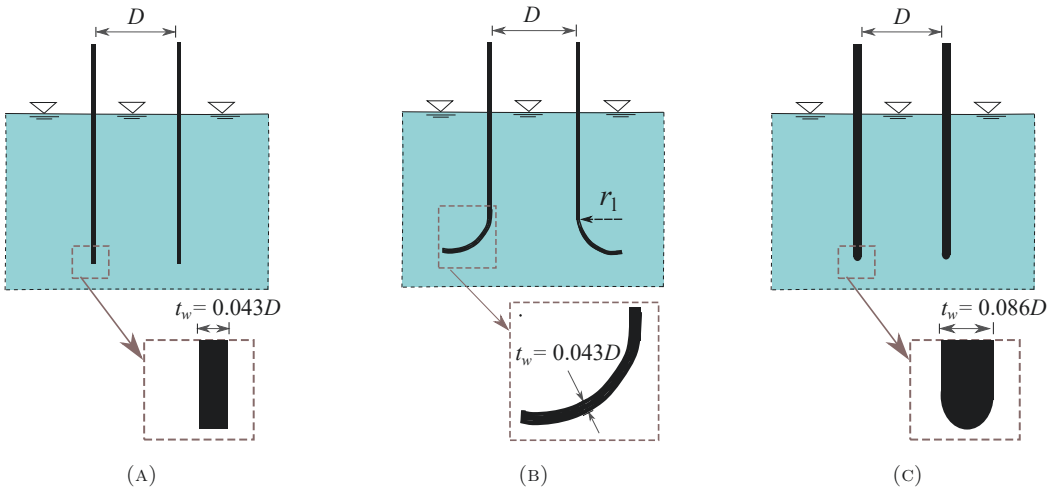

Figure 3.2: Cross-sectional view of an OWC with: (A) a straight and sharp-edged (SE), (B) a bell-shaped (BS) and (C) a straight and semicircular-ended (SC) mouth.

3.2.3 Internal water surface

Figure 3.3 concerns the heave decay characteristics for Case III with an initial displacement height of $\eta_o^i/D = 0.73$. All of the data relates to the OWC with a SE mouth outlined in Figure 3.2(A). In this figure, the instantaneous internal elevations and the instantaneous time are normalised by the initial displacement height η_o^i and the theoretical natural period T_n, respectively. Figure 3.3(A) provides time-histories of the normalised internal surface elevations, η^i/η_o^i, predicted by six simulations based upon varying grid arrangements. All of the calculations were undertaken us-

ing the LES dynamic Smagorinsky turbulence model (Germano et al., 1991), with full details of the adopted grids given in Table 3.3. A total of 11 grids were investigated. These include variation in the vertical grid size Δz near the free surface, and the radial grid size Δr of water column. In all cases, the grid resolution near the wall is effectively determined by the number of radial cells. Having employed the exponential function of grid-space grading within the *blockMesh* option of Open Foam, the normal distance of the first cell to the wall can be determined. Since the mesh is static throughout the simulation, this normal distance directly dictates the wall spacing unit, a variable that indicates the resolution of the boundary layer. With the flow modelling under investigation involving an unsteady-periodic flow, the boundary layer thickness will change periodically. Table 3.3 gives the maximum wall-spacing unit, y^+, calculated at the time when the thickness of boundary layer is at minimum. The grids outlined in Table 3.3 form the basis of the present grid independence study.

Table 3.3: Grid arrangements for a freely decaying water column inside the OWC with a SE mouth

Grid ID	Grid Resolutions		Max Wall	Cell Aspect-ratio	Number of cells
	$b/\Delta r$	$\eta_o^i/\Delta z$	Spacing Unit y^+	AR	(million)
$A1$	14	5	21	5.96	0.1
$A2$		14		1.99	0.4
$B1$		7		4.86	0.2
$B2$	16	10	20	3.40	0.3
$B3$		14		2.43	0.5
$C1$		10		3.81	0.4
$C2$	18	14	18	2.72	0.6
$C3$		20		2.01	0.7
$D1$		10		5.95	1.0
$D2$	28	14	16	4.25	1.4
$D3$		30		1.99	2.3

Table 3.3 indicates that for each radial grid size, Δr, the grid resolutions near the free surface were varied vertically. The vertical grid size in the volume above the SWL was uniform; the associated cell aspect ratio, $AR = \Delta z/\Delta r$, outlined in the table. In contrast, the vertical grid resolution located closer to the sharp edge was increased such that the AR at this edge was approximately equal to one. This generated the highest resolution at this location, where high gradients of velocity and pressure fields were expected to exist. Unlike the variation in Δz, the grid in the azimuthal direction at a radial location had comparable size. This was directly

dictated by the Δr of the structured mesh implemented in the present computational domain.

The purpose of the present calculations was to evaluate the sensitivity of the predicted internal water surface elevation, η^i, on the grid resolution. This analysis reveals that the vertical grid size, Δz, is the most influential factor. Comparisons of time-histories of the internal water surface elevation obtained from Grid $B2, C1$, and $D1$, where $\Delta z = \eta_o^i/10$, give identical results; the root-mean-square variation being less than 0.5%. Likewise, in the case where $\Delta z = \eta_o^i/14$, Grid $B3, C2$ and $D2$ also produce near-identical results; the root-mean-square variation being less than 0.6%. These results confirm that grid resolution in the radial direction, Δr, is less crucial. This in turn suggests that the boundary layer at $y^+ \leq 20$ provides an insignificant change in predicting the internal water surface.

The selected cases shown in Figure 3.3(A) also confirm that the simulated internal water surface elevations converge to the experimental data of Knott & Mackley (1980) as the mesh is refined. Grid $A1$, having the coarsest mesh ($\Delta z = \eta_o^i/5$), results in the largest discrepancies. Although the natural period of the oscillating water column is well predicted, its corresponding peak values deviate from the experimental maxima by 15%; the percentage errors becoming larger for smaller peak amplitudes. For grids with $\Delta z = \eta_o^i/10$, the differences with the experimental data appear to be very small. Moreover, no significant improvements are related for small values of Δz. These results suggest that with $\Delta z \leq \eta_o^i/10$ adopted as a minimum grid resolution in a freely decaying OWC model, the time-history of the internal surface elevation is expected to be accurate.

The results shown in Figure 3.3(A) were acquired using the LES dynamic Smagorinsky model. This model necessitates a double filtering when modelling the subgrid-scale stress. As a result, the computational requirement is more expensive than the classical Smagorinsky model (Smagorinsky, 1963). However, a comparison between calculations based upon these alternative turbulence models given in Figure 3.3(B), shows that the classical Smagorinsky model is less accurate in predicting both the peak amplitudes and the natural period of oscillation. This unphysical behaviour is due to the constraint of the eddy viscosity model, in which the Smagorinsky constant is held constant throughout the flow simulation. As a result, the subgrid-scale stress is unlikely to diminish at the wall boundary; at this boundary, only the viscous

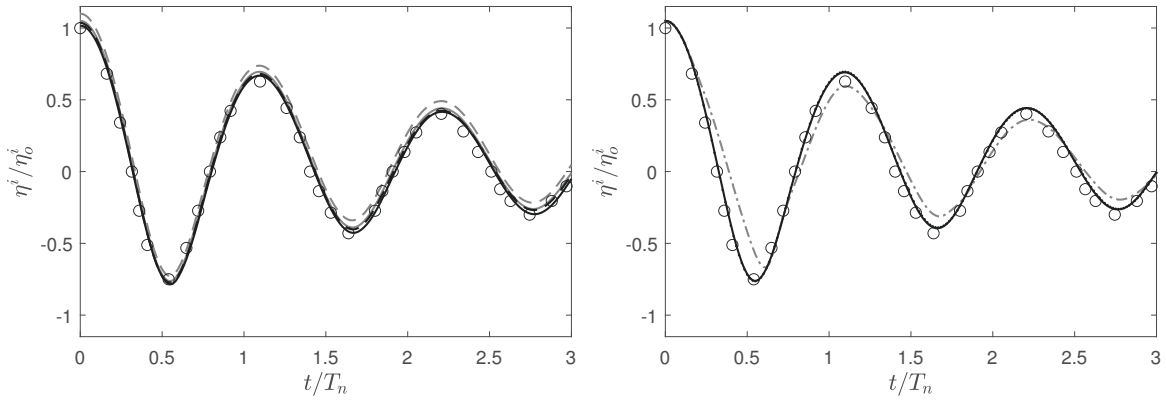

(A) (B)

Figure 3.3: (A) A grid independence study of the normalised internal water surface elevations, η^i/η^i_o, that freely decay inside an OWC with a SE mouth is undertaken for Case III using the LES dynamic Smagorinsky with various grids: Grid $A1$ [— —], Grid $B2$ [——], Grid $C2$ [— —], and Grid $D3$ [——], and (B) Comparisons of internal water surface elevations from different turbulence modellings: LES classical Smagorinsky [— · —] and RANS k-ω SST [▪ ▪ ▪ ▪]. All simulated elevations are compared to the experimental data [○] by Knott & Mackley (1980).

shear-stress applies, and any additional viscosity may cause excessive dissipation. This argument is supported by the two features of the predictions shown in Figure 3.3(B): the under-estimation of the peak amplitude and the longer natural period of oscillation estimated from the classical Smagorinsky model. This result has wider implications, suggesting limitations in applying the classical Smagorinsky model when seeking to describe a wall-bounded flow. The model is well known for its inability to smoothly transition the eddy-viscosity values near the solid wall. This has been observed, when using this particular flow model, in the context of channel flows (Piomelli et al., 1988) and axisymmetric bluff body flows (Lee & Cant, 2017). Given the present simulations, it is proven that this latter model also has a tendency to over-estimate the physical dissipation near the wall in the unsteady-periodic flow bounded by a cylindrical hollow structure. Conversely, the RANS k-ω SST model gives very good agreement with the experimental data relating to this flow problem. This suggests that both the LES dynamic Smagorinsky and the RANS k-ω SST models are sufficiently accurate to predict the internal surface elevation within an OWC with a SE mouth modelled under the present grid arrangement. A further description of all the turbulence models implemented within the present study is provided in Appendix D.

In considering the advantages and downsides of the turbulence modellings imple-

mented in the present study, the computational time and root-mean-square error in each model are provided in Table 3.4. This data relates to the earlier comparisons of the internal water surface elevations during three theoretical natural periods T_n shown in Figure 3.3(b). The numerical simulation for any turbulence modelling was undertaken using four processors handling an identical mesh (based upon Grid $B2$). Table 3.4 indicates that the LES classical Smagorinsky model has the largest percentage of error estimated to be 41%. The dynamic Smagorinsky model produces a more accurate result; however, the computational time is about 20% more costly than the classical model. The longest computational time corresponds to the RANS k-ω SST model. This is associated with iteratively solving the two additional governing equations in the model for every time increment in the simulation; these equations governing the turbulent kinetic energy and turbulent specific dissipation rate.

Table 3.4: The computational time and the root-mean-square error from different turbulence modellings.

Turbulence modelling	Computational time [min]	Root-mean-square error [%]
LES classical Smagorinsky	90	41
LES dynamic Smagorinsky	108	11
RANS k-ω SST	132	12

Figure 3.4 provides additional comparisons to the experimental data of Knott & Mackley (1980). This concerns varying initial surface displacements η_o^i/D. Taken as a whole, the agreement between the experimental data and the numerical simulation (based upon Grid $B2$ and the LES dynamic Smagorinsky model) is good. Full details of the root-mean-square errors can be seen from Table 3.5. These errors were computed using data of the internal surface elevations at various times. Specifically, the comparisons shown in Figure 3.4 confirm two important aspects of the system dynamics. First, the natural period of oscillation agrees well; evidence of this being provided by the phase match at subsequent oscillations in Figure 3.3(a). Second, the damping characteristic is also modelled accurately; the simulated rate of decay being very similar to the experimental observations (Figures 3.3(a) and 3.4). In Figure 3.4, the decay rate is largest in the case of the maximum η_o^i/D (Figure 3.4(c)). This implies that the decay rate is dependent on the amplitude of the motion of the water column.

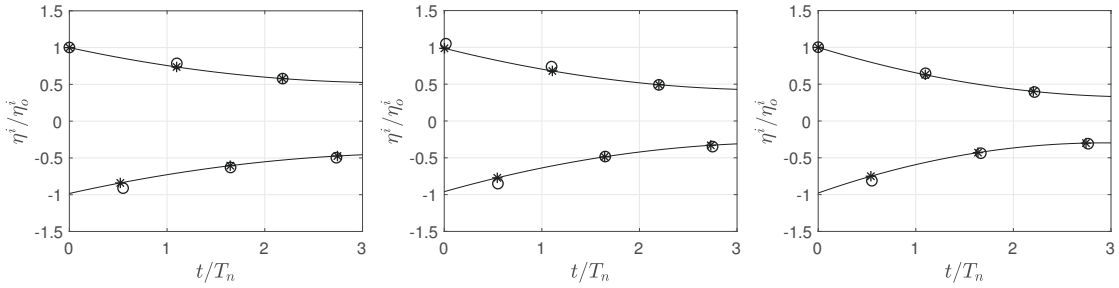

(A) $\eta^i_o/D = 0.27$ (B) $\eta^i_o/D = 0.54$ (C) $\eta^i_o/D = 0.73$

Figure 3.4: Comparison of decaying peak amplitude values of water surface oscillations predicted from the numerical viscous model [$\circ$] and the experimental model ($*$) (Knott & Mackley, 1980) and the 2$^{\text{nd}}$-order polynomial fits for the experimentally predicted peak amplitudes [——].

Table 3.5: The root-mean-square errors in different decay tests.

η^i_o/D	Root-mean-square error [%]
0.27	11
0.54	10
0.73	11

In order to confirm the wider applicability of these findings, a convergence study was also undertaken for an OWC with a BS mouth; the duct geometry being defined by a streamlined and radially curved mouth as shown in Figure 3.2(B). A circular wall with a lip radius of $r_l = D/2$ was fitted to a straight tube; the height of this curved section defined so that the draft is equal to that of the OWC with a SE mouth. The cylinder diameter and wall thickness were also kept constant. Data relating to this case is provided on Figure 3.5. This concerns time-histories of the internal water surface elevation for the case with an initial displacement of $\eta^i_o/D = 0.86$. Comparisons are provided between the experimental observation of Knott & Mackley (1980) and a number of numerical simulations involving different grid resolutions; full details of the latter are provided in Table 3.6.

As in the previous case, a set of grid arrangements was utilized and the sensitivity of the predicted internal water surface elevations to the grid parameters is evaluated. The grid sensitivity study reveals that the time-series of elevations calculated using the grids with identical vertical grid resolutions yield good agreement with the experimental data; the difference in amplitude and phase being unidentifiable. The effects of radial grid and boundary layer resolutions are, once again, considered insignificant. Furthermore, grids with $\Delta z \leq \eta^i_o/10$, as shown in Figure 3.5(A), provide

sufficiently accurate predictions. Evidence of this is provided by the errors of the numerically predicted peak amplitudes which are consistently less than 5%. However, caution needs to be exercised when using grids with a high cell aspect-ratio. Such grids may cause unphysical results such as "wiggles" in the velocity field at the interface. However, the present result suggests that provided the cell aspect-ratio is less than six, the numerical simulations exhibit no unphysical extreme values. Given this aspect-ratio constraint ($AR \leq 6$), and a vertical grid-resolution of $\Delta z \leq \eta_o^i/10$ as minimum requirements, the estimation of the time-varying internal water surface elevations in an OWC with a BS mouth is expected to be accurate.

Table 3.6: Grid arrangements for a freely decaying water column inside the OWC with a BS mouth

Grid ID	Grid Resolutions		Max Wall	Cell Aspect-Ratio	Number of cells
	$b/\Delta r$	$\eta_o^i/\Delta z$	Spacing Unit y^+	AR	(million)
$A1$	14	5	24	4.84	0.1
$B1$		7		6.21	0.1
$B2$	16	10	23	4.34	0.2
$B3$		14		3.10	0.3
$C1$	18	10		4.86	0.3
$C2$		14	22	3.47	0.4
$D1$		10		7.60	0.8
$D2$	28	14	18	5.43	1.1
$D3$		18		4.22	1.4
$E1$		14		6.52	1.8
$E2$	30	18	17	5.07	2.3
$E3$		22		4.11	2.6

With regard to the turbulence modelling, the classical Smagorinsky model again inaccurately predicts the peak amplitudes and the natural period of oscillation inside the OWC with a BS mouth. Figure 3.5(b) indicates the under-estimation of the amplitudes and the over-estimation of the natural period by this Smagorinsky model. Once again, the excessive dissipation by the eddy viscosity at the wall and the implementation of a fixed Smagorinsky constant are the main causes. In contrast, both LES dynamic Smagorinsky model and the RANS k-ω model give equally good agreement with the experimental data. Given a reliable turbulence model, Figure 3.5 provides an insight into the decay rate of the oscillating water column inside a bell-shaped mouth. The water surface elevation inside this streamlined mouth shape is damped more slowly when compared to the OWC with a SE mouth. This obser-

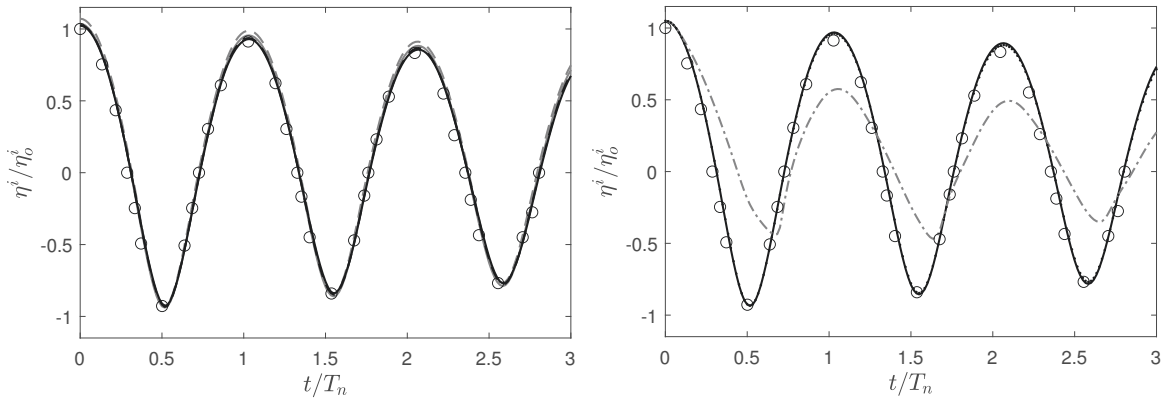

(A) (B)

Figure 3.5: Comparisons between the experimental data [○] and (A) a grid independence study of the normalised internal water surface elevations, η^i/η^i_o, that freely decay inside an OWC with a BS mouth using the LES dynamic Smagorinsky from various grids: Grid $A1$ [— —], Grid $C2$ [——], Grid $D3$ [— —], and Grid $E3$ [——], and (B) computations of predicted elevations from different turbulence modellings: LES classical Smagorinsky [— · —] and RANS k-ω SST [▪▪▪▪].

vation is confirmed by both the progressively smaller reductions of successive peak amplitudes and the smaller natural period of oscillation; the latter being closer to the theoretical value, T_n. The reduced damping is readily explained in terms of the reduced flow separation associated with this specific mouth inlet. This is confirmed by qualitative observation of the flow field reported by Knott & Mackley (1980).

3.2.4 Circulation and vortex trajectory

When the boundary layer separates at a sharp corner, this shear layer will move along with the boundary layer and form a rolled-up vortex sheet. For a specific geometry like a cylindrical OWC, the vortex formation is similar to the process of fluid ejection from a tube or nozzle, generating a vortex ring at the lower edge outside the water column. This occurs during the downward displacement of the water column. A positive vorticity at the inner wall of the water column feeds the cylindrical vortex sheet with an inner circulation Γ_i. In contrast, a negative vorticity at the external wall with a circulation Γ_e reduces the total circulation Γ. The total circulation Γ, that roughly defines the strength of a vortex ring, is the summation of the inner circulation, Γ_i, and external circulation, Γ_e. According to Didden (1979), the total circulation is derived from the circulation rate $d\Gamma/dt$. For the case of axisymmetric

flow during vortex formation, this is defined as:

$$\frac{d\Gamma}{dt} = \frac{d\Gamma_i}{dt} + \frac{d\Gamma_e}{dt}, \tag{3.1}$$

$$\Gamma(t) = \int_0^t \int_0^b \omega_\theta u_z dx dt + \int_0^t \int_{b_o}^\infty \omega_\theta u_z dx dt, \tag{3.2}$$

where b_o is the outer wall radius, ω_θ the azimuthal component of vorticity perpendicular to an angular cross-sectional area and u_z is the z-component of fluid velocity.

Figure 3.6(A) shows the convergence study appropriate to the description of the total circulation that feeds the first downstroke vortex being formed when the water column moves downwards, in the negative z direction. The reduction of the total circulation Γ by the increasing external circulation Γ_e indicates the onset of the vortex shedding. Figure 3.6(B) describes the corresponding trajectory of the first vortex ring during the first two periods of oscillation. To define the position of the vortex core (X_v, Z_v), the central weight of the vorticity distribution is quantified at every instant in time. This method has been formerly implemented by Lawson & Dawson (2013) and serves as an alternative to tracking the peak vorticity location. By adopting the first method, fluctuations in the position of the vortex core were minimised. The important process in this quantification is to identify the region of vorticity that is located inside the vortex core S_{core}. This was achieved by adopting a vortical structure identification based upon the Q-criterion (Hunt et al., 1988).

It can be seen from Figure 3.6 that during the initial formation stage when the circulation is feeding from the vorticity at the boundary layer into the cylindrical vortex sheet, the vortex ring increases in diameter (increasing X_v). This occurs alongside the increasing total circulation. When the formation phase ends at time $t = 0.483T_n$, a contraction phase begins during which the shedded vortex ring experiences a sudden reduction in diameter. This occurs during the following upward displacement of the water column. This evident contraction phase is in line with many former findings, notably by Didden (1979) and Hettel et al. (2007). The interaction of the vortex with a solid boundary, in this case the mouth-inlet wall, leads to the formation of an upwardly moving vortex ring with an oppositely-signed vorticity field. This develops inside the water column and leads to a reduction in the strength of the former vortex ring.

Following the end of the contraction phase, when the water column again reverses

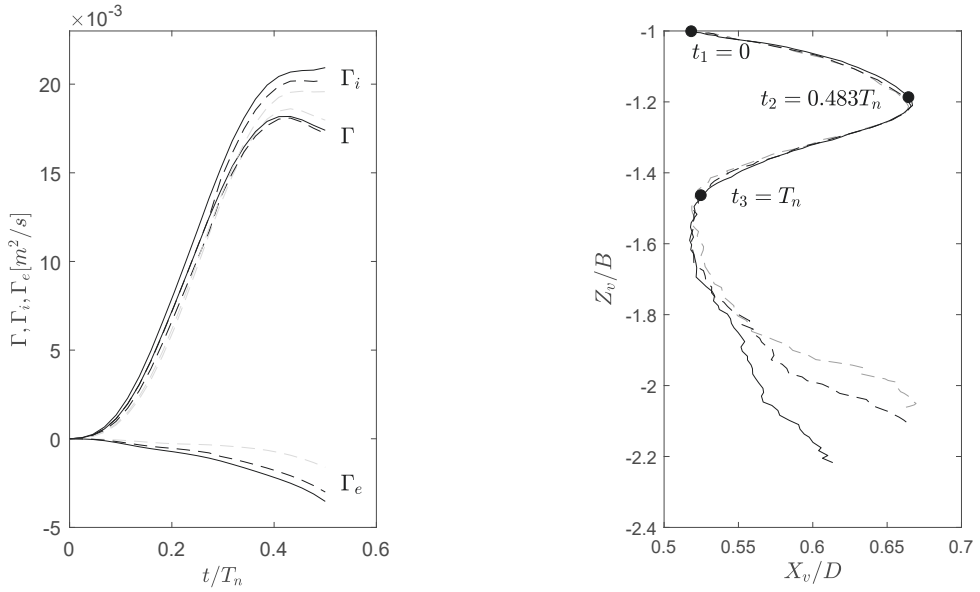

(A) Circulations Γ (B) Trajectory motions $(X_v/D, Z_v/D)$

Figure 3.6: (A) Total circulation that forms the first downstroke vortex ring Γ, and (B) the corresponding trajectory motions of the vortex ring $(X_v/D, Z_v/B)$ during the first two periods of oscillations inside an OWC with a SE mouth from Case III ($\eta_o^i/D = 0.73$) predicted from various grids: Grid $A1$ [— —], Grid $C2$ [— —], and Grid $D3$ [———]; details of the latter given in Table 3.3.

its direction of travel (at $t = T_n$), the viscous diffusion process begins. This is characterised by the increasing diameter of the vortex ring and the growing size of the vortex core; this final phase begins at time $t = T_n$ in Figure 3.6.

Within Figure 3.6, it is notable that both the total circulations and the vortex trajectory motions converge as the mesh density is increased. The difference in the vortex motions during the formation and contraction phases under varying grid arrangements is unidentifiable when compared to that in the diffusion phase. This fact and the similarity of the vortex phases with the observation from the former studies, suggest that the present numerical model is reliable when it comes to predicting the vortex dynamics. Furthermore, the good agreement of the internal surface elevations (Figure 3.3(A)) indicate that the large-scale motions, including the vortex ring formation in the numerical model, were sufficiently resolved.

The only exception to the mesh convergence relates to the vortex trajectory during the viscous diffusion phase. This is expected since the mesh resolution located far from the mouth inlet is much coarser than that very close to the mouth inlet. Most importantly, it may be argued that the process of the viscous diffusion due to time-

dependent diffusion entrainment may not be closely relevant to a damping mechanism of an OWC system. This can be justified on three counts:

(i) the energy bounded in a vortex is not conserved,

(ii) the vortex location in the beginning of this final stage is far from the mouth inlet ($Z_v/B \approx -1.50$) and,

(iii) the vortex propagates away from this location.

Based upon these arguments, it is safe to neglect the numerical error due to the coarse mesh in this distant area. Quantitative evidence confirming that the energy loss associated with the damping of an OWC system is largely determined by the kinetic energy of the vortex located close to the inlet is provided in Chapter 6.

3.3 Numerical modelling of forced water column oscillations

3.3.1 Boundary conditions

An oscillating water column that decays in amplitude will continuously be in a transient state. As such, the steady and periodic behaviour of the flow in an OWC is not represented. It therefore follows that, an estimation of the hydrodynamic force, which is known to be a function of the oscillation frequency and amplitude, is not appropriate if the estimation is based upon a transient state.

Within a Forced Water Column Test (FWCT), a sinusoidal function of displacement is prescribed to mimic a moving piston (wall) placed above the internal surface elevation within the OWC. The air trapped between this wall and the water surface is assumed to be incompressible so that the water column moves in unison with the displacement of the 'rigid' air volume. Consequently, the elevation of the water column is directly dictated by the prescribed wall displacement. The surface at the chamber boundary, noted in Figure 3.1(c), is now acting as the wall and its displacement is varied in the form of $\eta(t) = \eta_o^i \cos(\omega_f t)$, where η_o^i is now the amplitude of the internal water surface elevation, $\eta^i(t)$, and $\omega_f = 2\pi/T_f$ is the angular forcing frequency. Previously, in Chapter 2, ω was defined as the angular frequency in both radiation and scattering potential flow problems. Hereafter, ω_f is specifically

defined for radiation and forced oscillation problems to distinguish it from the wave frequency, ω.

The boundaries of the computational domain in a Forced Water Column Test (FWCT) necessitate slightly different conditions to those that have been implemented in the earlier decay tests (DT). Specifically, the moving chamber boundary, Γ_c, is one on which the amplitude of the internal water surface elevation or the forcing amplitude, η_o^i, is prescribed. This is noted in Table 3.1 as prescribed η_o^i for FWCT. On this boundary, Γ_c, a kinematic boundary condition is applied to impose a zero-flux condition and hence the normal fluid velocity is set equal to the normal velocity of the chamber wall $\vec{u}_c$. A Dirichlet boundary condition for the velocity variable is thus applied. Accordingly, the pressure variable would be defined by a Neumann boundary condition. The boundary conditions appropriate to the numerical model of this forced oscillation test are mathematically expressed in Table 3.1.

3.3.2 Internal water surface and air pressures

Two different forcing amplitudes were considered for the convergence studies. These cover the full range over which the subsequent analysis will be undertaken. The two test cases, Case I and II, correspond to forcing amplitudes of $\eta_o^i/D = 0.25$ and 1.6, respectively. The forcing frequencies were fixed for both cases at $\omega_f^2 B/g = 0.87$, where the draft B is set at 0.16 m and the cylinder aspect-ratio D/B is now 0.435. For a FWCT, the variables of interest are:

(i) the internal water surface defining the water column displacements,

(ii) the external water surface to evaluate the wave radiation profile, and

(iii) the air pressure to quantify the hydrodynamic properties of the water column.

The sensitivity of these variables to the grid parameters is evaluated by varying one parameter at one time.

It is important to note that the mesh implemented within the FWCTs is dynamic; the mesh having to follow the movement of the chamber wall boundary. As a result, *interDyMFoam*, an Open Foam multiphase problem solver for a dynamic mesh, is employed to solve the boundary value problem. The grid arrangement is similar to the static mesh in the DT. Tables 3.7 and 3.8 show the grid details for the present

cases. Case I involves a small forcing amplitude and, as a result, it is easier to achieve a higher resolution of boundary layer ($y^+ = 10$). A less dense mesh may be used for this case. However, a resolution with $y^+ \geq 16$ is not suggested here, because a larger wall spacing unit will set a lower radial grid resolution ($\Delta r \geq b/12$). This, in turn, enforces cells with a high aspect-ratio at the outer computational boundary.

Table 3.7: Grid arrangements for a FWCT: Case I, $\eta_o^i/D = 0.25$.

Grid ID	Grid Resolutions			Max Wall	Cell Aspect-Ratio	Number of cells
	$b/\Delta r$	$\eta_o^i/\Delta z$	$\lambda/\Delta x$	Spacing Unit y^+	AR	(million)
$A1$	12	5	180	16	1.27	0.16
$B1$		5	180		1.96	0.34
$B2$	14	7	250	14	1.40	0.56
$B3$		10	360		0.98	1.07
$C1$		5	180		1.61	0.78
$C2$	16	7	250	13	1.12	1.32
$C3$		10	360		0.81	2.23
$D1$		7	180		3.07	1.22
$D2$	18	10	250	11	2.15	2.25
$D3$		14	500		1.54	3.56
$E1$	22	10	250	10	1.64	2.58

Table 3.8: Grid arrangements for a FWCT: Case II, $\eta_o^i/D = 1.6$.

Grid ID	Grid Resolutions			Max Wall	Cell Aspect-Ratio	Number of cells
	$b/\Delta r$	$\eta_o^i/\Delta z$	$\lambda/\Delta x$	Spacing Unit y^+	AR	(million)
$A1$	12	5	45	30	4.36	0.28
$B1$		10	65		6.20	0.68
$B2$	16	14	75	27	3.57	1.00
$B3$		16	85		2.75	1.18
$C1$		14	75		4.36	1.60
$C2$	20	16	85	25	4.31	1.86
$C3$		20	105		2.85	2.44
$D1$		16	85		4.67	2.67
$D2$	24	20	105	21	3.94	3.45
$D3$		24	125		2.78	4.20

Given the grid parameters outlined in both tables, the water surface simulations using the grids with identical vertical grid resolutions have matching results in both phase and amplitude. This again confirms that the radial grid resolutions are less important in capturing the water surface elevations. Overall, the numerically predicted internal surface elevation in Figure 3.7 is near convergent as the vertical grid

size is progressively refined. Evidence of this is given by the peak amplitude of the normalised water surface elevation, approaching the expected value of one. Grids with a vertical resolution of $\Delta z = \eta_o^i/10$ result in errors of approximately 5% in both cases. This resolution is deemed to be sufficiently accurate for the present study. Furthermore, the fact that the computed internal free-surface elevations of both cases match the prescribed wall displacements suggests that the assumption of air incompressibility works as expected. Simulated internal water surface elevations can thus be prescribed based upon the displacement of a moving wall above the internal free-surface.

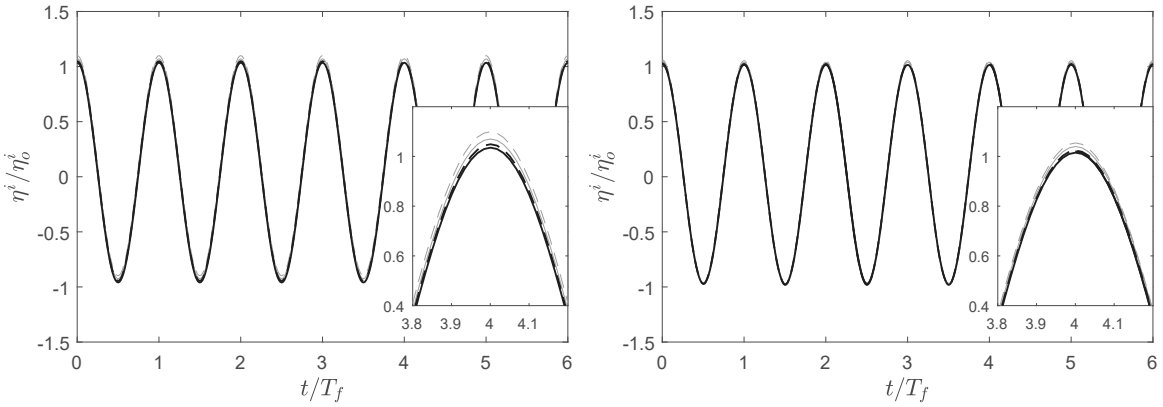

(A) Case I, $\eta_o^i/D = 0.25$

(B) Case II, $\eta_o^i/D = 1.6$

FIGURE 3.7: Internal water surface elevations of the water column, η^i, due to forced excitations are normalised with the forcing amplitude, η_o^i, for an OWC with a SE mouth, diameter of $D = 0.07$m and forcing frequency of $f_f = 1.16Hz$. Comparisons are given from various grids: Grid $A1$ [— —], Grid $B2$ [——], Grid $C3$ [— —] and Grid $D3$ [——].

In addition to the internal water surface elevations, convergence studies were also undertaken in respect of the air pressures. The air pressure data were collected at one location consistently above the instantaneous free-surface. For all simulations, the wall chamber distance from the mean water surface, as depicted in Figure 3.1(C), was defined by $Z_{\max} \geq 5\eta_o^i$. This allowed the water surface to reach the maximum excursion with no possiblity of water entering the chamber boundary. In doing so, unambiguous air pressure data can be obtained. Since the air pressures in the simulations are spatially invariant in both the vertical and horizontal directions, recording data of time-varying air pressure at one location for each case was considered accurate and sufficient; the data being representative of all locations.

The time-varying air pressures of the two forced oscillation cases are presented in

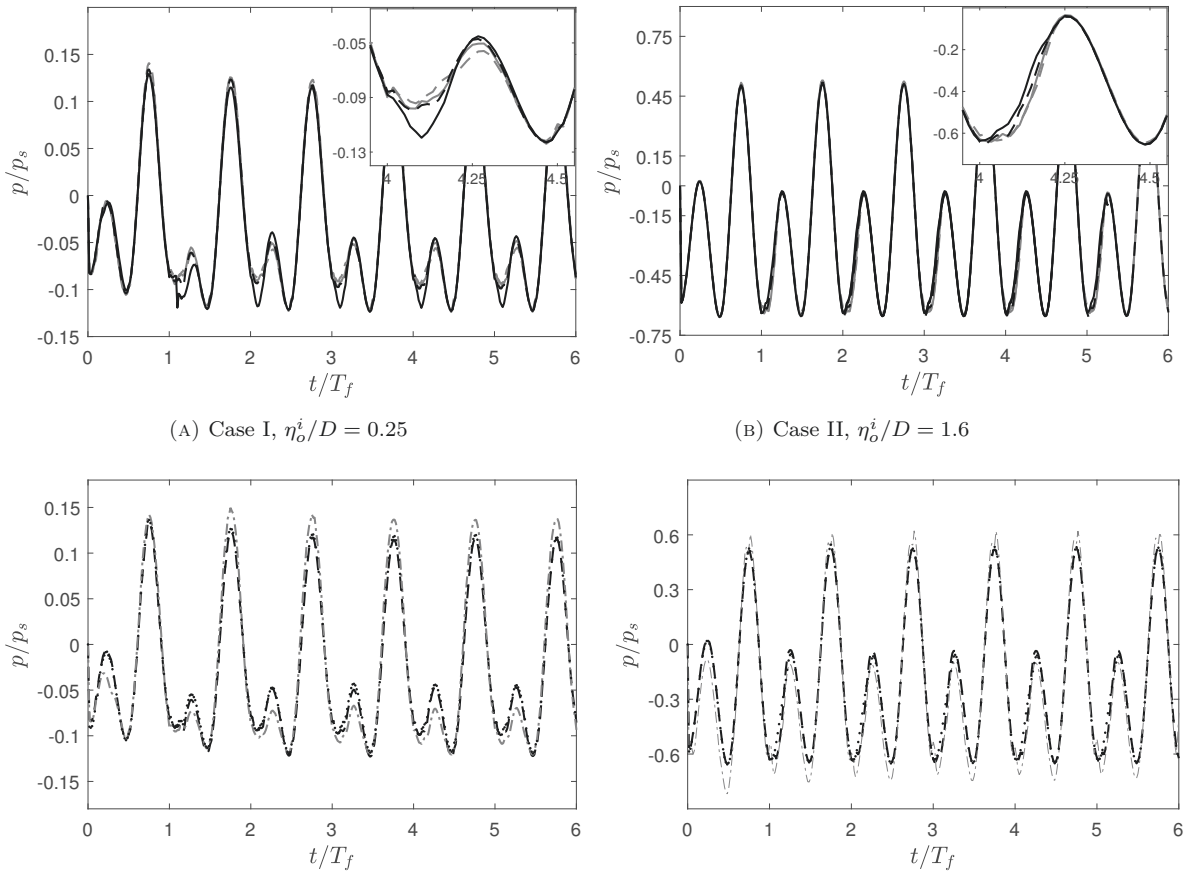

(A) Case I, $\eta_o^i/D = 0.25$

(B) Case II, $\eta_o^i/D = 1.6$

(C) RANS k-ω SST & LES, Case I

(D) RANS k-ω SST & LES, Case II

Figure 3.8: (A)-(B) Grid independence studies of air pressures, p, normalised by a pressure of $p_s = \rho g \eta_o^i$ for the two cases of an OWC with a SE mouth. The results are based upon the LES dynamic Smagorinsky with various grids: Grid $A1$ [— —], Grid $B2$ [———], Grid $C3$ [— —] and Grid $D3$ [———], and (C)-(D) computations undertaken using different turbulence models but a constant grid resolution (Grid C3): LES classical Smagorinsky [— · —] and RANS k-ω SST [▪▪▪▪].

Figure 3.8. In this figure, the instantaneous air pressures are normalised by a pressure $p_s = \rho g \eta_o^i$. Unlike the water surface elevations, the pressure fields are insensitive to the vertical grid resolution. This is to be expected as the air pressures are spatially uniform above the instantaneous water surface. However, with respect to the radial grid and boundary layer resolutions, the predicted air pressures vary. Overall, the time-varying air pressures are near convergent with increases in the mesh density. Evidence of this is provided by the converged period and positive peak pressures in Figures 3.8(A) and (B). In contrast, achieving a converged solution for the double-peaked characterisctic of the pressure time-history, that occurs when the free surface is descending, appears to be more challenging. Despite the slight difference in the

characterisation of the double peaks predicted using different grid arrangements, grids with a resolution of $\Delta r \leq b/20$ and $y^+ \leq 25$ produce insignificant changes in the other peak values when compared to the finest mesh resolution.

At this stage, it is necessary to comment further on the implementation of turbulence models in the FWCTs, particularly in estimating the time-varying air pressures. First, it is relevant to note that the water surface elevations are identical regardless of the turbulence model employed. This is to be expected given the forced nature of the problem. However, the predictions of the air pressure are more sensitive and exhibit marked differences (Figures 3.8(c) and (d)). While the LES dynamic Smagorinsky model and the RANS k-ω SST model give effectively identical results, the classical Smagorinsky model differs. Although the period of the pressure oscillations appears to be uniformly well predicted (again consistent with a forced problem), the classical Smagorinsky model over-estimates the air pressures (see Figures 3.8(c) and (d)). In seeking to explain this, it should be noted that the air pressure drives the water column to move according to the prescribed displacement. Therefore, the corresponding force must balance all other forces that act on the water column. This includes the damping force associated with the eddy viscosity that is over-estimated near a wall boundary by the classical Smagorinsky model. Based upon these results, it is therefore concluded that in modelling an OWC, the implementation of the classical Smagorinsky model is not recommended.

3.3.3 Verification of air pressures

The success of the present numerical calculations in respect of the air pressures arising in a forced oscillation test can be judged by comparisons to the experimental data of Fung (1998). This former study involved forced displacements of water columns inside an OWC with a SE mouth by making use of piston (wall) movement as the excitation mechanism. Both forcing frequencies and amplitudes were varied. In addition to verifying the numerical calculations, these comparisons will provide further insights into the characteristics of air pressures under varying forcing frequencies.

The geometry of the numerical domain was identical to that adopted by Fung (1998); a sketch provided in Figure 3.1. Three excitation frequencies were considered corresponding to $\omega_f^2 B/g = 0.20, 0.79$ and 1.34; the middle value corresponding to the damped natural frequency and hence a resonant condition. The forcing am-

plitude was held fixed for the three cases. Figure 3.9 provides comparisons with the experimental data. The vertical grid resolutions employed in these tests are $\Delta z = \eta_o^i/10$, and the radial grid and boundary layer resolutions are respectively set at the minimum requirements discussed earlier: $\Delta r = b/16$ and $y^+ = 20$. In general, the comparisons show good agreement both in respect of the phase and the pressure amplitudes. One notable exception arises in the resonant condition, where the air pressure measurements are distinctly nonlinear. Although the numerical simulation shown in Figure 3.9(b) is able to capture some of the double-peaked characteristics of the air pressure, the discrepancies with the laboratory data are clear. This occurs in both the magnitude and phase of the calculated air pressures. However, given that the recorded pressures at this frequency have the smallest amplitude, it may be reasonable to conclude that the error is (at least) partly due to experimental effects. Nevertheless, given the satisfactory agreement observed in Figures 3.9(a) and (c), the numerical model is clearly capable of capturing the nonlinear characteristics of the observed pressures in these forced oscillation tests.

The characteristics of the phase shift between the internal water surface elevations and their corresponding air pressures are notable. At the lower frequency, $\omega_f^2 B/g = 0.20$, the air pressure is in phase with the water column displacement (Figure 3.9(a)). In contrast, at the higher frequency, the air pressure is π out of phase from the displacement (Figure 3.9(c)). At the resonant condition, a phase shift of approximately $\pi/2$ is apparent from the time-history shown in Figure 3.9(b). These varying phase shifts observed within the air pressures, reflect the significance of the damping force. The in-phase or π-out-of-phase conditions suggest a small damping force, while the $\pi/2$ phase difference indicates the largest damping force.

Clearly, the magnitude of the air pressure that excites the oscillating water column under the resonant condition is the smallest. This may be explained by the fact that under a resonant condition, the inertial force almost balances the restoring force driven by buoyancy. Therefore, the air pressure acting above the internal free-surface only has to act against the damping forces; a relatively small pressure required to keep the water column oscillating according to the prescribed displacement.

Further consideration of the amplitudes of the air pressures under varying forced frequencies is provided in Figure 3.10. Specifically, the data relates to conditions when the water column is at its maximum (or minimum) displacement. Interestingly,

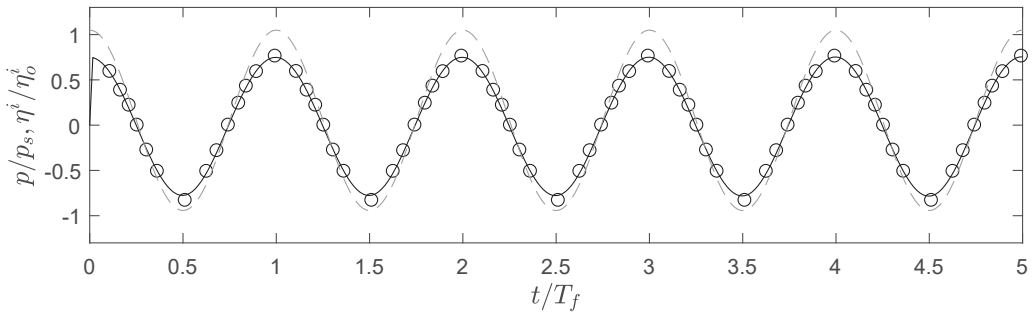

(A) forcing frequency $\omega_f^2 B/g = 0.20$

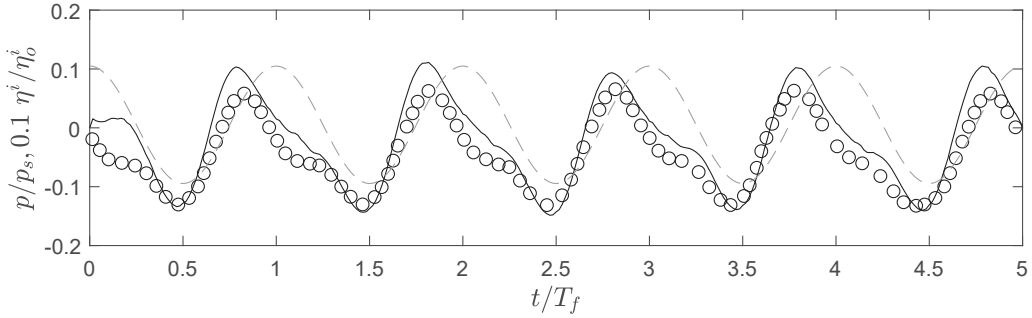

(B) forcing frequency $\omega_f^2 B/g = 0.79$

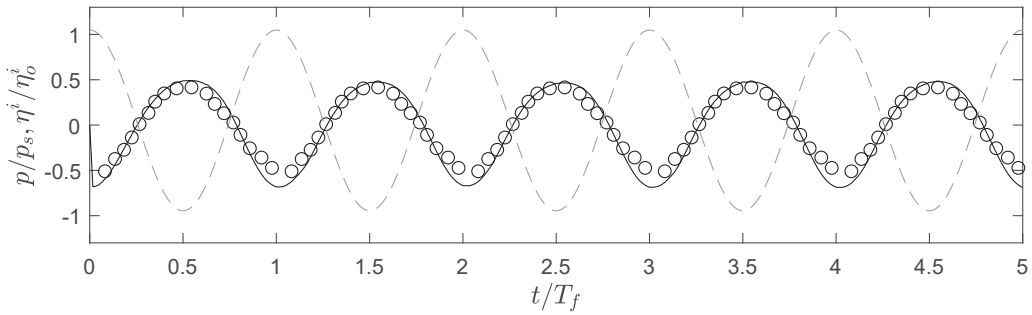

(C) forcing frequency $\omega_f^2 B/g = 1.34$

FIGURE 3.9: Time-histories of the internal water surface elevations, η^i/η^i_o [— —], and the corresponding air pressures, p/p_s [———], above the water columns undergoing forced excitations with the sinusoidal excitation amplitude of $\eta^i_o/D = 0.144$ and $D = 0.104m$; the calculations compared to the experimental data [○] by Fung (1998) for varying forcing frequencies: $\omega_f^2 B/g = 0.20, 0.79,$ and 1.34.

the air pressures are found to be asymmetrical with respect to the frequency axis. This suggests that at lower forcing frequencies, the magnitudes of the air pressures that excite the water column to move downwards are larger than those during an upward displacement. The explanation for this can be understood from the following

mathematical formula derived from Equation (2.37):

$$p_{\eta^i_{min}} = \left[\rho(B - \eta^i_o) + A_m\right] \omega_f^2 \eta^i_o - \rho g \eta^i_o, \tag{3.3}$$

$$p_{\eta^i_{max}} = -\left[\rho(B + \eta^i_o) + A_m\right] \omega_f^2 \eta^i_o + \rho g \eta^i_o, \tag{3.4}$$

where $p_{\eta^i_{min}}$ and $p_{\eta^i_{max}}$ are the air pressures when the water column is at its minimum and maximum displacement, respectively. At the lower frequency, the restoring force is the dominant force component. Clearly, this force is less reduced when the water column displacement is minimum (Equation (3.3)). As a result, the absolute magnitude of the air pressure is larger than that at the maximum displacement. Conversely, with a higher forcing frequency, the air pressure has a larger absolute magnitude when the water column is at its maximum displacement. This is related to the dominance of the inertia force under a high-frequency excitation. In this case, the force has its largest amplitude when the instantaneous mass bounded by the wall is at its peak value (Equation (3.4)). This happens when the water column arrives at its maximum position. Importantly, the unequal absolute magnitudes of the air pressure at the maximum and minimum displacement given a constant forcing frequency indicate nonlinearity in the air pressure. This nonlinearity source is associated with the instantaneous mass (or excursion) of the water column.

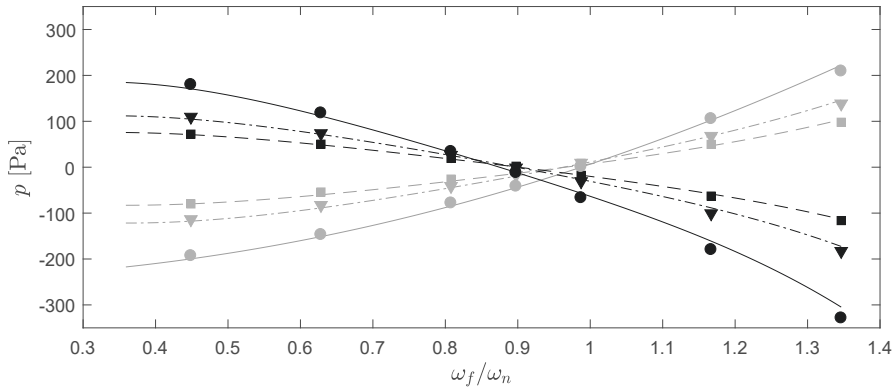

Figure 3.10: Air pressures p when the water columns are at their maximum displacement [— —, —·—, ——] and at their minimum displacement [— —, —·—, ——] are numerically predicted over varying forcing frequencies and amplitudes and are compared to the experimental data from Fung (1998): [■, ■] for $\eta^i_o/D = \pm\ 0.096$, [▼, ▼] for $\eta^i_o/D = \pm\ 0.144$, and [●, ●] for $\eta^i_o/D = \pm\ 0.24$.

At a resonant condition, nonlinearities in the air pressure may be associated with vortex. At present, this is simply a speculation based upon the argument that the

damping force associated with vortex under a resonant condition is important. The vortex may introduce high-harmonic contents in the air pressure. A large excursion of water column oscillation may also contribute to the nonlinearities. This is suggested from the earlier explanation about the air pressures at the lower and higher frequencies and the dependence of the normalised air pressure on the forcing amplitude; the latter indicated from Figures 3.8(A)-(B). An investigation of the vortex formation and motion under a forced oscillation is provided in Chapter 4, with a further confirmation of the nonlinearities in forces provided in Chapter 5.

3.3.4 Wave radiation profiles

The results of a convergence study relating to the external water surface elevation at the radial location of $r/\lambda = 0.04$, is presented in Figure 3.11(A). In this case, the external water wave radiates away from the OWC; the latter undergoing the forced excitation described in Section 3.3.2. The external water surface elevations are found to be very small. As a result, achieving a resolution as high as that described in respect of the internal water surface is challenging. Indeed, there is no possibility that we could achieve a vertical resolution of $\Delta z = a\,(r)\,/10$, where $a\,(r)$ is the local radiated wave amplitude. In an attempt to address this, the vertical grid size in the external wave field is set equal to that adopted to describe the internal free-surface in absolute terms, $\Delta z = \eta_o^i/10$.

Figure 3.11(A) provides comparisons of the time-varying external wave elevations calculated using various grid configurations. The external wave radiates under the forcing amplitude condition of $\eta_o^i/D = 1.6$. These comparisons show that the wave elevation calculated using Grid $C3$ ($\Delta z = \eta_o^i/20$, $\Delta r = b/20$), exhibits small deviations (less than 5 %), when compared to the two coarser meshes, Grids $A1$ and $B2$. Furthermore, no significant difference is evident when the surface elevation is calculated using the finest mesh; Grid $C3^*$ with $\Delta z = \eta_o^i/80$. In this latter grid, the external free-surface area has been locally refined twice; the resulting number of cells being prohibitively large at almost 45 million cells. Interestingly, comparison with the data generated on Grid $D3$ ($\Delta z = \eta_o^i/24$, $\Delta r = b/24$) shows that the wave crest heights predicted using Grid $C3$ and Grid $D3$ are equal; the root-mean-square variation being less than 0.6%. In Grid $D3$, the refinement is applied in all directions, across the entire computational area. Based upon these results, it is reasonable

to consider that Grid $B2$ is sufficiently fine to accurately model the external wave elevations. This is based upon two facts: the insignificant differences between the simulation results of Grids $C3, C3^*$ and Grid $D3$, and the small deviation of the result from Grid $B2$ when compared to Grid $C3$.

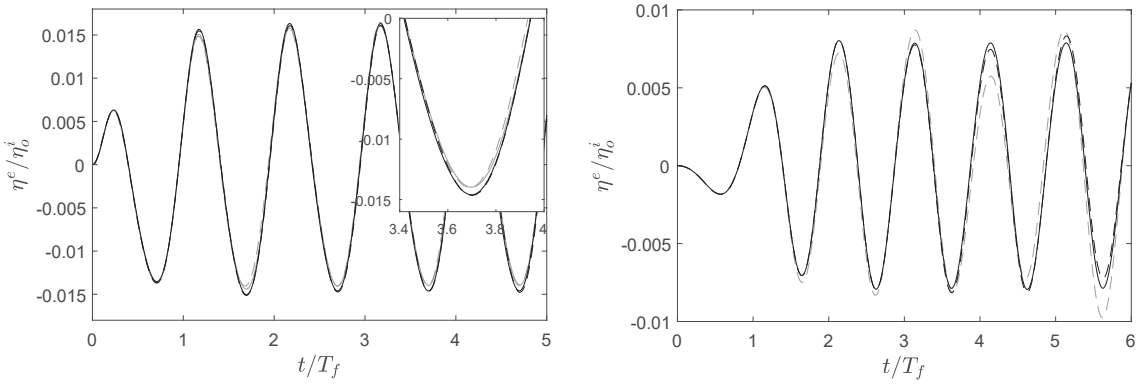

(A) Case II, $\eta_o^i/D = 1.6$ (B) η^e at $r/\lambda = 0.5$ for $R_f = 1, 4$ and 8λ

FIGURE 3.11: (A) Time-histories of external water surface elevations, η^e, normalised with the forcing amplitude, η_o^i, for Case II, predicted using various grids: Grid $A1$ [— —], Grid $B2$ [——], Grid $C3$ [— —] and Grid $C3^*$ [——], and (B) The effect of wave reflections from the outer boundaries on η^e at $r/\lambda = 0.5$ for $R_f = \lambda$ [— —], 4λ [— —], and 8λ [——].

In seeking to achieve a steady state for the entire flow field, including the externally radiated wave field, it is necessary to simulate multiple oscillations of the water column. However, the longer the simulation the greater the potential problem of wave reflections from the outer boundary of the cylindrical test tank. In order to investigate this, three cylindrical test tanks with varying radial dimensions were considered ($R_f = 1, 4$ and 8λ). Figure 3.11(B) shows a comparison between the radiated wave fields predicted at $r/\lambda \approx 0.5$. This location has been shown because it is sufficiently distant from the outer wall of the OWC that the evanescent modes are negligible. Comparison with the longest domain, $R_f = 8\lambda$, reveals that the radiated wave amplitudes in the last two wave periods differ by about 2% for $R_f = 4\lambda$, and about 10% for $R_f = \lambda$. Given the need to address steady-state conditions, data sampling will be required for up to 6 oscillations of the water column. The present results suggest that if $R_f = 4\lambda$, the predicted data will be free from any reflected wave components arising from the outer domain boundary.

Finally, Figure 3.12 concerns the spatial variation of the radiated wave amplitude for two very different amplitudes. The discretisation of one wave length is deter-

mined, so that the cell aspect-ratio along the external interface is fixed ($AR = 2$); the number of cells in one wave length is thus determined by this requirement, with the values given in Tables 3.7 and 3.8. The external wave amplitudes are then computed using a Fast Fourier Transform (FFT) analysis of the time-varying external waves at a number of radial locations. The amplitudes of the fundamental frequency, $\eta_o^{e(1)}$, are then taken as the wave amplitudes at the respective radial distance from the outer wall cylinder; the radial variation in the amplitude being normalised by the corresponding forcing amplitude, η_o^i. These normalised wave profiles collapse well at the far-field. This suggests the validity of linear wave radiation. However, in the near-field, the profile appears to be reduced with the increasing forcing ampliude. This hints at the possible importance of vortex shedding in the near-field. Further discussion of the wave radiation in the near- and far-fields is provided in Chapter 4.

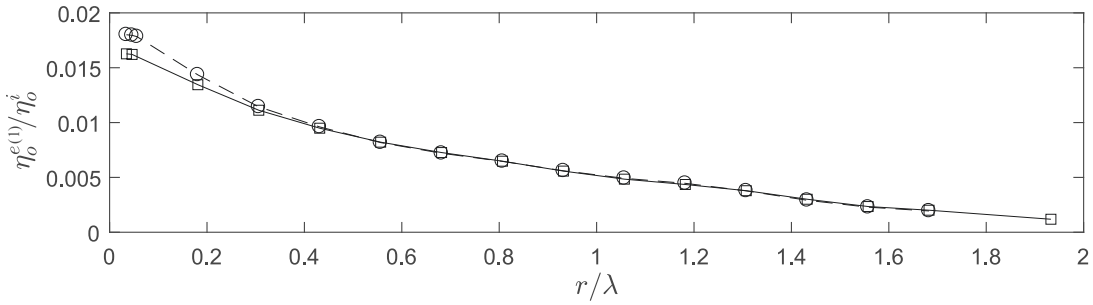

Figure 3.12: Radial variations in the amplitude of the fundamental frequency of the radiated wave field arising due to OWCs undergoing two various forcing amplitudes: Case I with $\eta_o^i/D = 0.25$ [$\circ$], and Case II with $\eta_o^i/D = 1.6$ [$\square$].

3.4 Two-dimensional wave modelling

3.4.1 Numerical wave tank

Investigations of a numerical wave tank were carried out to understand how best to model wave generation and to evaluate the wave-modelling capability of OpenFOAM. In terms of numerical wave generation, *waves2Foam* is a toolbox that is built upon Open Foam. Within this toolbox, the boundary conditions at the numerical wave generator are defined using the theoretical water wave theories supported by the toolbox. On the inlet boundary, the theory is used to define u, α, and $\partial p/\partial n$. On the open atmosphere boundary and bed (or wall) boundary of the numerical wave

tank, the boundary conditions are similar to those illustrated in Figure 3.1.

To successfully model wave propagation, wave reflection at the outlet boundary needs to be minimised. This is achieved by using a relaxation zone which seeks to gradually blend the computed solution with a known condition. At the outlet boundary, this known condition relates to still water. Accordingly, a fixed value of zero is defined for u, while a zero gradient (Neumann) boundary condition is given for α and p. Furthermore, when the wave domain includes a structure, in the present case of an OWC, this will also reflect waves which must be dissipated at the inlet boundary. To achieve this, a second relaxation zone is also necessary immediately in front of the inlet boundary. Within the present study, the relaxation zones were defined according to Mayer et al. (1998). This approach is readily utilised within *waves2Foam*. A wave relaxation zone of length $L_R = \lambda$ was employed at the wave making or inlet boundary, while a zone of length $L_R = 1.5\lambda$ was adopted at the outlet boundary. These zone lengths are expected to minimise wave reflections to less than 1% (Jacobsen et al., 2012). A sketch of a numerical wave tank with the boundaries defined and the position of the relaxation zones noted is provided in Figure 3.13.

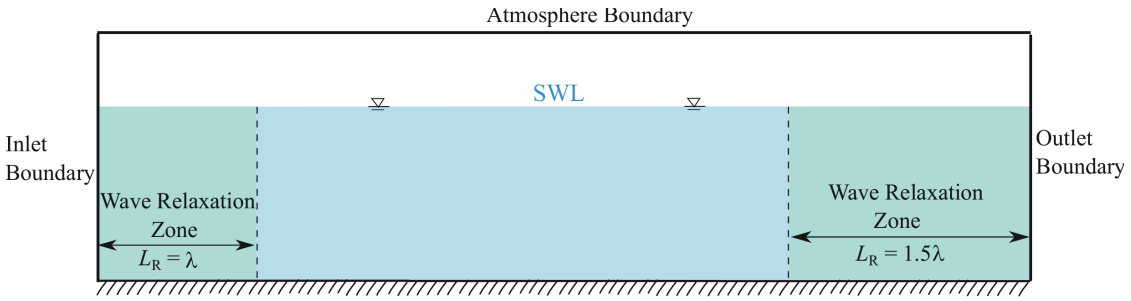

Figure 3.13: Sketch of a numerical wave tank, its boundary conditions and relaxation zones.

Initially, a RANS model was implemented within the numerical wave tank and it was found that the wave amplitudes were excessively dissipated; the time-varying water surface elevation reducing with time. This result is associated with the build-up of unphysical turbulence at the free-surface. As described in Appendix D, the production term $\tilde{P}_k$ in the transport equation of the turbulence kinetic energy is defined on the basis of strain rate. This approach introduces an unphysical large eddy-viscosity in a potential-flow area defining a non-breaking wave field. Jacobsen et al. (2012) suggests that this can be avoided by expressing the productions in terms of the curl of velocity field in a RANS model. However, this improvement has not

been provided in any RANS model within OpenFOAM. In contrast, the simulations using an LES model show little or no evidence of excessive large-eddy viscosity at the free-surface. Accordingly, the LES dynamic Smagorinsky model will be employed for all subsequent simulations. This is consistent with the earlier findings in which the LES dynamic Smagorinsky model was also shown to be the preferred option in terms of modelling the flow separation and physical dissipation in an OWC.

Apart from the aforementioned issues, numerical wave attenuation with increasing horizontal distance from the wave maker was also problematic. To illustrate this problem, a numerical wave tank with its inlet and outlet boundaries respectively located at $x = -3.5\lambda$ and 6λ was considered. The dimensions of the wave relaxation zones defined for these boundaries were in accordance with those indicated in Figure 3.13. Various time-marching numerical schemes were adopted. These included the Backward (three-time level) scheme, the Crank-Nicholson scheme with the option of a blending factor, and the Euler scheme (Ferziger & Peric, 2002). All these schemes are supported and implicitly applied within Open Foam. The simulated results arising from this numerical set-up are presented in Figure 3.14. This shows the downstream variation in the computed wave height, H, normalised by the theoretical wave height, H_o, for a wave of period $T = 1.0$s and wave steepness of $\frac{1}{2}H_o k = 0.1$. In each case, the wave heights at different relative horizontal locations x/λ are presented. In this way, the energy conservation of a time-marching scheme for a numerically generated wave in an initially still water tank can be evaluated. This figure indicates that the higher-order schemes such as the Backward and Crank-Nicholson schemes lead to small wave height amplifications. Conversely, the low-order Euler scheme produces a reduction; the magnitude of which increases with the horizontal distance x/λ from the wave maker. Considering these results, the Crank-Nicolson scheme with a blending factor of 0.5 gives the best result. As a result, this approach was adopted for all subsequent simulations of regular waves propagating into a stagnant ambient.

Having investigated the appropriate relaxation zone length and the preferred time-marching scheme, the grid resolution adopted in the model was evaluated. A minimum vertical resolution of $\Delta z = H_o/10$ and a maximum cell aspect-ratio of $AR = 2$ were set for the numerical cells near the water surface. The time step, Δt, is chosen such that the Courant-number was set to $C_o = 0.1$, where $C_o = u\Delta t/\Delta x$, with Δx being the horizontal cell length near the free surface. The success of the

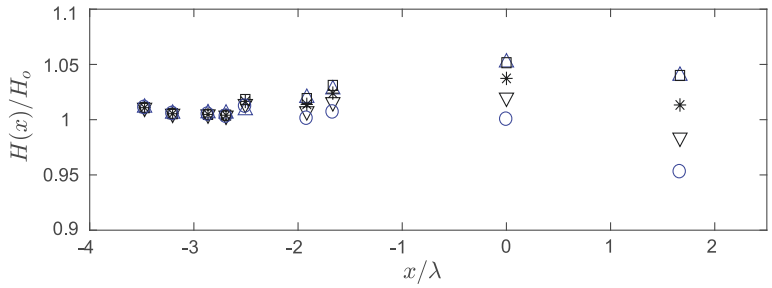

Figure 3.14: Predicted wave heights H, normalised by the theoretical input wave height H_o, at increasing horizontal locations, x/λ, based upon different time-marching schemes: the Backward [□], Crank-Nicholson 09 [△], Crank-Nicholson 05 [∗], Crank-Nicholson 02 [▽], and the Euler scheme[○].

numerical simulations is presented in Figure 3.15. This concerns time-histories of the water surface elevations, $\eta(t)$, at different locations; the numerical results compared to the analytical Stokes' second-order solution. Two different wave conditions are considered. The first, Case I, corresponds to the case presented in Figure 3.14. The second, Case II, considers a wave period of $T = 1.3$s and a wave steepness of $\frac{1}{2}H_o k = 0.06$. In both figures, the theoretical wave elevations have been shifted so that they match the time-varying numerical elevations at their first wave gauge. At all subsequent gauge locations, only the corresponding time-varying numerical elevations are presented.

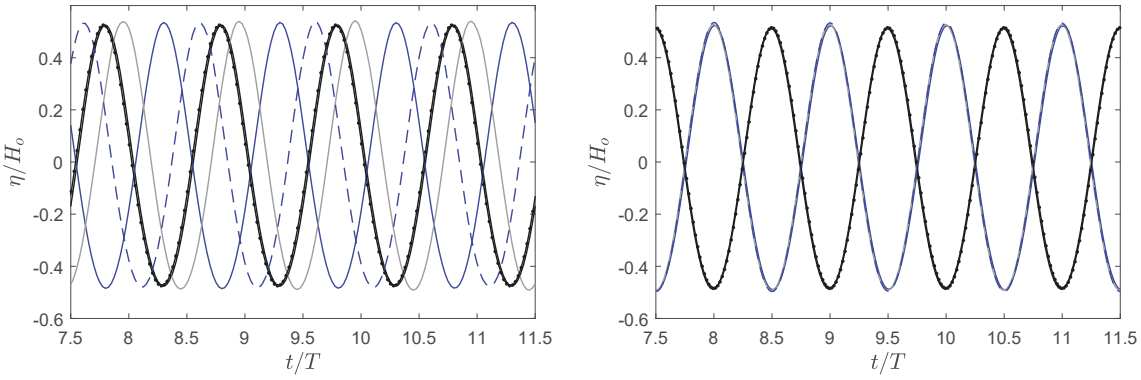

(A) Case I, $T = 1.0s$ and $\frac{1}{2}H_o k = 0.1$

(B) Case II, $T = 1.3s$ and $\frac{1}{2}H_o k = 0.06$

Figure 3.15: Time-histories of the incident wave elevations, $\eta(t)$, for (A) wave case I at $x/\lambda = -3.2$ [——], $x/\lambda = -1.7$ [——], $x/\lambda = 0$ [——] and $x/\lambda = 1.7$ [– –], and (B) wave case II at $x/\lambda = -2.5$ [——], $x/\lambda = -1.0$[——], $x/\lambda = 0$ [——] and at $x/\lambda = 1.0$ [– –]. In both cases the numerical predictions are compared to the analytical wave theory [— · —] at $x/\lambda = -3.2$ and -2.5.

The data presented in Figure 3.15 highlights two points: (i) the numerically

predicted wave amplitudes at different locations are uniform, and (ii) the phase shifts of the waves also match the theoretical values. Evidence of this latter effect is provided by the fact that the normalised elevation η/H_o at $x = -3.2\lambda$ is π out of phase relative to that at $x = -1.7\lambda$ in Case I. Likewise, the value of η/H_o at $x = -2.5\lambda$ shows a π phase shift from the elevation at $x = -1.0\lambda$ in Case II. These two figures suggest that the numerical dissipation of the wave amplitude has been successfully minimised. Moreover, the chosen grid resolution and the numerical scheme are sufficiently accurate to effectively model waves.

3.4.2 Scattering and dissipation of surface waves by plates

Having established the success of the wave generation, this section considers the wave interactions with a single-plate and a bi-plate structure. Figure 3.16 gives a schematic view of a rigid plate located at the centre of the numerical wave tank. In defining this layout, the length of the relaxation zones are exactly as described previously. Moreover, within this system, the energy components correspond to the incident waves, the reflected and transmitted wave components and the energy loss. The first is defined by the input energy, while the last is associated with flow separations and other dissipative mechanisms. The validation was undertaken by evaluating these energy components using an energy conservation principle. In undertaking this step, the relative importance of these energy components and the physics underpinning this particular fluid-structure interaction problem can be explored. To achieve this, the reflection coefficient, C_r, and the transmission coefficient, C_t, are as defined in Equation (2.30) and calculated using the method proposed by Lin & Huang (2004).

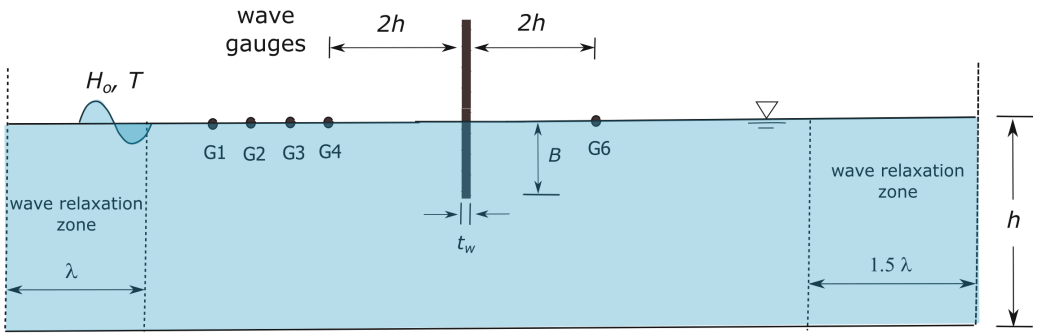

Figure 3.16: A schematic description of a single rigid plate fixed in a numerical wave tank.

In applying this method, the numerical wave tank was first alllowed to achieve a

steady state and an FFT analysis was applied to the predicted water surface elevations. The method by Lin & Huang (2004) was implemented for this analysis. The time-histories of wave elevations at four wave gauges were sampled at $40/T$, where T is the wave period. In terms of the reflection coefficient, data was predicted at gauge positions G1, G2, G3 and G4 (on Figure 3.16) located in the upstream field in front of the single plate. Likewise, the transmitted amplitude was obtained from an FFT analysis of $\eta(t)$ recorded at the downstream wave gauge, G6. All gauge positions were sufficiently distant from the wall so that the effect of any standing wave modes (or evanescent modes) was negligible. This was achieved by ensuring that the gauge positions were at least twice the water depth from the wall. Given the incident wave amplitude, both the transmission and reflection coefficients were quantified solely from the first-order harmonic components arising from the FFT analysis.

Figure 3.17 concerns the variation of the reflection and transmission coefficients, C_r and C_t, with KB, where B is the draft of the plate and $K = \omega^2/g$ is the deep water wave number corresponding to $2\pi/\lambda_o$; λ_o defining the deep water wave length. Two plate drafts corresponding to $B = 0.1$m and 0.2m are considered. Overall, the data presented in Figure 3.17 exhibits the expected trends:

(i) The proportion of wave energy transmitted into the far-field increases with the wave length,

(ii) The plate with a deeper draft reflects more incident wave energy, and

(iii) The reflection coefficients increase and, consequently, the transmission coefficients decrease with increasing KB.

However, comparisons with the experimental data given by Stiassnie et al. (1984) show some departures. This is almost certainly due to an inconsistency in the incident wave amplitudes; full details of which are not explicitly stated in the account of the experimental study. Nevertheless, the numerical model clearly captures the underpinning physics. This is indicated most clearly by two points:

(i) The smaller values of the transmission coefficients, C_t, when compared to the theoretical values, and

(ii) The reflection coefficients, C_r, being in close agreement with the analytical results.

Importantly, these effects are observed in both the laboratory data and the numerical predictions.

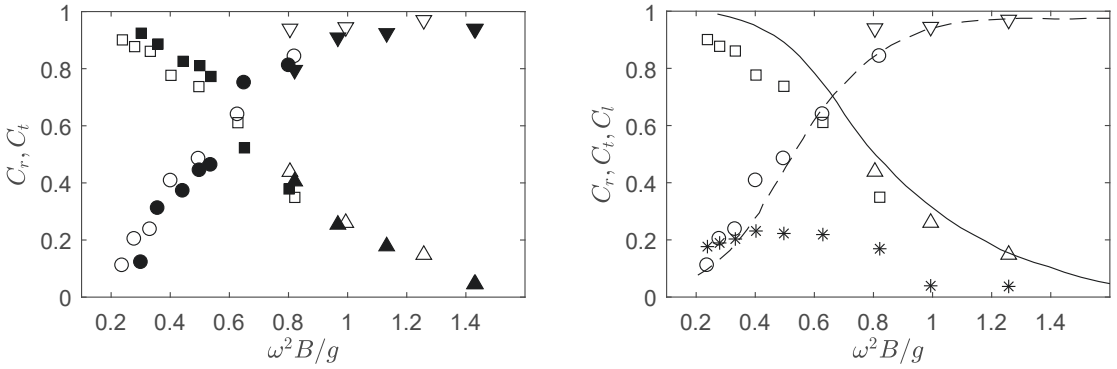

(A) C_r and C_t (B) C_r, C_t and C_l

Figure 3.17: Reflection C_r, transmission C_t and energy loss coefficients C_l for a vertical plate rigidly held in a wave tank with the water depth of $h = 1.3$m and varying incident wave frequencies $\omega^2 B/g$; comparisons between numerical predictions for drafts of $B/h = 0.08$ [$\circ$, $\square$] and $B/h = 0.16$ [$\triangledown$, $\triangle$], experimental data [$\blacksquare$, $\bullet$, $\blacktriangledown$, $\blacktriangle$] and analytical coefficients, C_r [$-\,-$] and C_t [——], extracted from Stiassnie et al. (1984). The numerically predicted C_l [$*$] is also shown.

Adopting an energy balance principle, the energy loss coefficient C_l can be evaluated. This is expressed as $C_l = 1 - (C_r^2 + C_t^2)$. The results presented on Figure 3.17(B) show that C_l has a maximum value of about 20%. Evidently, C_l is more pronounced for longer wave periods; the coefficient being inversely proportional to the KB parameter at a constant incident wave amplitude. This result may be explained by the fact that given a constant incident wave amplitude, a longer wave has a longer fluid particle path length. In effect, the longer the wave the larger the major axis of the elliptical motion describing the orbital motion. Since this path is normal to the bottom tip of the plate, longer waves will be associated with vortex shedding having a strong circulation. This effect is directly akin to an increase in the effective KC number.

Given points (i) and (ii) noted above, it may be concluded that the energy loss associated with the vortices shed at the plate edge is due to a reduction of the transmitted waves; the surface friction being assumed to be negligible. In contrast, the reflected waves are not influenced by the vortex shedding. In an attempt to verify this argument, additional tests were undertaken. These involved predicting the reflection and transmission coefficients for three different $\omega^2 B/g$ cases. In each case, multiple values of the wave steepness, $\frac{1}{2}Hk$, were considered, where H is the incident

wave height and k the wave number. The data arising from these calculations are presented on Figure 3.18(A). These results show that the reflection coefficients, C_r, are relatively invariant to the increasing wave steepness $\frac{1}{2}Hk$, whereas the transmission coefficients, C_t, exhibit a decrease. This, in turn, produces an increase of the energy loss coefficients, C_l (Figure 3.18(B)). This analysis explains the former experimental observation shown in Figure 3.17.

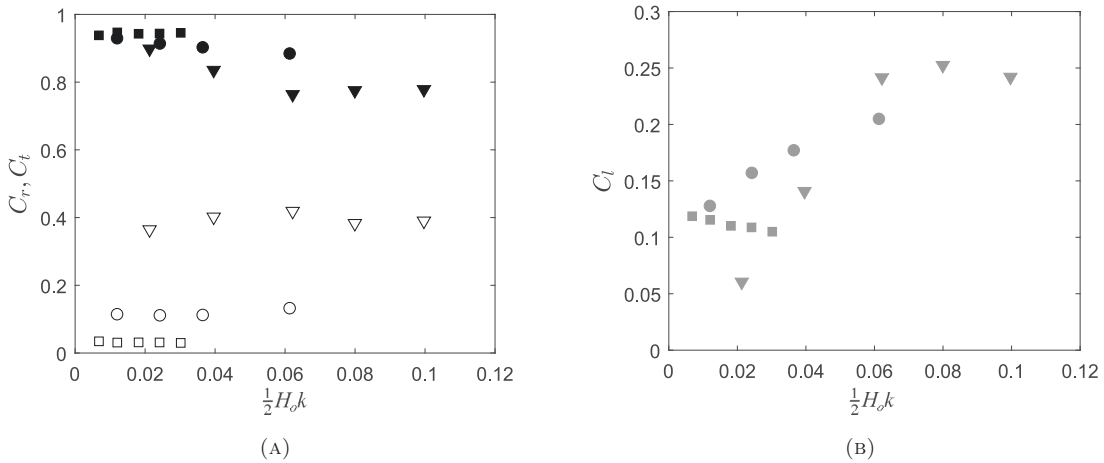

(A) (B)

Figure 3.18: (A) Reflection C_r, transmission C_t , and (B) energy loss coefficients C_l for a vertical plate over varying wave steepness $\frac{1}{2}Hk$ conditions. C_r [□, ○, ▽], C_t [■, • and ▼], and C_l [■, •, ▼] are numerically predicted for $\omega^2 B/g = 0.12, 0.24,$ and 0.4, respectively.

A similar energy transfer mechanism applies when an incident wave encounters a bi-plate structure. In this case, a gap space exists between two parallel-sided plates. Figure 3.19 presents the reflection, transmission and energy loss coefficients for a bi-plate structure with a gap space of $w = 3B$ and draft B being equal to the single plate discussed earlier. The transmission coefficients, C_t, predicted from the viscous solver and the experimental data are again over-estimated by an analytical solution. Conversely, the reflection coefficients, C_r, are generally well predicted by the analytical solution except in the range of very high frequencies. This finding is important for two reasons. First, a bi-plate structure is close to an OWC. Second, it reveals that the transfer of energy from the 'transmission' components to the 'loss' components remain significant. Moreover, related laboratory results showing similar effect have been reported by Knott & Mackley (1980) and Sarmento (1992).

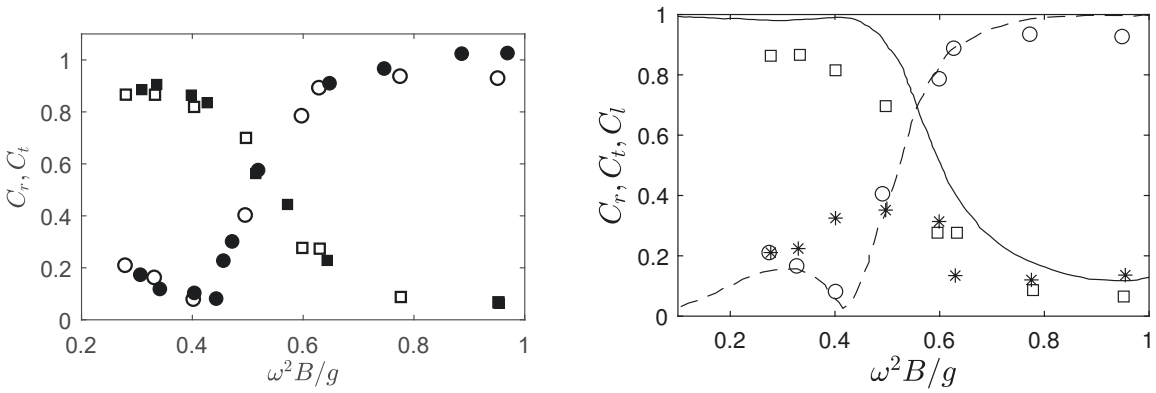

(A) (B)

FIGURE 3.19: Reflection C_r [$\circ$], transmission C_t [$\square$] and energy loss coefficients C_l [$*$] for a bi-plate with draft $B = 0.1$m and gap space $w = 3B$ placed inside a wave tank under varying incident wave frequencies $\omega^2 B/g$; the present numerical predictions compared to the experimental results [■, •] and analytical solutions [— — , ——], extracted from Stiassnie et al. (1986).

3.5 Numerical modelling of cylindrical OWCs

Validations of two-dimensional problems involving an analysis of energy components have been described above. For a cylindrical OWC, an investigation of the wave-induced oscillations requires a three-dimensional model. Unfortunately, there are no existing experimental studies in defining the energy components in such a domain. As an alternative, the discussion that follows concerns other relevant variables.

Figure 3.20 concerns the response amplitude operators (RAO) of an OWC with a cylinder aspect-ratio of $D/B = 0.31$. The draft B is set to 0.3m. Within this model, the incident wave frequencies are varied, defining the wave steepness within a range of $0.04 \leq \frac{1}{2} H_o k \leq 0.06$. The hydrodynamic pressures at two vertically varying locations inside the water column are also shown. These pressures correspond to the magnitude of the first-harmonic pressure, normalised by $\frac{1}{2}\rho g H_o$. The normalised pressures at the higher vertical location are denoted by $\overline{p}_1$, while those nearer the bottom mouth by $\overline{p}_3$. The numerically predicted variation in the RAO and the two pressures are compared to the experimental data (Sykes et al., 2008).

The comparisons provided on Figure 3.20 show good agreement across the full range of frequencies. In particular, the RAO is well predicted at frequencies near the resonant condition. Interestingly, both the RAO and the pressures rapidly reduce in the higher frequency range ($\omega^2 B/g \geq 0.9$); the pressures $\overline{p}_3$ being close to zero for frequencies lying within the range ($\omega^2 B/g \approx 1.1 - 1.12$). In this regard, the

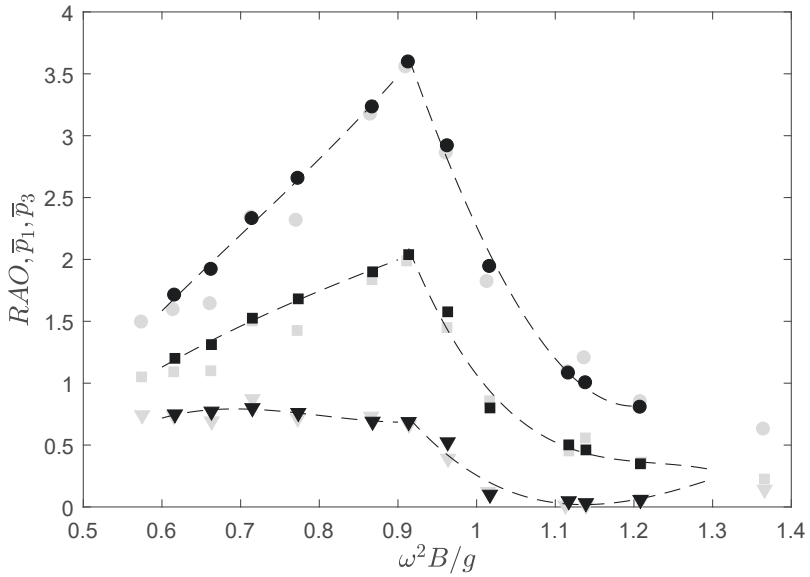

Figure 3.20: Numerically predicted RAOs [−•−] inside a cylindrical OWC in a three-dimensional wave tank, and the hydrodynamic pressures $\overline{p}_1$ and $\overline{p}_3$, measured on the wall at two vertical positions $\overline{z}_1 = -0.48B$ [−■−] and $\overline{z}_3 = -0.9B$ [−▼−] in the water column. In each case, comparisons are provided with the experimental data given by Sykes et al. (2008) [• , ■ , ▽].

viscous flow solver provides a very good description of the laboratory data. Furthermore, both the numerical and experimental data indicate that the pressure near the mouth of the OWC, $\overline{p}_3$, is relatively invariant across the lower frequencies. It is also relevant to note that the hydrodynamic pressure $\overline{p}_3$ at the location closer to the mouth is smaller than the pressures $\overline{p}_1$ near the internal free-surface across the entire frequencies. In seeking to explain this, the smaller pressures at the wall and near the mouth may indicate a local increase in the velocity field. As such, non-uniform velocity profiles along the draft and at the cross-sectional area of the bottom mouth should not be discounted. Indeed, that the velocity field within the water column is non-uniform is provided in Chapter 4.

To further validate the numerical prediction of the wave excited OWC, the phase shifts of the pressure measured at different vertical locations are considered in Figure 3.21; the phase shifts being relative to the internal water surface. While the agreement is far from perfect, the overall trend matches the experimental data. In particular, the numerical predictions reveal that the pressures are in phase with the internal water surface elevations in the lower frequency range and have a π phase shift in the higher frequency range. This is similar to the data relating to the forced

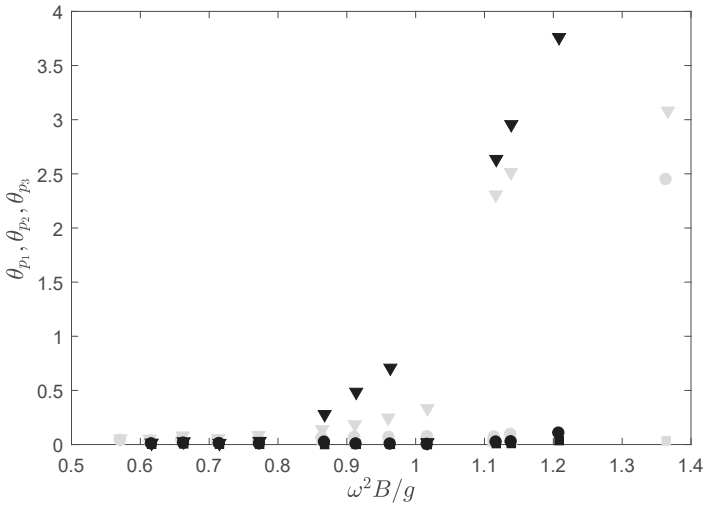

Figure 3.21: The relative phase shifts ϕ_{p_1}, ϕ_{p_2}, and ϕ_{p_3} at three locations inside the OWC: $\overline{z}_1 = -0.48B$ [■], $\overline{z}_2 = -0.67$ [●] and $\overline{z}_3 = -0.9B$ [▼]; the numerical predictions compared to the laboratory data [■ , ● , ▽] reported by Sykes et al. (2008).

oscillation tests outlined in Figure 3.9. Further detailed consideration of these phase changes is given in Chapter 5.

3.6 Concluding remarks

This chapter has evaluated the capability of Open Foam to model OWCs under various excitation mechanisms. The freely damped and forced oscillations of water columns placed within a cylindrical test tank have been numerically simulated. Having established the minimum grid requirements as $\Delta z \leq \eta_o^i/10$ and $y^+ \leq 20$, both the internal water surface and the air pressure were accurately modelled. While the accuracy of the internal water surface was less sensitive to the boundary layer resolution y^+, the accuracy of the air pressure prediction was less sensitive to the vertical grid resolution, Δz. Having considered the appropriateness of several turbulence models, the preferred approach is to apply the LES dynamic Smagorinsky model. Importantly, the adoption of the LES classical Smagorinsky model for the implementation in a wall-bounded flow problem within an OWC tends to under-estimate both the internal water surface elevation and the natural period. In contrast, the air pressure acting above the internal water surface is over-estimated.

Having adopted the preferred viscous solver, the characteristics of the air pres-

sures, notably the double peaks under a resonant state and during a downstroke displacement of water column could be successfully predicted. Equally, the asymmetrical pressures measured when the water column was at its extreme displacement could also be predicted. It is speculated that these nonlinear characteristics in the forcing may be related to both vortex shedding and large excursion of water column oscillation.

Finally, the evaluation of the solver capability has been extended to model wave generation and wave interactions with the structures in two- and three-dimensional wave basins. In both cases, comparative studies have demonstrated the solver's capability to capture the physics in the flow problem under investigation. The crucial requirement is to minimise the numerical dissipation and wave attenuation, showing the generation and preparation of the desired wave amplitudes. The present model has been shown to be capable of predicting the scattered and transmitted waves by the plate structures. Furthermore, the response amplitude operators of the water column inside a cylindrical OWC can also be estimated accurately.

Having minimised the numerical dissipation and wave attenuation, the physical energy loss can be reliably quantified based upon an energy conservation principle. Application of this principle has confirmed the correlation of the transmitted wave energy with the energy loss. Preliminary calculations suggest that the energy loss associated with vortex shedding explains the over-estimation of the transmitted wave energy by an inviscid linear analytical solver. This will be further considered in subsequent chapters.

4

Radiated wave and rotational flow fields

4.1 Chapter overview

Building upon the model validations described in Chapter 3, an investigation of the radiated wave fields around OWCs is undertaken. This investigation includes an analysis of the radiated waves in the fields near and far from the OWCs. In order to simulate the radiated wave fields, a linear potential and a viscous flow model were implemented. The linear analytical solution proposed by Evans & Porter (1997) was adopted in the former, while the forced water column oscillation described in earlier chapters were numerically modelled in the latter. A comparison between the two solutions provided in Section 3.3.4 has briefly shown the reduction of the radiated wave amplitude in the viscous flow, and indicated the nonlinear dependence of the radiated wave amplitude on the amplitude of the internal water surface elevation.

Returning to gap flow or moonpool studies, Ananthakrishnan (1999, 2015) confirmed that the radiated wave amplitudes were smaller than those predicted by the inviscid solutions. Indeed, he concluded that the reductions of the wave amplitudes arose as a result of the damping effects of viscosity. However, Kristiansen & Faltinsen (2008) and Kristiansen & Faltinsen (2012) confirmed that discrepancies in the predicted wave radiations generated by two closely adjacent boxes shown in Faltinsen et al. (2007) were associated with flow separation. The explanation for this relates

to the deviations being evident both in the near- and far-fields from the boxes. The deviation was even more pronounced as the amplitude of the box motion increased.

At this stage, it is important to acknowledge the potential vortex effect on the radiated wave fields associated with OWCs. This will be explained in the present chapter. By comparing the two solutions and analysing the radiated wave and rotational flow fields arising due to the forced water column oscillations, it is expected that the validity of the linear potential theory can be understood on the basis of a physical explanation. Overall, this chapter concerns the following topics:

1. Methods for analysing the rotational flow field arising in a forced water column oscillation model,

2. Description of the water particle kinematics defining the rotational flow fields under forced excitations with varying key parameters,

3. Characterisation of the radiated waves in the fields around an OWC, and

4. Vortex effects on these wave fields and the validity of linear radiation theory.

This chapter is organised as follows. Section 4.2 provides the key parameters of the test cases under investigation. At first, the rotational flow fields and the external water surface elevations at the outer wall of the OWCs are described. The characteristics of these radiated waves are explained in Section 4.3. Furthermore, the failure of the linear radiation theory is discussed. To confirm the physical cause of the evident nonlinearities, methods to evaluate the properties of a vortex and the flow repeatability are described in Section 4.4.

Using these methods, the variations of the vortex properties with the key parameters are investigated, and the influence of the vortex motion on the characterisation of the near-field radiated waves is explored. Based upon this work, the physical mechanisms that provoke the nonlinear characteristics of the motions are discussed in Sections 4.5-4.8. Following on, the far-field radiated waves are observed. The description of these wave fields is provided in Section 4.9. Finally, the influence of the vortex on the effective draft of the OWCs, and the consistency of this result with the characteristics of the near-field radiated waves are explained in Section 4.10.

4.2 Test cases

In the present analysis, the radiated wave field produced by an OWC was numerically generated in a Forced Water Column Test (FWCT). The time-varying internal water surface elevation in this model was computed as a harmonic function of $\eta^i(t) = \eta^i_o \cos(\omega_f t)$, where the amplitude of this internal water surface elevation, η^i_o, was prescribed. The boundary conditions imposed in the computational domain was as defined earlier in Table 3.1; the validation study relating to this numerical model having been described in Section 3.3.

In undertaking the present analysis, the internal water surface amplitude or forcing amplitude, η^i_o, prescribed in the FWCT was varied. This changes the values of two key parameters: the forcing amplitude number ($F_n = \eta^i_o/B$) and the Keulegan-Carpenter number ($KC = 2\pi\eta^i_o/D$). In addition to varying the forcing amplitude η^i_o, the cylinder aspect-ratio D/B and the draft of the water column B were varied. The range of these parameter values is outlined in Table 4.1. The angular frequency ω_f in each case is fixed at 7.28 rad/s. In respect of the mouth shape condition, the OWCs under consideration have either a straight and sharp-edged (SE) mouth or a bell-shaped mouth (BS) with a lip radius r_l set to $0.5D$. All these OWC models have a fixed wall thickness t_w defined as $0.043D$.

Table 4.1: Test cases for analysing the radiated wave field

Test cases	D/B	F_n (η^i_o/B)	KC $(2\pi\eta^i_o/D)$	Frequency $(\omega_f^2 B/g)$	B [m]	Mouth shape
FWCT 1	0.150	0.11-0.71	4.50-29.00	0.87	0.16	SE
FWCT 2	0.435	0.11-0.71	1.60-10.00	0.87	0.16	SE
FWCT 3	1.250	0.11-0.71	0.50-3.50	0.87	0.16	SE
FWCT 4	0.250	0.39	10.00	0.52	0.28	SE
FWCT 5	0.150	0.24	10.00	0.32	0.46	SE
FWCT 6	0.072	0.11	10.00	0.16	0.96	SE
FWCT 7	0.150	0.11-0.71	1.60-10.00	0.87	0.16	BS

4.3 An observation of near-field radiated waves

4.3.1 Radiated waves in a linear potential and viscous flow

Having defined all the relevant model parameters, this section contrasts the wave radiation generated by the OWCs with SE mouths in a linear potential and a viscous

flow model. The results from these models show that the radiated wave amplitudes are axisymmetric and exponentially decaying with the radial distance from the water column. Examples of the radiated wave profiles generated at different forcing frequencies were shown earlier in Figure B.2. This means that the radiated wave profile resembles the wave radiation arising from a heaving truncated cylinder. The explanation for this relates to the principle of energy conservation applied to the energy flux of the radiated wave due to an oscillating cylindrical body (see Equation B.5). Given this fact, the characterisation of the radiated wave field around an axisymmetric OWC can be evaluated in one angular direction.

To begin, the test cases noted as FWCT 1, 2 and 3 in Table 4.1 are considered. In each case, the external water surface elevation, η^e, at the outer wall was closely observed given that the radiated wave propagates outwardly from the centre of the water column. Figure 4.1 presents the time-varying external water surface elevations, $\eta^e(t)$, at the wall of the three cylinders. In this figure, the external water surface elevation, η^e, for each case is normalised by the corresponding internal water surface amplitude (or forcing amplitude), η_o^i, to indicate the relative external surface elevation, $\overline{\eta^e} = \eta^e/\eta_o^i$. This normalised external surface elevation $\overline{\eta^e}$ at the outer wall, also referred to as the normalised near-field radiated wave elevation, is presented along with a fraction of the normalised internal water surface elevation, $\overline{\eta^i} = \eta^i/\eta_o^i$, to provide a comparison between these two elevations. Specifically, Figure 4.1 shows that the near-field radiated wave elevations η^e in all cases respond immediately to the forced excitations in a transient state once the corresponding water column was released from its initial displacement; the latter being determined from the forcing amplitude, η_o^i. Importantly, the near-field radiated wave elevations, η^e, achieved a steady-state response within the first two forcing periods, T_f.

Figure 4.1 confirms the similarity between the steady-state wave shapes in the steady states predicted by the linear potential and viscous flow models. This suggests that the oscillatory responses of the near-field wave elevation subjected to the forced water column oscillation can be reasonably predicted by the linear potential solution. Specifically, the physical phase difference between the near-field wave elevation and the water column in the viscous flow may be qualitatively estimated from the linear potential flow model. Theoretically, the near-field wave elevation, η^e, has an approximately $\pi/2$ phase difference relative to the water column, (or internal water

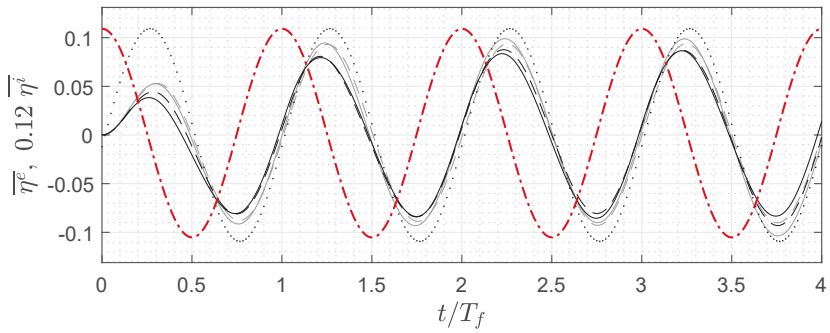

(A) Cylinder aspect-ratio $D/B = 1.25$

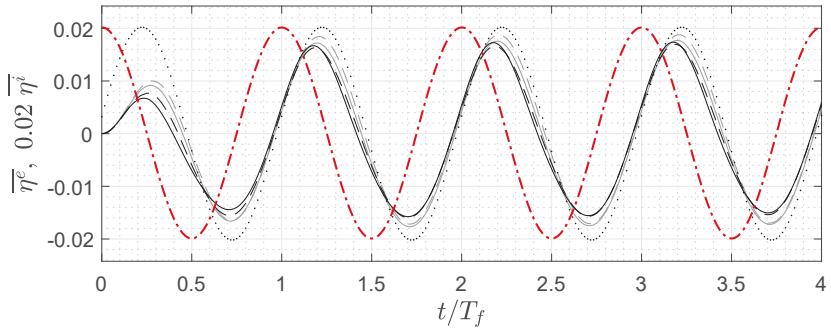

(B) $D/B = 0.435$

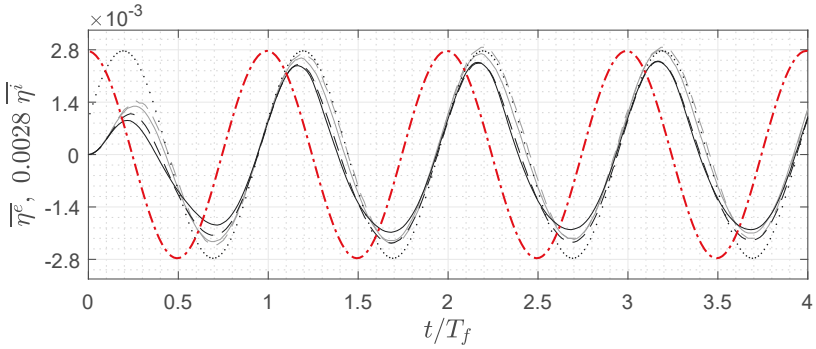

(C) $D/B = 0.15$

FIGURE 4.1: Time-histories of the normalised near-field radiated wave elevations, $\overline{\eta^e}(t)$, and the normalised internal surface elevation, $\overline{\eta^i}(t)$ [— · —], for various cylinders D/B and varying forcing amplitude numbers η_o^i/B: 0.11 [— —], 0.22 [——], 0.44 [— —] and 0.71 [——] predicted from the viscous flow solver and compared to the linear potential solutions [· · · ·].

surface). From a physical standpoint, this points to the presence of a peak value in the near-field wave elevation when the water column is in an equilibrium condition or vice versa.

4.3.2 Streamlines of a linear potential flow in near-field

Figure 4.2 presents a sequence of plots describing the potential flow streamlines that pass around the outer wall and the bottom of an OWC with a SE mouth; the chosen flow-field representing the near-field flow area. The streamline arrows are also presented in this figure to indicate the flow direction. The figure demonstrates the theoretical phase of the external water surface elevation at the wall relative to the water column. In the following description of the flow field, the streamlines and the velocity vectors are presented at different phases of the water column oscillation during one oscillation period. The chosen phases are denoted by the solid symbols on Figure 4.2(A). This figure also shows the internal and external water surface elevations during this period.

The initial phase when the water column has just begun to move downwards at time $t = 1.04T_f$ is considered in Figure 4.2(B). This instant time corresponds to Point (B) on Figure 4.2(A). It is evident from these figures that the external flow and the external free-surface are upwardly displaced as a result of the downward displacement of the water column. The upward displacement of the external water surface continues until this free-surface is restored to the mean water level by the gravitational force at $t = 1.25T_f$.

The reversal in the movement of the external free-surface at the wall radiates waves that travel outwards from the water column. This phase can be observed from the streamline direction of the external free-surface that has changed by $t = 1.26T_f$ (Figure 4.2(C)). Simultaneously, the internal free-surface subjected to the forced excitation continues to move further downwards from the mean water level (Point (C) on Figure 4.2(A)). This continued forced displacement of the water column results in a further upward displacement of the external flow at the wall near the bottom mouth. During this phase, the streamlines of the returning external free-surface converge with the streamlines of the mass flux outgoing from the water column at a vertical location above the draft (Figure 4.2(C)). With the increasing influence from the external water surface in the near-field, this vertical position progressively decreases and approaches the bottom edge (on Figure 4.2(D)). This arises when the external surface elevation at the wall has already returned to the mean water level. This happens (approximately) when the internal free-surface has gained a minimum elevation at $t = 1.5T_f$ (Point (D) on Figure 4.2(A)).

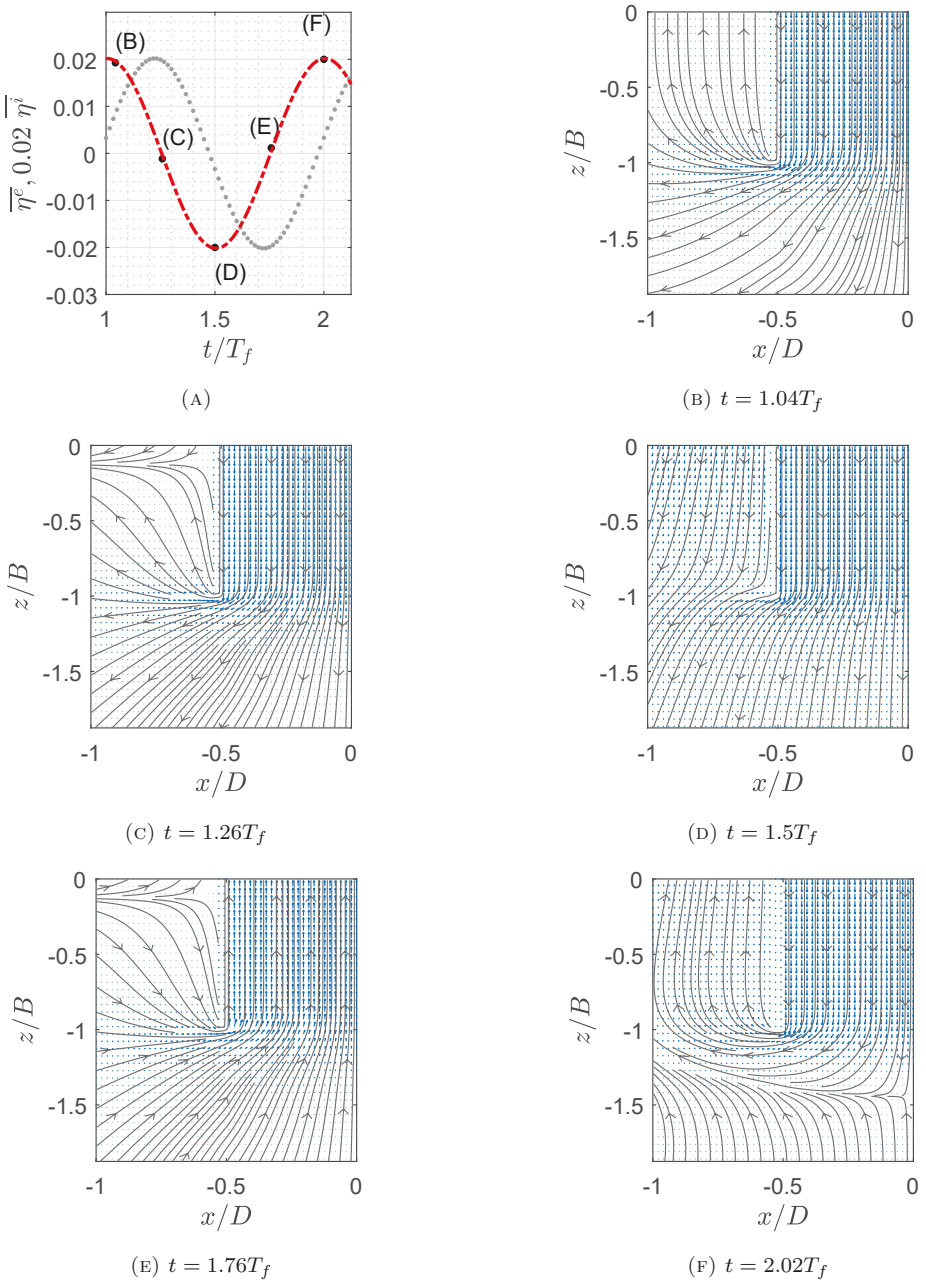

(A)

(B) $t = 1.04T_f$

(C) $t = 1.26T_f$

(D) $t = 1.5T_f$

(E) $t = 1.76T_f$

(F) $t = 2.02T_f$

Figure 4.2: Potential flow streamlines [——] around the bottom edge of an OWC with a SE mouth and the velocity vectors presented from different phases [•] in one period of internal [— · —] and external water surface oscillation [· · · ·].

The forced oscillation of the water column continues to restore the internal free-surface back to the mean water level in the subsequent phase. The external free-surface and the external flow near the bottom edge follows the upward displacement of the water column. As a result, the external free-surface moves downwardly, arriving at a minimum elevation at $t = 1.75T_f$. When this occurs, the restoring stage of

the external free-surface begins. This is again indicated by the streamline direction at the free surface shown in Figure 4.2(e). While the external free-surface is returning to the mean water level, the external flow near the bottom mouth continues to follow the upward displacement of the water column. As such, the streamlines of the external free-surface diverge from the incoming external-flow streamlines near the mouth (Figure 4.2(e)). Over the next quarter period of oscillation, the influence from the free surface becomes increasingly dominant. The vertical location at which the streamlines diverge, gradually approaches the bottom edge, while the water column continues its upward displacement. Finally, the internal free-surface gains a maximum elevation at $t = 2.0T_f$. At this instant in time, all the external and internal flows show an upward direction; this condition being similar yet having a flow direction opposite to that shown earlier in Figure 4.2(d). The water column at this instant time is momentarily still and will immediately repeat the sinusoidal displacement. A plot showing that the water column has just moved from its maximum elevation is presented in Figure 4.2(f). This corresponds to point F on Figure 4.2(a).

In a potential flow, the absence of rotational flow conditions means that the flow streamline pattern is periodic. Therefore, the flow streamlines that exist from the subsequent displacements of the water column are identical to those from former cycles. Furthermore, it is noticeable that the outgoing and incoming flow streamlines near the edge have 90° curvatures. As expected in a potential flow, this suggests that the flow is attached at the corner.

4.3.3 Further insights into wave radiation

Earlier studies concerning flows past a plate or square cylinder have shown that a viscous flow will separate when encountering a corner edge, even when the flow has a small KC number (Bearman et al., 1985, Smith & Stansby, 1991). In the present test cases, the smallest KC number is 0.5, with the corresponding β in the order of 10^4. This indicates that flow separation will occur in all the flow conditions involving the OWCs with SE mouths defined in Table 4.1. Nevertheless, the present linear potential flow solver has clearly demonstrated some success in qualitatively predicting the oscillatory response of the external free-surface at the outer wall. Given this fact, it may be arguable that the response of the near-field radiated wave substantially

depends on the balance between the gravitationally restored wave motion at the wall and the oscillatory flow in the water column. This is suggested from the streamline direction of the external free-surface, and the fact that it clearly responds to the external flow entering and exiting the bottom mouth.

However, comparisons between the numerically predicted wave elevation and the linear analytical solution indicate discrepancies. Indeed, Figure 4.1 clearly shows that the peak external water surface elevations in the viscous flow are over-estimated by the linear potential solution. This is evident in all cases including the smallest forcing amplitude case of $\eta_o^i/B = 0.11$. Furthermore, the phase difference between the near-field wave elevation η^e and the internal surface elevation η^i is smaller than the theoretical phase difference in all test cases. These discrepancies raise important questions concerning the validity of linear radiation theory in the near-field.

To understand the physical cause of these discrepancies, the deviation trends observed in Figure 4.1 are evaluated. Close-up views of the maximum and minimum elevations calculated using the two very different solvers are shown in Figure 4.3. Again, the normalised internal surface elevations are also presented in red. This figure provides clear evidence of the nonlinear characteristics of the near-field radiated wave elevation, η^e. Specifically, evidence of the nonlinearities is given by the progressive reduction of the normalised peak elevation and the phase difference with changes in the forcing amplitude.

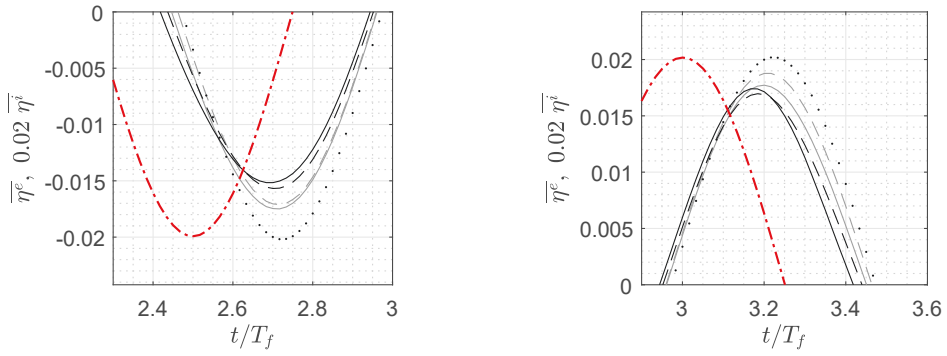

(A) (B)

Figure 4.3: Close-up views of Figure 4.1(B) showing (A) the minimum amplitudes and (B) maximum amplitudes of the normalised near-field radiated wave elevations compared to the linear potential solutions [· · · ·], and the normalised internal surface elevations [— · —], for varying forcing amplitudes η_o^i/B : 0.11 [— —], 0.22 [——], 0.44 [— —] and 0.71 [——].

The level of discrepancy is also found to be dependent on the direction of travel of

the water column. Both the normalised peak external elevation and the phase shift at a given forcing amplitude vary depending on the motion of the water column. This is based upon two considerations: (i) the amplitude reduction is more pronounced when the water column has recently begun to move upwards from its minimum elevation (Figure 4.3(A)), and (ii) the reduced phase difference is more evident from the downward displacement of the water column (Figure 4.3(B)).

The reduced amplitude and the reduced phase difference necessitate a physical investigation. From an energy perspective, the former may imply the proportion of the radiated wave energy is lost and unavailable to displace the near-field wave elevation. However, a reduced phase difference may also indicate the faster development of the near-field radiated waves when compared to the potential prediction. At first sight, this appears at odds with a "loss" of energy. Importantly, the physical mechanisms that cause this progressively reduced amplitude and progressively reduced phase difference are not well understood. Given the assumed flow irrotationality inherent to the linear potential theory, it is likely that the physical cause of the deviations is related to the presence of a rotational flow component. To seek confirmation of this, the kinematics of the flow field will be quantitatively and qualitatively described.

4.4 Methods of quantifying and describing the vortex motion

4.4.1 Downward and upward moving vortex rings

Figure 4.4 shows three different types of vortex rings that are formed and convected during the first one and a half periods of oscillation. In this figure, the vorticity field is viewed from the azimuthal component of vorticity ω_θ, that is perpendicular to the meridional section of a vortex ring. Figure 4.4(A) shows that the first downwardly moving vortex ring is located outside the water column and will be shed before the first stage of downward displacement completes. The next observation from Figure 4.4(B) reveals an upwardly moving vortex ring, generated inside the mouth. This develops when the water column is upwardly displaced. It is evident that this upwardly moving vortex ring involves vorticity that is opposite in sign to the vorticity field of the earlier vortex ring associated with the downward movement of

fluid (Figure 4.4(A)). Furthermore, the upward vortex ring is persistently attached to the inside wall throughout the ascending phase of the water column. In other words, no vortex shedding occurs in this second stage.

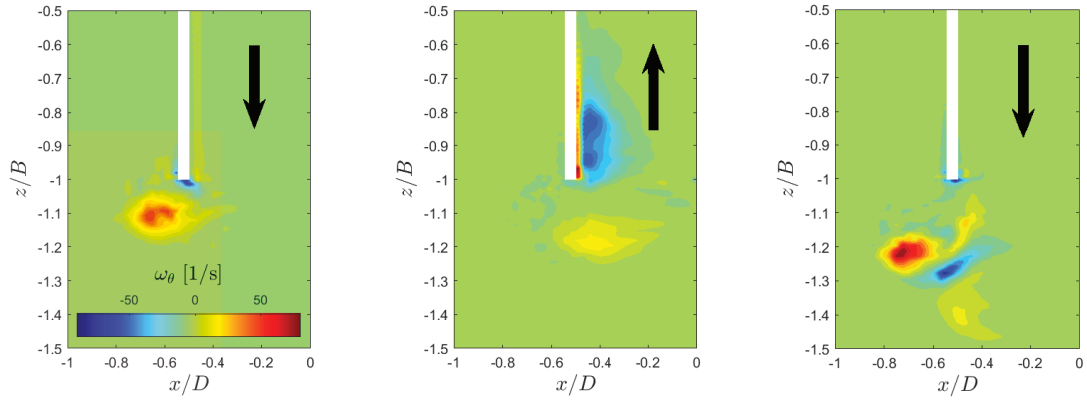

Figure 4.4: (A) A single downward vortex developing outside the wall during the first downward displacement, (B) a single upward vortex developing inside the water column during the reversed displacement and (C) a pair of shed vortices observed in a subsequent downward displacement.

Following on, a new downward vortex ring is generated when the water column is downwardly displaced for the second time. Together with the former upward vortex ring, it forms a pair of vortex rings. This pair of vortex rings has oppositely signed vorticity fields and is detached before the second downward displacement completes. A close-up view showing this pair of vortex rings is presented on Figure 4.4(C). For an OWC driven by a harmonic forced excitation, the detachment of a pair of vortex rings occurs in every subsequent downward displacement.

Given this observation, it is notable that the location of a vortex ring, referred to as vortex hereafter, depends on the travel direction of the water column. This may potentially signify the directional dependence of the vortex and its effect on the near-field radiated waves. This speculation requires further detailed investigation of the water particle kinematics defining the rotational flow field. In undertaking this work, data from a repeatable flow field needs to be obtained. Without this, any interpretation will be of limited value. Referring to Figure 4.4, it is evident that a repeatable flow field does not exist during the first one and a half periods of oscillation. In fact, it is challenging to determine the flow repeatability based solely upon a qualitative description of the flow field. As a result, a rigorous quantification of the flow field needs to be adopted. A description of the methods implemented to

achieve this is provided in the section that follows.

4.4.2 Quantification of circulation

The properties of a vortex may be affected by any vortex interactions. Therefore, the flow repeatability should be evaluated based upon its overall properties. Within the present study, the circulation of a vortex was quantified to infer the flow repeatability. The method previously described in Section 3.2.4, was implemented to evaluate time-histories of the total circulation in the first few forcing cycles. As explained earlier in this section, the shear layers on both the outer wall and the inner wall are both accumulated into a growing downward vortex. As a result, two different sources of vorticity fluxes affect the total circulation of a downward vortex. In contrast, for an upward vortex, formed inside the water column, the accumulated vorticity flux only originates from the shear layers that separate at the edge and are rolled into the upward vortex. It therefore follows that the total circulation generated during an upward displacement can be quantified based upon the vorticity fluxes that develop in the shear layers near the inner wall.

At this stage, it should be noted that the total circulation only describes the vorticity fluxes being ejected during the displacement of the water column. As a result, this total circulation may not accurately reveal the actual strength of the growing vortex. To overcome this difficulty, an evaluation of the vortex circulation based upon the Stokes' theorem, $\Gamma = \iint \omega_\theta \; dx \; dz$, was also undertaken using a surface integration. This quantification reveals the actual vortex strength, and serves to provide a useful comparison to the total circulation.

The integration to estimate a vortex circulation requires data describing the dominant component of the vorticity field in an angular section of the vortex; the azimuthal component of the vorticity field ω_θ again being evaluated. Initially, the iso-vorticity contour levels were determined based upon the sign of the ω_θ vorticity field. The identification of the vorticity field based upon its sign was formerly implemented to study the rotational flow fields generated by forced oscillating cylinders (Jeon & Gharib, 2004) and vortex ring generators (Gharib et al., 1998, Krueger et al., 2006). This was undertaken to separate the vorticity field of one vortex from its pair and was also implemented within the present study. An example of the vorticity field, ω_θ, with different levels of vorticity contour is shown in Figure 4.5(A). These

contour lines correspond to the vorticity field when a second downward displacement takes place. The peak positive value of ω_θ was estimated to be 79 1/s.

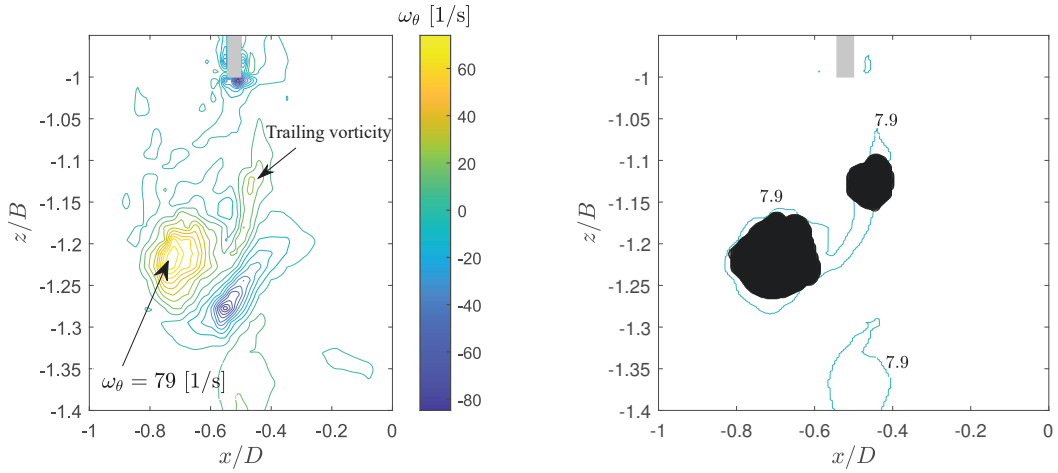

(A) (B)

Figure 4.5: (A) Iso-vorticity contours of the vorticity field ω_θ generated during a second downward displacement and (B) the corresponding vortical area inside the iso-vorticity contour based upon ten percent of the peak azimuthal vorticity ω_θ when $\eta_o^i/B = 0.22$.

In adopting the proposed approach, an area of integration based upon the dominant vorticity component also needs to be defined. Following the approach proposed in Gharib et al. (1998) and Krueger et al. (2006) to estimate a vortex circulation, the area was determined using a minimum iso-vorticity contour level defining the vortex. This minimum contour level was defined by a threshold value. By limiting the vorticity field based upon this value and taking the vorticity sign into account, the iso-vorticty contour associated only with the vortex and the area for integration can be identified. However, it should be noted that this area might not only include the rotational area (or vortical area), but also cover an adjacent shear-layer area. This includes the trailing vorticity field behind a leading vorticity field; evidence of the latter seen on Figure 4.5(A). In the studies cited above, the vortex circulation was estimated after the vorticity field in the vortex was detached from the trailing vorticity field. Within the present study, this approach cannot be implemented. The explanation for this lies in the fact that the new vortices generated during subsequent displacements may immediately influence the earlier vortices.

To isolate only the vortical area, the vortex identification method based upon the Q-criterion (Hunt et al., 1988, Haller, 2005) was employed. This criterion defines a

vortex by considering a second invariant of $\nabla \boldsymbol{u}$.

$$Q = \frac{1}{2}\left[|\boldsymbol{\Omega}|^2 - |\boldsymbol{S}|^2\right], \tag{4.1}$$

$$\boldsymbol{\Omega} = \frac{1}{2}\left[\nabla \boldsymbol{u} - (\nabla \boldsymbol{u})^T\right], \tag{4.2}$$

$$\boldsymbol{S} = \frac{1}{2}\left[\nabla \boldsymbol{u} + (\nabla \boldsymbol{u})^T\right], \tag{4.3}$$

where $\boldsymbol{\Omega}$ is the vorticity tensor and $\boldsymbol{S}$ the rate-of-strain tensor. These equations indicate that $Q > 0$ represents the existence of a vortex. This criterion defines a vortex as an area where the vorticity tensor dominates the rate-of-strain tensor. Adopting this criterion, the downward vortex corresponding to the vorticity field shown in Figure 4.5(A), is indicated by the black region inside an iso-vorticity contour on Figure 4.5(B). The benefits of adopting this criterion include: (i) the capability to clearly identify the rotational flow corresponding to the vortex under observation in a flow where multiple vortices exist, and (ii) the acurate estimation of the circulation of a vortex located very close to a wall boundary, at which the vorticity magnitude associated with a shear flow is also large.

Care should be exercised to ensure that the area with positive values of Q is surrounded by a minimum iso-vorticity contour that corresponds to the downward vortex. Figure 4.6 concerns the variations of the total and the vortex circulation, Γ, with threshold value and forcing amplitude number η_o^i/B. Figures 4.6(A)-(C) present the variations of the circulations computed from the flow field data describing the first downward displacement, while Figures 4.6(D)-(F) present the corresponding variations from a subsequent downward displacement. It is evident that the threshold value should not be larger than 30% of the peak azimuthal vorticity component. Otherwise, the vorticity field belonging to the downward vortex will not be fully quantified. Referring back to Figure 4.5(B), the vorticity field with positive values of Q is plotted within the 10% of the peak value of ω_θ. Interestingly, the deviation between the total and the vortex circulations shown in Figures 4.6(A)-(C), is most evident under the largest forcing amplitude of $\eta_o^i/B = 0.71$. This clearly indicates that large vorticity fields are not part of the downward vortex generated in this η_o^i/B condition. These fields by the Q criterion are not a vortical area.

In a one-dimensional slug model (Krieg & Mohseni, 2013), the circulation rate is computed as $d\Gamma/dt = 1/2u^2\,(t)$, with u denoting the velocity of an internal free-

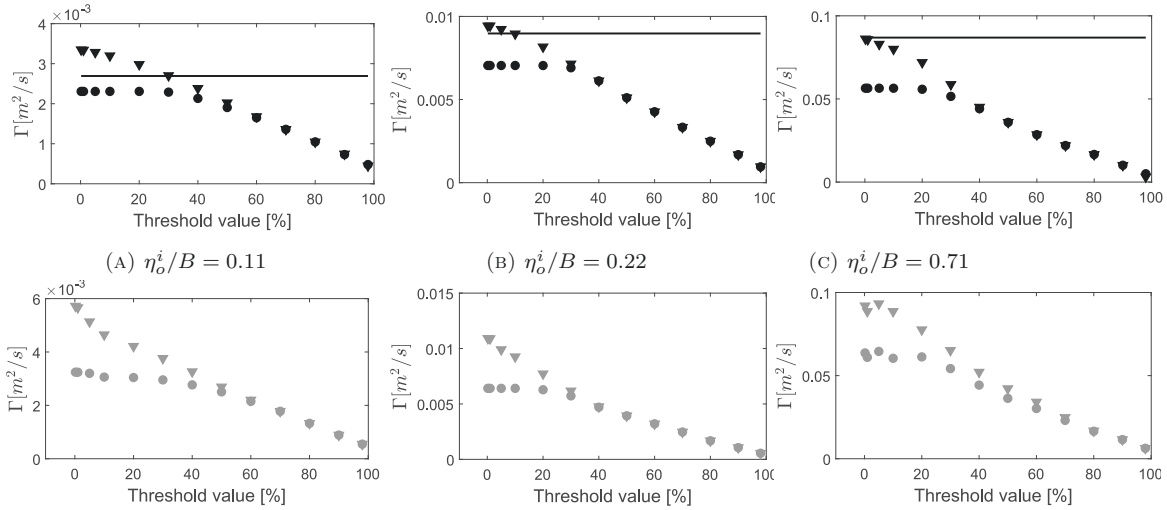

(A) $\eta_o^i/B = 0.11$ (B) $\eta_o^i/B = 0.22$ (C) $\eta_o^i/B = 0.71$

(D) $\eta_o^i/B = 0.11$ (E) $\eta_o^i/B = 0.22$ (F) $\eta_o^i/B = 0.71$

FIGURE 4.6: Variations of the total and vortex circulation Γ with the threshold value were computed from the flow field data describing (A)-(C) the first downward displacement and (D)-(F) a subsequent downward displacement for varying forcing amplitude numbers η_o^i/B. The lines represent the total circulations, the triangles denote the vortex circulations quantified using iso-vorticity contour and the circles indicate the vortex circulations quantified using both iso-vorticity contour and Q-criterion. Note: the scale of the vertical axis changes between the sub-plots.

surface. The circulation for a sinusoidal function of velocity is thus predicted by $\Gamma = \pi/4\omega_f \left(\eta_o^i\right)^2$ and estimated to be $0.0018, 0.007$ and 0.074 m^2/s in the case of $\eta_o^i/B = 0.11, 0.22$ and 0.71, respectively. These values and those shown in Figure 4.6 are in the same order of magnitude. The present calculations thus seem to be reasonable. To further confirm these calculations, the dependence of the total and the vortex circulation on the grid resolution was analysed. Figure 4.7 shows the circulations produced by the vorticity fluxes at both sides of the wall, the total and the vortex circulation computed using different grid resolutions for $\eta_o^i/B = 0.71$. In this figure, Γ is normalised by UD; the value of U representing the velocity magnitude of the internal free-surface defined by $\eta_o^i\omega_f$ and D the diameter. In undertaking this analysis, the radial grid size Δr was varied while keeping the aspect ratio near the edge being approximately one. All figures confirm that the circulations are near convergent with increases in the grid resolution. Specifically, Figure 4.7(C) reveals that the discrepancy between the values of $\Gamma/(UD)$ computed in a case of grid resolution and in the finest resolution case, increases rapidly when $b/\Delta r \leq 16$. This insight is consistent with the requirement for achieving the converged solutions for a pressure time-history (see Section 3.3.2) and the trajectory vortex motion during a

formation phase (see Section 3.2.4). The requirement was thus implemented in the numerical simulations undertaken for the present analysis.

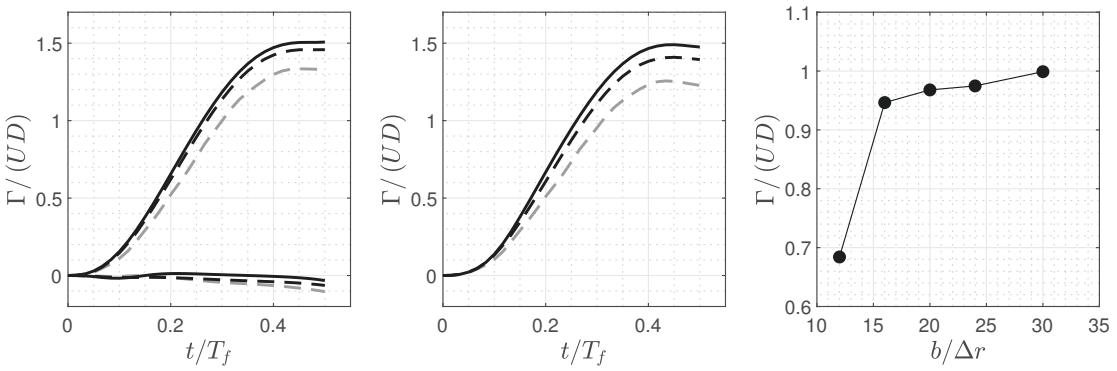

(A) (B) (C)

Figure 4.7: A convergence study of (A) the circulations produced by the vorticity fluxes at the outer and the inner wall, (B) the total circulation and (C) the vortex circulation generated during the first downward displacement of the forced oscillations with $\eta_o^i/B = 0.71$. Figures 4.7(A)-(B) indicate the computed circulations by [— —], [— —] and [——] for $b/\Delta r = 12$, 20 and 30, respectively, while Figure 4.7(C) by [•].

4.4.3 Flow repeatability

Adopting the method of quantification noted above, Figure 4.8 shows the circulations obtained from three different cases of forcing amplitude numbers, η_o^i/B, at a constant cylinder aspect-ratio of $D/B = 0.435$. The value of the circulation, Γ, is again normalised by UD. Within this figure, time-histories of the normalised values of the circulation arising from the internal and external boundary layers, the total and the vortex circulations are all presented over the first four forcing periods. The following description will explain the important findings outlined in Figure 4.8 and the flow repeatability for each case of η_o^i/B.

Figures 4.8(A) and (B) show that the vortex circulations generated from the first downward displacement at $\eta_o^i/B = 0.11$ and 0.22, approximately match their corresponding total circulations. This contrasts markedly with Figure 4.8(C), which shows that the vortex circulation deviates from the total circulation at a large forcing amplitude number of $\eta_o^i/B = 0.71$. The deviation as also inferred from Figures 4.6(A)-(C), is partly associated with the vorticity fields in the trailing shear-layer area behind the leading downward vortex during its formation. This trailing shear-layer area is more evident with a larger displacement of water column. Earlier studies have

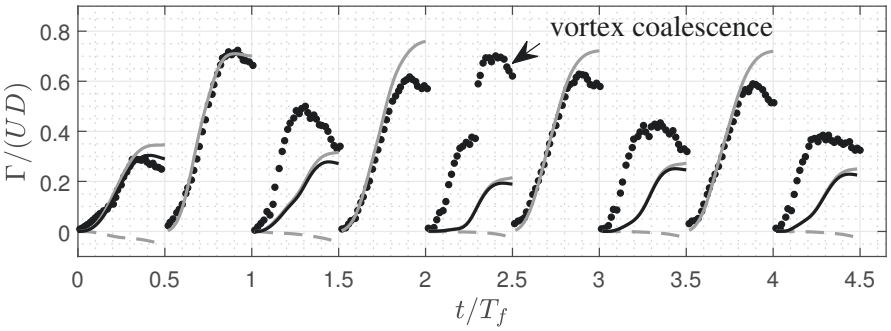

(A)

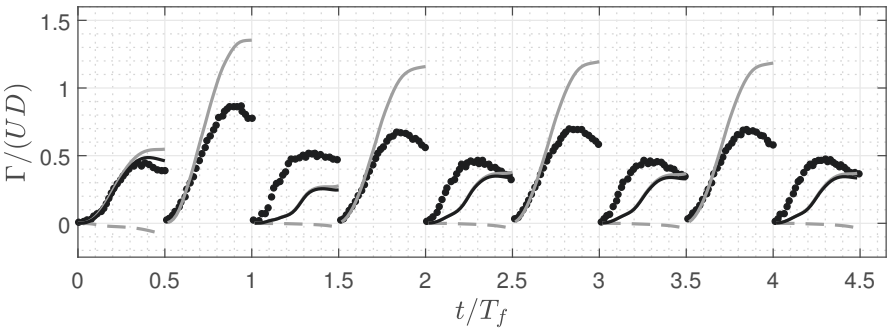

(B)

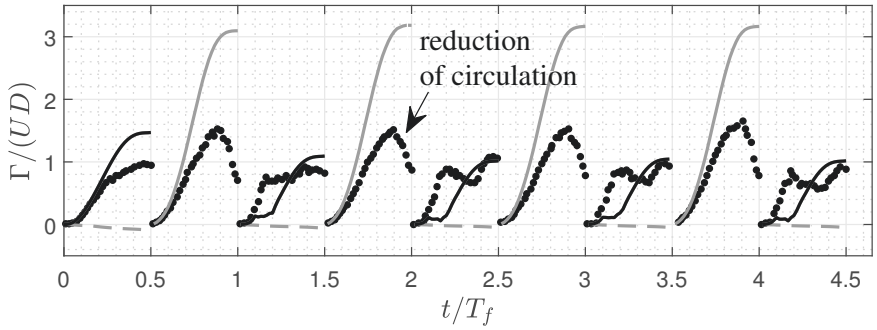

(C)

FIGURE 4.8: The circulations quantified from the vorticity fluxes at the outer wall [– –] and inner wall [——], the total [——] and vortex circulations [•] during the first few cycles of forced oscillations with a forcing amplitude number η_o^i/B: (A) 0.11, (B) 0.22, (C) 0.71. Note: the scale of the vertical axis changes between the sub-plots.

also established a possible discrepancy between the total circulation and the vortex circulation. For example, Gharib et al. (1998) and Zhao et al. (2000) conducted experimental studies of the fluid ejected by a long and non-oscillatory stroke out of a circular tube. Their flow visualisations confirmed the existence of a long trailing jet behind the leading vortex.

Unlike the first downward vortex, an upward vortex is generated inside the mouth

during an upward displacement of the water column (Figure 4.4(B)). Figure 4.9(A) shows that the shear layers separated inside the water column are re-attached at the wall above the upward vortex. Generally, these shear layers have large vorticity magnitudes shown in Figure 4.9(B)). However, when based upon the definition of the Q-criterion, they are not part of the vortical area (Figure 4.9(C)). This further explains that the separated shear layers also eject vorticity flux into non-vortical fields. The fact that the vortex circulation is smaller than the total circulation is therefore entirely reasonable.

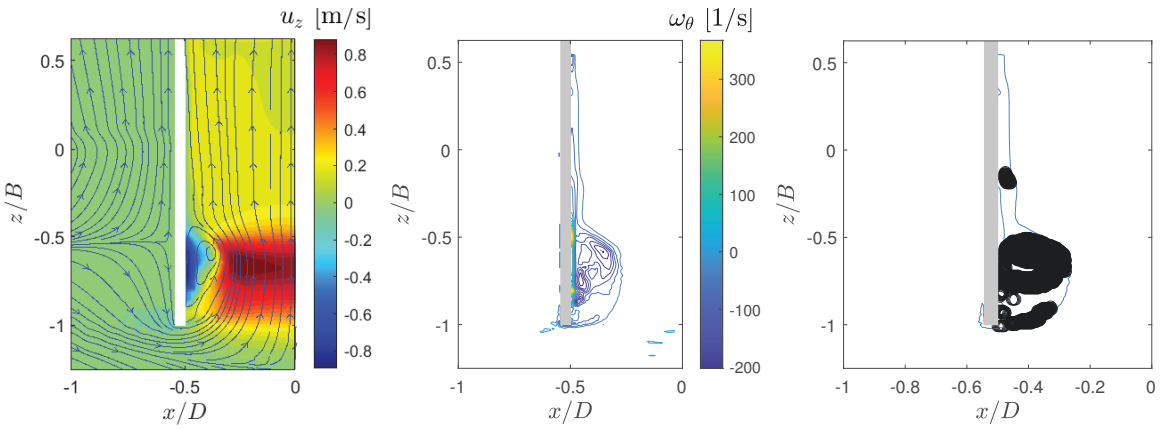

Figure 4.9: (A) Re-attachment of the separated shear layers during an upward displacement, (B) the vorticity field and (C) the vortical area corresponding to the upward vortex.

The fact that the vortex circulation of an upward vortex less accurately approximates the corresponding total circulation is due, in part, to another reason. While the upward vortex with its vorticity field is being formed, secondary vorticity fields develop between this upward vortex and the wall boundary. These oppositely-signed secondary vorticity fields may induce vorticity cancellation of the upward vortex. This is inferred from the reduction of the upward vortex circulation before the displacement ends, with the most marked reduction occuring under the largest amplitude condition (Figure 4.8(C)). The evidence from the flow field is presented in Figure 4.10. This figure shows a sequence of contour plots describing the development of multiple secondary vorticity fields that develop at the inner wall. Specifically, Figures 4.10(B) and (C) confirm that the developed secondary vorticity fields have sign opposite to the primary vorticity field, which is associated with the upward vortex. This phenomenon of multiple vorticity fields is similar to the laboratory observation reported in Walker et al. (1987), who also found the secondary vorticity

fields induced by a vortex ring when it impacts on a wall boundary.

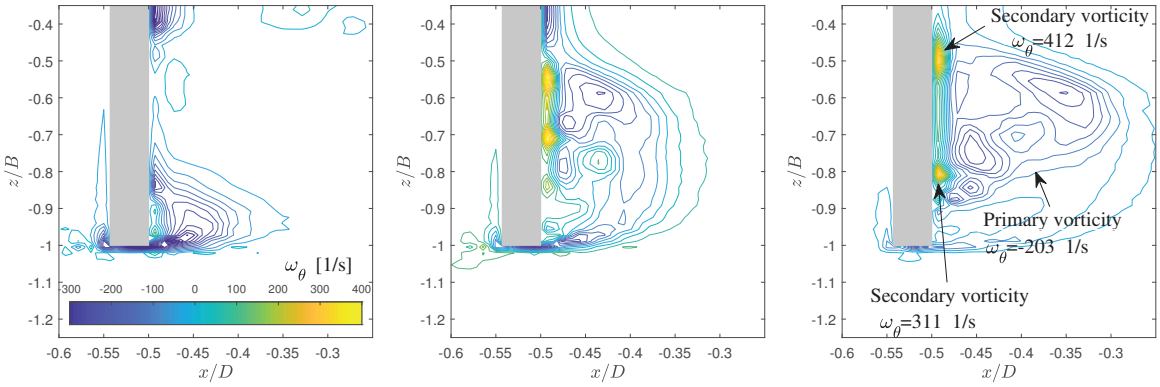

(A) (B) (C)

Figure 4.10: Development of the primary and secondary vorticity fields during an upward displacement at time t: (A) $2.63T_f$, (B) $2.88T_f$ and (C) $2.97T_f$.

At this stage, it should be noted that the quantification of a total circulation based upon the flow field data describing the first downward and upward displacement is only associated with the vortex being generated during that displacement. This concept differs from all subsequent downward displacements. The total circulation generated during a subsequent downward displacement is the net circulation contributed from the growing downward vortex and the earlier upward vortex; essentially, it arises from the combination of a pair of vortices. In contrast, the vortex circulation is quantified only from the vorticity field of the growing downward vortex. This point explains why the magnitude of the total circulation is smaller when compared to the corresponding vortex circulation.

Figure 4.8 indicates that the value of vortex circulation generated during a subsequent downstroke displacement is influenced by both vortex formation and vortex interaction. Furthermore, these two processes are both dependent on the forcing amplitude number. For example, the locations of vortices formed under the largest excitation condition ($\eta_o^i/B = 0.71$) will be sufficiently distant from the mouth inlet. This ensures little interaction between the generated vortices. As a result, the vortex circulations generated during the second and subsequent downward displacements appear to be relatively identical. In this case, the flow field repeatability, which is evaluated from the repeatability of the circulation of each downward displacement, is first exhibited at time $t = 2T_f$ (Figure 4.8(C)). In contrast, the flows with a smaller forcing amplitude requires a larger number of oscillations to achieve

a repeatable flow condition. Evidence of this is given by the following description. Figure 4.8(a) shows a sudden increase of the vortex circulation generated during the third downward displacement at $\eta_o^i/B = 0.11$. This condition is due to the earlier downward vortices that have inadequate strength to propagate away from the mouth of the OWC. Consequently, the second downward vortex is retracted due to the influence from the subsequent upward displacement. In the next displacement, the new downward vortex pulls more closely to this second vortex. As a result, both vortices coalesce into a larger single vortex with a stronger circulation. This merged vortex has now become sufficiently strong to propagate far from the mouth and is therefore less affected by the subsequent displacements. Overall, the flow begins to show a relatively repeatable flow field after the first three periods of oscillation.

4.4.4 Quantification of impulse and kinetic energy

Essentially, the circulation of a vortex quantifies the strength of the vortex and hence its abilitiy to propagate away from the location where it was initially formed. However, it does not explicitly indicate the amount of kinetic energy transferred from the ejected shear layers at the wall into the growing vortex. The amount of kinetic energy in the vortex and its dependence on the forcing amplitude cannot be inferred from the circulation. Conversely, the quantification of the kinetic energy may be useful to relate the vortex effect to the amount of energy lost in the near-field radiated wave elevation. As a result, quantification of the kinetic energy associated with a vortex is an important step in understanding the flow and the importance of its rotational components.

Krieg & Mohseni (2013) proposed the kinetic energy formula associated with a jet flow. This method is directly applicable to an OWC since a water column that experiences an outgoing displacement from a circular tube is considered analogous to a jet flow. Based upon their note, the rate of transfer of kinetic energy associated with the ejected volume of fluid from inside a bounding wall is given by:

$$\frac{dEk_v}{dt} = \pi \int_0^\infty \left(\rho u_z^2 + \rho u_x^2 + 2p\right) u_z x dx, \tag{4.4}$$

with the velocities of u_z and u_x being calculated on the y-plane and at the mouth ($z = -B$). The kinetic energy associated with this approach is referred to as the

total kinetic energy. To estimate the amount of kinetic energy in a vortex, the slug model proposed by Mohseni & Gharib (1998) was employed. This defines the kinetic energy as $Ek_v = \Gamma I/2\eta_o^i$, where Γ and I are the vortex circulation and vortex impulse, respectively; the latter estimated using a surface integration defined by

$$I = \rho\pi \iint \omega_\theta x^2 \; dx \; dz. \tag{4.5}$$

This definition will be used in the analysis which follows.

4.5 Progressively reduced amplitude with forcing amplitude number

4.5.1 Radiated waves and vortex properties

An FFT analysis of the time-histories of the radiated wave elevations presented in Figure 4.1 was performed. This reveals that the near-field radiated waves are weakly nonlinear. This is argued on the basis that the evidence of their second-order harmonic components are small; evidence of this being provided in Section 4.8. At first, it is instructive to investigate the relationship between the vortex properties and the first-order radiated wave amplitude. In this analysis, the cylinder aspect-ratio, D/B, was kept constant, while the forcing amplitude, η_o^i, was varied; the relevant data corresponding to the test cases FWCT 1 noted in Table 4.1.

Having numerically modelled these test cases, the first-order radiated wave amplitude, $\eta_o^{e(1)}$, is presented as a function of the forcing amplitude number, η_o^i/B in Figure 4.11(A). Alongside this, Figure 4.11(B) presents the variations of the total and vortex circulations Γ with the η_o^i/B number. In the latter figure, each symbol indicates the vortex circulations that were produced during the first (black) and fourth (gray) downward displacements under a specified η_o^i/B number. Similarly, the lines presented on Figure 4.11(B) are the total circulations estimated from the data describing the flow field associated with the two displacements. All these variables were quantified at the condition when the internal free-surface was at its minimum elevation. To infer the strength of the vortex relative to the water column oscillation, the circulations Γ, as presented in Figure 4.11(B), are again normalised by a quantity of UD.

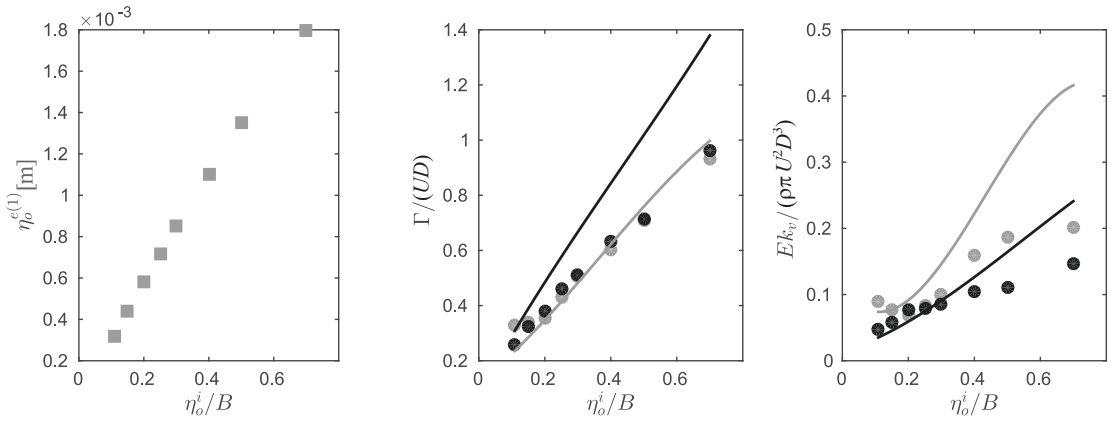

(A) (B) (C)

Figure 4.11: (A) Variations of the first-order component of the external surface amplitude $\eta_o^{e(1)}$, (B) the total and vortex circulation $\Gamma/(UD)$, and (C) the total and vortex kinetic energy $Ek/(\rho\pi U^3D^2)$ with the forcing amplitude number η_o^i/B; all the variables in Figures 4.11(B)-(C) were quantified either from the flow field data of the first [black] or fourth [gray] downward displacement, where the lines represent the total circulation and total kinetic energy (in (B) and (C)), and the symbols represent the vortex circulation and vortex kinetic energy (again in (B) and (C)).

The properties of a single vortex that is formed during the first downward displacement are not affected by vortex interactions. As a result, the quantification of the vortex circulation from the data describing the first downward displacement will clearly show the relationship between the vortex formation and the forcing amplitude. However, it was initially unclear whether vortex interactions were irrelevant to the near-field radiated waves. Specifically, whether its effects on the progressive amplitude reduction, if any, could be safely ignored. With this in mind, it was decided to quantify the properties using the data from two flow fields: the first downward displacement when a single vortex is formed, and the fourth displacement when the effects of any vortex interaction will have become established.

Variations in the vortex strength with the forcing amplitude are presented in Figure 4.11(B). The relationship between the two variables calculated from the two different flow fields is clearly not identical. This is most evident from the total circulations, indicated by the lines. The total circulation is smaller when calculated from the fourth downward displacement, compared to the first. Moreover, this is true across the entire range of forcing amplitude numbers. The explanation for this lies in Figure 4.4 and (particularly) Figure 4.8, indicating that the total circulation generated from the second and any subsequent downward displacements is the net circulation from the pair of vortices shed during the displacement. In these cases, the

summation of the two oppositely-signed vorticity fluxes reduces the magnitude of the total circulation. On the other hand, the circulation of the downward vortex formed during its initial formation phase, may gain additional circulation from the former downward vortices. This occurs if these vortices are located sufficiently close to the mouth after their formation. A vortex coalescence may happen and, consequently, increase the vortex circulation. Based upon these considerations, the deviations between the vortex circulations quantified from the two different flow field data at small forcing amplitudes are considered reasonable.

To help understand the rotational flow field from an energy perspective, Figure 4.11(c) shows the relationship between the total kinetic energy based upon Equation (4.4) and the vortex kinetic energy Ek_v based upon Γ and I (Equation (4.5)); both considered as a function of increasing forcing amplitude. As in the quantification of the circulation, these physical variables were also estimated from the two different flow fields. In considering this variable, both kinetic energies are normalised by $\rho\pi U^2 D^3$; the latter being related to the total kinetic energy relative to the kinetic energy of the oscillating water column.

The total kinetic energy observed in Figure 4.11(c) shows that this variable quantified from the fourth displacement field deviates from the corresponding vortex kinetic energy. The quantification of the total kinetic energy gives the summation of the kinetic energy associated with a pair of shed vortices. In contrast, the vortex kinetic energy is only associated with the downward vortex being formed during the displacement. This explains the discrepancies between the values of the vortex and the total kinetic energy obtained from the fourth displacement fields. It is also evident that there are discrepancies between these two values estimated from the first displacement fields. It has already been noted that the trailing shear layers are not rolled into the leading vortex. As such, the vortex circulation consistently under-estimates the total circulation, particularly at large forcing amplitude numbers. Given this insight, the under-estimation of the vortex kinetic energy can easily be understood.

Given these observations, the following conclusions are highlighted.

(i) A nonlinear relationship between the vortex formation on the forcing amplitude applies. This is based upon the variations in the normalised total and vortex circulation, evaluated from the first displacement field and presented in Figure

4.11(b).

(ii) A nonlinear relationship between these normalised values and the forcing amplitude is also proven from the repeatable flow-field data.

(iii) The vortex interaction plays a minor role in reducing the wave amplitude; evidence of this being provided from point (ii) and the progressive reduction of the radiated wave amplitudes earlier shown in Figure 4.1(b).

(iv) The first three points noted above are consistent with the variations in the normalised total and vortex kinetic energy; these normalised values also showing a nonlinear relationship with the forcing amplitude.

4.5.2 Vortex effects on wave radiation

Figure 4.12(a) concerns the total kinetic energy Ek_v of the vortex motion relative to the propagating wave energy; the latter based upon the first-order radiated wave amplitude at $r = 0.57D$. The ratio of these two energy components is plotted in terms of the forcing amplitude and reveals that the relative importance of the total kinetic energy Ek_v increases. Importantly, this happens while the near-field radiated amplitude, $\eta_o^{e(1)}/\eta_o^i$, decreases; evidence of the latter given in Figure 4.1(b). This suggests a relationship between the vortex strength and the near-field wave radiation, an effect that clearly needs to be investigated.

Evidence of the vortex effect is further confirmed from Figure 4.12(b). This presents the total kinetic energy, Ek_v, relative to the excitation energy, Ek_f; the latter defining the energy necessary to ensure the system oscillates under a specified forcing amplitude η_o^i at a given forcing period T_f. This excitation energy, Ek_f, can be mathematically expressed as

$$Ek_f = \int_t^{t+T_f} pA_c u dt, \tag{4.6}$$

where p is the air pressure, A the water column cross-sectional area and u the internal free-surface velocity. Under a resonant condition, this energy includes the components associated with an added mass force and the damping forces. Initially, it was unknown yet whether the nonlinear damping in this system was primarily governed by the vortex motion. This will be further considered in Section 6.3.1.

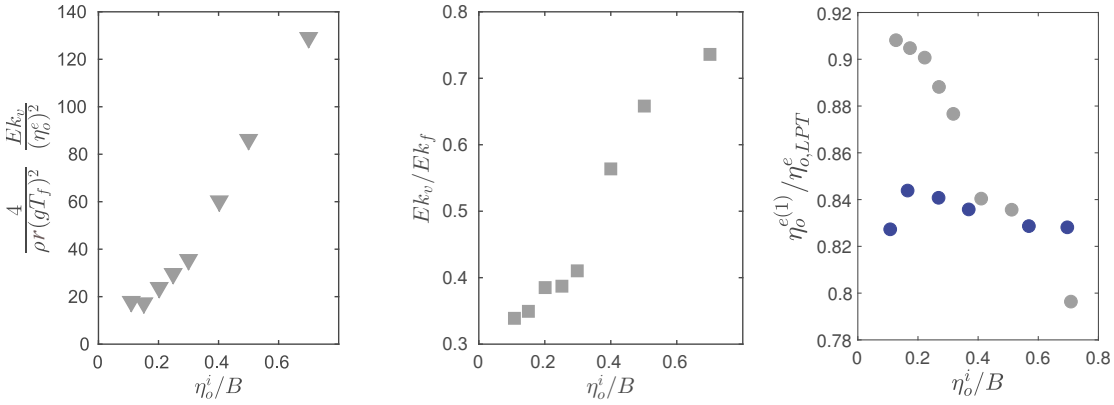

(A) (B) (C)

Figure 4.12: Proportions of the total kinetic energy Ek_v relative to (A) the propagating wave energy [▼] and (B) the excitation energy Ek_f [■], as well as (C) the corresponding first-order radiated wave amplitudes $\eta_o^{e(1)}$ [●, ●] relative to the theoretical values $\eta_{o,LPT}^e$; all data presented as a function of forcing amplitude number η_o^i/B for an OWC with a SE mouth [gray] and a BS mouth [blue]. Note: the theoretical values were only computed for the SE mouth.

which confirms the importance of the vortex damping. Taking this insight forward and evaluating the Ek_v/Ek_f value, it is shown that the vortex makes an increasingly significant contribution to the excitation energy as the forcing amplitude increases.

In parallel, Figure 4.12(C) shows that the near-field radiated wave amplitude appropriate to an OWC with a SE mouth progressively reduces from its theoretical value as the increasing forcing amplitude increases. The reduced amplitude, $\eta_o^{e(1)}/\eta_{o,LPT}^e$, is quantified as the ratio between the numerically predicted near-field radiated amplitude, $\eta_o^{e(1)}$, and the theoretical value, $\eta_{o,LPT}^e$; LPT being the abbreviation for Linear Potential Theory. Importantly, this ratio is less than 1.0, consistently reducing with an increasing forcing amplitude. Given this trend and the former results presented in Figures 4.11(B), 4.11(C) and 4.12(B), it can be concluded that the reduction in $\eta_o^{e(1)}/\eta_{o,LPT}^e$ is closely linked to the increase in the normalised values of the total circulation, $\Gamma/(UD)$, and the total kinetic energy, $Ek/(\rho\pi U^3 D^2)$. Given this understanding, the progressive reduction of the near-field radiated wave amplitude with the increasing forcing amplitude can be explained in terms of the increasing importance of the vortex motion. Moreover, a comparison with the reduced amplitudes, $\eta_o^{e(1)}/\eta_{o,LPT}^e$, for the cases of an OWC with a BS mouth (test cases FWCT 7 on Table 4.1), is also presented on Figure 4.12(C). This data supports this explanation; the progressively reduced amplitude being markedly reduced by the absence of vortices.

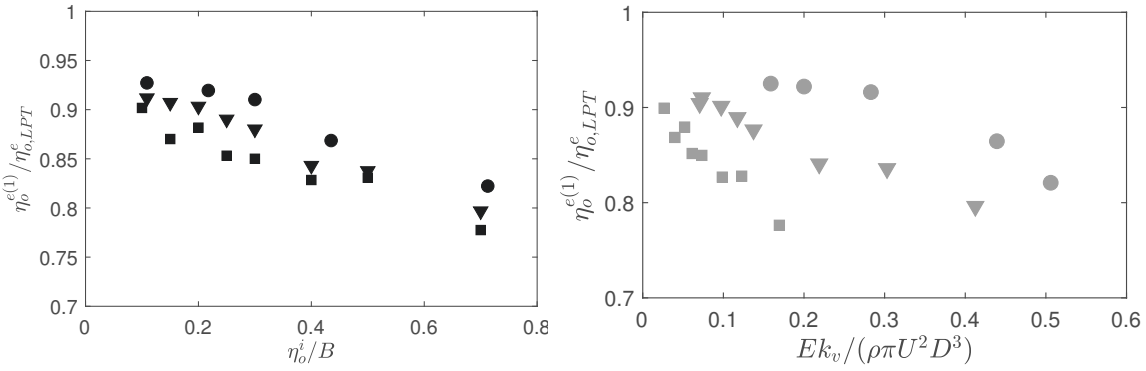

(A) (B)

FIGURE 4.13: Reduced amplitudes, $\eta_o^{e(1)}/\eta_{o,LPT}^e$, as functions of (A) forcing amplitude number η_o^i/B and (B) total kinetic energy relative to the water column, $Ek_v/(\rho\pi U^2 D^3)$, for varying cylinder aspect-ratios: $D/B = 1.25$ [■, ■], 0.435 [▼, ▼] and 0.15 [●, ●]. Note: the sub-script LPT refers to Linear Potential Theory.

Following on, Figure 4.13(A) confirms the reduced near-field radiated amplitudes for all other cylinder cases (Table 4.1). These results are consistent with the growing importance of the vortex motion; the latter confirmed by the total kinetic energy $Ek_v/(\rho\pi U^2 D^3)$ presented on Figure 4.13(B). Moreover, the percentage of the energy loss computed as $1 - (\eta_o^{e(1)}/\eta_{o,LPT}^e)^2$, shows the maximum percentage being 40% for the largest forcing amplitude ($\eta_o^i/B = 0.71$) and the largest cylinder diameter ($D/B = 1.25$). This is clearly a very significant effect.

4.6 Reduced amplitudes with KC and D/B numbers

4.6.1 Variations in vortex circulation and reduced amplitude

The progressive amplitude reductions observed in Figure 4.1 are dependent on the cylinder aspect-ratio. This is considered in Figure 4.14(A) which shows the reduced amplitude when the water column is downwardly displaced. Within this figure, the reduced amplitude is defined as the ratio of the maximum radiated wave amplitude, η_{max}^e, to the theoretical value, $\eta_{o,LPT}^e$. This ratio is presented as a function of a dimensionless number defined by the forcing amplitude relative to the cylinder diameter $2\eta_o^i/D$; the latter being related to KC number definition as $2\pi\eta_o^i/D$.

In considering this data, the largest cylinder case, with a cylinder aspect-ratio of $D/B = 1.25$, shows the steepest and the most pronounced range of amplitude

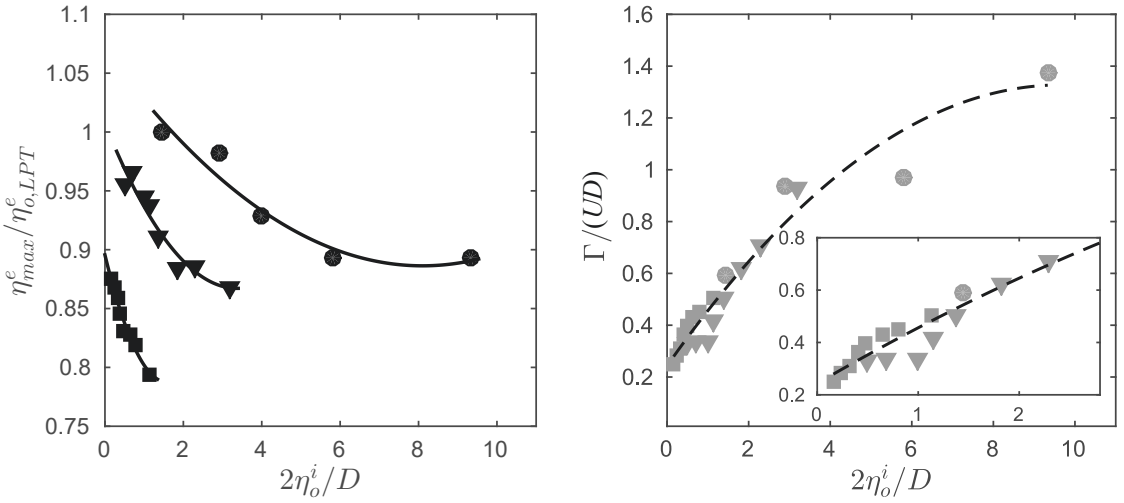

(A) (B)

Figure 4.14: (A) Reduced amplitudes, $\eta^e_{max}/\eta^e_{o,LPT}$, and (B) vortex circulations, $\Gamma/(UD)$, plotted in terms of the dimensionless number $2\eta^i_o/D$ for various cylinder aspect-ratios: $D/B = 1.25$ [■, ■], 0.435 [▼, ▼] and 0.15 [●, ●], and the 2nd-order polynomial fits for the curves of $\eta^e_{max}/\eta^e_{o,LPT}$ [——] and $\Gamma/(UD)$ [— —].

reductions. In contrast, the smallest cylinder ($D/B = 0.15$) exhibits the smallest reductions. This confirms that the reduced amplitudes at a constant forcing amplitude number show marked variations depending on the cylinder diameter. In seeking a physical explanation of this data, it is thus instructive to relate the vortex properties to the KC number.

The normalised vortex circulation generated when the water column is at its minimum elevation is provided in Figure 4.14(B). In all cases, the circulations were quantified using the data from the fourth downward displacement of the water column. Overall, the trend of $\Gamma/(UD)$ observed from the symbols and the fitted curve appears to be (approximately) hyperbolic; the value of $\Gamma/(UD)$ increasing with KC number but appearing to be convergent at a certain KC number. At present, it is necessary to recall that the increased value of $\Gamma/(UD)$ at a large KC number implies an increased vortex strength relative to the mass and velocity of the water column. This vortex strength, as explained in Section 4.4.3, is interpreted from the normalised circulation, $\Gamma/(UD)$. With large circulation, $\Gamma/(UD)$, the vortex may be sufficiently strong to self-propagate away from the bottom mouth and will thus be less affected by the upward and downward vortices generated during the subsequent displacements. This hints at the relationship between the value of $\Gamma/(UD)$

and the location of the vortex in its formation phase. Indeed, the present numerical results reveal that the vortices having smaller values of $\Gamma/(UD)$ are typically located nearer the mouth. This is also consistent with the $\Gamma/(UD)$ curve shown in Figure 4.14(b); the vortices belonging to the largest cylinder have the smallest range of normalised circulations and their locations are closer to the mouth when compared to the other smaller cylinders. To expand upon this argument, the vortex locations will be considered in the section that follows.

4.6.2 Physical explanation for the amplitude reduction

To investigate the vortex location, a vortex ring is viewed as a closed vortex line. Following the Biot-Savart Law, the contributions of the velocities induced by a closed vortex line in x- and z-directions, $u_{x,ind}$ and $u_{z,ind}$, on the external free-surface and at the angular section of $\theta = \pi$, can be mathematically formulated as follows:

$$u_{x,ind} = \frac{\Gamma}{4\pi} \int_0^{2\pi} \frac{-R_v|Z_v|\cos\theta}{|Di|^3} d\theta, \tag{4.7}$$

$$u_{z,ind} = \frac{\Gamma}{4\pi} \int_0^{2\pi} \frac{-(R_v^2 + \frac{1}{2}R_v D\cos\theta)}{|Di|^3} d\theta, \tag{4.8}$$

$$Di = -(D/2 + R_v\cos\theta)\vec{i} - R_v\sin\theta\vec{j} + |Z_v|\vec{k}. \tag{4.9}$$

Within these solutions, Z_v is the central weighted position of the azimuthal vorticity distribution ω_θ in z-coordinate and R_v is the corresponding radial coordinate; the latter being related to X_v as $R_v = |X_v|$. This follows the notation adopted in the vortex trajectory described earlier in Section 3.2.4.

Given Equation (4.7), it is known that the velocity induced by a vorticity distribution at the core position of $(-R_v, Z_v)$, consistently has a sign opposite to the x-component of the theoretical velocity at the external free-surface and in the angular direction of $\theta = \pi$. This indicates the reduction in the theoretical velocity due to the vortex. The positively directed horizontal velocity driven by the vortex during a downward displacement at the location noted above, reduces the 'background' velocity that is dictated by the balance between the gravitational force and the water column oscillation. The direction of this 'background' velocity may be inferred from the streamlines in the potential flow presented in Figure 4.2(c). It may be logical to consider that the superposition of the background velocity, U_{LPT}, predicted from

the linear potential theory, and the vortex-induced velocity, $u_{x,ind}$, approximates the actual velocity.

Implementing Equation (4.7), the x-component of the induced velocity $u_{x,ind}$ can be estimated. The values of $u_{x,ind}$ over varying KC and D/B numbers are shown in Figure 4.15(A). In this figure, the induced velocities $u_{x,ind}$ are nondimensionalised by U_{LPT}. This figure shows that the normalised velocities due to the vortices in the case of the largest D/B are pronounced. Given this evidence, the more significant values of $\eta^e_{max}/\eta^e_{o,LPT}$ provided on Figure 4.14(A) for the largest D/B are reasonable.

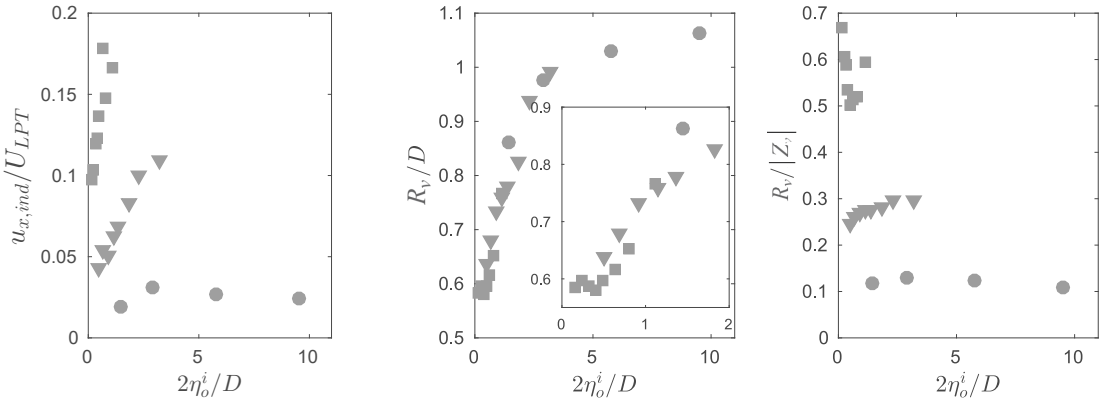

(A) (B) (C)

Figure 4.15: (A) The velocity induced by a vortex, $u_{x,ind}$, relative to the theoretical velocity, U_{LPT}, calculated at the outer wall, (B) the vortex radial location relative to the cylinder diameter, R_v/D, and (C) relative to the vortex vertical location, $R_v/|Z_v|$, are presented as a function of $2\eta^i_o/D$ at varying D/B: 1.25 [■], 0.435 [▼] and 0.15 [●].

Having investigated Equation (4.7), the factors determining the induced velocity in the x-direction can be identified as the radial location of the vortex relative to both the cylinder diameter, R_v/D, and its vertical location, $R_v/|Z_v|$. In addition, the dimensional circulation Γ of the vortex also has impact on the induced velocity. That these three factors are critical is suggested by the simplified form of the maximum contribution from the velocity field, $du_{x,ind}$. This is mathematically expressed by:

$$du_{x,ind} \propto \frac{\Gamma}{4\pi} \frac{R_v|Z_v|}{\left[\sqrt{(D/2-R_v)^2+|Z_v|^2}\right]^3}, \tag{4.10}$$

$$\propto \frac{\Gamma}{4\pi} \frac{R_v/|Z_v|^2}{\left[\sqrt{\left(\frac{D/2-R_v}{|Z_v|}\right)^2+1}\right]^3}. \tag{4.11}$$

Equation (4.11) implies that $du_{x,ind}$ increases if the value of $R_v/|Z_v|^2$ is large, and the value of $(D/2 - R_v)$ approaches zero. Given these effects, the curves of R_v/D and $R_v/|Z_v|$ are presented as a function of $2\eta_o^i/D$ in Figures 4.15(B) and (C), respectively. A value of R_v/D approaching 0.5 and a large value of $R_v/|Z_v|$ may indicate a significant $du_{x,ind}$. Indeed, the near-field radiated waves around the largest cylinder of $D/B = 1.25$ within the range of small KC numbers, that experience the most significant amplitude reductions, are characterised by the vortices with the radial locations R_v/D being closest to the wall. It is also a fact that the relative values of R_v/Z_v in this cylinder case are the largest.

The explanation given above is further discussed as follows. The variation of $\Gamma/(UD)$ observed in Figure 4.14(B) actually indicates the importance of the first factor, R_v/D, on the induced velocity, $du_{x,ind}$. A vortex with a strong circulation ($\Gamma/(UD) \gg$) at a large KC number tends to move itself more radially out ($R_v/D \gg$). In contrast, a vortex generated under a small KC number and hence a small $\Gamma/(UD)$ value, tends to be weak relatively to the inertia force of the water column. As a result, the location during the formation phase, after the ejection, is closer to the cylinder wall ($R_v/D \ll$). This is evident from Figure 4.15(B).

The second factor, namely the radial location relative to the vertical location $R_v/|Z_v|$, can be explained as follows. A forcing amplitude condition applied to a cylinder with a large diameter, generates a vortex with a large radius R_v and a small Γ/UD. The latter indicates the location of Z_v being close to the bottom edge. Given these two considerations, the resulting $R_v/|Z_v|$ will always be larger for a large diameter of vortex.

Under a low KC condition, however, it is likely that the former vortices of the same sign will be retracted close to the bottom edge. This may cause a stretching in the growing downward vortex. As such, the resulting vertical location Z_v of this vortex will be located further below the draft and thus reduces $R_v/|Z_v|$. As shown in Figure 4.15(C), the $R_v/|Z_v|$ values quantified from the fourth displacement field, fluctuate and show a non-monotonic trend. Nevertheless, within the present range of D/B conditions, the variations of R_v are considerably larger than the variations of Z_v. In other words, the vertical location Z_v has an insignificant effect under a constant draft B. On the other hand, the importance of Z_v becomes more evident under varying drafts. Additional simulations from FWCT 4, 5, and 6 outlined in

Table 4.1 support this idea. These models have an identical diameter and varying drafts, representing varying cylinder aspect-ratios with $D/B = 0.25, 0.15$ and 0.07. With a constant forcing amplitude, the effect of the vortex on the amplitude reduction becomes less important with the increasing Z_v. The reduced amplitude, $\eta^e_{max}/\eta^e_{o,LPT}$, increases up to 0.92 from the earlier reduced amplitude of $\eta^e_{max}/\eta^e_{o,LPT} = 0.86$ at $D/B = 0.435$.

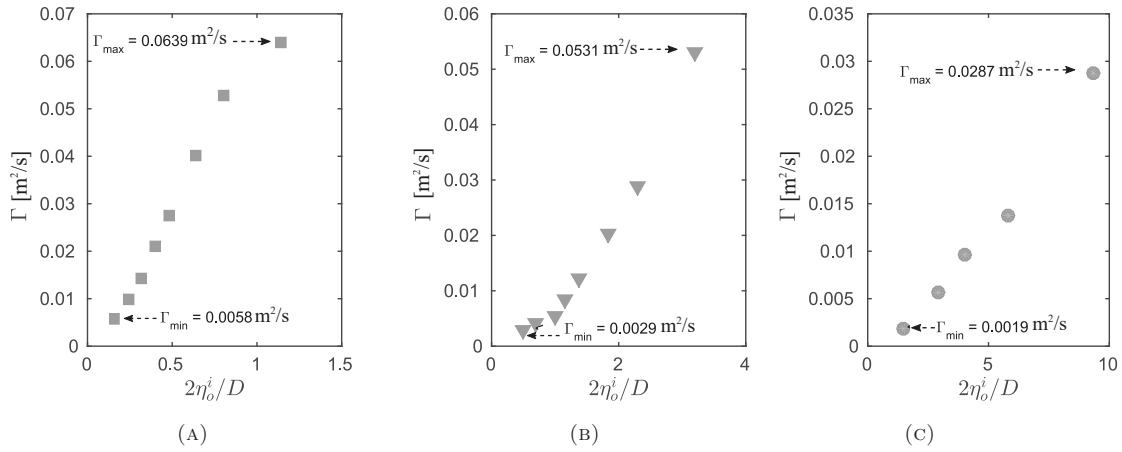

Figure 4.16: Vortex circulations, Γ, over varying $2\eta^i_o/D$ numbers for different cylinder aspect-ratios D/B: (A) 1.25 [■], (B) 0.435 [▼] and (C) 0.15 [●].

The third factor, the (dimensional) vortex circulation Γ, is shown to be dependent on the cylinder diameter. This is observed in Figure 4.16. At a constant focing amplitude number, the water column with a larger inertia force induces an increased fluid velocity near the edge where the flow separates. The circulation Γ is consequently larger when compared to the water column with a smaller inertia force. Figure 4.16 provides the variation of the vortex circulation with KC number for each D/B number. The vortex circulations quantified from the case of $D/B = 1.25$ are estimated to lie in the largest range of circulations ($0.0058 \leq \Gamma \leq 0.0639$ m^2/s). This range clearly exceeds the circulation range for the two cases of smaller cylinders.

4.7 Progressively reduced phase difference

4.7.1 Fluid velocities and water surface elevations

To understand the mechanism that drives the progressive reduction in the phase difference (Figure 4.1), the velocity of the fluid at varying locations inside and outside

the water column are investigated. This involves comparisons between the velocities of the internal and external free-surface calculated from the linear potential and viscous flow models. To obtain the required data, the fluid velocities in the potential flow were analytically derived, whereas the fluid velocities in the viscous flow were sampled from the numerical data. These variables are presented as their normalised values relative to the velocity of the internal free-surface; the latter defined as $\eta_o^i \omega_f$.

To begin, the normalised vertical velocities $\overline{u_z^i}$ on the axisymmetric centre at three different vertical elevations of $z = 0, -B/2$ and $-B$ are presented in Figure 4.17. This figure shows that the fluid at the bottom mouth moves less rapidly when compared to that located nearer the internal free-surface; evidence of this being provided by both the potential and the viscous flow models. However, in the viscous flow, the fluid at the centre of the mouth experiences a delay. Figure 4.17(B) shows that the peak fluid velocities at this location occur at times $t = 2.78T_f$ and $t = 3.3T_f$. This happens after the velocity of the viscous fluid near the internal free-surface has gained its extreme values.

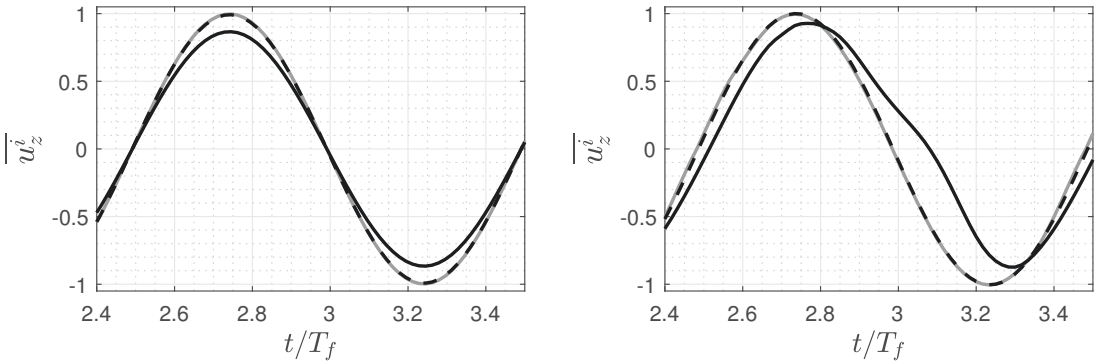

(A) (B)

Figure 4.17: Comparisons of the time-varying fluid velocities, $\overline{u_z^i}(t)$, on the axisymmetric centre of the column at three vertical locations: $z = 0$ [——], $z = -B/2$ [— —] and $z = -B$ [——] predicted from (A) the linear potential solution and (B) the viscous flow solver.

The delay in the fluid velocities at the centre of the mouth is due to the flow separation at the bottom edge. Evidence of this is provided in Figure 4.18. This shows a sequence of vertical velocity profiles across the mouth during a water column displacement. Figure 4.18(A) concerns the velocity profiles during an upward displacement of the water column, while Figure 4.18(B) presents the corresponding sequence during a downward displacement. Both these figures confirm that the fluid in the vicinity of the edge has to move rapidly so that it may pass by the edge at the

early stage of a displacement. Simultaneously, the fluid at the centre has to move less rapidly in order to satisfy mass conservation. As a result, the velocity has the largest magnitude in the vicinity of the edge at an early phase of the water column displacement. This is evident from the velocity profiles across the mouth being not uniform up to the edge (Figure 4.18).

In addition, the fluid particles near the mouth are not in phase with those at (or near) the internal free-surface. Specifically, the fluid near the inner side of the edge experiences a deceleration phase earlier than that at the free surface; the deceleration phase being defined as the period when the absolute magnitude of the velocity reduces. Didden (1979) observed a similar process inside a circular jet. In this case, a large fluid velocity near the edge was observed when the flow was impulsively started from a still condition through a piston displacement. The fluid at the edge experienced a deceleration phase, while the fluid was continuously displaced at a constant piston velocity.

Within the present model, this earlier deceleration phase for the fluid near the edge is most evident in the downward displacement stage shown in Figure 4.18(b). The fluid velocity in the vicinity of the edge ($x/D \leq -0.48$) in the starting flow, starts to decelerate at time $t = 3.10T_f$. This occurs before the internal free-surface begins to slow down at $t = 3.25T_f$. In Figure 4.18(b), the former is indicated by (——) and the latter by (——). As a result of this earlier deceleration phase and mass conservation, the velocity at the centre of the mouth may continue to increase, although the fluid at the edge and near the free-surface have already started to slow down. This event is shown to occur at $t = 3.3T_f$ as indicated by (——) on Figure 4.18(b). This represents the delay observed in Figure 4.17(b). As the deceleration phase continues, the velocity profile gradually becomes relatively uniform across the mouth. An example of this profile occurs at time $t = 3.35T_f$ and is noted by (——) on Figure 4.18(b).

At first sight, the delay in the fluid velocities at the centre appears inconsistent with the progressive reduction in the phase difference between the near-field radiated wave elevation, η^e, and the internal surface elevation, η^i. However, the fact that the fluid at the bottom edge decelerates earlier, may provide an explanation. In the following description, the fluid velocities near the outer wall and at the bottom edge ($x = -0.57D, z = -B$) computed from both the viscous and potential flow models

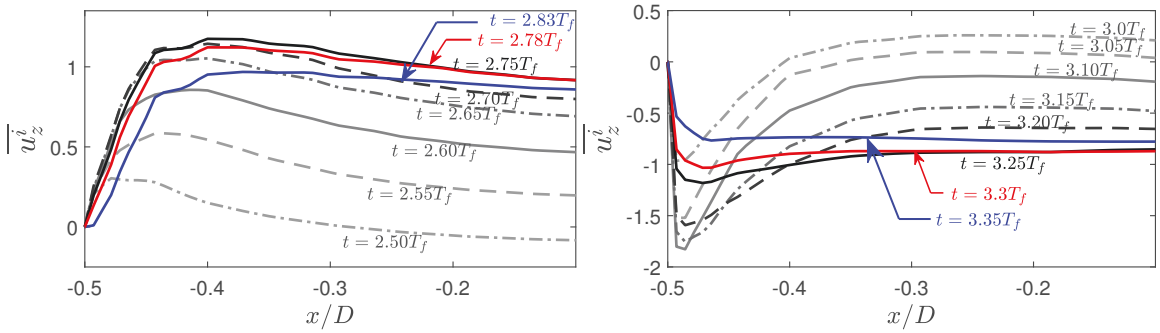

(A) (B)

Figure 4.18: Vertical velocity profiles, $\overline{u_z^i}(z)$, across the mouth during (A) an upward and (B) a downward water column displacement at sequential times.

are compared. For easier interpretation, comparisons of the normalised elevations, $\overline{\eta^e}$ and $\overline{\eta^i}$, are re-presented in Figure 4.19(A). Alongside this, the normalised vertical velocities near the bottom edge (outside the water column), $\overline{u_z^B}$, in the two contrasting flows are compared in Figure 4.19(B).

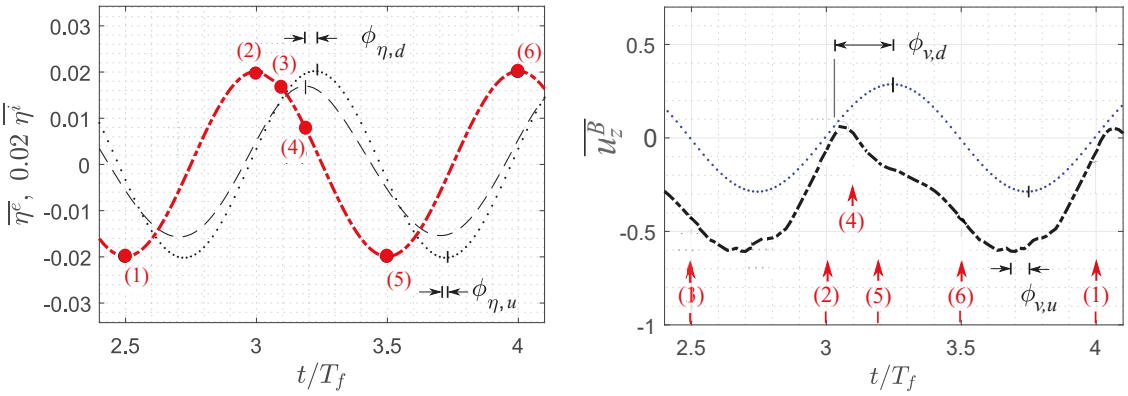

(A) Surface elevation η (B) Fluid velocity $\overline{u_z^B}$

Figure 4.19: Time-varying normalised values of (A) the internal surface elevation $\overline{\eta^i}(t)$ [— · —] and near-field wave elevation $\overline{\eta^e}(t)$, and (B) the velocity $\overline{u_z^B}(t)$ near the outer wall of the edge; $\overline{\eta^e}$ and $\overline{u_z^B}$ being predicted by the viscous [— — , — · · —] and potential flow solution [· · · · , · · · ·].

Figure 4.19 shows time-histories of the external and internal surface elevations and the fluid velocity near the outer wall at $z = -B$. On the figure, six sequential times are denoted by numbered symbols. The first symbol marks the onset of the upward displacement of the water column. The normalised internal water surface elevation, $\overline{\eta^i}$, turns upwards at time $t = 2.5T_f$ (Point (1), Figure 4.19(A)). Simultaneously, the fluid near the outer wall of the bottom edge moves downwards in the potential flow and continues to move in this direction during this displacement. This can be

confirmed by the negative value of the corresponding fluid velocity, that begins at $t = 2.5T_f$ (Point (1) on Figure 4.19(b)) and ends at $t = 3.0T_f$ (Point (2) on Figure 4.19(b)). Likewise, the fluid near the outer wall of the bottom edge in the viscous flow consistently has a negative direction during the upward displacement.

With the onset of a downward displacement (Point (2) on Figure 4.19(a)), the fluid near the outer wall of the bottom edge only turns upwards for a very short time interval in the viscous flow. Point (3) on Figure 4.19(b) indicates that at $t = 3.1T_f$, the direction of the fluid at this location immediately reverses after the onset of the downward displacement. In contrast, the corresponding fluid in the potential flow, consistently turns upwards until the downward displacement completes. Evidence of this can be seen from the positive value of the corresponding fluid velocity. This begins at $t = 3.0T_f$ (Point (2), Figure 4.19(b)) and ends at $t = 3.5T_f$b (Point (5), Figure 4.19(b)). This description of the flow direction indicates an important difference between the potential and the viscous flows. In the viscous flow, the stage when the external free-surface returns from its maximum elevation, occurs at time $t = 3.2T_f$ (Point (4) on Figure 4.19(a)). Clearly, this happens after the fluid near the outer wall at the bottom edge changes in direction (Point (3) on Figures 4.19(b)) and before a subsequent upward displacement begins (Point (5) on Figures 4.19(a) and 4.19(b)). Conversely, in the potential flow, the returning stage occurs before the direction of the fluid near the outer wall at the bottom edge changes as a result of the subsequent upward displacement.

Figure 4.19(a) also shows that the value of $\phi_{\eta,d}$ is larger than its counterpart, $\phi_{\eta,u}$, where, $\phi_{\eta,d}$ and $\phi_{\eta,u}$ denote the phase shift between the extreme values of the near-field radiated wave elevations in the potential and the viscous flows; the subscript d denoting a downcoming and the subscript u an upcoming. A similar observation is also seen from the phase shift between the extreme values of the velocities at the bottom edge, $\phi_{v,d} > \phi_{v,u}$, on Figure 4.19(b). Given this similarity, the phase shift in the near-field radiated wave elevation, is clearly related to the fluid motion at the bottom edge.

4.7.2 Relationship between reduced phase difference and vortex formation

In seeking to explain the observations noted above, it should be noted that vortex formation can profoundly change the surrounding velocity fields. To explore this, the present section provides both flow visualisations and vertical velocity profiles over the full draft of the water column. Taken together, these confirm that the change of the flow direction at the outer side of the bottom edge is indeed due to vortex development.

Figures 4.20 and 4.21 provide close-up views of the streamlines that exit or enter the mouth of the OWC at sequential times during a water column displacement. Within these figures, the velocity vectors and the contour plot of the velocity field predicted by the viscous flow solver, at each instant in time, are superimposed; the latter being presented by the absolute velocity magnitude, $|\overrightarrow{u}|$. The direction of the water column displacement is defined by the black arrow plotted on the water column area. Furthermore, the profiles of the vertical velocity calculated near the outer wall, $\overline{u_z^e}$, over the full draft of the water column are presented at sequential times; the overline of $\overline{u_z^e}$ again indicating the normalisation by the velocity of the internal free-surface. In addition, the analytically predicted velocity profiles (based upon linear potential theory) are provided as a comparison to the velocity profiles associated with the viscous flow.

To begin, the sequence of the streamlines and the velocity field generated by downward displacement are presented in Figure 4.20. Figure 4.20(a) shows a close-up view of the streamlines at an early stage of this displacement, at time $t = 3.05T_f$. At this time, a small downward vortex has developed on the outside of the water column. This originates from the fluid that was ejected through the area between a former upward vortex and the inner wall. By observing closely Figure 4.20(a), it is clear that the location of the small downward vortex is exactly below the bottom edge, and that this vortex has not moved itself radially out from the outer wall.

The horizontal position of this downward vortex indicates that the radial flow above this vortex, near the outer wall, has not been induced by the vortex. However, given that the fluid located nearer the outer wall turns upwards, the fluid at this location clearly has responded to this vortex and the downward displacement of the water column. In fact, this is consistent with the vertical velocity profile of $\overline{u_z^e}$ in the

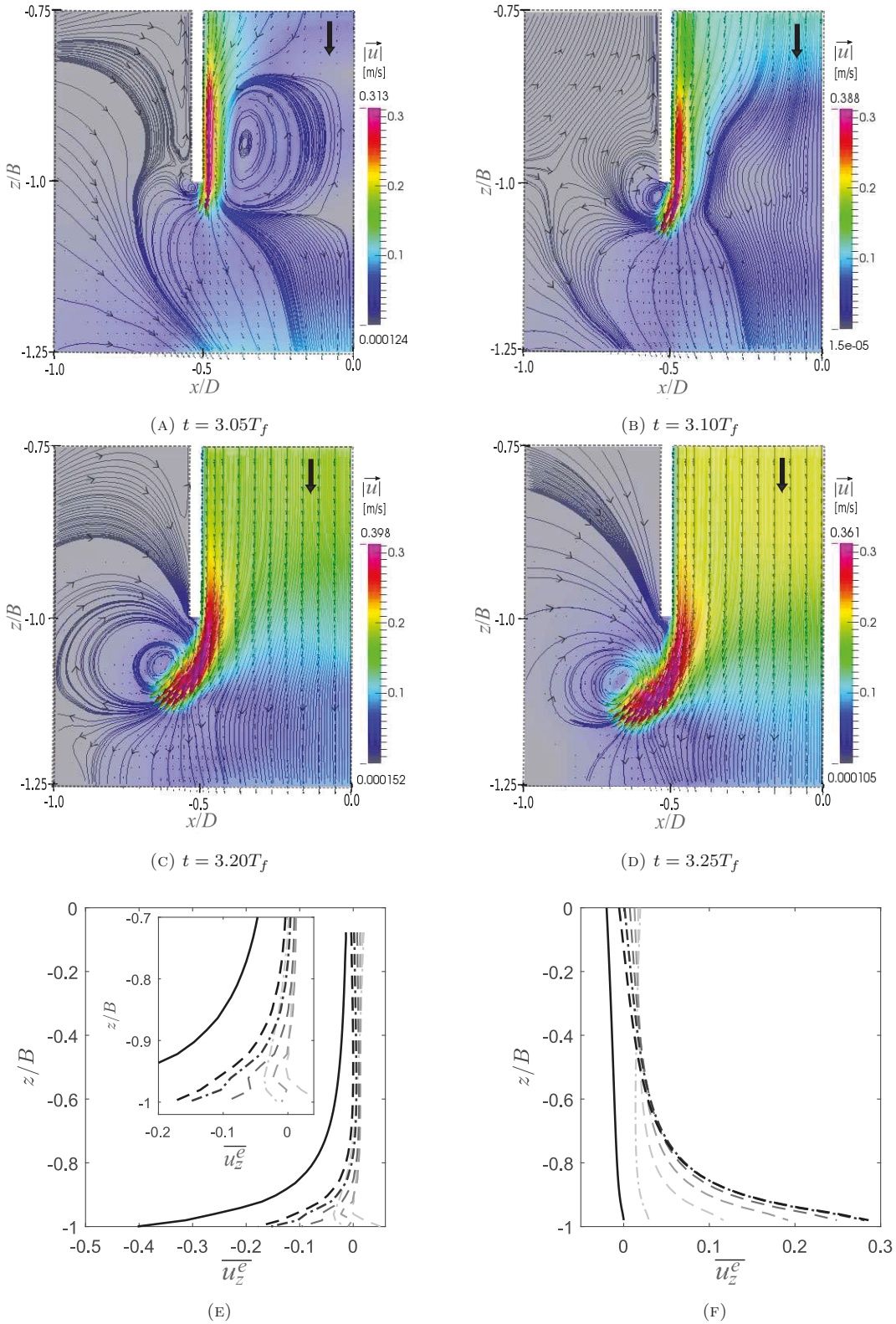

(A) $t = 3.05T_f$

(B) $t = 3.10T_f$

(C) $t = 3.20T_f$

(D) $t = 3.25T_f$

(E)

(F)

Figure 4.20: (A)-(D) Close-up views of the streamlines around the mouth in a viscous flow simulation, together with the vertical velocity profiles near the outer wall, $\overline{u_z^e}$, predicted by (E) the viscous flow and (F) the potential flow solver for a downward displacement of the water column at times: $3.0T_f$ [— · —], $3.05T_f$ [— —], $3.10T_f$ [— —], $3.15T_f$ [— —], $3.20T_f$ [— · —], $3.25T_f$ [— —], and $3.50T_f$ [——].

viscous flow (Figure 4.20(E)). At time $t = 3.0T_f$, the vertical velocity profile over the draft of the water column, as indicated by $(- \cdot -)$, has a negative value at $z = -B$. This arises from the previous upward displacement. At time $t = 3.05T_f$, this has changed: the profile of $\overline{u_z^e}$, indicated by $(- -)$, has a positive velocity over the draft. Nevertheless, the influence of the downward vortex has not affected the external flow located further from the outer wall. This can be observed in the external fluid at this location that moves downwards at this instant in time (Figure 4.20(A)). Evidently, the previous upward displacement of the water column continues to dominate this external fluid.

Following on, Figure 4.20(B) shows the streamline and the velocity field at time $t = 3.1T_f$; this corresponds to the time indicated by Point (3) on Figure 4.19(B). At this time, the vortex location has changed; the horizontal position of the downward vortex having moved further away from the outer wall. It is also clear from Figure 4.20(B) that the rolling-up of this vortex has induced a radial velocity; the direction of the flow on the outer side of the bottom edge having reversed. This is confirmed by the vertical velocity profile at $t = 3.1T_f$, presented by $(- -)$ on Figure 4.20(E). The vertical velocity of $\overline{u_z^e}$ now has a negative value over a greater depth located above the bottom edge. However, at higher elevations above the bottom edge, this velocity becomes positive. Based upon these results, it can be concluded that the change in the flow direction is associated with the vortex rolling-up, the increasing radial location of the vortex and its growing strength.

At subsequent times, the downward vortex continues to grow in size. For example, Figure 4.20(C) indicates closed streamlines in the instantaneous flow field at $t = 3.2T_f$. At this point, the fluid above the vortex has been influenced such that the flow is inwardly directed towards the vortex. Again, this is consistent with the vertical velocity profile. Figure 4.20(E) confirms the negative velocity associated with the profile given by $(- \cdot -)$. This profile reduces exponentially, approaching zero at the external free-surface. The zero velocity indicates a maximum near-field radiated wave elevation. Evidently, this event occurs after the flow direction at the bottom edge has changed, and the horizontal position of the downward vortex has moved to the left side of the outer wall.

Figure 4.20(C) also shows that the fluid velocity near the outer wall incorporates a stagnation point that moves progressively upwards. This reduces the momentum

flux of the fluid above this location and hence limits the height of the external water surface. At later times, $t = 3.25T_f$, on Figure 4.20(D), the vortex location has shifted downwards and the fluid velocity at the outer wall becomes negative at all elevations. At this stage of downward displacement, the near-field radiated wave elevation is clearly dependent on the formation of the vortex.

In the absence of flow separation, the flow direction near the outer wall of the bottom edge never changes. Indeed, the reversal of the flow direction on the outer wall above the bottom edge does not occur until the external free-surface reverses; evidence of this being seen from Figure 4.2(C). The analytical velocity profiles observed in Figure 4.20(F) also confirm this. The vertical velocity of $\overline{u_z^e}$ at the external free-surface has a zero magnitude when $t = 3.25T_f$. This is clearly delayed relative to the viscous flow prediction. Indeed, comparisons between the velocity profiles predicted from the two contrasting flow models, together with the streamlines associated with the viscous model, allow the reduction in the phase difference associated with a downward displacement to be understood.

Following on, Figure 4.21(A) presents close-up views of the streamlines at the beginning of an upward displacement. This shows that at $t = 3.55T_f$ the flow has separated at the bottom edge. The fluid velocity increases in the vicinity of the inner side of the bottom edge, but the development of a new upward vortex is not yet observed. In contrast, evidence of a growing upward vortex is evident when the increased velocity field is located inside the water column. This is shown in Figure 4.21(B) corresponding to time $t = 3.75T_f$, when the upward displacement ends. Importantly, this figure also reveals the near-parallel streamlines along the outer wall. The streamlines suggest that the external flow only moves in one direction and its flow direction is consistent with the upward displacement of the water column. This is confirmed in both Figures 4.21(C) and (D). The smaller relative change in the phase shift during an upward displacement, shown in Figure 4.19(A), can now be explained by the absence of significant vortex effects at the bottom edge.

4.7.3 Relationship between reduced phase difference and circulation

The progressively reduced phase difference observed in Figure 4.1 is driven by vortex formation. This is based upon two arguments:

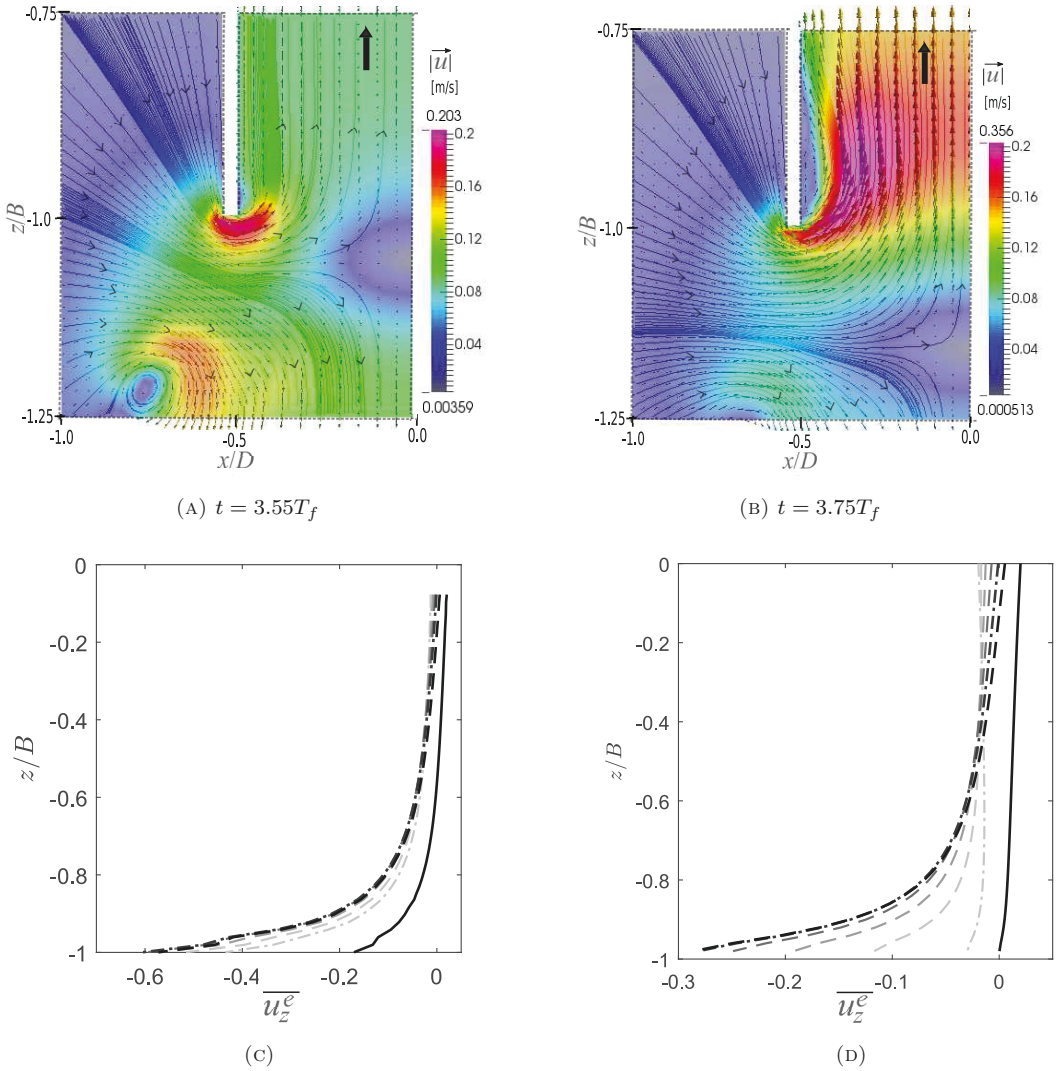

(A) $t = 3.55T_f$ (B) $t = 3.75T_f$

(C) (D)

Figure 4.21: (A)-(B) Close-up views of the streamlines around the mouth in a viscous flow simulation together with the vertical velocity profiles near the outer wall, $\overline{u_z^e}$, predicted by (C) the viscous flow and (D) the potential flow solver for an upward displacement of the water column at times: $3.50T_f$ [— · —], $3.55T_f$ [— —], $3.60T_f$ [— —], $3.65T_f$ [— —], $3.70T_f$ [— · —], $3.75T_f$ [— —], and $4.0T_f$ [——].

(i) The reduced phase difference of a near-field radiated wave elevation relative to the internal free-surface is related to vortex formation at the bottom edge, and

(ii) The properties of a vortex, including its circulation, are nonlinearly dependent on the forcing amplitude.

Given this understanding, the rate of generation of circulation at the outer wall should be evaluated. Following the formula of circulation, expressed in Equation

(3.2), the circulation rate at the outer wall is determined by:

$$\frac{d\Gamma_e}{dt} = \int_{b_o}^{X_v} \omega_\theta u_z dx, \tag{4.12}$$

where ω_θ again denotes the azimuthal component of the vorticity distribution, b_o the radius of the outer wall and X_v the horizontal position of the vortex core relative to the axisymmetric centre.

At an early stage of a downward displacement, the flow with non-zero vorticity exists for $x > |R_v|$. This is indicated by the streamlines provided on Figure 4.20(A). Consequently, the upper boundary of the integration in Equation (3.2) is defined by X_v in Equation (4.12), where $X_v = R_v$ for $x > 0$. In considering this approach, only the circulation rate generated at the outer wall is presented; the contribution from the vorticity distributions over $x > X_v$ was neglected. Furthermore, the quantification was only undertaken if the location of the vortex, X_v, was outside the wall.

Figure 4.22(A) concerns the circulation rate produced at the outer wall, $\frac{d\Gamma_e}{dt}$; the data normalised by the velocity of the internal free-surface. The time when the circulation rate becomes non-zero indicates the onset of vortex rolling-up, with the radial location of the vortex X_v being outside the wall. Clearly, the vortex rolling-up occurs earlier as the forcing amplitude increases. This is consistent with an earlier study of vortex formation at a piston mouth. Hettel et al. (2007) considered the influence of flow acceleration on the vortex formation. Their study involved both sinusoidal and linear functions of piston velocity, concluding that the stronger the acceleration of the piston, the earlier the formation process begins. Building upon this work, it is reasonable to conclude that the fluid acceleration and deceleration at the bottom edge of the OWC speeds up with the forcing amplitude. This in turn caused the earlier vortex formation and the earlier beginning of circulatory flows outside the wall.

To explore the relationship between the progressively reduced phase difference and the strength of the vortex, the phase differences for varying forcing amplitudes are plotted against the total kinetic energy of the vortex in Figure 4.22(B); the rate of the transfer of the kinetic energy (as defined in Equation (4.4)) was estimated. Within this figure, the phase difference is defined as the phase between the first-order component of the near-field radiated wave elevation and the internal surface elevation within the OWC. The normalisation of this phase difference by the theoretical

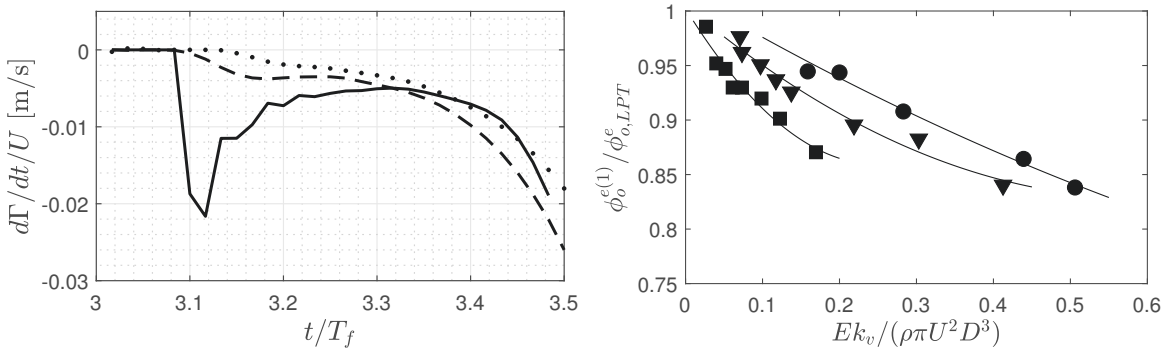

(A) (B)

Figure 4.22: (A) Circulation rates generated by the external flow $\frac{\partial \Gamma_e/\partial t}{U}$ for a cylinder of $D/B = 0.435$ with varying forcing amplitudes $\eta_o^i/B = 0.11$ [▪▪▪▪], 0.22 [— —] and 0.71 [——] and (B) reduced phase differences of the near-field radiated waves $\phi_o^{e(1)}/\phi_{o,LPT}^e$ as a function of the total kinetic energy relative to the water column $Ek_v/(\rho\pi U^2 D^3)$ for varying cylinder aspect-ratios: $D/B = 1.25$ [■], 0.435 [▼] and 0.15 [●], with the 2nd-order polynomial fit [——].

(linear, potential) value indicates the reduced phase difference, $\phi_o^{e(1)}/\phi_{o,LPT}^e$. Figure 4.22(B) shows the variations of the reduced phase differences with the relative value of $Ek_v/(\rho\pi U^2 D^3)$ for three cases involving different cylinder aspect-ratios D/B. The results show the progressive reduction in the phase difference with the increasing vortex strength, $Ek_v/(\rho\pi U^2 D^3)$ value. The largest percentage reduction is estimated to be 15%. This is comparable to the percentage reduction in the amplitude reduction shown in Figure 4.13(A). This is perhaps to be expected; phenomena being closely related as they are driven by the same underlying mechanism.

4.8 Second harmonics of near-field radiated waves

Bai & Eatock Taylor (2006) investigated the radiated waves generated by a truncated solid cylinder undergoing forced heaving oscillations using a fully nonlinear potential flow solver. Based upon their calculations, they found little evidence of strong free-surface nonlinearity; the result based upon the fact that time-histories of the wave run-up appear to be symmetric and show negligible high-frequency fluctuations. Figure 4.23(A) extends this work to consider the radiated waves around a cylindrical OWC. Specifically, Figure 4.23(A) describes the magnitudes of the second-harmonic relative to the first-harmonic radiated wave components, $\eta_o^{e(2)}/\eta_o^{e(1)}$, for varying η_o^i/B. In all cases, the relative magnitudes of the second-order radiated wave components

are small. Indeed, the largest ratio was estimated to be 10%; arising in the case of the smallest D/B and the largest η_o^i/B number.

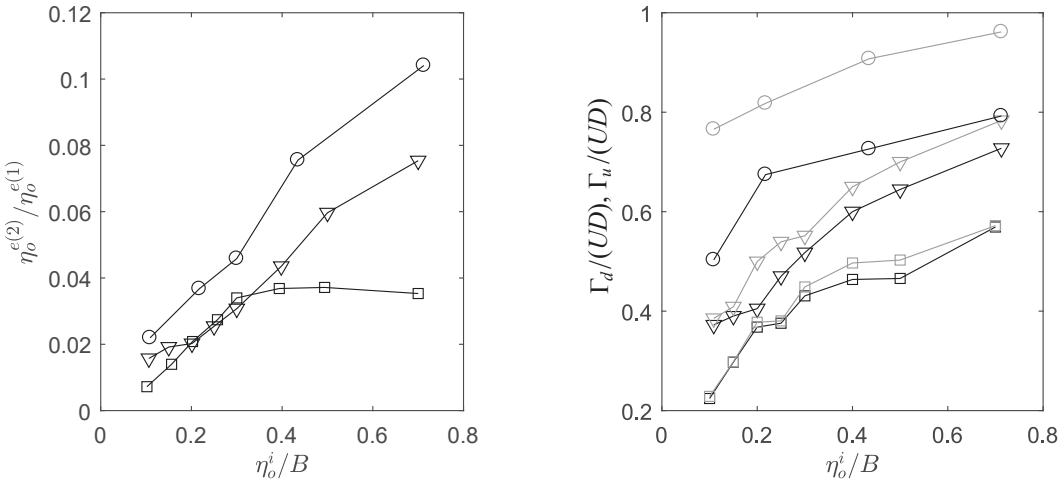

(A) (B)

Figure 4.23: (A) The second-order component, $\eta_o^{e(2)}$, relative to the first-order component, $\eta_o^{e(1)}$, of the near-field radiated wave, and (B) the vortex circulations arising from the downward and upward displacements, Γ_d/UD [Black] and $\Gamma_u/(UD)$ [Grey], for varying forcing amplitude numbers η_o^i/B and cylinder aspect-ratios D/B: 1.25 [□], 0.435 [▽], and 0.15 [○].

To put these results into context, Figure 4.23(B) presents the normalised vortex circulation, $\Gamma/(UD)$, when the external wave elevation is both at a maximum and minimum amplitude. In each case, the figure presents the variation in the normalised vortex circulation with η_o^i/B, for three D/B ratios. Importantly, it shows that the upward vortex circulation, $\Gamma_u/(UD)$, is larger than or equal to the downward vortex circulation, $\Gamma_d/(UD)$ for all cases (η_o^i/B and D/B). Given that an amplitude reduction becomes more significant with increasing $\Gamma/(UD)$, it is logical to conclude that the physical cause of the increased amplitude reduction during an upward displacement results from the more significant vortex circulation. As a result, the dependence of the vortex circulation on the direction of the travel of the water column, contributes to the wave asymmetry in the time-varying near-field radiated wave elevations, as shown in Figure 4.1.

4.9 Observations of far-field wave radiations

The radiated wave in a far-field, generated by an OWC, predominantly contains a progressive wave mode (see Section B.3 of Appendix B). This radiated elevation may be accurately predicted from the corresponding radiation damping coefficient, b_1. Observations of the far-field radiated wave may therefore provide insights into the influence of a vortex motion on this important hydrodynamic coefficient.

To begin, the far-field radiated wave elevation at a radial location far from the outer wall of an OWC with $D/B = 0.435$ has been investigated. In presenting this work, the location to be addressed must be sufficiently distant from the outer wall such that the exponentially decaying wave modes are negligible. Based upon the method of evaluation described in Appendix B, this location was chosen as $x \approx 0.56\lambda$. At this location, the exponentially decaying wave modes account for less than 0.5% of the propagating wave modes.

Figure 4.24(A) describes the first-harmonic (fundamental) component of the far-field radiated wave amplitudes, $\eta_o^{e(1)}$, as a function of the forcing amplitude number, η_o^i/B. This data describes a linear relationship between the first-harmonic of the radiated wave amplitude and the forcing amplitude in the far-field. Building on this, Figure 4.24(B) reveals that the reduced amplitude in the far-field is relatively invariant over a broad range of forcing amplitudes. In this case, the reduced amplitude, $\eta_o^{e(1)}/\eta_{o,LPT}^e$, is the first-order component of the far-field radiated elevation, $\eta_o^{e(1)}$, normalised by the linear potential solution, $\eta_{o,LPT}^e$. The apparent dependence of the reduced amplitude on the forcing amplitude in the far-field is in marked contrast to its dependence in the near-field. This suggests that the progressive amplitude reduction (believed to be associated with vortex effects) does not apply in the far-field. Further evidence of this is provided in Figure 4.24(C). This contrasts the phase angle between the far-field radiated wave elevation and the internal surface elevation and the corresponding data for the near field. While the former shows a progressive reduction with increasing η_o^i/B number, the latter is broadly invariant and very closely predicted from the theoretical (linear, potential) solution.

The results presented in Figures 4.24(B) and (C) provoke an immediate question: in progressively reducing the radiated wave amplitude, do the vortex effects considered earlier primarily act on the exponentially decaying terms? To address this, the first-order radiated wave amplitude normalised by the respective forcing amplitude,

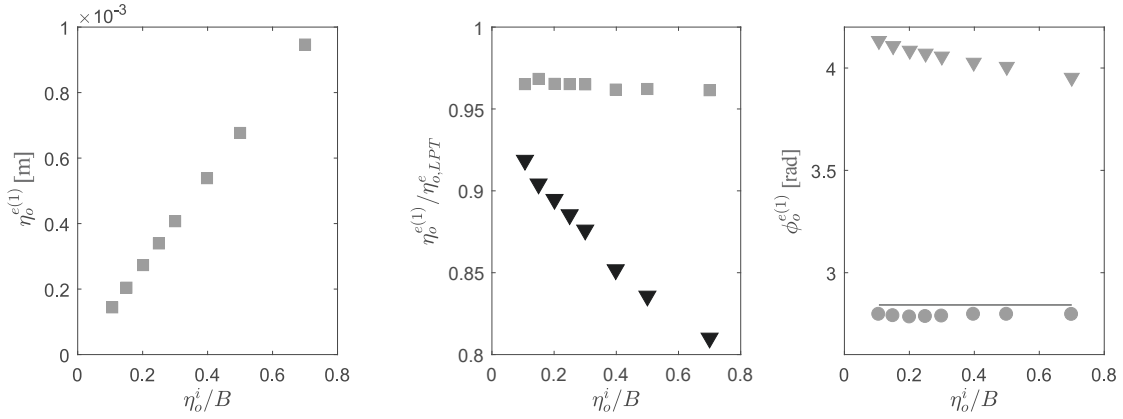

(A) (B) (C)

Figure 4.24: First-order components of (A) the far-field radiated wave amplitudes $\eta_o^{e(1)}$ [■], (B) the reduced amplitudes $\eta_o^{e(1)}/\eta_{o,LPT}^e$ [■] in the far-field and the near-field [▼] and (C) the first-order phase differences $\phi_o^{e(1)}$ relative to the internal water surface [▼] and relative to the near-field radiated wave [●]; the latter being compared to the linear potential solution [——].

η_o^e/η_o^i, is investigated at varying radial locations. This extends from the outer wall to the location where the contribution from the exponentially decaying modes is considered neglegible. Figure 4.25(A) presents these radial variations in the normalised wave amplitude for three different forcing amplitudes. Clearly, the radial variations show the most pronounced reductions at the wall and the smallest reductions where $x \geq 0.5\lambda$. This suggests that the progressive amplitude reductions only occur at radial locations where the exponentially decaying wave modes remain significant.

Figure 4.25(B) provides further evidence of this. In this case, the radial variations in the normalised wave amplitude were quantified by considering only the progressive wave modes arising from a viscous flow solution. To achieve this, the radial profiles of the progressive wave mode amplitudes were re-calculated using the quantified radiation damping b_1 and Equation (B.7). The radial profile was also theoretically evaluated from the analytical radiation potential given in Equation (2.17); the exponentially decaying terms in this equation being neglected. The resulting comparisons, presented on Figure 4.25(B), show a negligible variation with the forcing amplitude. All the corresponding profiles obtained from the viscous flow model concide well with the theoretical profile, except at the outer wall. This deviation is most likely due to the inclusion of the standing wave numbers when deriving the outgoing radiated wave coefficient α_o^R. At all other radial locations, the profiles are in good agreement with the theoretical profile computed from the progressive wave

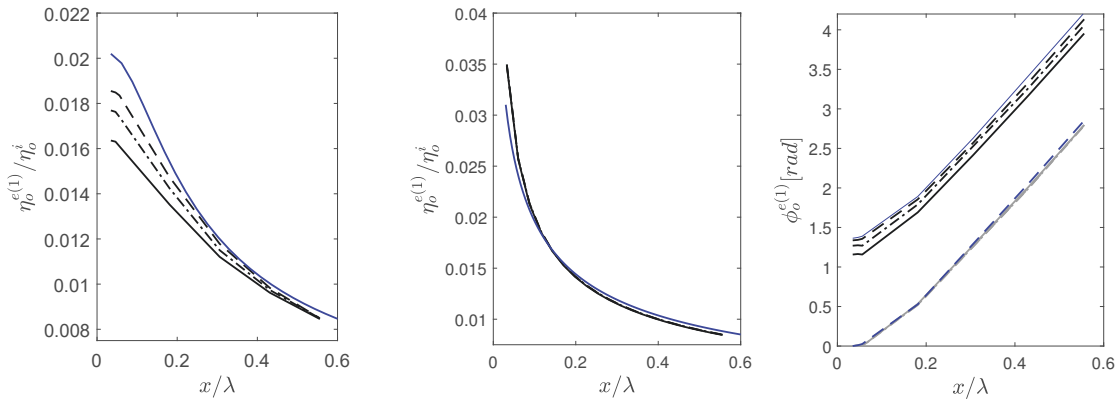

(A) (B) (C)

Figure 4.25: Radial variations in (A) the radiated wave amplitude of the first-harmonic frequency, $\eta_o^{e(1)}/\eta_o^i$, including the exponentially decaying wave modes and (B) without these modes, and (C) the phase angle of the radiated wave elevation, $\phi_o^{e(1)}$, relative to the internal water surface elevation [Black] and the near-field radiated wave elevation [Grey] for three forcing amplitude cases: $\eta_o^i/B = 0.11$ [— —, — —], 0.3 [— · —, — · —], and 0.71 [——, ——]; comparisons to the theoretical variations [——, — —] being provided.

mode. Taken together, these results suggest that the vortex effect primarily reduces the radiated wave energy associated with the exponentially decaying wave modes and not the progressive wave modes.

In respect of the second vortex effect, the radial profiles of the phase difference relative to the internal water surface elevation and relative to the near-field radiated wave elevation are presented in Figure 4.25(C). The corresponding profiles analytically predicted are also presented in this figure. The radial profiles of the phase difference relative to the near-field radiated wave show good agreement with the linear potential solution. Conversely, the progressive reduction in the phase difference relative to the internal surface elevation is apparent along the radial location. These comparisons confirm that the vortex effect associated with the progressively reduced phase difference is evident in both the near- and far-fields.

Finally, Figure 4.26(A) presents the reduced amplitudes $\eta_o^{e(1)}/\eta_{o,LPT}^e$ in the far-field for each of the cylinder diameters. Again, the reduced amplitudes for each cylinder were estimated at the radial location where the exponentially decaying wave modes are negligible. These radial locations were chosen as $x = 0.53\lambda, 0.56\lambda$ and 0.62λ, for the D/B ratios of $0.15, 0.435$ and 1.25, respectively. In all cases, the results are similar to those presented in Figure 4.24(B); the reduced amplitudes being invariant to the increasing forcing amplitude. This suggests that a radiation damping

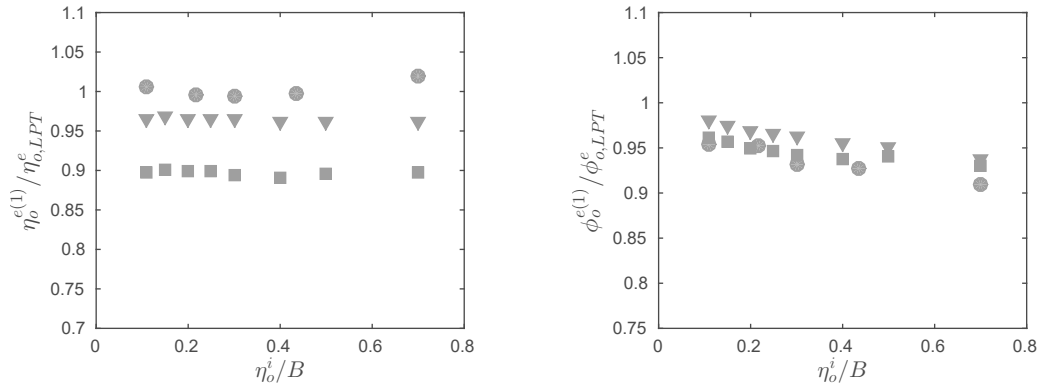

(A) (B)

FIGURE 4.26: (A) Reduced amplitudes $\eta_o^{e(1)}/\eta_{o,LPT}^e$ and (B) reduced phase differences $\phi_o^{e(1)}/\phi_{o,LPT}^e$ in the far-field radiations for varying cylinder aspect-ratios D/B: 1.25 [■], 0.435 [▼] and 0.15 [•].

coefficient, b_1, would be appropriate to the far-field, albeit one that is reduced relative to the linear predicted solution.

4.10 Effective draft

The reduction in the near-field radiated wave amplitude at the outer wall of an OWC is indicative of an increase in the effective draft of the column in a viscous flow. One possible explanation for this lies in formation of the vortex motion at the base of the OWC. To investigate this, comparisons are made between the present viscous flow calculation and a linear potential solution of variable draft; the latter being defined to match the radiated wave field. Figure 4.27 describes the approach implemented herein. This figure shows comparisons of the near-field radiated wave elevations corresponding to the actual draft, B, and the effective draft, B_e. Given the inherent assumptions of the linear potential flow, the matched amplitudes can be defined in terms of either the maximum or minimum radiated wave elevations. Figure 4.27(A)) concerns the former with $B_e = 1.19B$, while Figure 4.27(B) addresses the latter with $B_e = 1.31B$.

To establish a potential linkage between the effective draft and the vortex motion, Figure 4.28 concerns the variations of the effective draft, B_e, and the vortex locations with η_o^i/B and D/B. This figure only presents the vortices located nearest the mouth of the OWC. In each case, the location of the vortex is identified by: (i) the vertical locations of the lower and upper boundaries of the vortex, Z_b, and (ii) the vertical

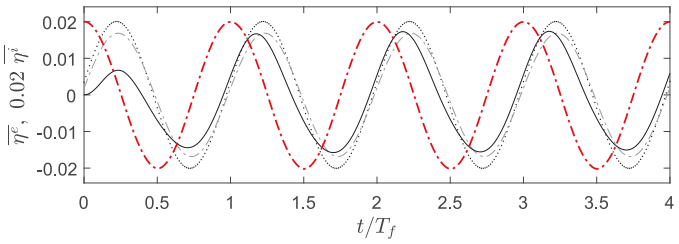

(A) Effective draft $B_e = 1.19B$

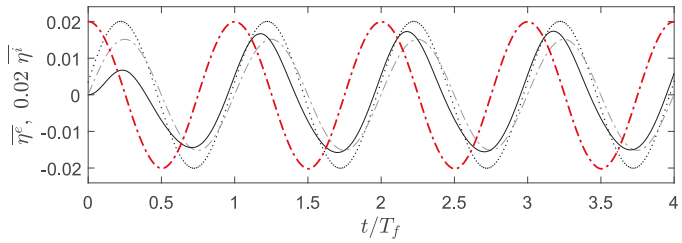

(B) $B_e = 1.31B$

FIGURE 4.27: Time-histories of the internal surface elevations, $\overline{\eta^i}\,(t)$[— · —], and the near-field wave elevations, $\overline{\eta^e}\,(t)$, generated by an OWC with an effective draft, B_e [— · —], are compared to those with the actual draft B in the viscous flow [——] and the potential flow model [· · · ·]; the cylinder aspect-ratio being $D/B = 0.435$.

location of the vortex centre, Z_v. The relevant values are denoted by $\overline{Z_b}$, $\overline{Z_v}$ and $\overline{B_e}$ on Figure 4.28; the overbar indicating values normalised by the actual draft, B. In addition, the location of a stagnation point, $\overline{Z_s}$, identified during an upward displacement of the column is also presented. This is discussed further below.

Following the methods discussed earlier, the Z_v values were given by the central weight of the azimuthal vorticity distribution, while the Z_b values were determined using the Q-criterion; the latter giving an estimation of the vortex boundary. In adopting this latter approach, the lower boundary of the vortex is defined by the vertical location where a vertical line passing through the vortex centre crosses the boundary on the lower side. Conversely, the upper boundary is defined by where the same vertical line crosses the boundary on the upper side. All these quantifications were extracted from the flow field data describing a maximum η^e_{max} or minimum elevation η^e_{min} of the near-field radiated wave.

Figure 4.28 confirms that the vortices having the most impact on the effective draft are those located nearest the bottom mouth. The explanation for this is described as follows. Figures 4.28(A), (C) and (E) present the locations of the downward vortices being generated when the radiated wave elevations are a maximum. Evidently, the vertical position of the lower boundary of a downward vortex, $\overline{Z_b}$, is closely

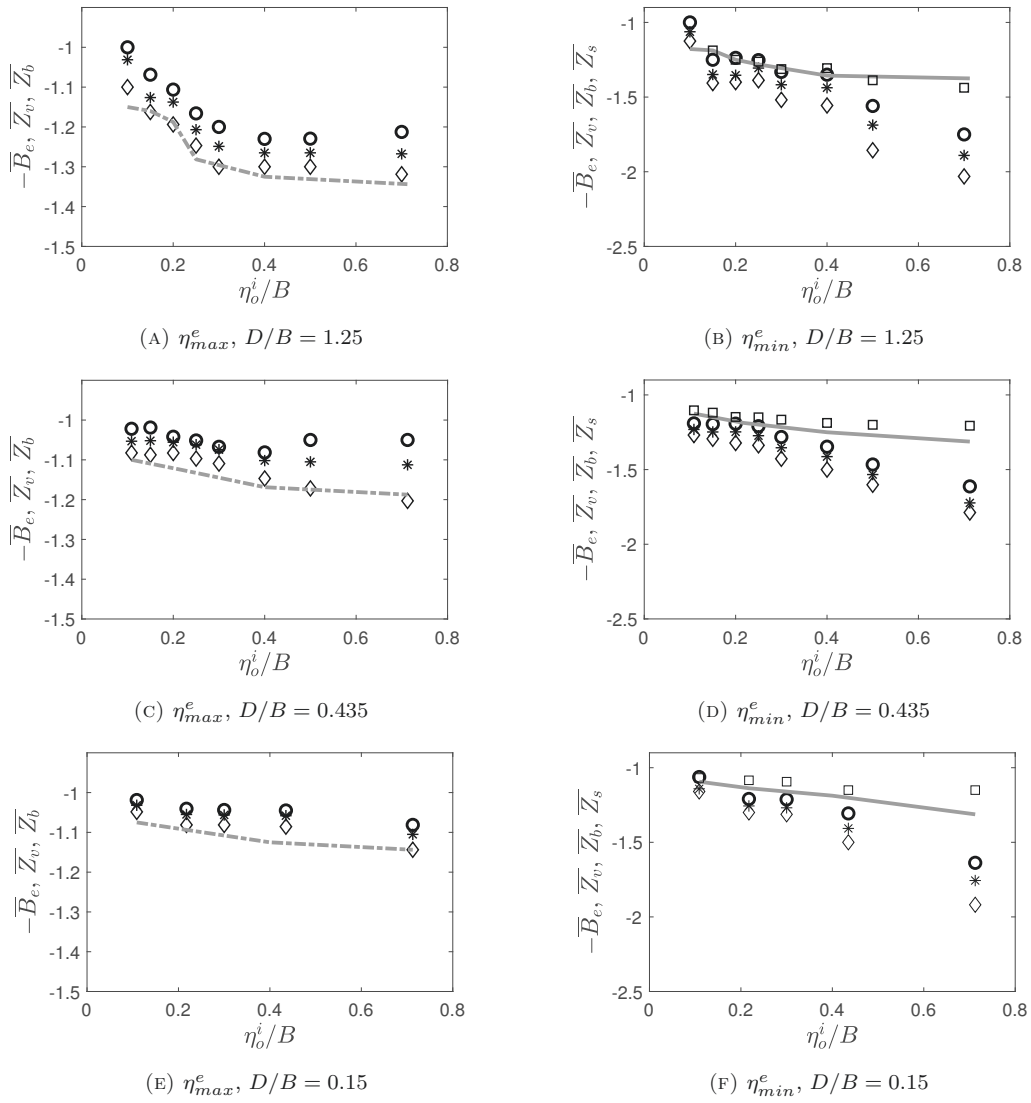

(A) η^e_{max}, $D/B = 1.25$

(B) η^e_{min}, $D/B = 1.25$

(C) η^e_{max}, $D/B = 0.435$

(D) η^e_{min}, $D/B = 0.435$

(E) η^e_{max}, $D/B = 0.15$

(F) η^e_{min}, $D/B = 0.15$

Figure 4.28: Vertical locations of the vortex centre, $\overline{Z_v}$ [$*$], the upper and lower boundaries of the vortex, $\overline{Z_b}$ [$\circ$, $\Diamond$], and the stagnation point, $\overline{Z_s}$ [$\square$] compared to the effective draft $\overline{B_e}$ that either matches the maximum η^e_{max} [— · —] or the minimum amplitude η^e_{min} [——] of the near-field radiated wave; all data expressed as a function of η^i_o/B ratios, for varying D/B ratios.

related to the effective draft that matches the maximum elevation, η^e_{max}. Conversely, Figures 4.28(B), (D) and (F) show that the vertical position of a stagnation point, $\overline{Z_s}$, is closely related to the effective draft that matches the minimum elevation, η^e_{min}.

To further explore the linkage between the effective draft and the vortex motion, Figure 4.29 shows two instantaneous flow fields corresponding to η^e_{max} and η^e_{min}. Figure 4.29(A) shows a plot describing the absolute velocity flow field, $|\overrightarrow{u}|$, superimposed on the streamlines when the near-field radiated wave is at a maximum elevation; this corresponding to Figure 4.28(C) with $\eta^i_o/B = 0.71$. The vortices formed during the

first few periods of oscillation are numbered in ascending order; a downward vortex denoted by an odd number and an upward vortex an even number. Figure 4.29(A) shows that the flow from the water column is unaffected by the former downward vortices (Points (1) and (3)), but passes between the lower edge of the currently growing downward vortex (Point (5)) and the former upward vortex (Point (4)). Beyond this point, the flow continues to move towards the external free-surface; the relevant streamlines being represented by the red line on Figure 4.29(A). While this occurs, the downward vortex is developing and still attached to the inner wall. The curve of the corresponding outer streamline of this flow resembles the streamline curve of the flow that passes the bottom edge with a draft, B_e, in a potential flow. This can be confirmed by referring to Figure 4.2(C). The figure shows a streamline curve that has a near-90° bend when passing the bottom edge. Setting B_e equal to the lower boundary of the downward vortex generated in a viscous flow therefore appears reasonable. This explains the data given on Figures 4.28(A), (C) and (E).

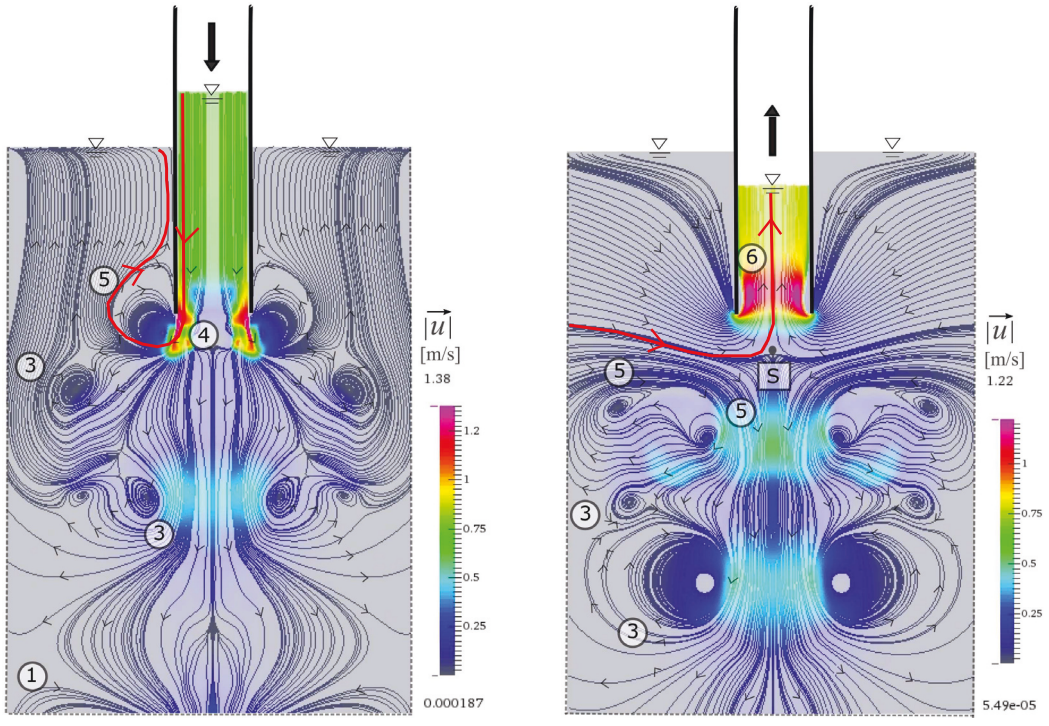

(A) (B)

Figure 4.29: The absolute velocity, $|\overrightarrow{u}|$, superimposed on the streamlines at two different phases showing: (A) η^e_{max} at $t = 2.2T_f$, and (B) η^e_{min} at $t = 2.7T_f$; the locations of vortices being indicated by the increasing numbers within ◯, the stagnation point indicated by $\boxed{S}$ and the streamline showing the effective draft indicated in red.

A related plot showing the velocity field and the streamlines when the near-field radiated wave is a minimum is presented in Figure 4.29(b). At this phase, the water column is being upwardly displaced. Consequently, the previously detached vortices (Points (3) and (5)) are retracted back near the bottom mouth. Simultaneously, a new upward vortex (Point (6)) is being formed inside the mouth. Again, the flow outside the cylinder avoids the detached vortices, that are now located below the bottom mouth. At this instant in time, the streamlines either enter the mouth or circulate the recently detached vortex (Point (5)). A stagnation point (Point S) exists between these diverging streamlines. Importantly, the diverging streamline curves show a close resemblance to the streamlines that have a near-90° curvature at the bottom edge in a potential flow (Figure 4.2(e)). As a result, the effective draft, B_e, is closely approximated by the elevation of this stagnation point and to a lower extent the upper boundary of the previous downward vortex (Point (5)); the relevant streamline again indicated in red.

4.11 Concluding remarks

This chapter has described new insights into the wave radiation generated by the forced oscillation of a water column. The radiated wave characteristics in the near- and far-fields and the vortex effects have been discussed in the context of the evolving flow field.

The first-order wave amplitude is the dominant component; the slight wave asymmetry being consistent with the small second-harmonic components. Based upon the first-order components of the radiated wave elevations, two distinct characteristics of the radiated waves in the near-field are identified. These are a progressively reduced amplitude and progressively reduced phase difference; both found to be nonlinearly dependent on the forcing amplitude. Given the quantifications of the normalised vortex properties, it is found that the amplitude reduction is due to the vortex formation at the bottom edge. The phase difference is also found to be directly related to the vortex formation. The present calculations confirm that the onset of a vortex rolling-up and the induced circulation at the outer wall occur earlier with an increased forcing amplitude. The induced radial velocity at the outer wall acts to speed up the time when the external free-surface is brought to rest.

In the far-field, the radiated waves also experience a vortex effect; the radiated wave elevations occuring earlier than theoretically predicted. This is a direct consequence of the progressively reduced phase difference. However, the far-field radiated wave amplitude shows no variation with the forcing amplitude. This suggests that the vortex formation only reduces nonlinearly the wave energy associated with the exponentially decaying or evanescent wave modes.

Given these insights, it is reasonable to conclude that linear radiation theory is valid when seeking a radiation damping coefficient and this coefficient will be satisfactorily predicted by a linear analytical solution. However, the linear theory is not valid in the near-field. Specifically, the location of the vortex closest to the bottom mouth of an OWC has a significant influence on the effective draft, B_e.

5

Nonlinear forcing and motions

5.1 Chapter overview

Chapter 4 confirmed that the vortex formation and its subsequent convection was the dominant source of nonlinearity in the radiated wave fields produced by forced oscillations. In considering the performance of an OWC at sea, the interaction of the device with incident waves may provoke additional nonlinearities. Indeed, earlier numerical and laboratory studies, reviewed in Chapter 2, have revealed the existence of high-frequency effects in both the air pressure and the response of the water column.

The importance of these additional nonlinearities relates to the fact that both the air pressure and the response affect the hydrodynamic efficiency. In addition, the response (or motion) of the water column is affected by the external excitation forces. As a result, an evaluation of the physical origins of any nonlinearities in the forces and motions is essential to understand how the high harmonics affect the hydrodynamic efficiency and how best to undertake the time-domain modelling of an OWC. With these points in mind, the present chapter provides an investigation of the nonlinearities in the forces and motions of an OWC under both wave and forced excitation mechanisms. The purpose of this chapter is to determine the nature of these additional nonlinearities and their relative importance.

5.2 Test cases

The purpose of the regular wave tests (RWTs) outlined in Table 5.1 is to explore the nonlinearities associated with:

(i) The diameter to incident wave-length ratio, D/λ,

(ii) The cylinder aspect-ratio, D/B,

(iii) The incident wave steepness, $A_o k$, and

(iv) The mouth shape.

In all of the test cases, the draft B is fixed at $B = 0.16$ m. The test cases included in RWT 1 explore the variation of D/λ by keeping all other parameters constant while varying the angular wave frequency, ω. Conversely, RWT 2-4 explore the D/λ variation by fixing ω and changing the column diameter, D. In addition, these cases also concern the variation with $A_o k$. All the test cases included in RWT 1-4 correspond to OWCs with straight and sharp-edged (SE) mouths. When compared to RWT 3, RWT 5-6 vary in respect of mouth shape; RWT 5 corresponding to a straight and semicircular-ended (SC), and RWT 6 a bell-shaped (BS) mouth with a lip radius of $r_l = 0.5D$. The wall thickness, t_w, for the SC end is two times larger than those for others. A schematic showing cross-sectional views of these mouth shapes was previously given in Figure 3.2.

Table 5.1: Regular wave test cases

Test cases	D/B	$A_o k$	D/λ	Mouth shape
RWT 1	0.435	0.10	0.03 - 0.09	SE
RWT 2	1.250	0.03 - 0.25	0.17	SE
RWT 3	0.435	0.03 - 0.30	0.06	SE
RWT 4	0.150	0.03 - 0.25	0.02	SE
RWT 5	0.435	0.10 - 0.27	0.06	SC
RWT 6	0.435	0.03 - 0.20	0.060	BS

The present study also considers Forced Air Pressure Tests (FAPTs). In contrast to the Forced Water Column Tests (FWCTs) discussed in Chapter 4, the air pressures acting above the internal free-surfaces were prescribed as sinusoidally varying functions. In considering both the FWCTs and the FAPTs, it is important to note

that neither represent the external wave excitation. However, the FAPTs are relevant when exploring the nonlinearities associated with:

(i) The angular forcing frequency, ω_f,

(ii) The amplitude of the air pressure, P_o, and

(iii) The mouth shape.

Within the FAPTs, the draft in all the test cases was again fixed at $B = 0.16$ m. As indicated in Table 5.2, FAPT 1 considers the variations of ω_f and P_o, while FAPT 2-4 explores the variations of P_o and the mouth shape. To complement these cases, additional FWCTs were undertaken: FWCT 1-3 in Table 5.2 considering the variations of the prescribed amplitude of the internal surface elevation, η_o^i, and the mouth shape.

Table 5.2: Forced oscillation test cases

Test cases	D/B	$P_o/\rho g$ [m]	$\omega_f^2 B/g$	η_o^i/B	Mouth shape
FAPT 1	0.435	0.0016 - 0.0170	0.71 - 1.11	-	SE
FAPT 2	0.435	0.0050 - 0.0400	0.87	-	SE
FAPT 3	0.435	0.0044 - 0.0356	0.87	-	SC
FAPT 4	0.435	0.0030 - 0.0203	0.87	-	BS
FWCT 1	0.435	-	0.87	0.11 - 0.71	SE
FWCT 2	0.435	-	0.87	0.11 - 0.71	SC
FWCT 3	0.435	-	0.87	0.11 - 0.71	BS

5.3 Numerical simulations

5.3.1 Computational domain

The computational domain for numerically simulating a FAPT case is closely related to the FWCT cases studied in Chapter 3. In numerically simulating a RWT case, the computational domain is defined by the dimensions of the OWC and the incident wave conditions; both described in Section 5.2. In respect of the numerical wave tank (NWT), the height, L_z, width, L_y, relaxation zone length, L_R, and the total length of the NWT, L_{NWT}, are as outlined in Figure 5.1 and were set identical to the validation study outlined in Section 3.5. Full details of these dimensions are given in

Table 5.3. In each simulation, a symmetric boundary condition was again applied; a half-cylinder located at $x = y = 0$ as noted on Figure 5.1.

Table 5.3: Dimensions of the NWT

Parameter name	Dimensionless parameter	Parameter value
Width	L_y/D	9
Height	L_z	$h + 4A_o$
Length	L_{NWT}/λ	6.5
Relaxation zone	L_R/λ	1-1.5

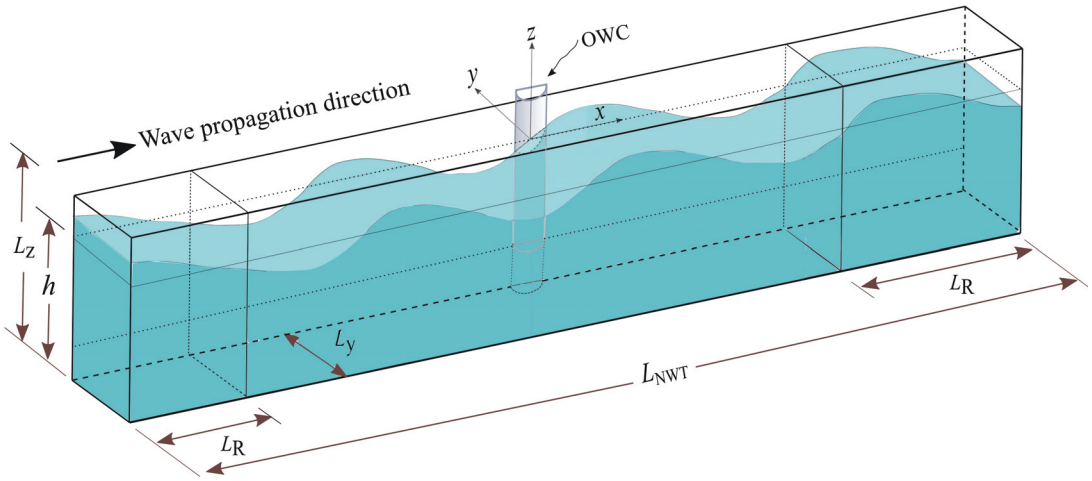

Figure 5.1: Schematic of the computational domain showing an OWC within the numerical wave tank.

The computational domain described above was discretised into a number of non-orthogonal grids. Figure 5.2 shows the mesh viewed from (A) above, (B) a side view and (C) a close up in the vicinity of the column. Figure 5.2(C) shows the increased mesh resolution close to the OWC, particularly at the lower end of the column. This grid resolution was set according to the grid independence studies presented in Section 3.3; with identical resolutions applied in the FAPT cases. Likewise, the grid resolution applied at the external free-surface, indicated by the blue line on Figure 5.2(B), was set in accordance with the requirement outlined in Section 3.4.1.

5.3.2 Initialisation method

In Chapter 3, the numerical simulation of a cylindrical OWC was initialised from a still water condition. This has two drawbacks. First, the computational time required

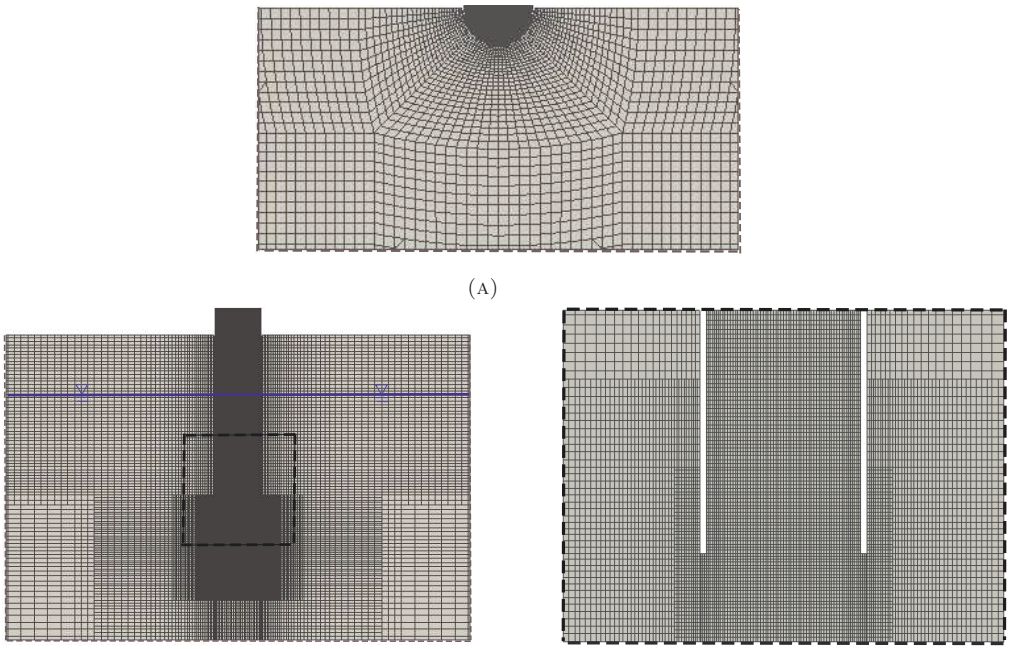

(A) (B) (C)

Figure 5.2: Computational mesh seen from different perspectives: (A) a top view, (B) a side view and (C) a close-up corresponding to the dashed box shown on (B).

to achieve a "steady-state" or developed response may be prohibitively long. Second, the wave height computed at the location of the water column may deviate from the theoretical input (see Figure 3.14).

To overcome these difficulties, an initial wave field was prescribed using an analytical wave theory. An example of a computational domain initialised in this way is given in Figure 5.3. In adopting this approach, the starting phase of the wave motion was defined such that an up-crossing elevation was located on the centre of the OWC. This was chosen to minimise both the error in the boundary condition on the wall of the OWC and the disturbance around the OWC at the beginning of a simulation. Figure 5.3(A) shows the initial horizontal fluid velocity field, u_x, on $y = 0$ and Figure 5.3(B) a close-up view of the surface elevation, with the wave slope located on the centre of the water column.

Direct comparisons between the 'developed' calculations based upon the two alternative initialisation methods are presented on Figure 5.4. This provides alternative predictions of the external water surface elevation, η^e, at an upstream location ($x \approx -D/2$), and the internal surface elevation, η^i; the former being referred to as the near-field scattered wave elevation and associated with the incident wave, the

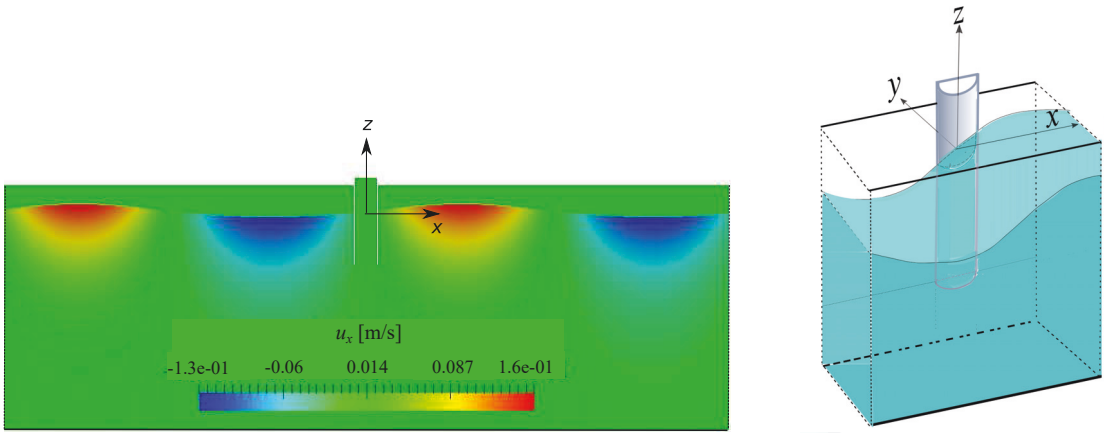

(A) (B)

Figure 5.3: Schematic of the computational domain with the initial condition showing: (A) the horizontal fluid velocity, u_x, on $y = 0$ and (B) a close-up isometric view of the water column.

oscillating water column and the disturbance due to the cylindrical structure. The results presented on Figure 5.4 correspond to the wave cases investigated in RWT 1 on Table 5.1. Good agreement is observed in all cases. In particular, Figures 5.4(A), (C) and (E) clearly reveal the high-frequency content within the external surface elevations, irrespective of which method of initialisation is adopted.

Within Figure 5.4, the time base indicated in black (at the bottom of each sub-plot) relates to initial still water conditions, whereas that indicated in blue (at the top of each sub-plot) relates to pre-defined wave conditions. In each case, the difference between these times indicates the computational saving associated with pre-defined wave conditions. For example, Figure 5.4(C) reveals that the number of wave cycles required for the internal surface elevation to achieve a developed state was three wave periods when computed with pre-defined wave conditions. This contrasts with the ten wave periods when calculations are initiated with a still water surface. Despite the significant computational saving associated with pre-defined wave conditions, the computational effort remain very substantial. With 96 processors handling 4.5 million cells, the calculation of nine wave cycles took approximately one week.

Time-histories of the vertical forces, $F_v\,(t)$, acting on the bottom cross-sectional area of the water column, are compared in Figure 5.5. Once again, good agreement between the two different methods of initialisation is shown in all cases of D/λ. Interestingly, for cases of $D/\lambda = 0.063$ and 0.06 on Figures 5.5(B) and (C), the asymmetrical shapes and high-frequency content of the vertical forces are identified

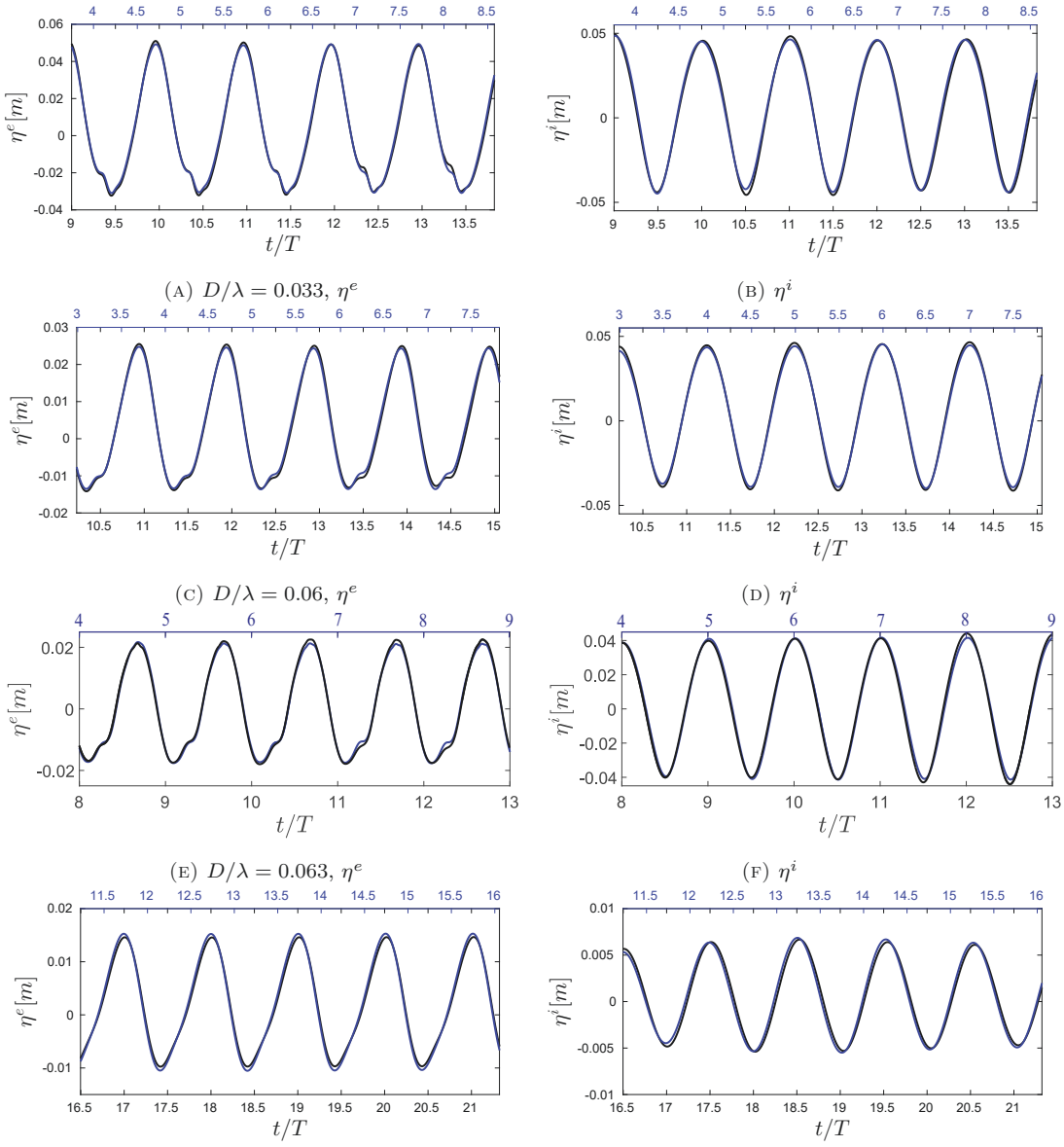

(A) $D/\lambda = 0.033$, η^e (B) η^i

(C) $D/\lambda = 0.06$, η^e (D) η^i

(E) $D/\lambda = 0.063$, η^e (F) η^i

(G) $D/\lambda = 0.087$, η^e (H) η^i

FIGURE 5.4: Comparisons of time-histories of the external water surface elevations $\eta^e(t)$ at $x \approx -D/2$, and the internal water surface elevations, $\eta^i(t)$ with [——] based upon an initial still water condition compared to [——] pre-defined wave conditions. All cases relate to a constant diameter of $D/B = 0.435$ subjected to varying wave periods and a constant wave steepness of $A_o k = 0.1$ (Test cases RWT1 on Table 5.1).

using both approaches. However, an initial still water condition seems to produce less 'stable' results. This may be due to wave reflections which seem to affect $F_v(t)$ more critically than η^i or η^e. Given the comparisons provided on Figures 5.4 and 5.5, initiation based upon pre-defined wave conditions is clearly preferable.

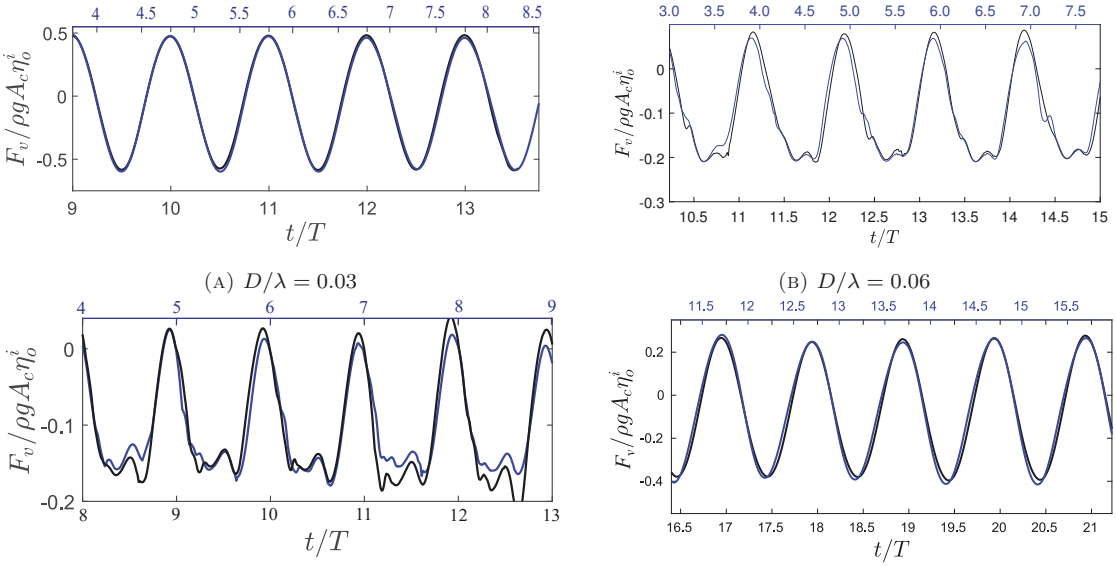

(A) $D/\lambda = 0.03$ (B) $D/\lambda = 0.06$

(C) $D/\lambda = 0.063$ (D) $D/\lambda = 0.087$

FIGURE 5.5: Time-histories of the vertical forces, $F_v(t)$, acting on the bottom cross-sectional area of the water column with [——] based upon an initial still water condition compared to [——] predefined wave conditions. All cases relate to $D/B = 0.435$ with D/λ varied but the wave steepness fixed at $A_o k = 0.1$. (Test cases RWT1 on Table 5.1)

5.4 Observations of scattered wave elevations

Figure 5.6 presents time-histories of the near-field scattered wave elevations, $\eta^e(t)$, normalised by the incident wave amplitude, A_o. These results relate to the test cases RWT 2, 3 and 4 outlined in Table 5.1. In each case, incident waves of varying steepness were considered; $A_o k = 0.03, 0.1$ and 0.2 corresponding to linear, weakly-nonlinear and nonlinear wave conditions. Across the three cases, the D/B ratios were 1.25, 0.435 and 0.15; the corresponding D/λ ratios being 0.17, 0.06 and 0.02. Each sub-plot provides a comparison between the scattered wave elevations computed from the viscous flow solver and the linear potential solution. In each case, the presented data has been shifted in time such that at $t = 0$ an incident wave crest exists at the centre of the water column.

In the largest relative diameter case ($D/\lambda = 0.17$ on Figure 5.6(A)), the near-field scattered wave elevations computed from the viscous flow model deviate from the linear potential solution. However, there is no evidence of high-frequency effects. In contrast, these effects are clearly noted in the two smaller relative diameters ($D/\lambda = 0.06$ and 0.02 on Figures 5.6(B) and (C)). In both these cases, the magnitude of the high-frequency scattered wave increases with the steepness of the incident wave, $A_o k$.

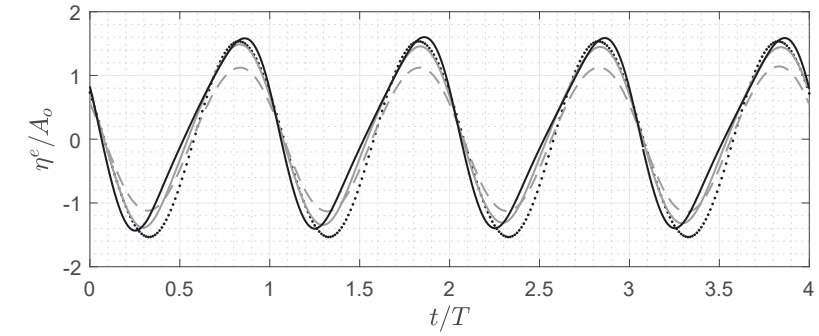

(A) $D/B = 1.25$ and $D/\lambda = 0.17$

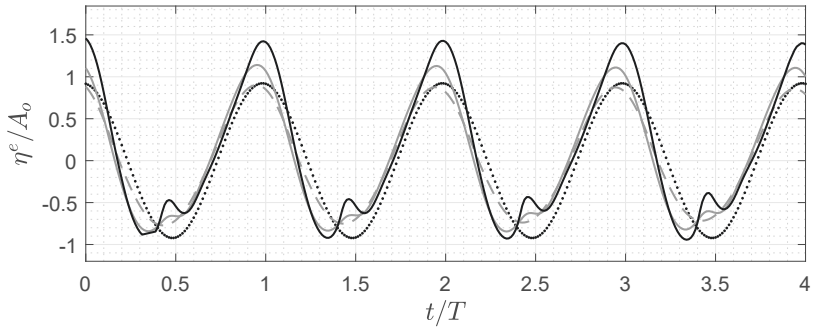

(B) $D/B = 0.435$ and $D/\lambda = 0.06$

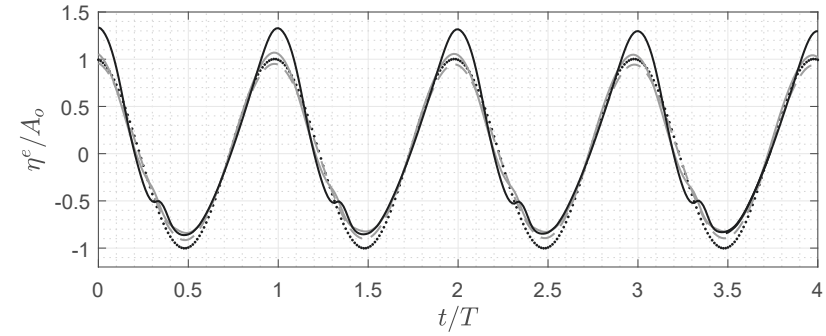

(C) $D/B = 0.15$ and $D/\lambda = 0.02$

Figure 5.6: Time-histories of the normalised near-field scattered wave elevations, $\eta^e(t)/A_o$, due to the wave excitations of varying steepness $A_o k$: 0.03 [— —], 0.1 [——] and 0.2 [——] for various aspect ratios (D/B) and relative diameters (D/λ) with comparisons to the linear potential solution [· · · ·].

Interestingly, with $A_o k$ held constant, the high-frequency scattered waves appear larger for $D/\lambda = 0.06$. Moreover, the phasing of the high-frequency elevations occurs earlier for $D/\lambda = 0.02$. These results confirm that the high-frequency scattered wave elevations are dependent on both the relative diameter, D/λ, and the incident wave steepness, $A_o k$.

These fndings are consistent with the laboratory observations of Masterton (2007),

and the numerical calculations of Swan & Sheikh (2015) and Kasiman (2017). These studies concerned bottom-mounted columns and argued that the high-frequency scattered wave elevation was associated with the motion of water around the circumference of the column. Specifically, they referred to the evolution of a non-concentric Type-2 scattered wave. Given that these effects appear identical to the present study, it is concluded that the high-frequency scattered waves shown in Figures 5.6(B) and (C), correspond to the arrival of the Type-2 scattered wave on the front face of the OWC. Indeed, this arrival is confirmed from Figure 5.7(A), and the appearance of the Type-2 wave is similar to that observed by Masterton (2007) (see Figure 5.7(B)).

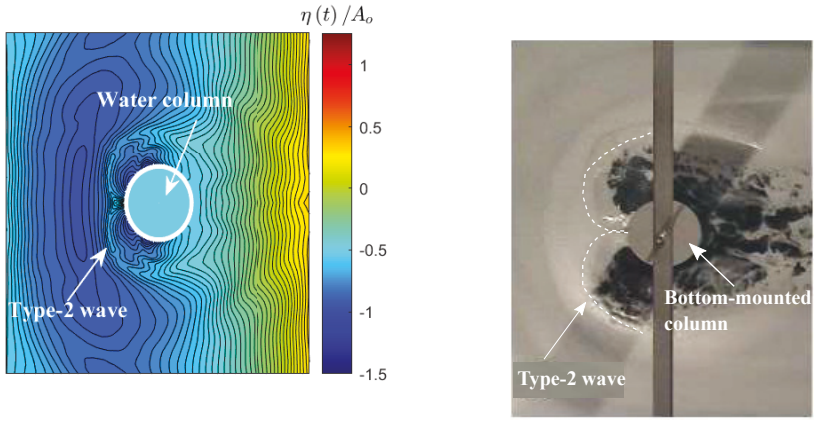

(A) (B)

FIGURE 5.7: Plan view of the surface elevation field showing the arrival of Type-2 wave on the front face of (A) the OWC and (B) the bottom-mounted column (Masterton, 2007).

5.5 Quantification of depth-varying inline pressures

The present objective is to investigate whether the high-frequency scattered wave elevations provoke nonlinearities or high harmonics in the vertical forcing of the OWC. The influence of the nonlinear scattered waves on the vertical excitation force has been studied by both Rodriguez (2016) and Bruggemann (2017); the former considering a heaving box and the latter a heaving truncated cylinder. In the case of the heaving box, the second-harmonic pressure was near-constant with depth and thus significantly influences the excitation force. In contrast, in the case of the heaving truncated cylinder, the second-harmonic pressure was strongly depth-dependent due to the curvature of the scattered wave field. As such, they had limited influence on the heaving force. However, both of these studies concerned large relative

diameters. In the case of small relative diameters, Masterton (2007) confirmed the presence of high-frequency inline forces experienced by a bottom-mounted cylinder, arguing that they were linked to structural 'ringing'. Kasiman (2017) was the first to show that the high-frequency scattered waves were the cause of the high harmonic inline forcing. The high harmonics that arise from the scattered wave elevation provoke the high harmonics in the inline force (Kasiman, 2017). Adopting these earlier considerations, the depth dependence of the high harmonics of the inline (or x-component) pressures acting on the OWCs will be evaluated.

At any depth location, the time-varying inline force, $F_H(z,t)$, acting on a projected area, A_p, of the cylindrical surface of an OWC was quantified as follows:

$$F_H\left(z,t\right) = \int_z^{z+\Delta h} \int_\pi^{2\pi} p\left(b_o,\theta,z,t\right) b_o \cos\theta \, d\theta \, dz, \tag{5.1}$$

where (r,θ,z) defines the usual cylindrical co-ordinates, $r = b_o$ the outer radius of the OWC, and the limits of the integration reflect the half cylinder modelled within the calculation. This inline force, F_H, was normalised by the projected area, $A_p = b_o \Delta h$, to compute the effective inline pressure. This computation was undertaken at varying depth locations to evaluate the depth-varying profile of the inline pressure. Figure 5.8(A) depicts a projected area, A_p, on the horizontally projected surface of the OWC; the surface being indicated by the grey rectangle on this figure. The sectional height of the projected area is set to $\Delta h = 0.035B$. In addition, the magnitude of the inline pressure, $F_{H,o}/A_p$, was normalised by $\rho g A_o$ to investigate its dependence on the incident wave amplitude, A_o.

Figure 5.8(B) defines the first three harmonic components of the normalised magnitude of the inline pressure, $F_{H,o}/\rho g A_p A_o$, based upon the undisturbed wave field. These cover the full draft of the water column. Clearly, with the increasing harmonic order, the value of $F_{H,o}/\rho g A_p A_o$ reduces significantly. With the structure present within the wave field, the value of $F_{H,o}/\rho g A_p A_o$ predicted by the linear potential solution is shown in Figure 5.8(C). Within this figure, the pressure due to the linear scattered wave is non-zero over the entire draft. Nevertheless, it shows a marked reduction with depth. Furthermore, the contribution of the incident wave on the pressure arising from the linear scattered wave is significant; the expectation being that the contribution from the high-harmonics of the incident wave will be small (Figure 5.8(B)).

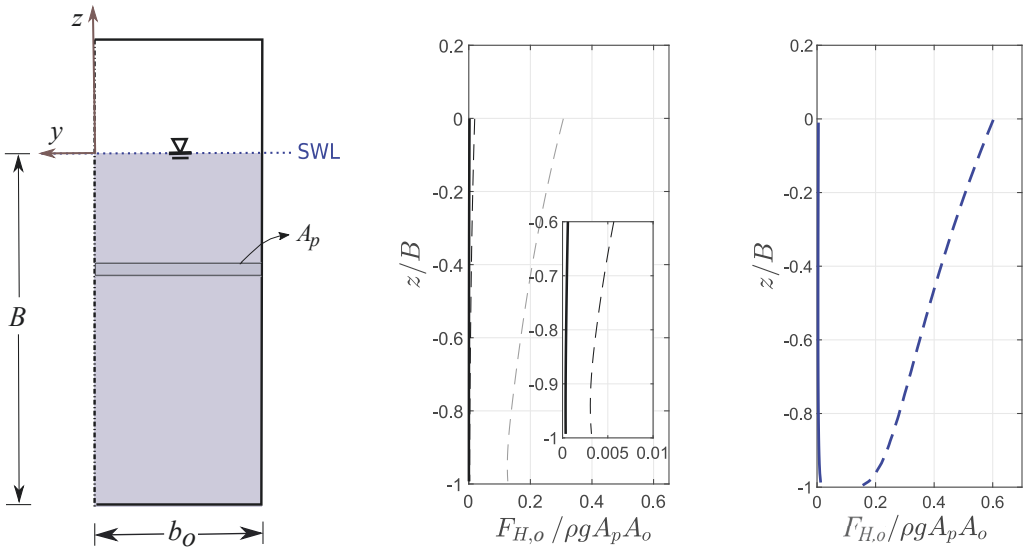

(A) (B) (C)

Figure 5.8: (A) Horizontally projected surface of an OWC and a projected area, A_p (B) depth-varying inline-pressure magnitudes, $F_{H,o}/\rho g A_p A_o$, arising from the first- [— —], second- [— —] and the third-order [——] incident wave pressures, and (C) $F_{H,o}/\rho g A_p A_o$ arising from the scattered [— —] and the radiated waves [——] computed from the linear potential solutions.

5.6 Effect of nonlinear scattered wave

In order to investigate the nonlinearities in the normalised inline pressure at a specific location, the projected areas are now classified into three different zones. Figure 5.9(A) shows that zone A covers the crest-trough region and zones B and C those areas where the column surface is continuously submerged. The sectional heights in the last two zones are also set to $\Delta h = 0.035B$. Figure 5.9 presents the time-histories of the normalised inline-pressures, $F_H(t)/\rho g A_p A_o$, acting in zones A, B and C; the data in this figure corresponding to the scattered wave elevations given in Figure 5.6(B). Figure 5.9(B) clearly exhibits a secondary loading cycle that can be accurately reconstructed by summing the first three-harmonic components of the pressure in zone A. Immediately below the wave trough (in area B-1), the high-frequency of the secondary loading cycle is clearly apparent (Figure 5.9(C)). As expected, this coincides with the phase of the high-frequencies identified in the scattered elevation (Figures 5.6(B)); both being explained by the arrival of the Type-2 scattered wave at the front face of the cylinder.

Importantly, Figure 5.9(C) also confirms that the existence of the secondary loading cycle and other nonlinear features, rapidly diminish with depth. For example,

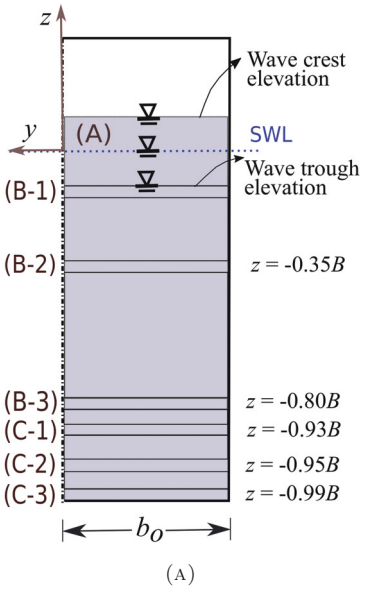

(A)

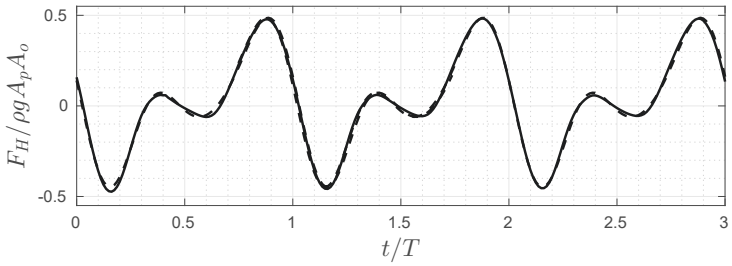

(B) Zone A

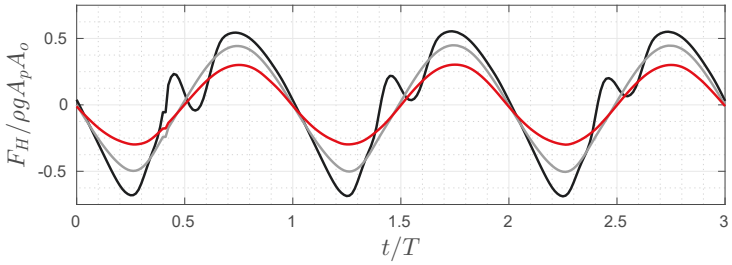

(C) Areas B-1, B-2, and B-3

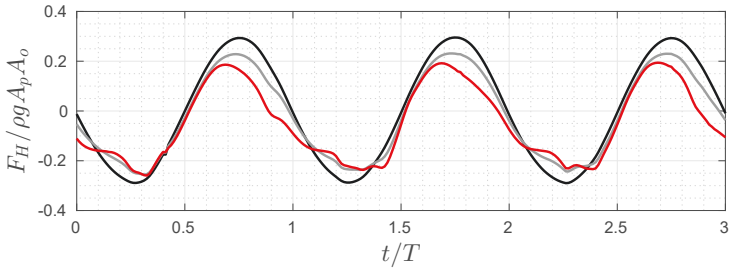

(D) Areas C-1, C-2, and C-3

Figure 5.9: (A) Projected areas and their average depth locations, and (B)-(D) time-varying normalised inline-pressures, $F_H(t)/\rho g A_p A_o$, on depth-varying areas: A [——], B-1 [——], B-2 [——], B-3 [——], and C-1 [——], C-2 [——], C-3 [——]. The inline force applied to zone A is compared with the force reconstructed from the summation of the 1^{st}, 2^{nd} and 3^{rd} harmonic components [– – –].

at $z/B = -0.8$ (area B-3), the time-history of the normalised inline-pressure is symmetrical and exhibits no secondary loading cycle. This suggests that the Type-2 scattered waves have little or no effect on the pressure on the lowest areas, where the vertical force F_v acts. This is in agreement with Kasiman (2017), who confirms that the high harmonics originating from the Type-2 scattered wave contributes a point load acting near the free-surface. However, the time-histories of the normalised pressures acting on the deeper areas ($z/B < -0.8$ in zone C on Figure 5.9(C)), indicate the occurence of different high-harmonic components. With the absence of a clear secondary loading cycle, the suggestion is that these changes are caused by a

different mechanism.

To further explore these effects, the depth-variation of the harmonic components of the inline pressures are evaluated in Figure 5.10. In undertaking this analysis, the magnitudes of the first three harmonic components of the inline force, $F_o^{(1)}$, $F_o^{(2)}$ and $F_o^{(3)}$, were estimated. The remaining higher-harmonics were all included in the higher-harmonic force component, $F_o^{(HO)}$; the latter computed as the difference between the inline force and the summation of the first three harmonics. Again, all the harmonic components are normalised by $F_s = \rho g A_p A_o$.

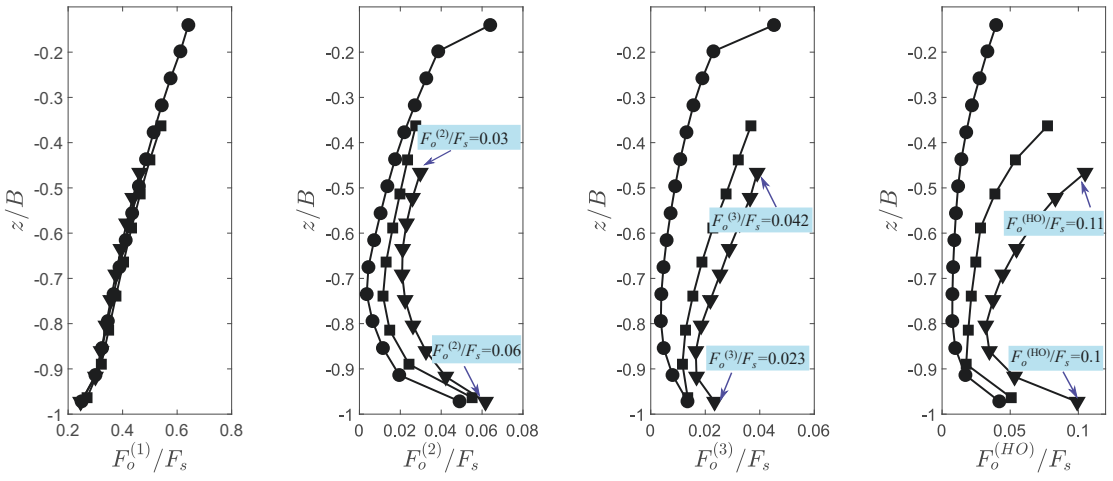

(A) (B) (C) (D)

Figure 5.10: The depth-variation in the harmonic components of the normalised inline-pressures: (A) $F_o^{(1)}/F_s$, (B) $F_o^{(2)}/F_s$, (C) $F_o^{(3)}/F_s$ and (D)$F_o^{(HO)}/F_s$ under three different wave-steepness conditions $A_o k$: 0.1 [−•−], 0.2 [−■−] and 0.3 [−▼−].

Figure 5.10 presents the depth-varying harmonic components of the normalised inline-pressures associated with incident waves of steepness $A_o k = 0.1, 0.2$ and 0.3. In all $A_o k$ cases, the first-harmonic component, $F_o^{(1)}/F_s$, dominates the normalised inline-pressure. Interestingly, the values of $F_o^{(2)}/F_s, F_o^{(3)}/F_s$ and $F_o^{(HO)}/F_s$ near the external free-surface, do not converge with the increasing harmonic order when $A_o k \geq 0.2$; evidence of this is given in Figures 5.10(B),(C) and (D). The earlier studies undertaken by Masterton (2007) and Kasiman (2017) also reported 'non-convergent' conditions in their studies. Indeed, they attributed this condition to the presence of the Type-2 scattered waves. Given that these waves were also observed in the present study, and both the D/λ and $A_o k$ values under consideration are close to those studied earlier, the results given in Figure 5.10 appear reasonable. Nevertheless,

these high harmonics make no contribution to the pressure at the bottom edge. This is confirmed by the profiles of $F_o^{(2)}/F_s$, $F_o^{(3)}/F_s$ and $F_o^{(HO)}/F_s$; each of which exhibits an exponential decay with depth below the wave trough. At greater depths, close to the mouth of the OWC, the presence of the higher harmonics again increases. It will be shown in subsequent sections that this is due to an entirely different effect.

5.7 Observations of nonlinear responses

5.7.1 Nonlinear response characteristics

The internal water surface elevations, η^i, within the OWCs are presented in Figure 5.11; the data being normalised by the incident wave amplitude, η^i/A_o. Once again, the time base has been shifted as described in Section 5.4. This data confirms that the high-frequency effects observed in the near-field scattered wave elevations do not appear in the internal surface elevations. This suggests that the responses of the water columns, η^i, are not influenced by the high harmonics in the near-field scattered wave elevations. This is consistent with the arguments outlined at the end of Section 5.6.

Nevertheless, nonlinearities do play a role in the internal surface elevations. This is supported by comparisons between the η^i elevations predicted by the linear potential theory and the viscous flow solver in Figure 5.11. To achieve these comparisons, the linear potential solutions have been scaled to appear on the same axis with the viscous flow solutions. Evidently, the linear potential solution over-estimates the normalised amplitude of the internal surface elevation, η_o^i/A_o, for each case of D/B and A_ok; the largest discrepancy occuring in the case of $D/B = 0.435$. Furthermore, the characteristics of the internal surface elevations indicate the existence of the nonlinearities. Three effects warrant particular attention:

(i) The η_o^i/A_o value, also referred to as the response amplitude operator or RAO, progressively decreases with increasing A_ok,

(ii) The progressively varying phase of η^i relative to the incident wave elevation at the centre of the water column, and

(iii) The asymmetry of η^i.

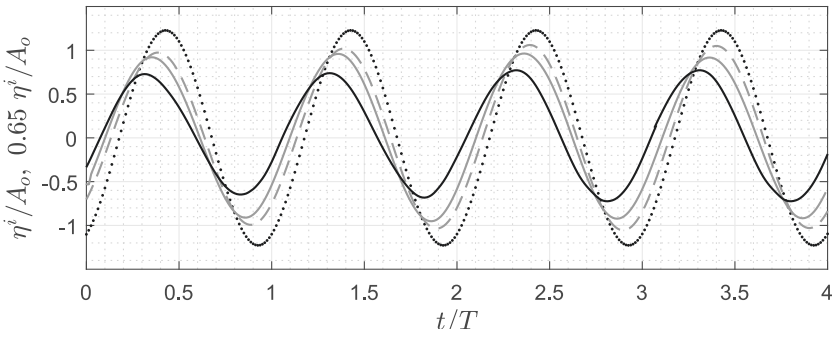

(A) $D/B = 1.25$, and $D/\lambda = 0.17$

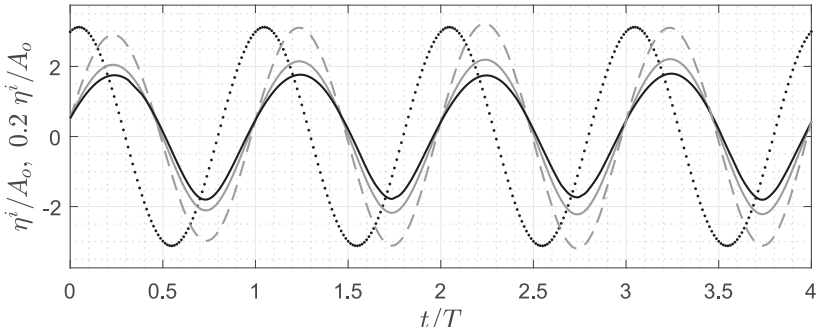

(B) $D/B = 0.435$, and $D/\lambda = 0.06$

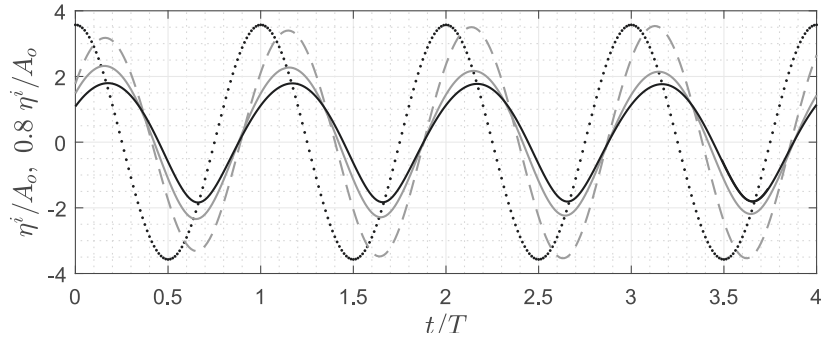

(C) $D/B = 0.15$, and $D/\lambda = 0.02$

FIGURE 5.11: Time-histories of the normalised internal water surface elevations, $\eta^i(t)/A_o$, for varying diameters, D/B, due to the wave excitations of varying incident wave steepness $A_o k$: 0.03 [— —], 0.1 [——] and 0.2 [——] compared with the linear potential solutions [· · · ·] scaled to appear on the same axis.

An example of point (i) is indicated by the red arrows on Figure 5.12(A). This shows a close-up view of η^i for $D/B = 1.25$. The value of η^i_o/A_o predicted from the viscous flow solution is approximately equal to one for linear incident waves ($A_o k = 0.03$). As $A_o k$ increases, the η^i_o/A_o value progressively decreases. This characteristic is evident from all cases shown on Figure 5.11.

Point (ii) is indicated by the blue arrows on Figure 5.12(A). This characteristic

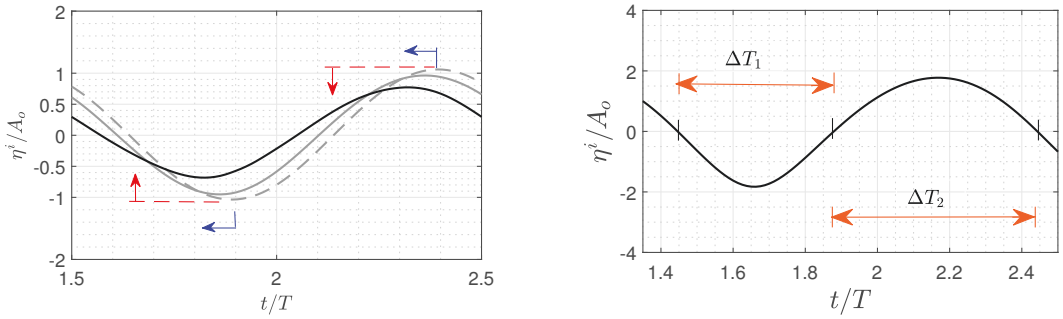

(A) (B)

Figure 5.12: Close-up views of the time-histories of $\eta^i(t)/A_o$ that indicate: (A) the progressively decreasing η_o^i/A_o (Red) and the progressively varying response phase shift (Blue) taken from the case of $D/B = 1.25$, and (B) the response asymmetry (Orange) taken from the case of $D/B = 0.15$ due to the wave excitations of various $A_o k$: 0.03 [– –], 0.1 [——] and 0.2 [——].

will subsequently be referred to as the progressively varying response phase difference. Figure 5.12(A) confirms that this progressively decreases as $A_o k$ increases. Conversely, it remains almost constant for $D/B = 0.435$, and progressively increases when $D/B = 0.15$ (Figures 5.11(B) and 5.11(C)).

Finally, point (iii) is demonstrated in Figure 5.12(B). The response asymmetry observed in η^i can be identified from the zero-crossing periods. Clearly, the values of ΔT_1 and ΔT_2 for the negative and positive η^i are not equal. The data presented in Figure **??** suggests that varying degrees of asymmetry occur in all cases.

5.7.2 Excitation condition and response phase difference

Prior to discussing the three nonlinear characteristics of η^i, the relationship between the excitation condition applied to an OWC and the response phase difference is discussed. Previously, Figure 5.11 confirmed that the response phase differences in a potential flow for $D/B = 1.25$ and 0.15 are approximately 180° and 0°, respectively. For $D/B = 0.435$, this variable is slightly larger than 0°. An explanation for this variation with the aspect ratio (D/B) is provided in Figure 5.13. This reveals the dimensionless frequencies, $\omega^2 B/g$, at which the theoretical peak values of η_o^i/A_o arise for the three D/B values. The dimensionless frequency value for each case corresponds to the so-called undamped natural frequency, ω_{nd}, for that case. In fact, this figure confirms the shift of $\omega_{nd}^2 B/g$ from the dimensionless piston natural frequency; the latter computed as $\omega_n^2 B/g = 1$. The shift relates to the average mass

of the water column since the departure of ω_{nd} from ω_n increases with diameter.

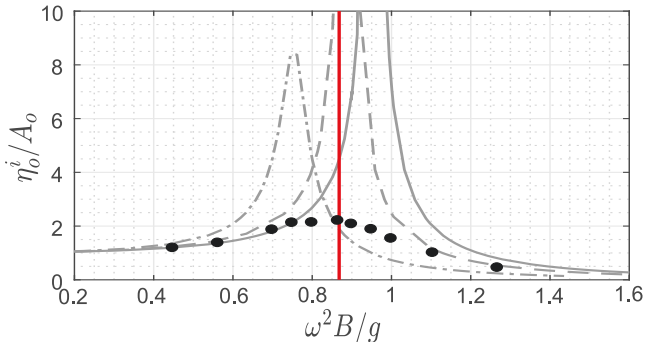

Figure 5.13: Response amplitude operators, η_o^i/A_o, for three OWCs with D/B : 1.25 [— · —], 0.435 [— —] and 0.15 [——] as a function of incident wave frequency, ω, predicted by the linear potential flow solver (for all cases) and computed by the viscous solver (for $D/B = 0.435$ [•]) under the weakly-nonlinear incident wave conditions ($A_o k = 0.1$); the incident wave frequency ω being indicated by [——].

Figure 5.13 also confirms the changes in the position of the undamped natural frequency, ω_{nd}, relative to the excitation frequency, ω; the latter being associated with the incident wave frequency in a wave excitation problem. This, in turn, alters the excitation condition and the response phase difference of the water column. Within these examples, the excitation frequency is $\omega^2 B/g = 0.87$, as indicated by the red line on Figure 5.13. With $\omega_{nd}^2 B/g = 0.76$, 0.89 and 0.96 for the three cylinder sizes ($D/B = 1.25, 0.435$ and 0.15), the largest diameter is under a high-frequency excitation, whereas the smallest cylinder ($D/B = 0.15$) is subject to a low-frequency excitation. In contrast, the ω_{nd} value for the middle-sized column lies close to, but is still larger than, the excitation frequency. This column has the largest analytically predicted responses as noted on Figure 5.11(b).

In a viscous flow, the damped natural frequency, ω_d, deviates from the undamped natural frequency, ω_{nd}. This deviation is clear from the OWC with $D/B = 0.435$; Figure 5.13 showing that the frequency at which the peak value of η_o^i/A_o is identified from the viscous flow solution is very close to the excitation frequency. This implies that this OWC is under a near-resonant condition in the viscous flow, and the response phase difference is now 90°; evidence for the latter seen from Figure 5.11(b). Furthermore, the fact that ω_d reduces from the ω_{nd} is consistent with the earlier laboratory and numerical studies by Morris-Thomas MT & Thiagarajan (2006) and Zhang et al. (2012). Indeed, comparisons between the analytical and the actual

hydrodynamic efficiencies confirm the reduced resonant frequency of an OWC in a viscous flow. This reduction is due to the hydrodynamic damping which, in turn, changes the excitation condition.

5.8 Physical origins of nonlinearities in motions

5.8.1 Progressively varying RAO and response phase difference

The phase difference in the response of an OWC driven by an oscillating air pressure progressively varies with the amplitude of the air pressure. The cases of FAPT 1 outlined in Table 5.2 confirm this. In these tests, the air pressures were computed as $p = -P_o \sin \omega_f t$, the cylinder diameter was fixed at $D/B = 0.435$, and the forcing frequencies were set to three different values: $\omega_f^2 B/g = 1.11, 0.87$ and 0.71. These values correspond to a high-frequency, a resonant and a low-frequency excitation respectively. Furthermore, the amplitude of the air pressure, P_o, defined by $\rho g A_o^P$, varies for each frequency case; A_o^P being analogous to a "static" displacement. A normalisation of the internal surface amplitude by this static displacement, η_o^i/A_o^P, estimates the response amplitude operator of the OWC.

Figure 5.14 provides the time-histories of the normalised air pressure, $p\left(t\right)/A_o^P$, and normalised internal surface elevations, $\eta^i\left(t\right)/A_o^P$. Within this figure, only the "steady-state" or developed motion of the internal free-surface are presented. In respect of the response amplitude, it is evident that the η_o^i/A_o^P value progressively reduces with the P_o value in all excitation conditions. In addition, the response phase difference relative to the sinusoidally fluctuating air pressure is notably different in the three excitation cases. In the high-frequency excitation, the phase difference progressively decreases with the air pressure amplitude (Figure 5.14(B)). Conversely, the phase difference in the resonant case is relatively invariant (Figure 5.14(C)), while in the low-frequency excitation it progressively increases (Figure 5.14(D)).

Comparisons between Figures 5.14 and 5.11 reveal identical trends in the response under the forced air pressure oscillations and regular wave excitations. Irrespective of the excitation mechanism, the response phase difference progressively varies, and the RAO value progressively decreases. This behaviour is typically observed in the harmonic response of a viscously damped system subjected to an excitation force. This leads to two conclusions: (i) the changes in the response phase difference are

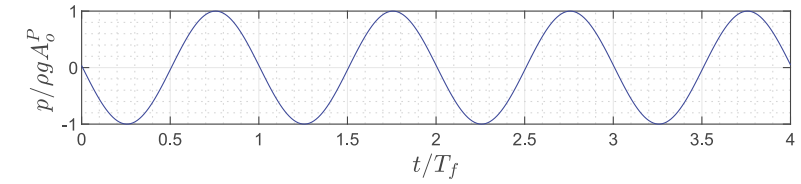

(A) p

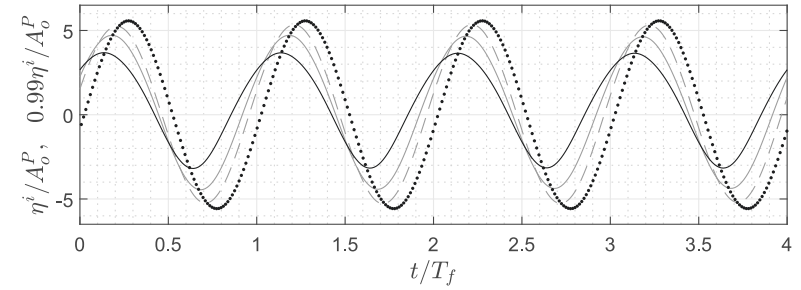

(B) $\omega_f^2 B/g = 1.11$

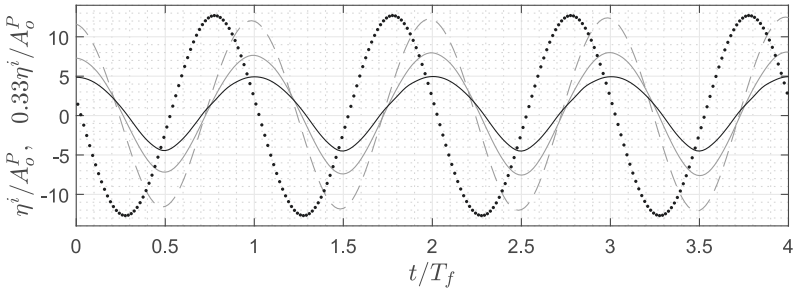

(C) $\omega_f^2 B/g = 0.87$

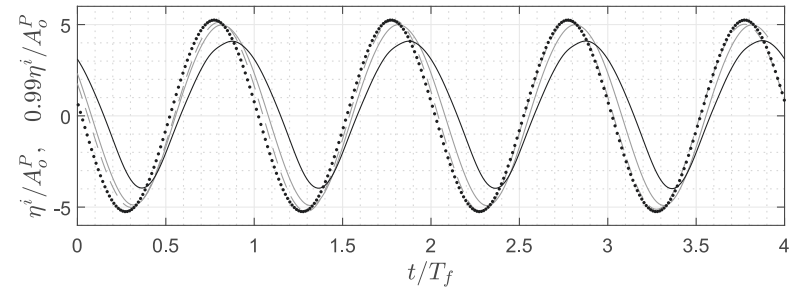

(D) $\omega_f^2 B/g = 0.71$

Figure 5.14: Time-histories of the normalised air pressure, $p\left(t\right)/\rho g A_o^P$ [——], and normalised internal surface elevations, $\eta^i\left(t\right)/A_o^P$, undergoing forced oscillations at varying forcing frequencies, $\omega_f^2 B/g$, and air pressure amplitudes, $P_o/\rho g = A_o^P$: 0.0016 m [— —], 0.005 m [——] and 0.017 m [——] compared with the linear potential solutions [· · · ·] scaled to appear on the same axis.

solely dependent on the excitation condition, and (ii) the response phase difference and the response amplitude operator are dependent on the amplitude of the forcing, either air pressure or incident wave. The physical cause of point (ii) is associated with the increased damping in the OWC.

5.8.2 Response asymmetry

The mass of the water column continuously varies with time, unlike the mass of an oscillating solid body. This varying mass is represented by a nonlinearity in the inertia force which may be the cause of the response asymmetry. To confirm this, the validity of three different descriptions of the water column are evaluated as follows:

(i) A fully nonlinear system as represented by Equation (2.37),

(ii) A partially nonlinear system with linear inertia and nonlinear damping:

$$[\rho A_c B + A_m]\,\ddot{\eta}^i + b_1 A_c \dot{\eta}^i + \frac{1}{2} b_2 \rho A_c \dot{\eta}^i |\dot{\eta}^i| + \rho g A_c \eta^i = F_t. \tag{5.2}$$

(iii) A partially nonlinear system with nonlinear inertia and linear damping:

$$\left[\rho A_c (B + \eta^i) + A_m\right] \ddot{\eta}^i + b_1 A_c \dot{\eta}^i + \frac{1}{2} b_2 \rho A_c \dot{\eta}^i + \rho g A_c \eta^i + \frac{1}{2} \rho A_c \dot{\eta^i}^2 = F_t, \tag{5.3}$$

where $F_t = pA_c$ is the excitation force that acts on the water column in a forced oscillation test.

As a first step, the curve-fitting solver within Matlab, *lsqcurvefit*, was applied to the viscous solution to estimate the hydrodynamic coefficients: the added mass, A_m, and the nonlinear damping coefficient, b_2. By implementing these hydrodynamic coefficients and solving the equations noted above, the internal surface elevation was re-simulated. In each case, an *ODE 45* solver within Matlab was applied. The re-simulated surface elevation is compared with the computation from the initial viscous flow solver to investigate the validity of each system.

Figure 5.15 presents the comparisons of the internal surface elevations arising from forced air pressure oscillations. The air pressure amplitudes were prescribed such that the response amplitude numbers, η_o^i/B, were 0.25 and 0.5. Clearly, Figure 5.15 shows that the surface elevations re-simulated from the fully nonlinear system (i) are in excellent agreement with the computed elevations. In contrast, the re-simulation using the linear inertia system (ii) produces a small deviation from the computed elevation for $\eta_o^i/B = 0.25$, and a marked discrepancy for $\eta_o^i/B = 0.5$. The discrepancy is indicated by the equal zero-crossing periods (up-crossing and down-crossing) of the re-simulated elevation. Interestingly, the linear damping and nonlinear inertia system (iii) and the fully nonlinear system (i) predict identical elevations.

Evidently, the nonlinear inertia force is responsible for the response asymmetry. A linear inertia system is accurate only when $\eta_o^i \ll B$.

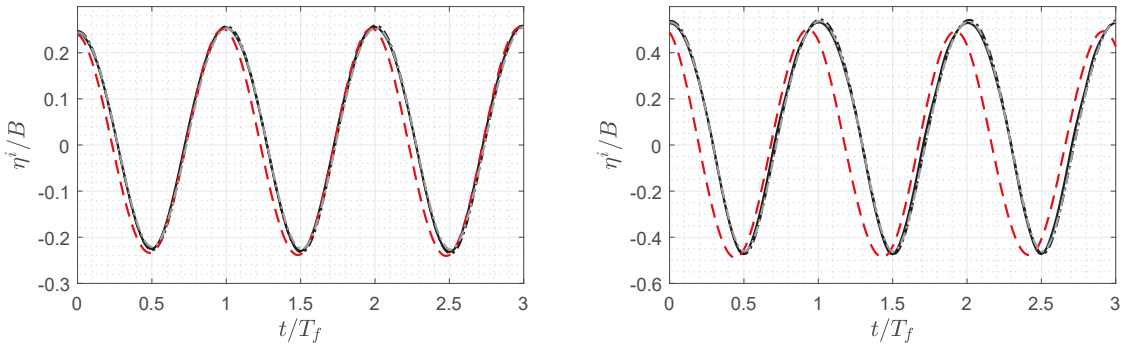

(A) $\eta_o^i/B = 0.25$ (B) $\eta_o^i/B = 0.5$

Figure 5.15: The internal surface elevations, η^i, computed by the viscous flow solver [——] and re-simulated using the mathematical formulations for: (i) a fully nonlinear system [— · —], (ii) a linear inertia and nonlinear damping system [— —], and (iii) a nonlinear inertia and linear damping system [— · —] due to the air pressure amplitudes of $P_o/\rho g$: (A) 0.005 m and (B) 0.017 m.

To further explore this response asymmetry, OWCs with different mouth shapes undergoing forced air pressure oscillations and incident wave excitations were numerically modelled. The numerical models correspond to the FAPT 2-4 and RWT 3, 5, 6 described in Tables 5.2 and 5.1, respectively. The various shapes under consideration are the SE, SC and BS mouths. For each mouth shape, the air pressure amplitudes, P_o, and the incident wave steepness, $A_o k$, were varied such that the response amplitude numbers, η_o^i/B, of all the tests were comparable. Three values of $\eta_o^i/B = 0.25, 0.5$ and 0.75 were considered. The only exception concerned the regular wave tests in which the breaking limit (Mehaute, 1976) imposed a maximum of $\eta_o^i/B = 0.6$.

Figure 5.16 presents the time-histories of the internal surface elevations computed using all models. These elevations were shifted in time such that the maximum response of η^i/B occurs at $t = 0$. Once again, only the "steady-state" or developed elevations are presented. Comparing the individual sub-plots confirms that the response asymmetry increases with the amplitude of the internal surface-elevation, η_o^i. In addition, this suggests that the response asymmetry is independent of any vortex shedding; the latter being markedly different when flow passes a sharp-edged (SE) or a streamlined body (Troesch & Kim, 1991). Indeed, the absence of vortex generation near a BS mouth was previously indicated by the absence of any reduction of the

radiated wave amplitude for increasing forced oscillation (Section 4.5.2).

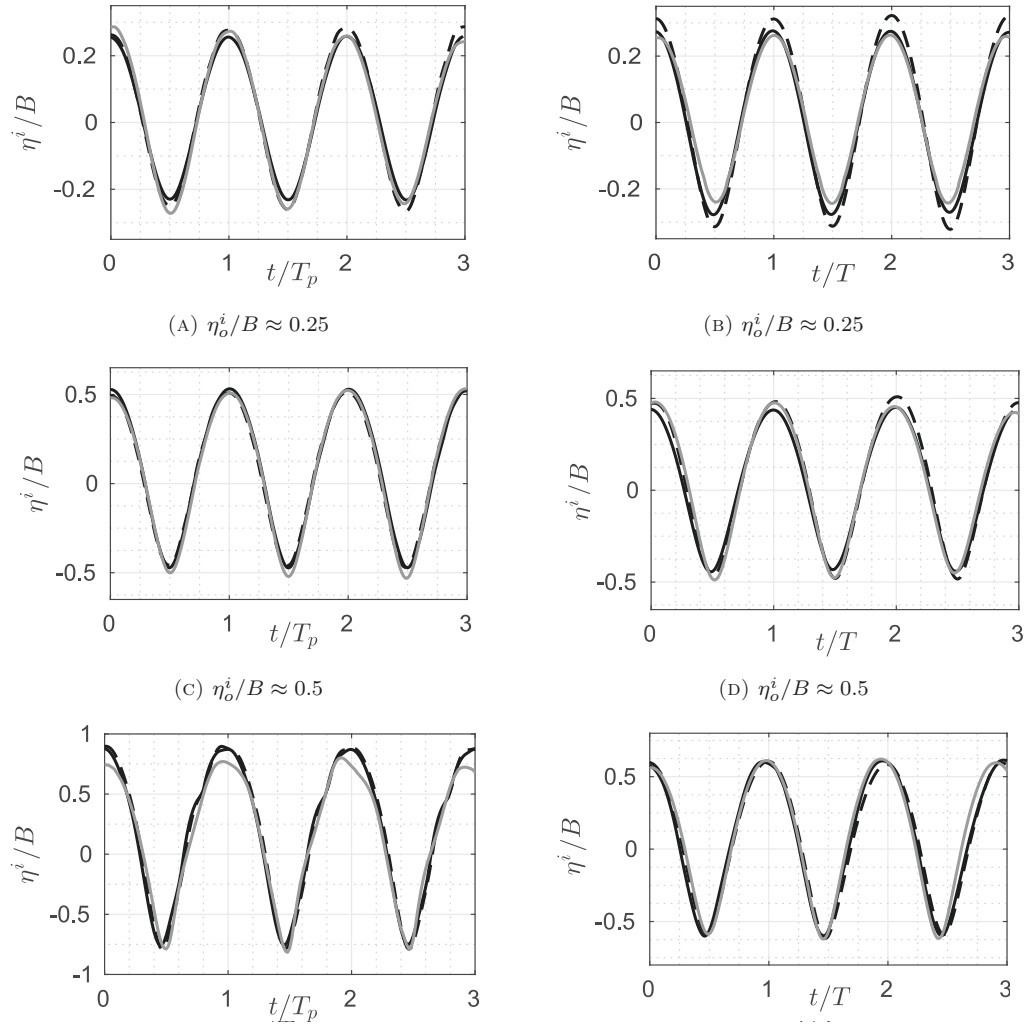

(A) $\eta_o^i/B \approx 0.25$ (B) $\eta_o^i/B \approx 0.25$

(C) $\eta_o^i/B \approx 0.5$ (D) $\eta_o^i/B \approx 0.5$

(E) $\eta_o^i/B \approx 0.75$ (F) $\eta_o^i/B \approx 0.6$

Figure 5.16: Time-varying internal surface elevations, $\eta^i(t)$, within OWCs with SE [——], SC [– –] and BS mouths [——] subjected to forced air pressure oscillations (the first column) and incident wave excitations (the second column) with various response amplitude numbers, η_o^i/B.

Further evidence of these effects is given in Figure 5.17. This contrasts the internal surface elevations, η^i, within three OWCs. These relate to SE mouths with $D/B = 0.435$ and 1.25, and a BS mouth with $D/B = 0.435$. In each case, the time-histories have been shifted so that $\eta^i(t) = 0$ at $t = 0$. Clearly, the response amplitudes, η_o^i, due to an incident wave of $A_o k = 0.2$ differ given the varying diameter and mouth shape. However, the response asymmetry becomes most pronounced for the largest η_o^i/B value. In these comparisons, this occurs in the BS mouth case. Confirmation of this nonlinear characteristic is indicated by the zero-crossing periods,

ΔT, in one oscillation. Taken together, Figures 5.16 and 5.17 confirm the importance of η_o^i/B number in determining the response asymmetry.

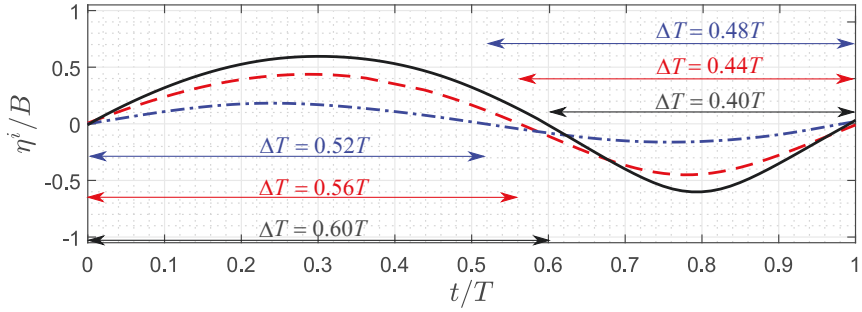

Figure 5.17: Time-histories of the internal surface elevations, $\eta^i(t)$, within OWCs with SE mouths and $D/B = 0.435$ (red) and 1.25 (blue) and a BS mouth with $D/B = 0.435$ (black).

Building on these results, the importance of the zeroth, $\eta_o^{i(0)}$, and the second harmonics, $\eta_o^{i(2)}$, on the response asymmetry is demonstrated by a harmonic reconstruction of an internal surface elevation. This was undertaken by progressively summing the first three harmonics of the elevation, as described on Figure 5.18. Specifically, Figure 5.18(A) shows that the zeroth and first harmonics do not represent the response asymmetry. In contrast, Figure 5.18(B) shows that while the second harmonic is critically important, the third harmonic is not. The arguments outlined thus far prove that neither vortex nor the nonlinear wave interactions with an OWC are responsible for the response asymmetry.

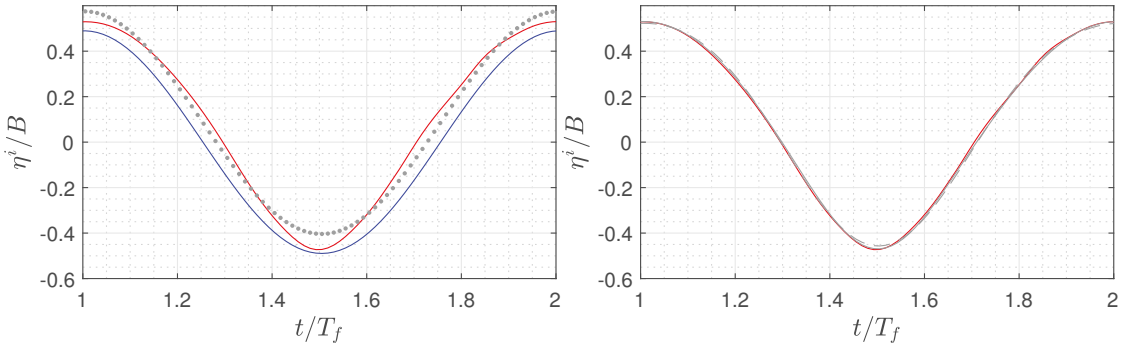

Figure 5.18: Time-varying internal surface elevation, $\eta^i(t)/B$ [——], approximated by (A) the 1^{st} [——], the sum of the 0^{th} and 1^{st} harmonics [· · ·], (B) the sum of the 0^{th}, 1^{st} and 2^{nd} [— —], and the 0^{th}, 1^{st}, 2^{nd} and 3^{rd} harmonics [——], for a FAPT with $\eta_o^i/B \approx 0.5$

5.9 Physical origins of nonlinearities in forces

The physical origins of the second- and higher-order harmonics in the forces acting at the bottom edge suggest a different effect. In seeking a physical explanation, the earlier variation of the mouth shape is re-considered. Figure 5.19 presents the depth-variation in the harmonic components of the normalised inline-pressures for OWCs with SE, SC and BS mouths. In each case, $D/B = 0.435$ and $A_o k = 0.1$.

In respect of the first-harmonic component, Figure 5.19(A) shows that the depth-varying profiles are independent of mouth shape, except at the bottom edge. The latter indicates that the inline pressure at the draft of the BS mouth increases because the lip radius effectively enlarges the diameter of the OWC. The explanation for this lies in the fact that the value of $F_o^{(1)}/F_s$ predicted from the linear potential solver increases with the diameter. For D/B ratios of 0.15, 0.435, and 1.25, these values at $z = -B$ are estimated to be 0.05, 0.15 and 0.48, respectively. The differences highlighted on Figure 5.19(A) are thus unrelated to any possible vortex effects.

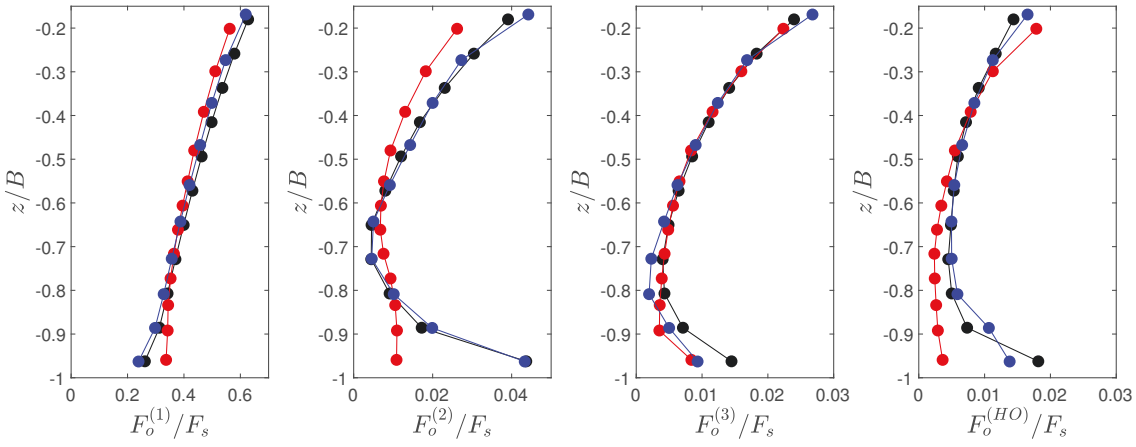

(A) (B) (C) (D)

FIGURE 5.19: The depth-variation in the harmonic components of the normalised inline-pressures: (A) $F_o^{(1)}/F_s$, (B) $F_o^{(2)}/F_s$, (C) $F_o^{(3)}/F_s$ and (D) $F_o^{(HO)}/F_s$ for three different mouth shapes: SE [–•–], SC [–•–] and BS [–•–].

A comparison of the second harmonic profiles shown in Figure 5.19(B), suggests a clear vortex effect; the data relating to the BS case being markedly different. The second harmonics of the normalised inline-pressures for the SE and SC mouth exhibit increasing amplitudes near the bottom edge. In contrast, the second harmonic amplitude associated with the BS mouth remains relatively invariant close to the

bottom edge. This trend is consistent with the higher-harmonic profiles observed in Figure 5.19(d), but is not replicated in the third harmonic profiles (Figure 5.19(c)).

In addition to the possible importance of the vortex motion, the water column oscillation may itself generate second-harmonic components in the pressure field. Previously, Figure 5.8(c) showed that the first harmonics of the normalised inline-pressure at varying depth locations was very small in a pure radiation flow. The pressure field generated by the water column oscillation may also contain second harmonics, with an axisymmetric distribution over the full draft of the water column. Indeed, the second harmonic of the normalised inline-pressure acting either on the projected upstream or downstream surface of the bell-mouthed OWC, has a depth-increasing profile near the bottom edge. This is observed in Figures 5.20(c) and (d). Indeed, the magnitudes of the pressures acting on these two surfaces, near the bottom edge, are approximately equal but opposite in sign. Evidence of this is given in Figure 5.21(a) which shows the time-varying second harmonics of the normalised inline-pressures, $F_H^{(2)}(t)/F_s$, on each surface (upstream and downstream) at $z = -B$. This explains why the second harmonics of the normalised inline-pressures computed for the whole surface, are relatively invariant near the bottom edge of the bell-mouthed OWC (Figure 5.19(b)). Conversely, the second harmonic profiles (Figures 5.20(c) and (d)) for the upstream and downstream surfaces of the semicircular-ended OWC, indicate a non-axisymmetric pressure distribution. Confirmation of this is given in Figure 5.21(b)). Clearly, these contrasting observations confirm that both the water column oscillation and vortex motion are responsible for generating the second harmonic of the pressure at $z = -B$.

5.10 Physical significance of force nonlinearities

5.10.1 Vertical force in a linear potential flow

To investigate the significance of the different sources of nonlinearity, the physical meaning of vertical force is sought from a linear potential flow computation. This is motivated by the fact that a pure radiation flow is well described by a linear potential solution; evidence for this having been provided in Sections 4.3.2 and 4.3.3.

In a forced oscillation test, the vertical force, acting perpendicular to the bottom cross-sectional area of the water column, physically represents the hydrodynamic

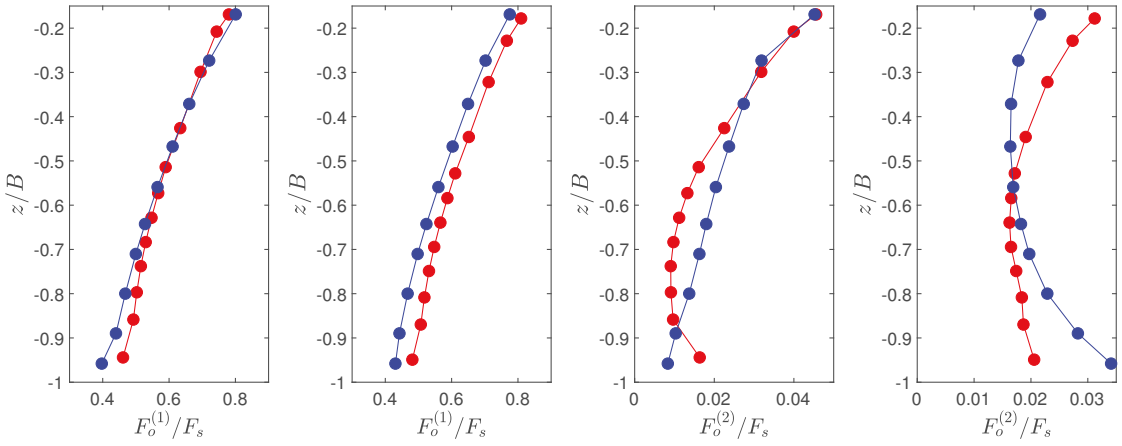

Figure 5.20: The depth-variation in the harmonic components of the normalised inline-pressures: $F_o^{(1)}/F_s$ and $F_o^{(2)}/F_s$ for the SC [–•–] and BS case [–•–]. The integration was conducted separately on the upstream (A)&(C) and downstream surfaces (B)&(D).

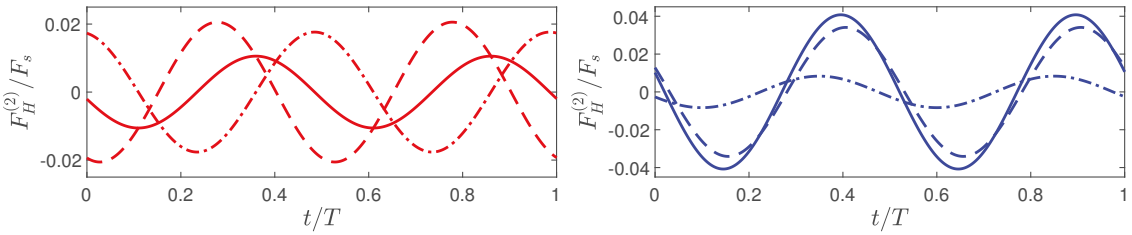

Figure 5.21: Time-histories of the second-harmonic normalised inline-pressures, $F_H^{(2)}(t)/F_s$, at $z=-B$ acting on the upstream [– · – , – · –] and downstream surface [– – , – –], and the summation of the two [—— , ——] for (A) the BS and (B) SC mouth.

force. In a linear potential flow, this can be estimated from the summation of the forces associated with the added mass and radiation damping. Figure 5.22 shows a good comparison between the vertical force, F_v, and the hydrodynamic force, F_r, in this potential flow. The mathematical formula that defines these two forces are given as follows:

$$F_v(t) = \mathrm{Re}\left[\rho\omega^2 (P_o/\rho g)\, e^{-i\omega t} \int_0^b \int_0^{2\pi} \phi_R(r,\theta,-B)\, r dr d\theta\right], \tag{5.4}$$

$$F_r(t) = \mathrm{Re}\left[\left(-A_m\omega^2 - i\omega b_1 A_c\right)(P_o/\rho g)\left(1-\omega^2/g\phi_R(0,0,0)\right) e^{-i\omega t}\right]. \tag{5.5}$$

Adopting these arguments, the vertical force under a forced oscillation test in a linear potential flow is simply associated with the oscillation of the water column.

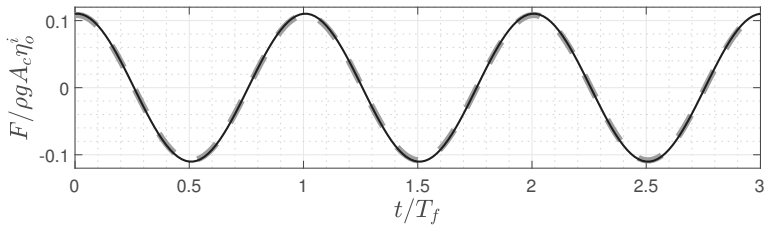

Figure 5.22: A comparison between the time-varying vertical force, $F_v(t)$ [——], and the hydrodynamic force, $F_r(t)$ [– –], acting on an OWC with $D/B = 0.435$ in a forced oscillation test; both forces were predicted from the linear potential theory.

5.10.2 Vertical force in a viscous flow

The linkage between the nonlinear characteristics of the vertical force and the flow field in a viscous flow is investigated to understand the relative importance of the nonlinearity sources. The vertical forces and the vorticity fields were computed from Forced Air Pressure Tests (FAPTs). The data presented herein corresponds to the responses shown earlier in Figure 5.16. Figures 5.23, 5.24 and 5.25 concern the OWCs with BS, SC and SE mouths, respectively. In each case, the first columns present the axisymmetric vorticity fields of ω_θ and their mirrored fields viewed on the $y = 0$ plane. Three different response amplitudes are considered ($\eta_o^i/B = 0.25$, 0.5 and 0.75); in each case the data relates to the condition when the internal free-surface is at its minimum elevation. Alongside each of these plots, the vertical force, F_v, experienced by the OWC is presented in its normalised form, $F_v/\rho g A_c \eta_o^i$.

The time-varying vertical forces experienced by the OWCs and the associated vorticity fields reveal two points.

(i) The high-frequency forcing (or secondary loading cycle) only exists when vortex shedding occurs, and

(ii) The force asymmetry, which could also be described as the response asymmetry, is observed for all mouth shapes.

Point (i) is confirmed in Figure 5.23; the secondary loading cycle being absent in the BS case. Indeed, these flows are considered irrotational, even at the largest response amplitude number of $\eta_o^i/B = 0.75$. In respect of point (ii), the evidence is seen even when vortices are shed near the SE and SC mouths (Figures 5.24 and 5.25). The force asymmetry is indicated by the unequal zero-crossing periods for the positive and negative F_v.

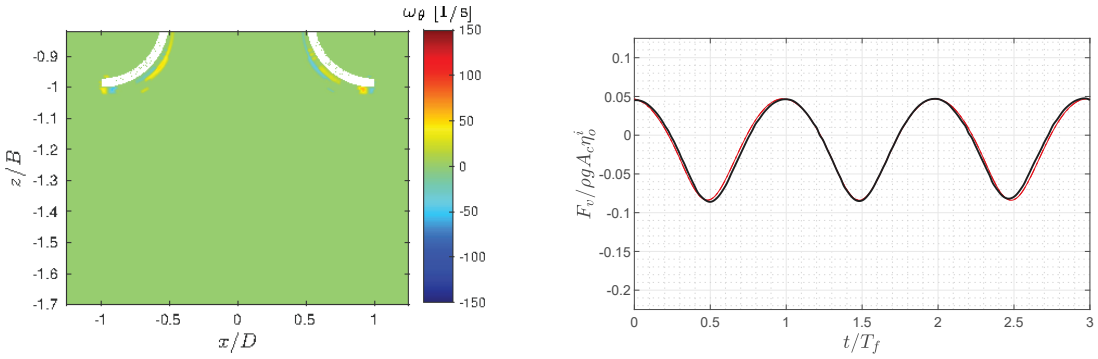

(A) $\eta_o^i/B = 0.25$

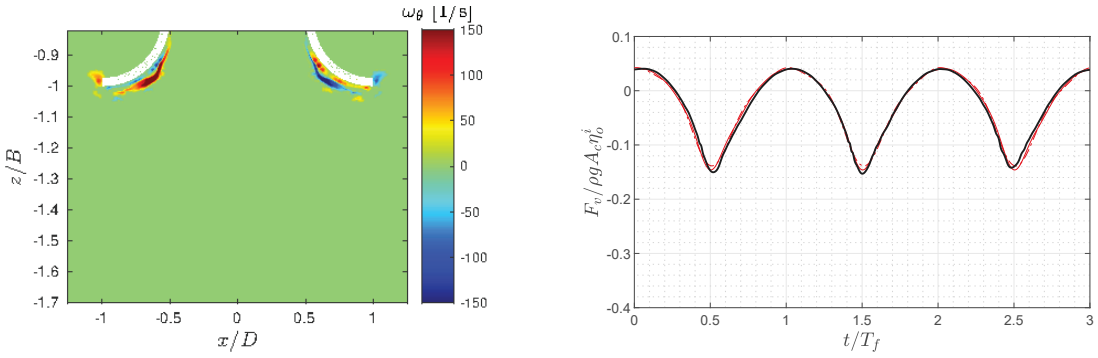

(B) $\eta_o^i/B = 0.5$

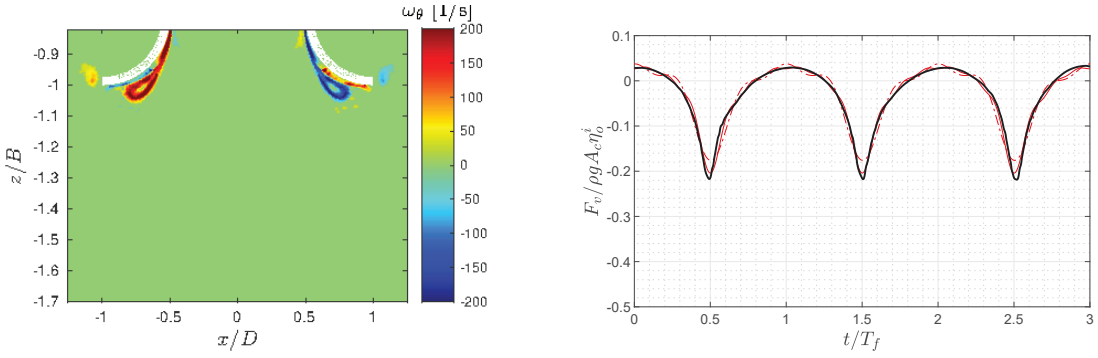

(C) $\eta_o^i/B = 0.75$

FIGURE 5.23: The vorticity fields of ω_θ located around a BS mouth undergoing forced oscillations and the associated time-varying vertical forces, $F_v(t)$ [——], approximated by the first three [— · —] and six [——] harmonic components.

To further investigate point (i), data relating to the SC and SE mouths is closely observed. Their corresponding forces exhibit secondary loading cycles when $\eta_o^i/B = 0.25$ (Figures 5.24(A) and 5.25(A)). These are periodic and only apparent during the downward displacement of the water column; the latter corresponding to the occurence of vortex shedding. The linkage between the vortex shedding and those cycles is confirmed using the pressure field computed at $z = -B$.

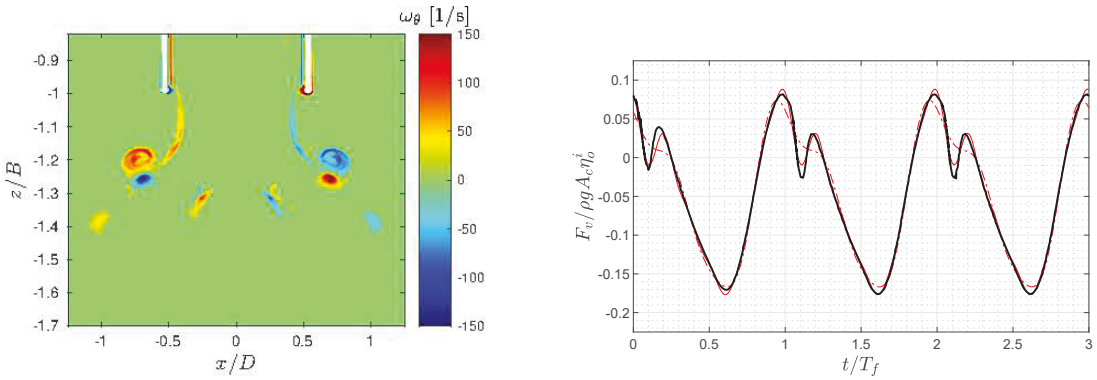

(A) $\eta_o^i/B = 0.25$

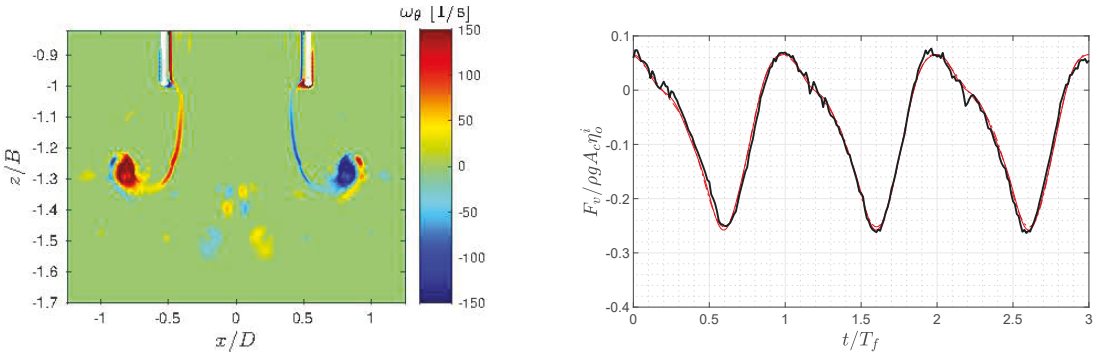

(B) $\eta_o^i/B = 0.5$

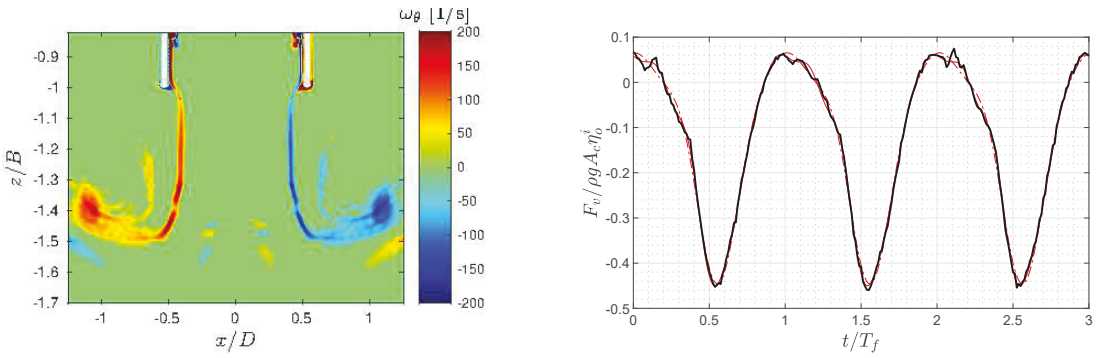

(C) $\eta_o^i/B = 0.75$

Figure 5.24: The vorticity fields of ω_θ located around a SC mouth undergoing forced oscillations and the associated time-varying vertical forces, $F_v(t)$ [——], approximated by the first three [— · —] and six [——] harmonic components.

A schematic showing an $x-y$ plane of the SE mouth at $z=-B$ and its unit outward normal vector is illustrated in Figure 5.26(A). Plan views describing the evolution of the pressure contours on this plane are provided on Figures 5.26(B)-(E). When the water column begins to move from its maximum elevation at $t=0$, the vertical force is predominantly driven by the water column. Evidence of this is seen

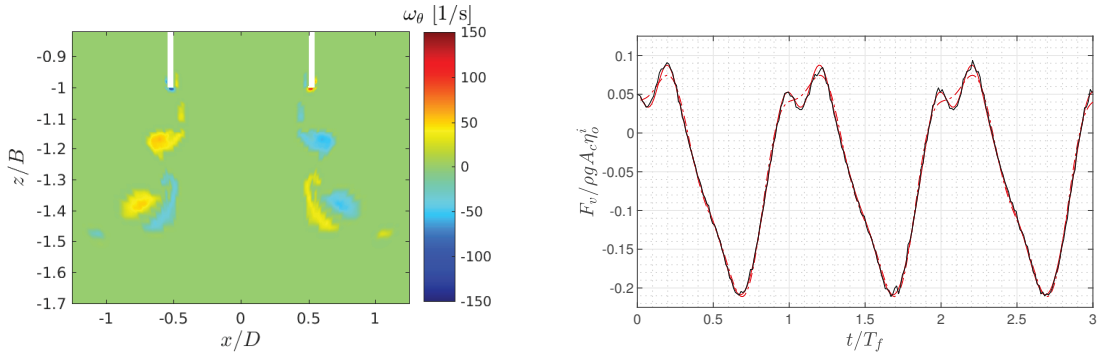

(A) $\eta_o^i/B = 0.25$

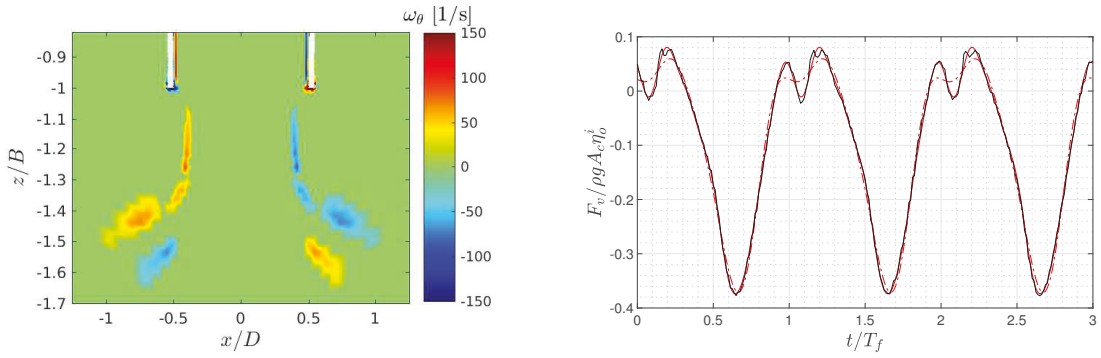

(B) $\eta_o^i/B = 0.5$

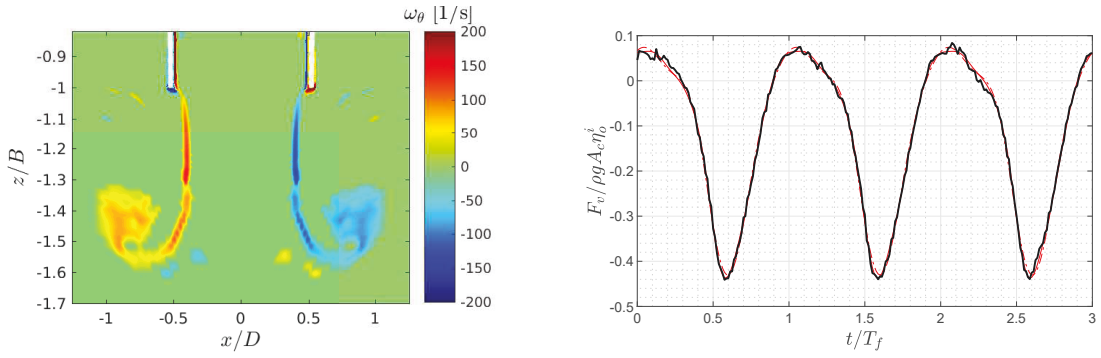

(C) $\eta_o^i/B = 0.75$

Figure 5.25: The vorticity fields of ω_θ located around a SE mouth undergoing forced oscillations and the associated time-varying vertical forces, $F_v(t)$ [——], approximated by the first three [— · —] and six [——] harmonic components.

from the local minimum pressure field near the centre of the water column (Figure 5.26(B)). Interestingly, immediately after this, the maximum pressure field induced by the vortex, indicated by the pink contour levels on Figure 5.26(C), develops locally near the bottom edge.

This local maximum pressure field is responsible for the rapidly decreasing vertical force shown in Figure 5.25(A), at the beginning of the downward displacement. The

explanation for this relates to two issues: (i) the area corresponding to the local maximum pressure field has decreased at $t = 0.15T_f$, while the area covering the local minimum pressure field remains constant (Figure 5.26(D)), and (ii) the rapid decrease in the vertical force has disappeared at $t = 0.15T_f$ (Figure 5.25(A)).

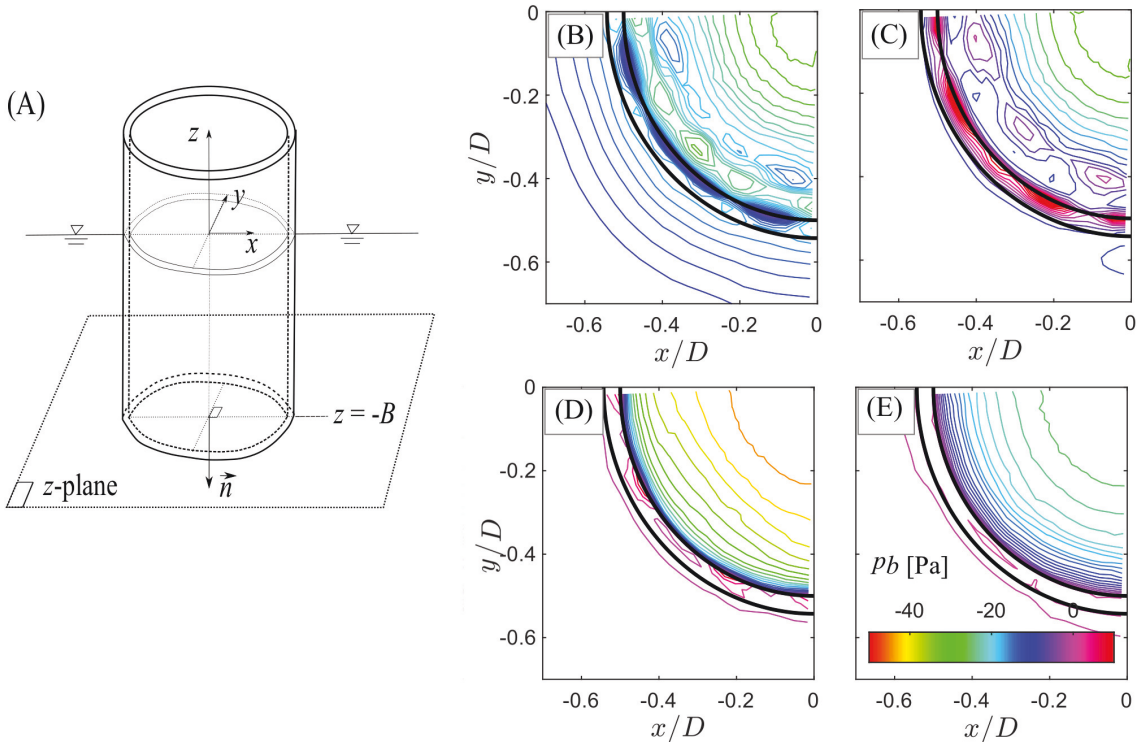

Figure 5.26: (A) A schematic showing an $x - y$ plane of the SE mouth at $z = -B$, and the evolution of the pressure contours on this plane when $\eta_o^i/B = 0.25$ at times: (B) 0, (C) $0.05T_f$, (D) $0.15T_f$ and (E) $0.25T_f$; the outer and inner wall being indicated by the black lines on Figures 5.26(B)-(E).

The decrease in the area covering the local maximum pressure field is associated with vortex motion because the vortex generated during a downward displacement always moves away from the mouth. During the remaining period of the displacement ($0.15T_f \leq t \leq 0.5T_f$), the magnitude of the local minimum pressure field continues to increase, but then decreases at a later time; the latter observed in Figure 5.26(E). Clearly, this evolution of the pressure field shapes the vertical force.

In Chapter 4, it was confirmed that vortex moves further from the SE mouth of an OWC at an increased η_o^i/B number. This fact and the understanding that the area of local maximum pressure field decreases due to vortex motion, indicate the less important influence of vortex on the vertical force. Indeed, the data presented on Figures 5.24 and 5.25 confirm this. As the response amplitude number, η_o^i/B,

increases, the presence of the secondary loading cycles reduces. Nevertheless, both the horizontal and vertical asymmetry[1] of the pressure time-history remains; the secondary loading cycle linked to the process of vortex shedding.

5.10.3 Relative importance of nonlinearity sources

The nonlinearity in the vertical force is also indicated by its high-harmonic components. The importance of these components can be evaluated from the reconstruction of the vertical force using varying harmonic components. In Figures 5.24(b), (c) and 5.25(c), the first three harmonics accurately represent the vertical forces with no secondary loading cycle. Otherwise, the first six harmonics are required to accurately represent the force time-history. Clearly, this confirms that the harmonics higher than the third are produced by the vortex motion. In respect of the force asymmetry associated with unequal zero-crossing periods, this is primarily driven by the second harmonic; the latter associated with both the oscillation of the water column and the vortex motion (Section 5.9).

To understand the relative significance of these different sources of nonlinearity, changes with the amplitude of the internal free-surface, η_o^i, are evaluated. In undertaking this, the FWCTs outlined in Table 5.2, were numerically modelled to compute the air forces, F_t. The reason for not using data describing the vertical force, F_v, is because this force depends on the fluid velocity near the bottom mouth, and this may deviate from the fluid velocity at the internal free-surface (Section 4.7).

An FFT analysis of the air-force time-histories for the OWCs with a variety of mouth shapes and forcing amplitude numbers, η_o^i/B, was undertaken. Data describing the normalised air pressures, $p/\rho g\eta_o^i$, is provided on Figures 3.8(a) and (b); the air pressure p defined by F_t/A_c. Figures 5.27(a)-5.27(d) concern the harmonic components of the normalised air-force, $\overline{F_{t,o}^{(1)}}$, $\overline{F_{t,o}^{(2)}}$, $\overline{F_{t,o}^{(3)}}$ and $\overline{F_{t,o}^{(HO)}}$, and their variations with the mouth shape and η_o^i/B number; the overbars indicating the normalisation defined by $\rho g A_c \eta_o^i$. Clearly, when compared to the other components, $\overline{F_{t,o}^{(HO)}}$ and $\overline{F_{t,o}^{(3)}}$ are small for all mouth shapes. In contrast, the $\overline{F_{t,o}^{(2)}}$ is comparable to the $\overline{F_{t,o}^{(1)}}$, and becomes the most important with the increasing η_o^i/B number.

Given Equation (2.37), the summation of the force terms, $F_{t,q}$, that contribute

[1]The term horizontal (or vertical) defining the plane about which the asymmetry is defined.

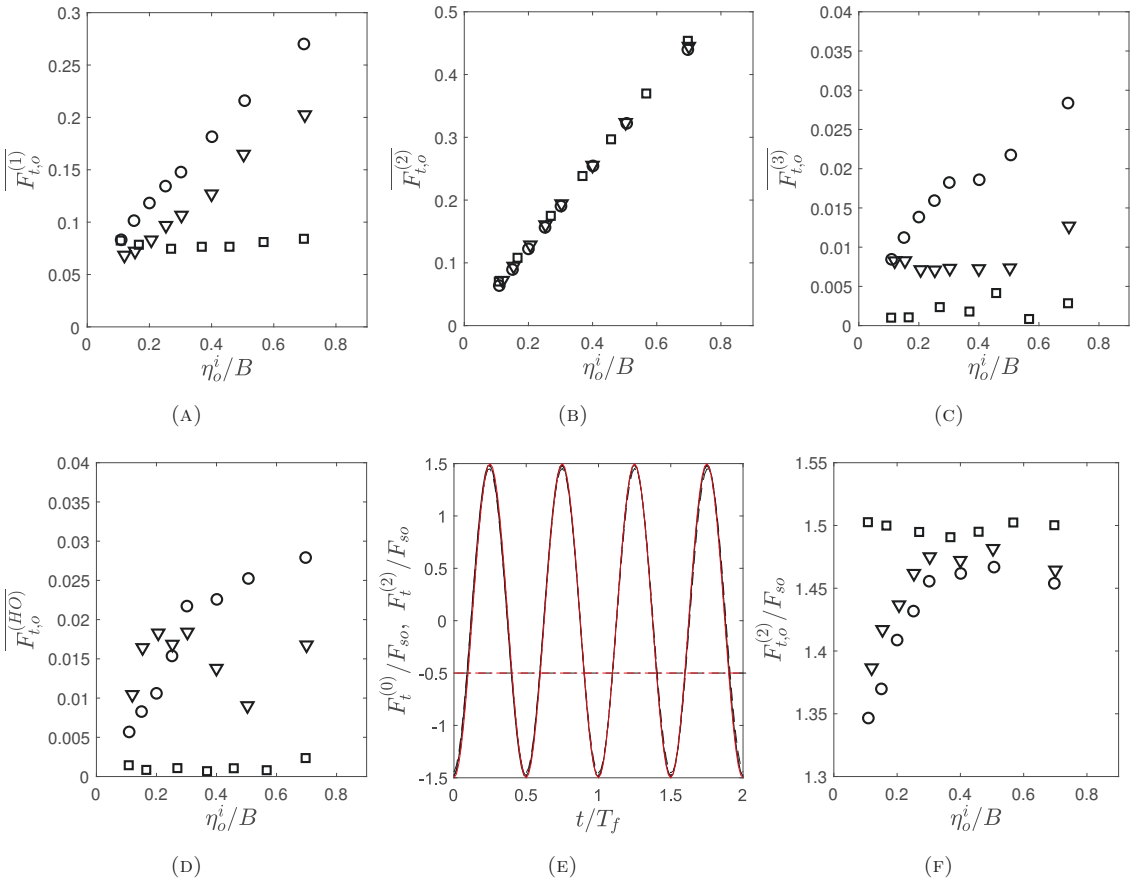

FIGURE 5.27: Harmonic components of the normalised air-forces: (A) $\overline{F_{t,o}^{(1)}}$, (B) $\overline{F_{t,o}^{(2)}}$, (C) $\overline{F_{t,o}^{(3)}}$, (D) $\overline{F_{t,o}^{(HO)}}$, and (E) Time-histories of the zeroth and the second-harmonic air-forces relative to the second-order excitation forces, $F_t^{(0)}(t)/F_{SO}$ [dashed lines] and $F_t^{(2)}(t)/F_{SO}$ [solid lines], for the BS mouth when η_o^i/B numbers: 0.25 and 0.5, and (F) The variation in the relative second-harmonic component, $F_{t,o}^{(2)}/F_{SO}$, with the η_o^i/B number and mouth shape: SE [$\circ$], SC [$\triangledown$] and BS [$\square$].

to the time-histories of the zeroth and second harmonics of an air force is given by:

$$F_{t,q} = \rho A_c \eta^i \ddot{\eta}^i + \frac{1}{2}\rho A_c \dot{\eta^i}^2 + \frac{1}{2} b_2 \rho A_c \dot{\eta}^i |\dot{\eta}^i|, \tag{5.6}$$

where η^i only contains a first harmonic component, and the subscript q indicates the quadratic product of this first harmonic. The first term corresponds to a nonlinear inertia force. In the absence of any nonlinear damping forces expressed as the third term, the time-varying zeroth and second harmonic forces, $F_t^{(0)}(t)$ and $F_t^{(2)}(t)$,

normalised by the amplitude of the second-order excitation force, F_{SO}, are defined:

$$F_t^{(0)}(t)/F_{SO} = -0.5, \tag{5.7}$$

$$F_t^{(2)}(t)/F_{SO} = -1.5cos2\omega_f t, \tag{5.8}$$

where F_{SO} is computed as $1/2\rho A_c \left(\eta_o^i \omega_f\right)^2$.

Figure 5.27(E) confirms that for the BS mouth, these equations accurately represent the $F_t^{(0)}(t)/F_{SO}$ and $F_t^{(2)}(t)/F_{SO}$ predicted from the FFT analysis. The accurate prediction proves that these two harmonics are driven by the water column oscillation when the flow is irrotational. Specifically, the variation in the relative value of the second-harmonic component, $F_{t,o}^{(2)}/F_{SO}$, with the η_o^i/B number and mouth shape is presented in Figure 5.27(F). Clearly, in the SE and SC cases, the $F_{t,o}^{(2)}/F_{SO}$ values converge to those for the BS mouth at large η_o^i numbers. This indicates that the contribution of the water column oscillation outweighs the nonlinear damping force as the η_o^i/B number increases. It is also important to note that this is consistent with the earlier arguments explaining why the secondary loading cycle reduces at large η_o^i/B numbers. It is thus concluded that when the forcing or response amplitude increases, the second harmonic force due to the water column oscillation becomes increasingly more important than that arising from the vortices generated near an SE or SC mouth.

5.11 Concluding remarks

This chapter has investigated the physical origins of the nonlinearities in the forces and motions within OWCs, and demonstrated their relative importance. To undertake this investigation, a variety of OWCs subject to incident wave excitations and forced oscillations were numerically modelled.

The nonlinearities in the motion of the internal water surface elevation within an OWC have been shown to be critically dependent on the amplitude of forcing, either air pressure or incident wave. Two characteristics associated with this are the progressively decreasing RAO and the progressively varying phase difference of the elevation. Both effects are dependent on the nonlinear damping appropriate to an OWC. In addition, the response asymmetry has been verified as a third nonlinear characteristic. This asymmetry is clearly observed from the zero-crossing periods of

the internal elevation. This effect has been directly linked to the instantaneously varying mass of the water column which drives a nonlinearity in the inertia force. This, in turn, causes the response asymmetry.

The nonlinearities in the forces have also been identified by investigating both the vertical force and the inline pressure. This aspect of the work has confirmed that the nonlinear characteristics incorporate both a force asymmetry and a secondary loading cycle. While the former is persistently in both irrotational and separated flow conditions, the latter is critically dependent on the vortex shedding of the mouth of the OWC. Importantly, the depth-variation in the harmonic components of the normalised inline-pressures underpins these two physical origins. Specifically, this variation confirms that the free-surface nonlinearity arising from Type-2 scattered waves has negligible effect on the vertical force and hence the motion of the OWC. Interestingly, an investigation into the relative importance of the two dominant effects proves that vortex shedding becomes less important as the amplitude of water column motion increases. This is supported by the substantially reduced secondary loading cycle at large response amplitudes.

6

Added-mass and nonlinear damping coefficients

6.1 Chapter overview

In linear superposition theory, the hydrodynamic force that acts on an OWC is assumed to be independent of the mechanism that excites the water column. In a viscous flow solution, the behaviour of vortices that arises from a wave excitation and a forced oscillation test may not be identical. As such, the associated hydrodynamic forces will not be comparable. The applicability of the hydrodynamic coefficients computed from a forced oscillation test, and used to predict the response of a water column in a wave-excitation problem, requires investigation.

In studies of oscillatory flows past fixed bodies, the applicability of the coefficients evaluated from a forced oscillation test has been investigated previously. For example, the force coefficients computed from the planar oscillatory flow in Sarpkaya (1977) have been shown to be in good agreement with Chakrabarti (1980) and Stansby et al. (1983); the latter running their experimental tests in shallow water-wave conditions. However, the coefficients evaluated in deep water-wave conditions show significant deviations from those recorded in planar oscillatory flows (see, for example, Stansby et al. (1983)).

In the context of an oscillating body, Chakrabarti & Cotter (1984) confirmed that the measured loads on a freely-oscillating tower subject to incident waves were reason-

ably well predicted using the hydrodynamic coefficients from forced tests. However, for this to be true, the range of KC numbers appropriate to these two different excitation mechanisms must be of a similar magnitude. Likewise, Koterayama & Nakamura (1988) confirmed the applicability of forced surging vertical cylinder tests to predict the hydrodynamic loads on the cylinder freely surging in regular waves. This was only valid provided that the relative KC range, defined by the velocity of the surging cylinder relative to the wave-induced velocity, was set equal to the KC range in the forced test.

Taken togeher, these results indicate that setting a comparable KC or relative KC condition in different excitations ensures the similarity in the flow kinematics and thus the applicability of the coefficients. The present study will build upon these results, investigating the applicability of a forced oscillation test and the validity of linear superposition theory in the context of an OWC. Specifically, the investigations that follow will consider:

1. The hydrodynamic coefficients for OWCs computed from forced oscillation tests, and

2. The relevance of these coefficients to the flow fields and the nonlinear forcing described in Chapters 4 and 5.

Having investigated both aspects, the applicability of the forced oscillation tests to the prediction of the responses of the water columns undergoing wave excitations will be evaluated. By investigating a broad range of flow conditions, the importance of the vortex motion in damping the response of the water column will be clearly established.

6.2 Method of quantifying hydrodynamic coefficients

In Section 5.8.2, the *lsqcurvefit* routine within Matlab was implemented to quantify the hydrodynamic coefficients for an OWC. The present chapter also adopts this approach. In undertaking this quantification, three important points are addressed:

(i) The inclusion of the nonlinear inertia and the second-order excitation term into Equation (2.37),

(ii) The dependence of the hydrodynamic coefficients on the direction of travel of the water column, and

(iii) An efficient test to evaluate the dependence of the resulting coefficients on key parameters.

It has already been shown in Section 5.8.2 that point (i) is essential to capture the response asymmetry of the internal surface elevation. Likewise, point (ii) is motivated by the earlier evidence that the direction of travel of the water column influences vortex motion (Section 4.8). To address this, the present study considers the so-called directionally dependent coefficients. These are computed by fitting Equation (2.37), using *lsqcurvefit*, over half-periods of oscillation. The results are then compared to directionally invariant coefficients, quantified by fitting the equation over one full period of oscillation.

In addressing point (ii), two OWCs with sharp-edged (SE) and bell-shaped (BS) ends undergoing Forced Air Pressure Tests (FAPTs) were numerically modelled. The directionally dependent coefficients were first quantified. The added-mass coefficient, $A_m/\rho A_c B$, and the nonlinear damping coefficient, b_2, for both OWCs are given in Table 6.1; the coefficients for both OWCs clearly shown to be directionally dependent.

Table 6.1: Hydrodynamic coefficients for OWCs with SE and BS mouths undergoing FAPTs

Mouth shape	Displacement	$A_m/\rho A_c B$	b_2
SE	Downward	0.17	1.39
	Upward	0.15	0.61
BS	Downward	0.08	0.27
	Upward	0.06	0.05

To investigate the importance of these effects, the η^i elevation within each OWC was re-simulated using both the directionally dependent and directionally invariant coefficients. Figure 6.1 shows comparisons between the η^i elevations computed by the viscous flow solver and the re-simulated η^i elevations. Once again, only the developed (or "steady-state") elevations are presented. In the SE case, Figure 6.1(a) shows a small discrepancy between computed and re-simulated elevations. In the BS case (Figure 6.1(b)), this discrepancy is even smaller. Importantly, in both the SE and BS cases, the implementation of either the directionally dependent or directionally

invariant coefficients provides a reasonably good prediction of the elevation computed by the viscous flow solver.

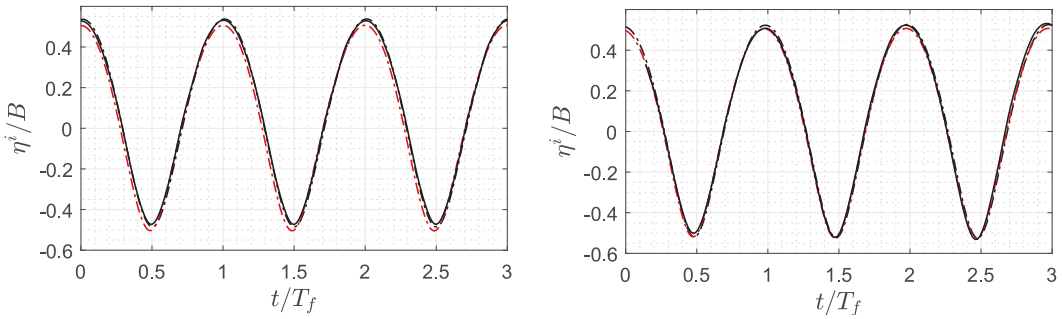

(A) SE case (B) BS case

Figure 6.1: Comparisons between the internal surface elevation, η^i, computed by the viscous flow solver [——] and the η^i elevation re-simulated using directionally dependent [— · —] and directionally invariant coefficients [— · —].

In considering point (iii) noted earlier, Forced Water Column Tests (FWCTs) with a variety of key parameters were numerically simulated. The key parameters are associated with the amplitude of internal water surface elevation, η_o^i, and the angular frequency, ω_f. To evaluate the appropriateness of data generated from a FWCT, the internal surface elevation, η^i, generated from a FAPT, is compared with the η^i elevation re-simulated using the directionally dependent coefficients computed from the FWCT. Figure 6.2 presents this data for OWCs with various mouth shapes and D/B ratios. Good agreement is observed across all the "steady-state" elevations for all OWCs. Indeed, the only departures arise in the transient-state elevation in the BS case. This indicates the dependence of the coefficient on the η_o^i value. Nevertheless, the comparisons confirm that the coefficients computed from a FWCT can be implemented to predict the nonlinear response arising from a FAPT.

6.3 Hydrodynamic coefficients under forced oscillations

6.3.1 Forcing amplitude number and cylinder aspect-ratio

This section concerns variations in the hydrodynamic coefficients with forcing amplitude number, η_o^i/B, and cylinder aspect-ratio, D/B. The key parameters and di-

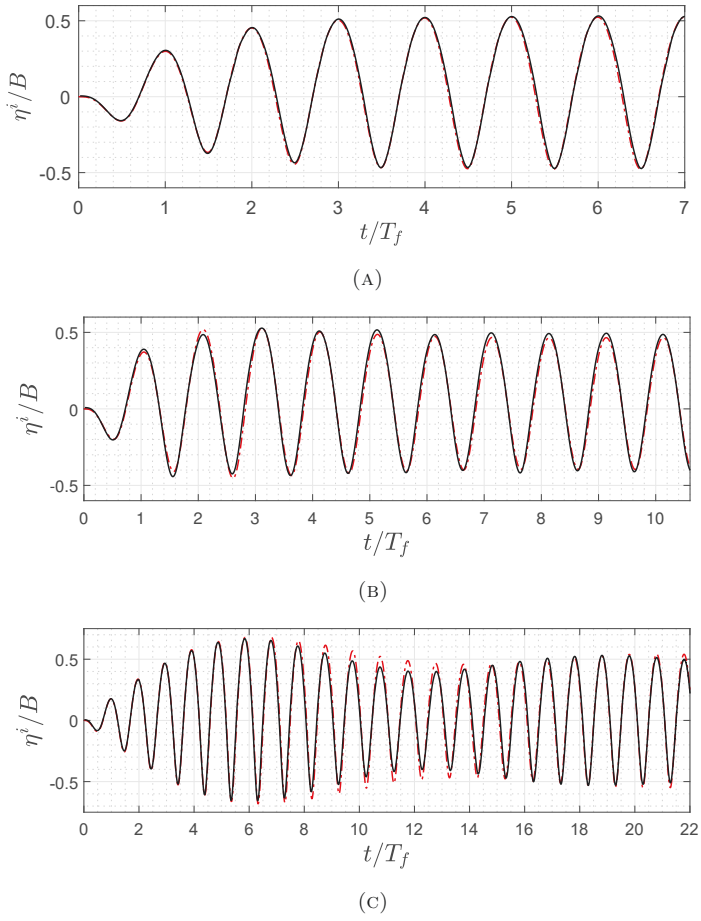

Figure 6.2: Comparisons between the internal surface elevations, η^i, predicted from FAPTs [——] and the η^i elevations re-simulated using the hydrodynamic coefficients from FWCTs [– –] for OWCs with: (A) SE mouth, $D/B = 0.435$ and air pressure amplitude, $P_o/\rho g = 0.017$ m, (B) SE mouth, $D/B = 1.25$, and $P_o/\rho g = 0.023$ m, and (C) BS mouth, $r_l = 0.5D$, $D/B = 0.435$ and $P_o/\rho g = 0.009$ m.

mensions outlined in Table 4.1 were adopted and the draft held constant at $B = 0.16$ m were adopted. In the paragraphs that follow, three important aspects of the modelling procedure will be addressed.

(a) **Added-mass coefficient and effective draft**

Figure 6.3(A) concerns the variation of the added-mass coefficient, $A_m/\rho A_c B$, with the η_o^i/B number for an OWC with a SE mouth and $D/B = 0.435$. The forcing frequency was set to $\omega_f^2 B/g = 0.87$. Direct comparisons between the viscous flow computation and the linear potential solution are shown; the former considering both the directionally dependent and directionally invariant coefficients for the OWC. Three trends require particular attention:

(i) The $A_m/\rho A_c B$ coefficients computed from the viscous flow solver are larger than those generated using the linear potential solution,

(ii) The discrepancy between the two different solutions increases with the η_o^i/B number, and

(iii) The $A_m/\rho A_c B$ values corresponding to the downward displacements are larger than those estimated from the upward displacements.

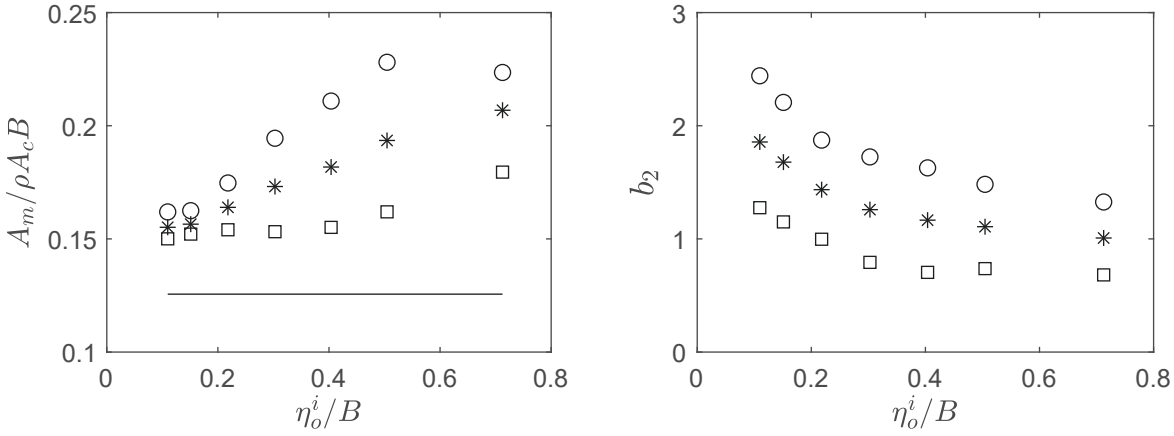

(A) (B)

Figure 6.3: (A) Variations of the added-mass coefficient, $A_m/\rho A_c B$, and (B) the nonlinear damping coefficient, b_2, with the η_o^i/B number in the case of OWC with a SE mouth and $D/B = 0.435$. The viscous flow solution is used to provide both directionally invariant [$*$] and directionally dependent coefficients; the latter corresponding to the upward [$\square$] and downward displacements [$\circ$]. Comparisons with the linear potential solution [——] are also provided.

The added mass, A_m, predicted from the viscous flow solver and the linear potential solution, corresponds to the damped natural frequency, ω_d, and the undamped natural frequency, ω_{nd}, respectively. In each case, the relevant frequency, ω_d or ω_{nd}, is defined by $\sqrt{\frac{g/B}{1+(A_m/\rho A_c B)}}$, following Yeung & Jiang (2014). This relationship, together with the earlier confirmation concerning the reduction of ω_d relative to ω_{nd} given in Section 5.7.2, explains point (i).

The fact that a linear potential solution is independent of the amplitude of excitation (imposed on a water column) is consistent with the independence of the $A_m/\rho A_c B$ coefficient on η_o^i/B number. As a result, the linearly predicted $A_m/\rho A_c B$ coefficient is presented by the line on Figure 6.3(A). The difference between this and the viscous flow calculations can be explained by:

(A) The increasing effective draft, B_e, with η_o^i/B number in a viscous flow (Section 4.10), and

(B) The relationship between ω_d and B_e expressed as $\omega_d = \sqrt{g/B_e}$ (Zhang et al., 2012).

Clearly, both these considerations indicate the reducing trend of ω_d as η_o^i/B increases. Given the relationship between ω_d and A_m noted earlier, this explains point (ii). Importantly, the progressive departure of $A_m/\rho A_c B$ from the linear potential solution is caused by the vortex motion at the mouth of an OWC.

In Section 4.10, it was shown that the effective draft during a downward displacement of the water column was larger than that during an upward displacement. This seems to be at odds with point (iii). The explanation for this lies in the vortex shedding. During a downward displacement, a pair of vortices is shed outside the water column (see Figures 4.20(A)-(D)). As such, the external fluid flow near the bottom mouth has an increased volume and hence fluid mass within a rotational flow field. At the same time, the water column must be displaced downwards due to the applied forcing. This, in turn, forces the rotational flow field away from the bottom mouth. As a result, a larger additional inertial force must be included in the applied forcing to accelerate the oscillating water column.

(b) **Nonlinear damping coefficient and nonlinear forcing**

Figure 6.3(B) shows an exponential decay of the nonlinear damping coefficient, b_2, with η_o^i/B. This is consistent with the earlier comments concerning the decreasing contribution of vortex motion to the second-harmonic component of the air force, $F_{t,o}^{(2)}$ (see Figure 5.27(F)). Figure 5.27(F) and Equation 5.6, that expresses the force terms contributing to the time-varying second-harmonic air-force, lead to two conclusions related to the SE mouth:

(i) The amplitude of the nonlinear damping force, F_{NL}, relative to the amplitude of the second-order excitation force, F_{SO}, exponentially decays with the increasing η_o^i/B number, and

(ii) The vortex motion, instead of surface friction, contributes the main source of nonlinear damping.

With F_{NL} equivalent to $b_2 A_c \left(\eta_o^i \omega_f\right)^2$, point (i) is consistent with the trend in the b_2 coefficient with the η_o^i/B number (Figure 6.3(b)). This decay signifies the reduced importance of the vortex motion as η_o^i/B increases.

Point (ii) is supported by the fact that the wall surface area of the OWC with the SE mouth is smaller than that with the BS mouth. In contrast, the data presented on Figure 5.27(f), indicates that the F_{NL} value is larger for the SE mouth. This is entirely consistent with the importance of the vortex motion.

(c) **OWCs with varying D/B ratios**

Figure 6.3 confirms that the variation of $A_m/\rho A_c B$ and b_2 with η_o^i/B are consistent irrespective of the directional dependence. Indeed, the directionally invariant values can be accurately estimated from the mean values of the corresponding directionally dependent coefficients. Based upon this, the following investigation concerns the directionally invariant coefficients for OWCs with SE mouths and a variety of cylinder aspect-ratios, D/B.

The variations of the added-mass coefficient, $A_m/\rho A_c B$, with KC number and D/B ratio are presented in Figure 6.4(a). The average mass of the water column clearly influences this coefficient. This is based upon the fact that the $A_m/\rho A_c B$ coefficient predicted by the linear potential solver, increases from 0.05 to 0.32 in the range of $0.15 \leq D/B \leq 1.25$. However, the vortex motion also affects this coefficient for all D/B ratios. The discrepancies between the linear potential solution and the viscous flow computation confirm this. The deviation of ω_d from ω_{nd} is thus evident for all D/B ratios.

Unlike $A_m/\rho A_c B$, b_2 has a smaller value at a constant KC number but an increased D/B ratio (Figures 6.4(a) and (b)). Interestingly, Figure 6.4(c) confirms that b_2 is less affected by D/B than η_o^i/B. However, it is notable that there is an appreciable variation under the smallest η_o^i/B condition; the b_2 coefficient estimated to lie between 2.0 and 2.5. Nevertheless, the variation of the b_2 coefficient with the η_o^i/B number for each D/B ratio is generally comparable. The curve of an exponential decay computed as $b_2 = 1.45e^{-4.79\eta_o^i/B} + 1.02e^{-0.05\eta_o^i/B}$ can fit all variations of this coefficient.

Figure 6.4(c) also confirms that the b_2 coefficients for all D/B ratios converge to 1.0 for large η_o^i/B. This provokes a question concerning the validity of using a single

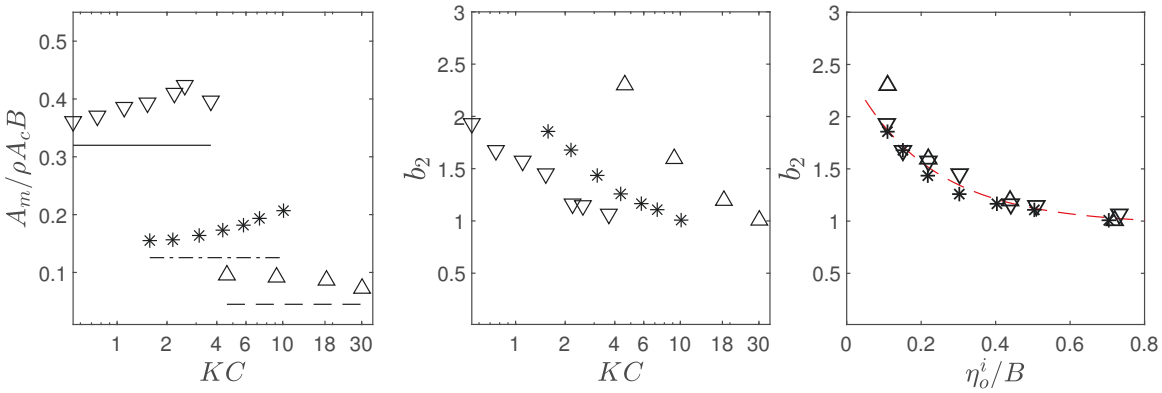

(A) (B) (C)

Figure 6.4: Variations of (A) the added-mass coefficient, $A_m/\rho A_c B$, with KC number and (B) the nonlinear damping coefficient, b_2, with KC and (C) η_o^i/B numbers predicted from the viscous flow solver [symbols] and comparisons with the linear potential solution [lines] for the OWCs with SE mouths and $D/B = 0.15$ [△, — —], 0.435 [∗, — · —] and 1.25 [▽, ——]. An exponentially decaying curve [— —] that fits the variations of the b_2 coefficient is also provided.

b_2 coefficient to predict the nonlinear responses of a water column subjected to any force amplitude. Figure 6.5(A) presents the ratio of the actual response amplitude, η_o^i, predicted from a FAPT, to the amplitude of the re-simulated elevation, $\eta_o^{i,*}$, for the three D/B ratios; the latter computed using the convergent b_2 coefficient and the corresponding $A_m/\rho A_c B$ coefficient. Specifically, Figure 6.5(A) proves that the smallest $\eta_o^i/\eta_o^{i,*}$ ratio (or the largest deviation) appears for $D/B = 0.15$ and at the smallest η_o^i/B number. This point is highlighted in blue. Furthermore, a comparison between the time-histories of the actual internal surface elevation, $\eta^i(t)$, and the re-simulated elevation, $\eta^{i,*}(t)$, for this case, is shown in Figure 6.5(B). Clearly, both the actual amplitude and the phase of the η^i elevation cannot be accurately estimated. This highlights the importance of applying coefficients according to the operational condition of an OWC.

6.3.2 Mouth shape

This section concerns the influence of mouth shape on the hydrodynamic coefficients. Two OWCs with different BS mouths involving lip radii of $r_l = 0.11D$ and $0.5D$, and an OWC with a SC mouth undergoing FWCTs were numerically modelled. In all cases, the aspect ratio was fixed at $D/B = 0.435$, and the forcing frequency again set to $\omega_f^2 B/g = 0.87$. Within Figure 6.6, the hydrodynamic coefficients for

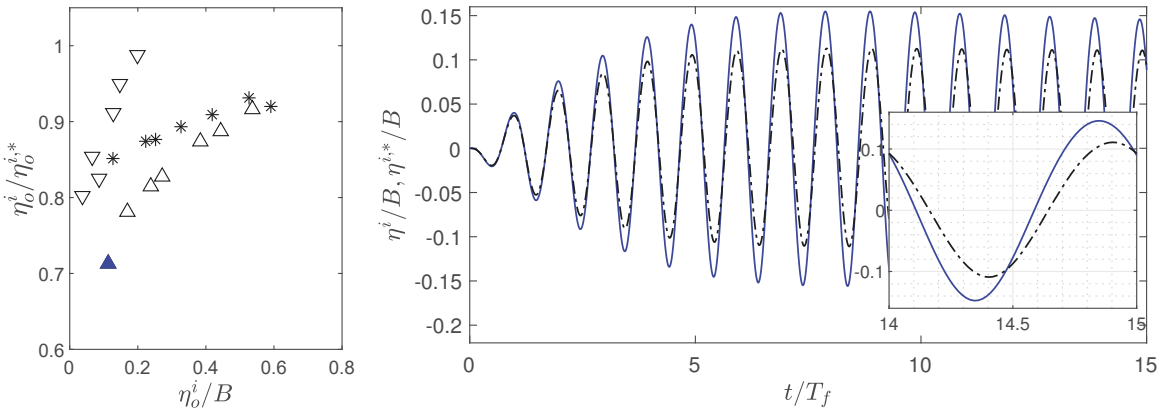

(A) (B)

Figure 6.5: (A) Ratios of the actual response amplitude to the amplitude re-simulated using the convergent coefficient, $\eta_o^i/\eta_o^{i,*}$, for the OWCs with $D/B = 0.15$ [△], 0.43 [∗], and 1.25 [▽], and (B) a comparison between the time-varying $\eta^i\,(t)$ elevation [— · —] and $\eta^{i,*}\,(t)$ elevation [——] for the OWC with $D/B = 0.15$; this corresponding to the symbol (▲) on Figure 6.5(A).

each OWC are presented as functions of the η_o^i/B number (indicated by the bottom black horizontal axis) and the KC number (indicated by the top blue axis); both the directionally dependent and directionally invariant coefficients being shown.

In the FAPTs considered earlier for Figures 5.16(A), 5.16(C) and (E), the response amplitude, η_o^i, for each mouth shape, was set to a comparable value. Consequently, to attain a desired response amplitude, the amplitudes of the air pressure, P_o, applied to the OWCs with different mouth shapes were adjusted. For example, for $\eta_o^i/B \approx 0.5$, the $P_o/\rho g$ values were 0.012 m in the SC case, and a lower value of 0.009 m in the BS case with $r_l = 0.5D$. This comparison of the required P_o value is consistent with comparisons of the $A_m/\rho A_c B$ coefficient and the b_2 coefficient in both cases (Figures 6.6(A) and (C)). Clearly, the directionally dependent and the directionally invariant coefficients in the SC case are larger than those in the BS case with $r_l = 0.5D$.

The larger values of $P_o/\rho g$, $A_m/\rho A_c B$ and b_2 coefficients for a mouth shape indicate stronger vortex generation near the mouth. Indeed, this can be confirmed from the vorticity fields near the SC and BS mouths presented earlier in Section 5.10.2. Given this view, comparing the coefficients for the BS cases with $r_l = 0.11D$ and $r_l = 0.5D$ shown in Figures 6.6(B)-(C), suggests the more pronounced vorticity field in the former.

The influence of the vortex motion is also evident from the variation of the added-mass coefficient with the key parameters. The $A_m/\rho A_c B$ coefficient in the BS case

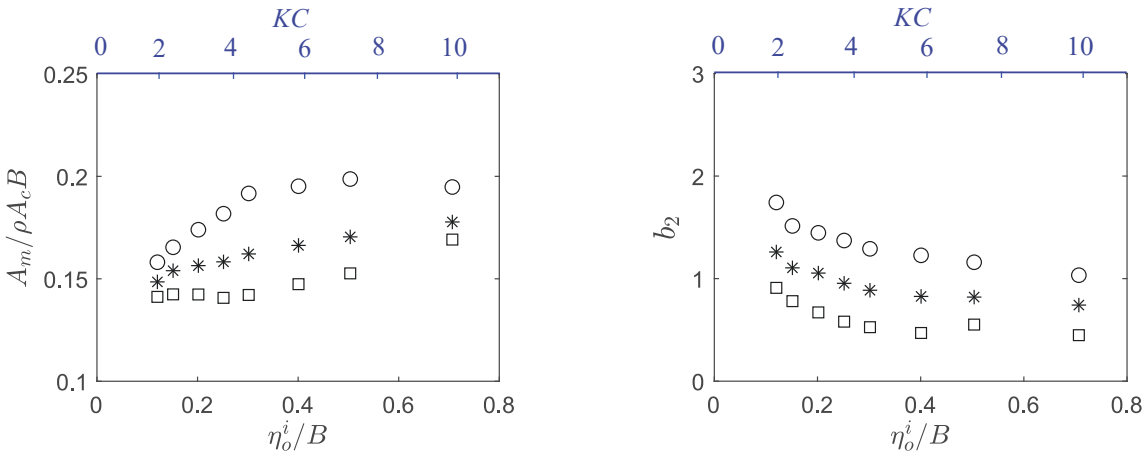

(A) SC case

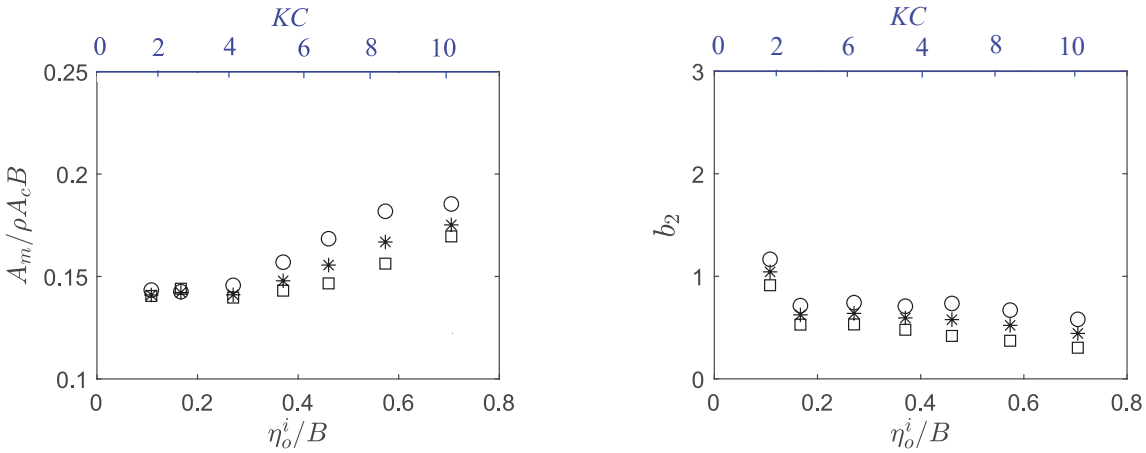

(B) BS case with $r_l = 0.11D$

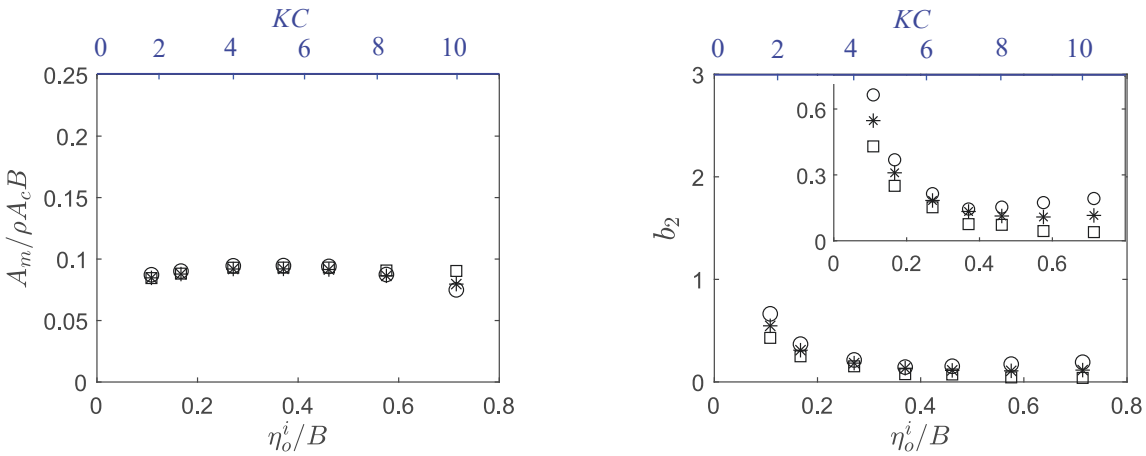

(C) BS case with $r_l = 0.50D$

FIGURE 6.6: Variations of the added-mass coefficient, $A_m/\rho A_c B$, and the nonlinear damping coefficient, b_2, with the mouth shape, η_o^i/B and KC computed as directionally invariant [$*$] and directionally dependent coefficients for upstroke [$\square$] and downstroke displacement [$\circ$].

with $r_l = 0.5D$ varies little with the η_o^i/B and KC numbers. The explanation for this lies in two earlier points: (i) added mass relates to effective draft (Section 6.3.1), and (ii) effective draft is associated with vortex motion and affects near-field radiated wave elevation (Section 4.10). It is thus reasonable to conclude that the added mass of an OWC also relates to the near-field radiated wave elevation. Given this view and Figure 4.12(c) showing the invariant first-order radiated wave amplitude with η_o^i/B number in the BS case with $r_l = 0.5$, the small variation of the $A_m/\rho A_c B$ coefficient in this case is reasonable.

One of the objectives when designing an OWC is to minimise the energy loss associated with vortices. This may be achieved by delaying the flow separation near the mouth. The delay is predicted by evaluating the minimum value of η_o^i at which the energy loss arising from the nonlinear damping mechanism increases. In making this evaluation, the averaged total energy loss, $\overline{El}$, was estimated as follows:

$$\overline{El} = \frac{2}{T_f}\int_t^{t+T_f/2}\left[pA_c - \left[\rho A_c\left(B+\eta^i\right)+A_m\right]\ddot{\eta^i} - \rho g A_c \eta^i - \frac{1}{2}\rho A_c \dot{\eta^i}^2\right]\dot{\eta^i}dt, \quad (6.1)$$

where the excitation energy, Ek_f, associated with the air pressure, p, was subtracted from all energy components except those associated with the nonlinear and linear damping forces. Again, the influence of the direction of the water column was considered. The $\overline{El}$ was thus estimated by averaging it over a half-period of oscillation.

Previously, Figure 4.11(c) confirmed that the vortex kinetic energy normalised by square of the internal free-surface velocity, $Ek_v/\rho\pi U^2 D^3$, increases with η_o^i/B. Within Figure 6.7, the $\overline{El}$ for each mouth shape was also normalised similarly; the velocity computed as $U = \eta_o^i\omega_f$. Given the evidence from Figure 4.11(c), a non-zero gradient of $\overline{El}/(\eta_o^i\omega_f)^2$ shown in Figure 6.7, implies the increasing importance of the vortex motion as the nonlinear damping.

Figures 6.7(a)-(b) do not exhibit a zero gradient in either the SE and SC cases. This suggests that the vortex motion primarily dampens the water column, even at the smallest η_o^i/B or KC value; the SC mouth having little effect on the flow separation. In considering this, Bearman et al. (1985) confirmed that at a certain KC number, the vortex shedding was insensitive to the local cross-sectional shape. In fact, Morris-Thomas MT & Thiagarajan (2006) showed that the hydrodynamic efficiency of a bottom-standing OWC was unaffected by the bottom shape of the front plate. In considering these earlier results, it is relevant to note that they

also considered SE and SC shapes. Given these results, the similarity in the data presented on Figures 6.7(A) and 6.7(B) are expected.

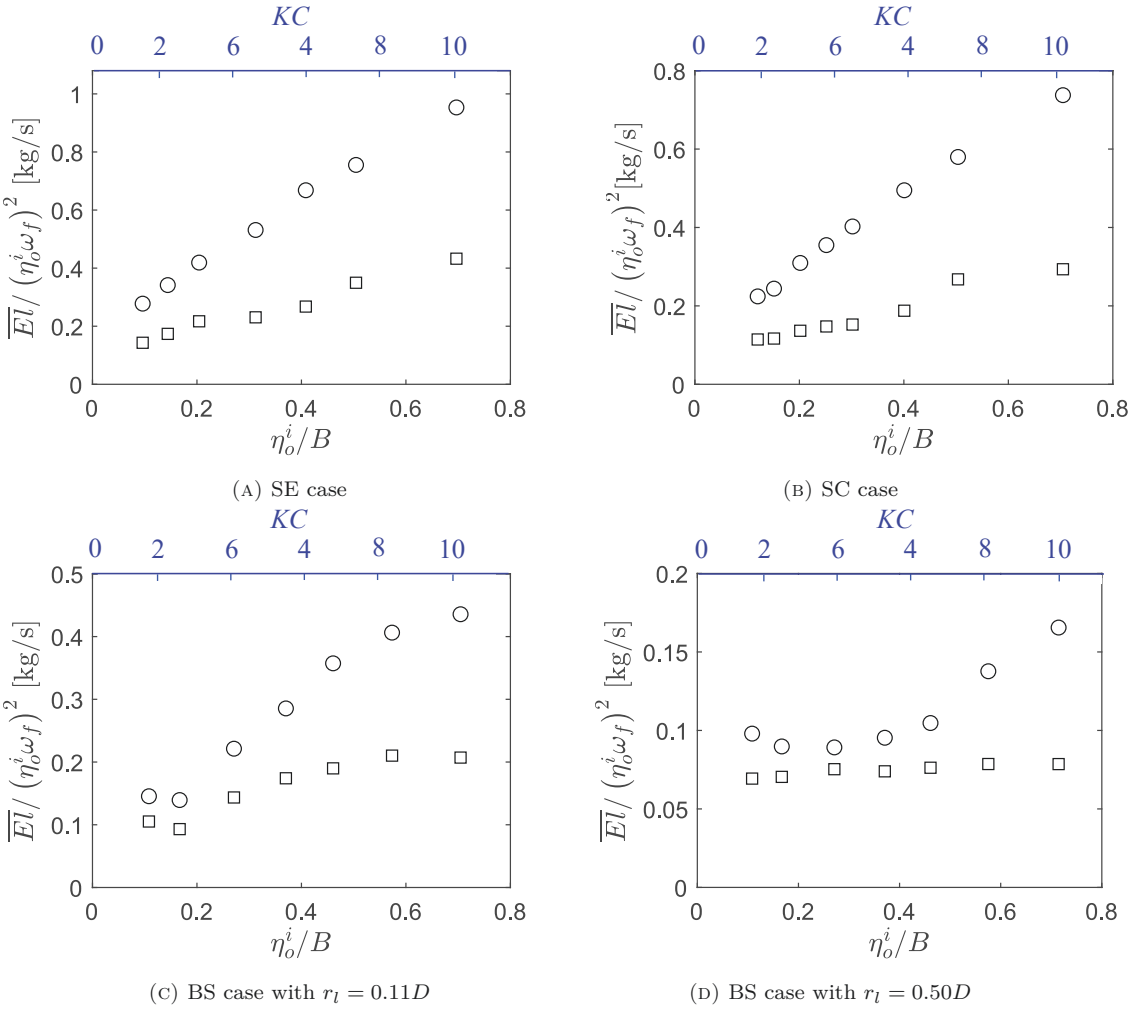

(A) SE case

(B) SC case

(C) BS case with $r_l = 0.11D$

(D) BS case with $r_l = 0.50D$

Figure 6.7: The average energy loss normalised by the square of the internal free-surface velocity, $\overline{El}/(\eta_o^i\omega_f)^2$, varying with mouth shape, η_o^i/B and KC, computed by considering the directional dependence: upstroke [□] and downstroke displacement [○].

When compared to the SE and SC cases, the BS mouth has more apparent effect. Figures 6.7(C) and (D) confirm that the nonlinear damping begins to contribute to the total energy loss at $KC \approx 3$ ($\eta_o^i/B \approx 0.21$) and $KC \approx 5$ ($\eta_o^i/B \approx 0.38$) in the BS cases with $r_l = 0.11D$ and $0.5D$, respectively.

The more dissipative performance of the SC case when compared to the BS cases relates to the radius of curvature. Increasing this in the former may reduce the damping and hence the b_2 coefficient. This is supported by Tanaka et al. (1983), who confirmed that the nonlinear damping coefficient for a square body with a sharp edge was reduced to half of its damping coefficient by rounding the edge with a

curve of radius $r_l = 0.5D$; D being the width of the body. Adopting this in the context of an OWC with a SC mouth requires an increase in the wall thickness. However, this may have two unintended consequences (disadvantages), particularly when considering high-frequency excitations:

(i) Wave scattering will be strengthened. This is indicated by the reflection coefficients for the plate models (see Figures 3.17 and 3.19).

(ii) The secondary effect of (i) is to reduce the response amplitude of the water column; the latter effect indicated from the reduced hydrodynamic efficiency in Morris-Thomas MT & Thiagarajan (2006).

Taking these points into consideration, a bell-shaped mouth is recommended to minimalize the vortex damping in an OWC.

6.4 Effect of frequency

6.4.1 Case I: Sharp-edged mouth

Given that an OWC can be excited at different frequencies, the present section seeks to evaluate the variation of the hydrodynamic coefficients over a practical range of frequencies. In addition, the influence of the Reynolds (Re) number determined by varying both frequency and amplitude of the internal free-surface, will be investigated.

In the first instant, an OWC with a SE mouth will be considered. To allow the widest possible comparisons, the key parameters defined in Fung (1998) were adopted. The forcing amplitude number, η_o^i/B, was set to three different values: $0.05, 0.075$ and 0.125. In each case, the forcing frequency was varied over the range of $0.2 \leq \omega_f^2 B/g \leq 1.75$. The directionally invariant added-mass and nonlinear damping coefficients are presented in Figure 6.8. In each case, both coefficients show a reduction with $\omega_f^2 B/g$.

To further explore the frequency variation, the OWCs evaluated earlier in Section 6.3.1 are also analysed. These examples include a broader range of forcing amplitudes: $0.11 \leq \eta_o^i/B \leq 0.71$. Figure 6.9(A) concerns the added-mass coefficient, $A_m/\rho A_c B$, highlighting two key points:

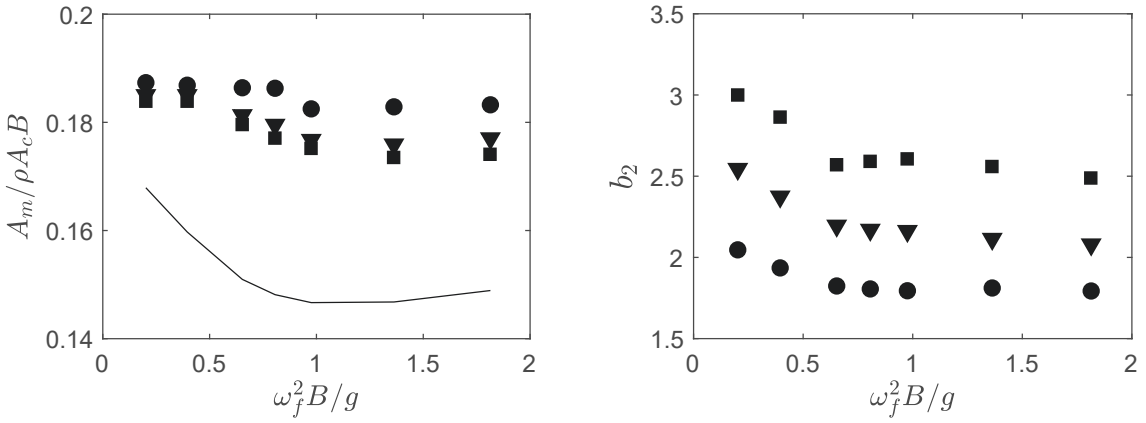

(A) (B)

Figure 6.8: (A) Added-mass coefficient, $A_m/\rho A_c B$, and (B) nonlinear damping coefficient, b_2, for the OWC with a SE mouth, $D/B = 0.52$ and $B = 0.2$ m varying with the $\omega_f^2 B/g$ for η_o^i/B numbers of 0.05 [■], 0.075 [▼], 0.125 [●]. A comparison to the linear potential solution [——] is also provided.

(i) The $A_m/\rho A_c B$ coefficient computed by the linear potential solver under-estimates the viscous flow solution at all frequencies.

(ii) The $A_m/\rho A_c B$ coefficient shows small variation with $\omega_f^2 B/g$ at all η_o^i/B numbers.

Points (i) and (ii) are also observed in the earlier computations (see Figure 6.8(A)). Concerning point (ii), evidence of this is given by the maximum percentage of variation of the $A_m/\rho A_c B$ estimated to be 15%. For $\omega_f^2 B/g > 0.7$, the variation is even less evident.

Addressing the damping coefficient, b_2, Figure 6.9(B) exhibits two trends:

(i) Its variation with the forcing frequency, $\omega_f^2 B/g$, is small, and

(ii) It converges to 1.0 for all forcing frequencies at large η_o^i/B.

Evidence of point (i) is given by the maximum percentage of variation estimated to be 15%. When compared to the variation with η_o^i/B, this percentage number is clearly smaller. Given these results, it is concluded that the b_2 coefficient for an OWC with a SE mouth operating at an η_o^i/B number can be reliably computed across the frequency range.

The influence of the Re number is also investigated by re-plotting the b_2 coefficients discussed in Figures 6.3(B) and 6.9(B). Figure 6.10 presents this data and

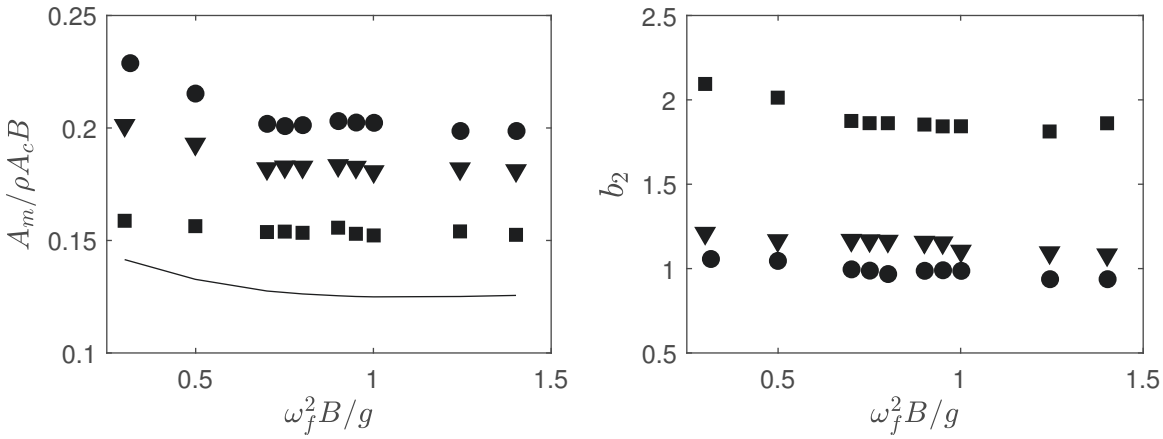

(A) (B)

Figure 6.9: (A) Added-mass coefficient, $A_m/\rho A_c B$, and (B) nonlinear damping coefficient, b_2, for the OWC with a SE mouth, $D/B = 0.435$ and $B = 0.16$ m varying with $\omega_f^2 B/g$ for $\eta_o^i/B = 0.11$ [■], 0.4 [▼], 0.71 [●]. A comparison to the linear potential solution [——] is also provided.

suggests that the effect of the Re number is insignificant provided $Re \geq 30000$.

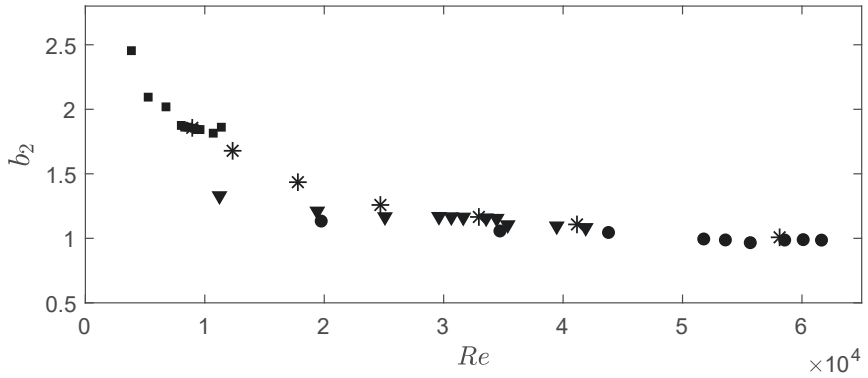

(A)

Figure 6.10: The variation of the b_2 coefficient with Re number for an OWC with a SE mouth. The data includes varying $\omega_f^2 B/g$ number with $\eta_o^i/B = 0.11$ [■], 0.4 [▼], 0.71 [●], and varying η_o^i/B with $\omega^2 B/g = 0.87$ [∗].

6.4.2 Flow description for Case I

To further confirm the small variation of added mass with frequency, the locations of the vortex motions developed under a low- and high-frequency excitation are examined. This is motivated by the earlier explanation concerning the influence of vortex motion on added mass (Section 6.3.1). The streamlines and velocity fields associated with each of these two cases are presented on Figures 6.11 and 6.12. The

sequence of the fields generated by a downward displacement of the water column is provided in each figure.

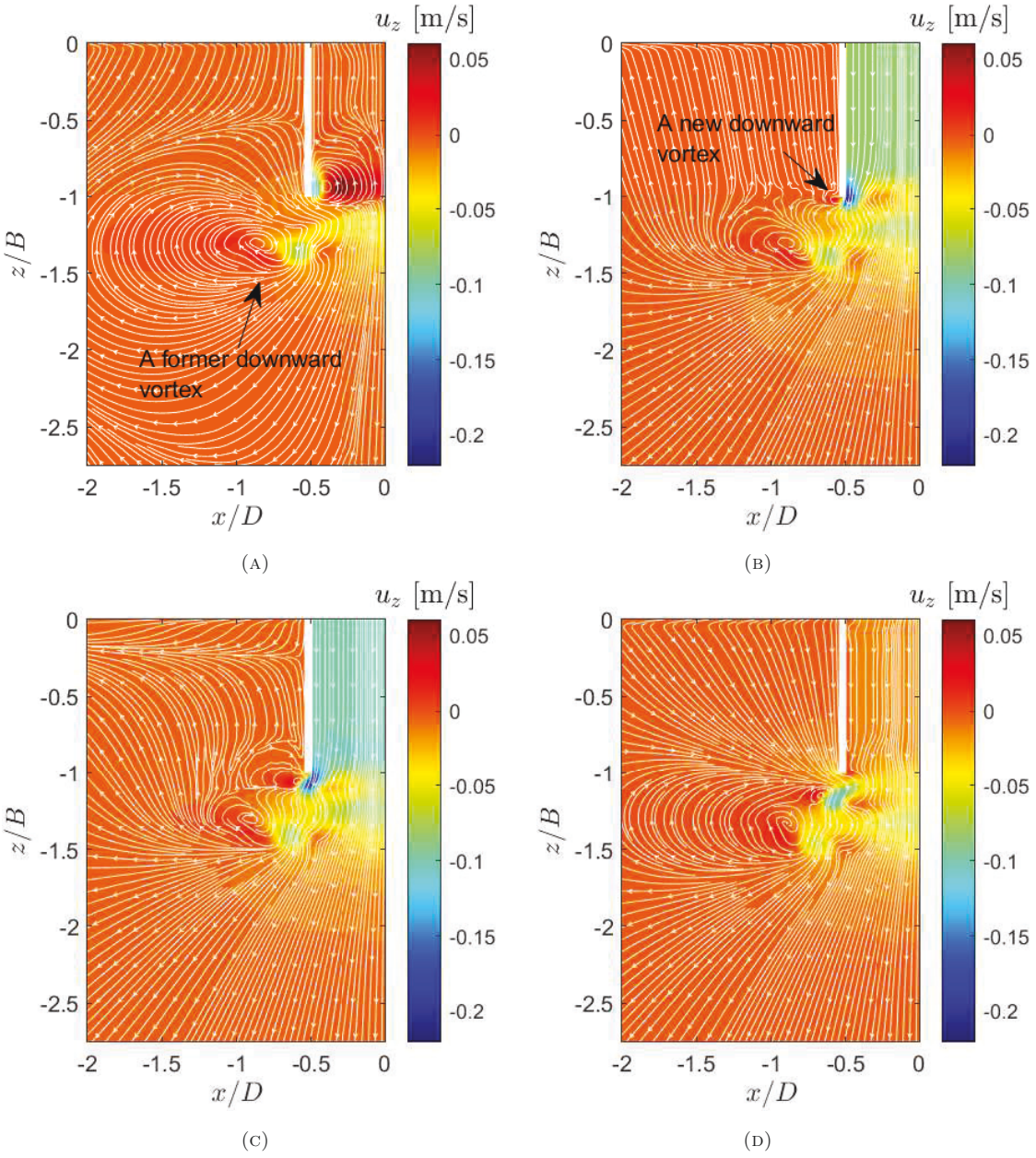

Figure 6.11: The streamline and vertical velocity fields, u_z, for a SE OWC predicted at times: (A) $t = 4T_f$, (B) $t = 4.15T_f$, (C) $t = 4.25T_f$ and (D) $t = 4.5T_f$ under a low-frequency excitation when $\omega_f^2 B/g = 0.5$ and $\eta_o^i/B = 0.11$.

Figure 6.11 concerns the flow field driven by a low-frequency excitation with $\omega_f^2 B/g = 0.5$ and at a small forcing amplitude number of $\eta_o^i/B = 0.11$. Figure 6.11(A) shows a "former" downward vortex located near the bottom edge at the beginning of a downward displacement of the water column ($t = 4.0T_f$). At $t = 4.15T_f$,

the near-field radiated wave elevation returns from its maximum elevation. At the beginning of this restoring stage of the η^e elevation, the size of the "former" vortex has reduced, and a new downward vortex has begun to generate (Figure 6.11(B)). The latter continues to develop in size until the internal water surface arrives at its mean free-surface (Figure 6.11(C)); the size indicated by the closed streamlines, denoted in black. As the downward displacement continues, the former vortex moves towards the new vortex. This is indicated by the adjacent locations of both vortices near the bottom edge, when the displacement completes (Figure 6.11(D)).

Comparing Figures 6.11 and 6.12, the differences between the low- and the high-frequency excitations relate to two points:

(i) The onset of the restoring stage of the η^e elevation, and

(ii) The field of the vertical velocity, u_z.

In the high-frequency excitation case, the restoring stage begins at $t = 4.28T_f$, immediately after the η^i elevation arrives at its mean position ($t = 4.25T_f$). In considering point (ii), the different velocity fields observed in Figures 6.11(C) and 6.12(B) arise due to the dependence of the velocity on the frequency. Despite these two differences, the vortex locations arising in the low frequency and high frequency excitations are very similar (see Figures 6.11(D) and 6.12(D)). Adopting the methods described in Sections 4.4.2 and 4.6.2, the normalised radial and vertical locations of the new vortex, R_v/D and $R_v/|Z_v|$, and the normalised vortex circulation, $\Gamma/(UD)$, are very similar; full details given on Table 6.2. When compared to the variations with the η_o^i/B number presented earlier in Figures 4.15(B) and (C), the variations with $\omega_f^2 B/g$ appear very small. Moreover, given the very small changes in the vortex strength (again detailed on Table 6.2), the small variation of the added mass with frequency is further confirmed.

6.4.3 Case II: Bell-shaped mouth

The variations of the hydrodynamic coefficients with the forcing frequency for the OWC with a BS mouth and $r_l = 0.5D$ are presented in Figure 6.13. In these cases, the forcing amplitudes are again considered to lie within the range $0.11 \leq \eta_o^i/B \leq 0.71$.

Comparison between the hydrodynamic coefficients in the BS case (Figure 6.13) and the SE case (Figure 6.9) confirms that the former exhibit a larger variation with

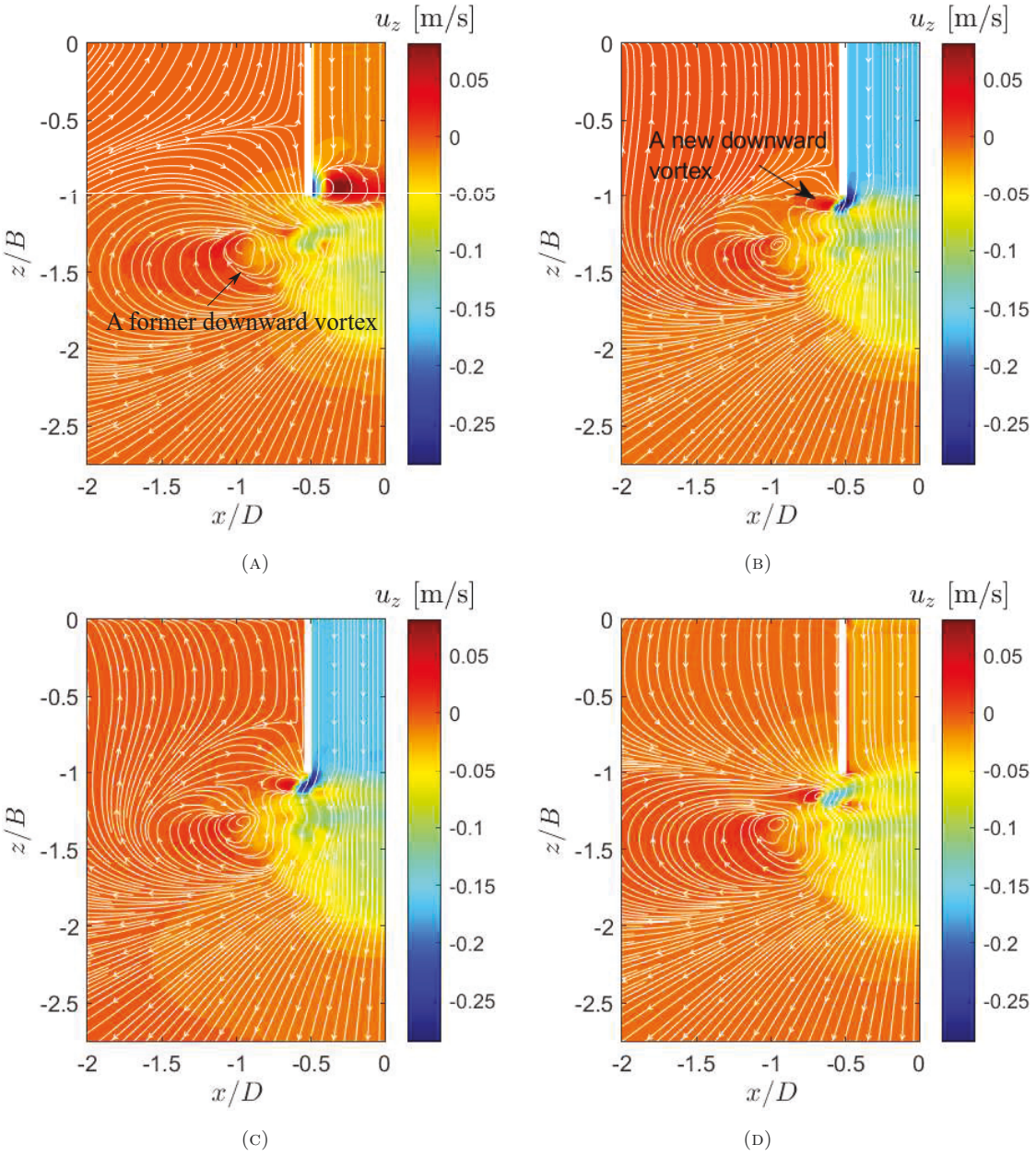

Figure 6.12: The streamline and vertical velocity fields, u_z, predicted at different times: (A) $t = 4T_f$, (B) $t = 4.25T_f$, (C) $t = 4.28T_f$ and (D) $t = 4.5T_f$ under a high-frequency excitation when $\omega_f^2 B/g = 1.4$ and $\eta_o^i/B = 0.11$.

frequency. Evidence of this is given in Table 6.3. In considering these results, the values were predicted under the smallest η_o^i/B condition for which a convergent b_2 coefficient was not established.

Following Section 6.4.1, the b_2 coefficients are re-plotted to show the influence of Re number. Figure 6.14 indicates that the BS case exhibits a more pronounced variation of the b_2 coefficient than the SE case shown earlier (Figure 6.10). This

Table 6.2: Vortex locations and circulations for the low-frequency and the high-frequency excitation cases

Excitation case	Vortex location R_v/D	R_v/Z_v	Vortex circulation $\Gamma/(UD)$
Low-frequency excitation (Figure 6.11)	0.62	0.25	0.31
High-frequency excitation (Figure 6.12)	0.64	0.25	0.33

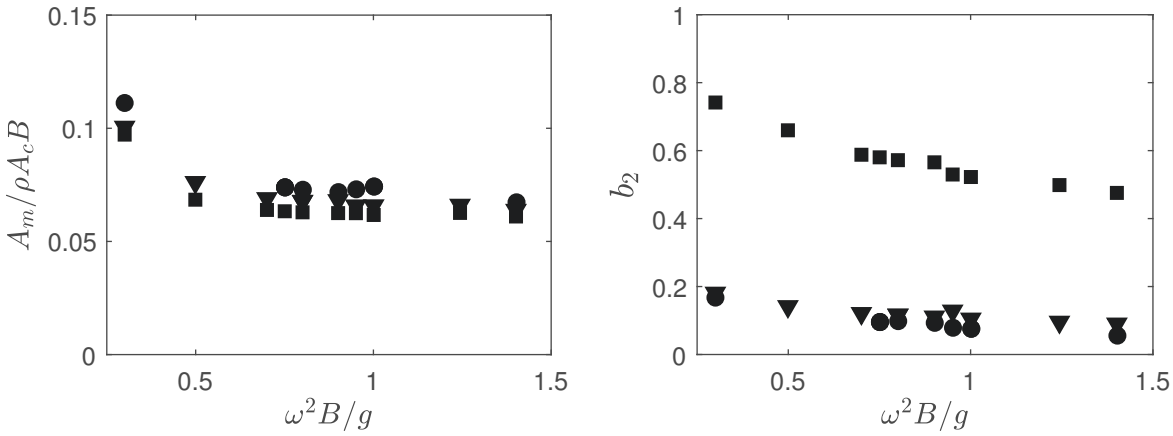

(A) (B)

Figure 6.13: (A) Variations of the added-mass coefficient, $A_m/\rho A_c B$, and (B) nonlinear damping coefficient, b_2, with $\omega_f^2 B/g$ for $\eta_o^i/B = 0.11$ [■], 0.4 [▼], 0.71 [●] for an OWC with a BS mouth, $r_l = 0.5D$ and $D/B = 0.435$.

suggests that an estimation of the hydrodynamic coefficients for an actual design of a bell-shaped OWC with $r_l = 0.5D$ using a small-scaled model, will most likely result in a conservative response prediction. In contrast, the coefficients predicted from a small-scaled model of a sharp-edged OWC are more likely to be reliable. These conclusions are based upon the assumption that Froude number scaling is applied in both cases as explained by the fact that vortex motion will be developed in a SE OWC irrespective of Re.

6.5 Relative importance of vortex formation

Figure 6.15(A) concerns the variations in the nonlinear energy loss, El_{NL}, and vortex kinetic energy, Ek_v, with forcing frequency for an OWC with a SE mouth. The data

Table 6.3: Range of the hydrodynamic coefficients for the OWCs with BS and SE mouths when $0.2 \leq \omega_f^2 B/g \leq 1.4$

Mouth shape	$A_m/\rho A_c B$	b_2
BS	$0.06 - 0.10$	$0.48 - 0.74$
SE	$0.15 - 0.16$	$1.86 - 2.10$

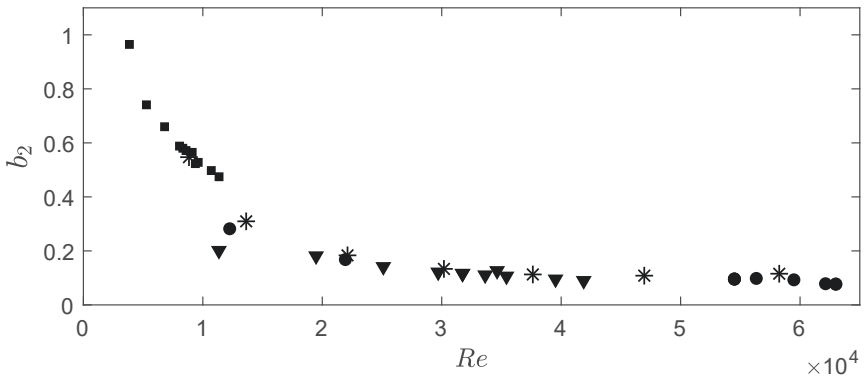

(a)

Figure 6.14: The variation of the b_2 coefficient with Re number for an OWC with a BS mouth and $r_l = 0.5D$. The data includes varying $\omega_f^2 B/g$ number with $\eta_o^i/B = 0.11$ [■], 0.4 [▼], 0.71 [•], and varying η_o^i/B with $\omega_f^2 B/g = 0.87$ [∗].

in this figure corresponds to the coefficients given in Figure 6.9 for $\eta_o^i/B = 0.11$. While El_{NL} was computed as $2/3\rho b_2 A_C (\eta_o^i)^3 \omega_f^2$, Ek_v value was estimated using the method described in Section 4.4.4. As expected, El_{NL} increases with the forcing frequency. Furthermore, the comparison between El_{NL} and Ek_v shown in Figure 6.15(a), proves that vortex formation is the primary source of the nonlinear damping for the OWC at all forcing frequencies.

The variation of El_{NL} shown on Figure 6.15(a) together with the small changes in b_2 (Figures 6.8(b) and 6.9(b)) prompt an investigation of the importance of vortex damping at varying frequencies. To address this, the ratio of the nonlinear energy loss, El_{NL}, to the mechanical energy of the water column, E_m, is evaluated; the latter computed by summing the energy to restore the displaced water column and the kinetic energy associated with the water column and the external fluid. Figure 6.15(b) presents the variation of El_{NL}/E_m with the $\omega_f^2 B/g$. Evidently, El_{NL}/E_m increases substantially under resonant or near-resonant conditions, when the frequency is at the damped natural frequency ($\omega_d^2 B/g = 0.87$ indicated by the blue line). Under a non-resonant condition, for example with the frequency shifted about 10% of the

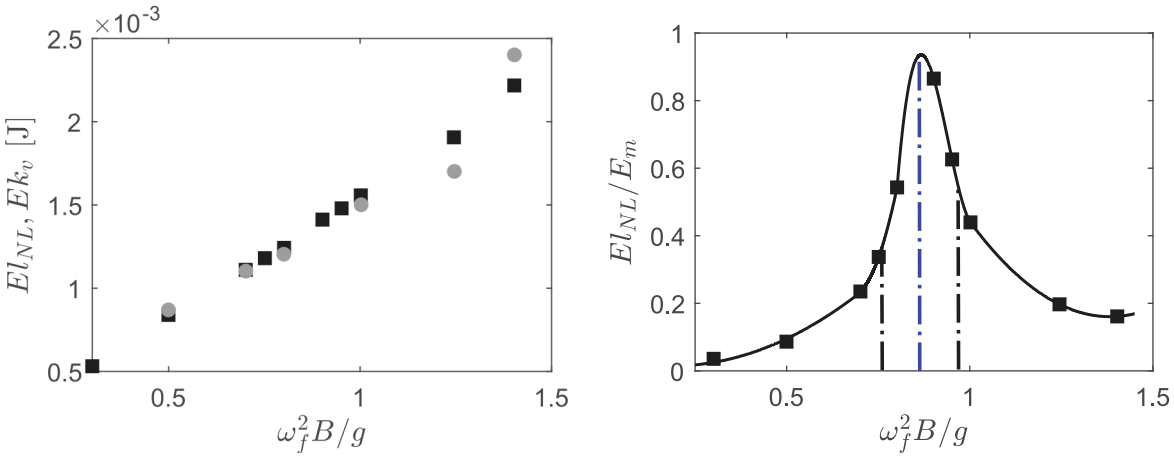

(A) (B)

FIGURE 6.15: Variations with $\omega_f^2 B/g$: (A) the nonlinear energy loss, El_{NL} [■], and the vortex kinetic energy, Ek_v [•], and (B) the ratio of the nonlinear energy loss to the mechanical energy, El_{NL}/E_m, for $\eta_o^i/B = 0.11$ [−■−]. The damped natural frequency, ω_d [— · —], and frequencies [— · —] 10% lower and higher than ω_d are also indicated.

resonant frequency, El_{NL}/E_m is 0.4 for a low-frequency excitation ($\omega_f^2 B/g = 0.77$) and 0.55 for a high-frequency excitation ($\omega_f^2 B/g = 0.97$); both frequencies indicated by the black dashed lines on Figure 6.15(B)).

The variation in El_{NL}/E_m suggests that the importance of vortex damping on the response amplitude depends on the nature of the excitation condition; specifically whether it is a low-frequency or high-frequency excitation. This is confirmed by the accuracy of the linear potential solution, $\eta_o^i/\eta_{o,LPT}^i$, shown in Figure 6.16. Within the figure, η_o^i denotes the response amplitude predicted from the viscous flow solution and $\eta_{o,LPT}^i$ the analytically predicted response amplitude using Linear Potential Theory (LPT). This figure also describes the normalised response amplitude, η_o^i/A_o^P, due to various forcing frequencies; where $A_o^P = P_o/\rho g$ is fixed at 0.01 m in FAPTs. Within these calculations, an OWC with SE mouth, $D/B = 0.64$ and $B = 0.11$ m was considered. It is clear that at the damped natural frequency ($\omega_d^2 B/g \approx 0.8$), $\eta_o^i/\eta_{o,LPT}^i$ is 0.24, its smallest value. Interestingly, at lower frequencies, $\eta_o^i/\eta_{o,LPT}^i$ is typically higher, indicating linear potential theory provides a better description of the response amplitudes than at the damped natural frequency. Conversely, at higher frequencies, the linear potential solutions are less accurate. This implies that the vortex more significantly dampens the response amplitudes in this range.

The significance of vortex damping is also clearly evident in wave excitation

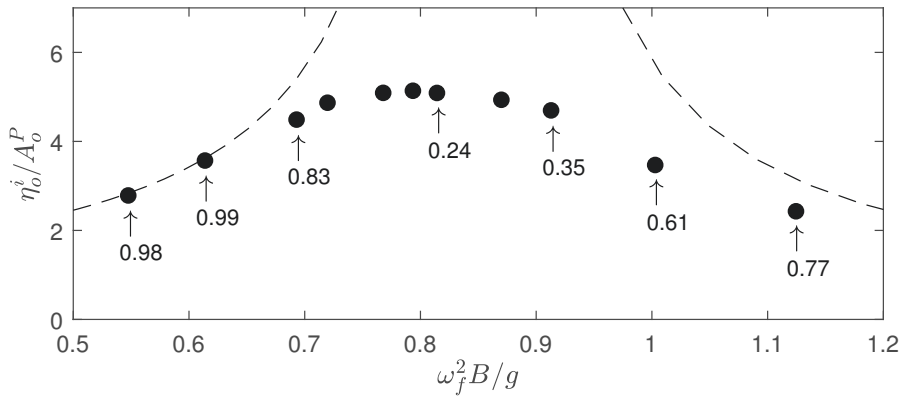

(A)

FIGURE 6.16: The response amplitude relative to the amplitude of air pressure, η_o^i/A_o^P, for an OWC with a SE mouth predicted from the linear potential solution [— —] and the viscous flow solver [•]; the ratio between the two, $\eta_o^i/\eta_{o,LPT}^i$, indicated by the numerical values. In all calculations, the air pressure amplitude, $P_o/\rho g = A_o^P$, was fixed at 0.01 m.

problems. The RAO, or η_o^i/A_o, for an OWC with a constant D/B ratio subjected to varying incident wave frequencies, ω, was shown earlier in Figure 5.13. Comparing the associated cases for low- and high-frequency excitations confirms that the discrepancies are more pronounced at higher frequencies. Likewise, the η_o^i/A_o values for OWCs with varying D/B ratios at a fixed wave frequency of $\omega^2 B/g = 0.87$ also confirm this. For example, the OWC with the largest D/B ratio, that experiences a high-frequency excitation, has larger discrepancies in η_o^i/A_o when compared to the smallest D/B ratio under a low-frequency excitation. Once again, the discrepancies are largest in the case of a medium D/B ratio under resonant excitations. Full details of the $\eta_o^i/\eta_{o,LPT}^i$ ratios for the three OWCs are provided in Figure 6.17.

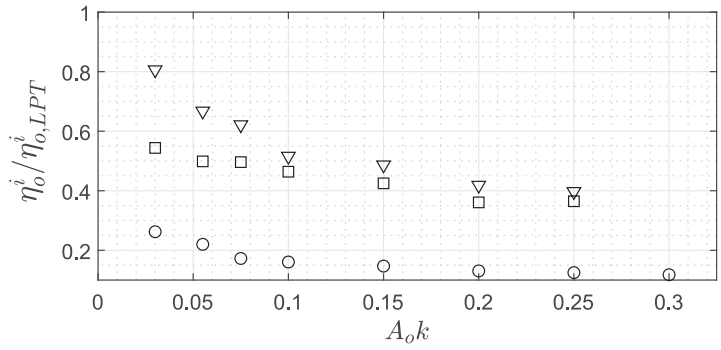

FIGURE 6.17: Ratios of $\eta_o^i/\eta_{o,LPT}^i$ for the OWCs with a variety of D/B ratios: 0.15 [▽], 0.435 [○] and 1.25 [□] undergoing wave excitations.

This finding may be generally applicable for any body heaving under a wave excitation. For example, the earlier laboratory studies undertaken by Rodriguez (2016) and Bruggemann (2017), who respectively investigated a box and a truncated cylinder, both heaving in waves, suggest that this may be the case. Interestingly, the present findings are at odds with the observations reported by Stiassnie et al. (1984), who found that the effect of the vortex motion on the wave transmission past a vertical plate was more pronounced in a low wave-frequency range. The explanation for this is as follows. In the plate case, the role of the vortex motion is a direct consequence of the path of the fluid particle that passes the plate edge. However, in the present context (the response of an oscillating body), the importance of the vortex motion is dependent upon the relative importance of the vortex damping force in a force balance. This is clearly very different.

6.6 Applicability of forced oscillation coefficient

The hydrodynamic coefficients for OWCs under forced oscillations have been evaluated. The present aim is to evaluate the applicability of these coefficients in wave-excitation problems. In the context of an OWC, the linear superposition theory may be valid if the following apply:

(i) The flow kinematics driven by different excitation mechanisms are similar, and

(ii) The hydrodynamic coefficients are assumed to be dependent on the amplitude of a water column motion.

Point (i) was addressed by Stansby et al. (1983), who confirmed good agreement between the force coefficients for planar oscillatory flow tests and those computed from shallow water wave tests. In addressing the appropriate variable to ensure similarity, the amplitudes of a water column, η_o^i, in both regular wave and forced oscillation tests will be made comparable. The explanation for this lies in the fact that the vertical velocity of a water column dictates the flow in a pure radiation problem. In respect of point (ii), the importance of this has been confirmed in Section 6.3.1. Any evaluation of the applicability of the hydrodynamic coefficients computed from a forced oscillation test must consider this dependence.

To undertake this evaluation, data describing the vertical force that arises in a FAPT and RWT is required. As described in Section 5.10, the force computed from

a FAPT physically represents the hydrodynamic force. In a RWT, the vertical force, F_v, acting in a potential flow physically represents the summation of the hydrodynamic force and the incident wave-excitation force; the latter commonly known as the Froude-Krylov force, F_{fk}. The vertical force arises due to the contributions from the pressure fields induced by the water column oscillation and the incident wave (Ashlin et al., 2017). However, the earlier explanation in Section 5.9 confirmed that in a viscous flow, nonlinearities associated with the vortex motion may affect the pressure at the draft of an OWC. This indicates that the wave-excitation force is effectively the total contributions from the incident wave and the nonlinearities associated with the vortex motion.

Given this understanding, the procedure to evaluate the applicability of a forced oscillation test is outlined as follows:

(a) The added mass, A_m, and the nonlinear damping coefficient, b_2, for an OWC are predicted from a FWCT; these A_m and b_2 variables are hereafter referred to as the forced oscillation coefficients.

(b) The radiation damping coefficient, b_1, is predicted from the LPT.

(c) The wave-excitation force is estimated by subtracting the vertical force of the RWT from that of the FAPT; both tests having a comparable η_o^i/B and KC number to satisfy the requirement of point (i) noted above.

(d) The original η^i elevation (corresponding to the RWT and evaluated from the viscous flow solver) is re-simulated by substituting the estimated wave-excitation force, F_{ext}, and the forced oscillation coefficients into Equation (2.40), and

(e) The values of A_m and b_2 coefficient are re-computed by implementing Equation (2.40), and fitting the original η^i elevation and the F_{ext} force over one period or half-periods of oscillation.

Provided that comparisons between (A) the re-simulated and the original η^i elevation, and (B) the re-computed coefficients and the forced oscillation coefficients are good, the latter are considered applicable for a wave-excitation problem.

6.6.1 Irrotational flow condition

At first, the applicability of the forced oscillation coefficients for an OWC with a BS mouth, $r_l = 0.5D$ and $D/B = 0.435$ is investigated. Two representative cases of $\eta_o^i/B \approx 0.25$ and 0.5 are considered. These respectively correspond to a wave steepness of $A_o k = 0.054$ and 0.13.

Figure 6.18 shows time-histories of the internal surface elevations, $\eta^i(t)$, driven by the regular wave excitations. The original and the re-simulated elevations agree well; both in terms of the amplitude and the phase of the elevation. Furthermore, the forced oscillation coefficients are in good agreement with the re-computed coefficients. Evidence of this is provided on Table 6.5.

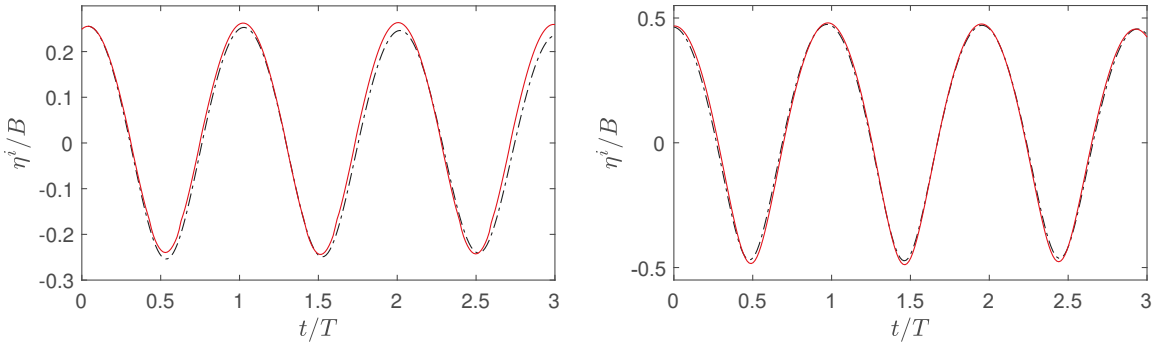

(A) (B)

Figure 6.18: Time-histories of the internal surface elevations, $\eta^i(t)$, within an OWC with a BS mouth, $D/B = 0.435$ and $r_l = 0.5D$; comparisons between the elevation re-simulated using the forced oscillation coefficients [— · —] and the original elevation [——], that responds to the incident waves with steepness of: (A) $A_o k = 0.054$ and (B) $A_o k = 0.13$.

Table 6.4: Directionally invariant coefficients computed from RWTs and FWCTs for the OWC with a BS mouth for different $A_o k$ cases

$A_o k$ and η_o^i/B	Test	$A_m/\rho A_c B$	b_2
$A_o k = 0.054$, $\eta_o^i/B = 0.25$	FWCT	0.09	0.20
	RWT	0.07	0.26
$A_o k = 0.130$, $\eta_o^i/B = 0.50$	FWCT	0.09	0.14
	RWT	0.07	0.13

This agreement confirms the applicability of the forced oscillation coefficients when predicting the wave-induced response of the water column. However, it should be noted that the vortex motion has no significance on the OWC for the present η_o^i/B

cases. The explanation for this lies in the two earlier confirmations: (i) the increasing importance of the nonlinear damping force begins at $\eta_o^i/B = 0.38$ (Figure 6.7(D)), and (ii) the flow is considered irrotational even at $\eta_o^i/B = 0.75$ (Figure 5.23(C)). On this basis, it is concluded that the forced oscillation coefficients are appropriate, provided that vortex damping plays no significant role on the response of the water column within a bell-mouthed OWC.

6.6.2 Separated flow condition

To extend these results, the hydrodynamic coefficients for OWCs with SE mouths undergoing different excitation conditions will now be addressed. These concern $D/B = 1.25$, 0.435 and 0.15, corresponding to a high-frequency, a resonant and a low-frequency excitation condition, respectively. All the OWCs were subject to RWTs with the wave frequencies held at $\omega^2 B/g = 0.87$.

These test conditions were replicated in FAPTs; the air pressure amplitudes, $P_o/\rho g$, prescribed such that the response amplitudes, η_o^i, in the FAPTs were again comparable to those in the RWTs. This is confirmed in Figures 6.19(A)-(C).

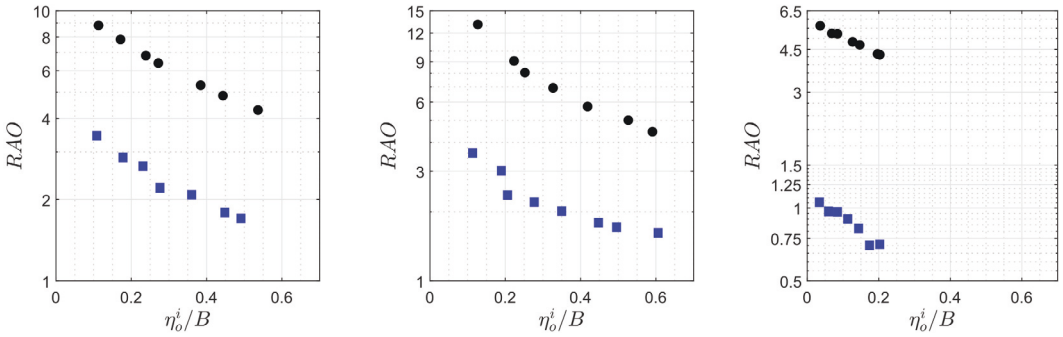

(A) $D/B = 0.15$ (B) $D/B = 0.435$ (C) $D/B = 1.25$

FIGURE 6.19: Response Amplitude Operators, *RAO*s, for the three different OWCs in response to FAPTs [●] and RWTs [■] in a viscous flow.

Resonant excitation condition

To begin, the applicability of the forced oscillation coefficients appropriate to a resonant condition is evaluated by undertaking the procedure (a)-(b) outlined earlier. The directionally dependent coefficients of $A_m/\rho A_C B$ and b_2 were re-computed from the RWTs. A comparison between these coefficients and the forced oscillation coefficients is presented in Figure 6.20. For ease of comparison, the forced oscillation

coefficients shown earlier in Figure 6.3, have been replaced with the 2^{nd}-order polynomial fitted lines on Figure 6.20.

Figure 6.20(b) confirms that the b_2 coefficient is in good agreement across all η_o^i/B numbers for each travel direction of the water column. In contrast, Figure 6.20(a) shows that the $A_m/\rho A_C B$ coefficient is in poor agreement; the largest departure being observed in the case of $\eta_o^i/B \approx 0.6$ ($A_o k = 0.3$).

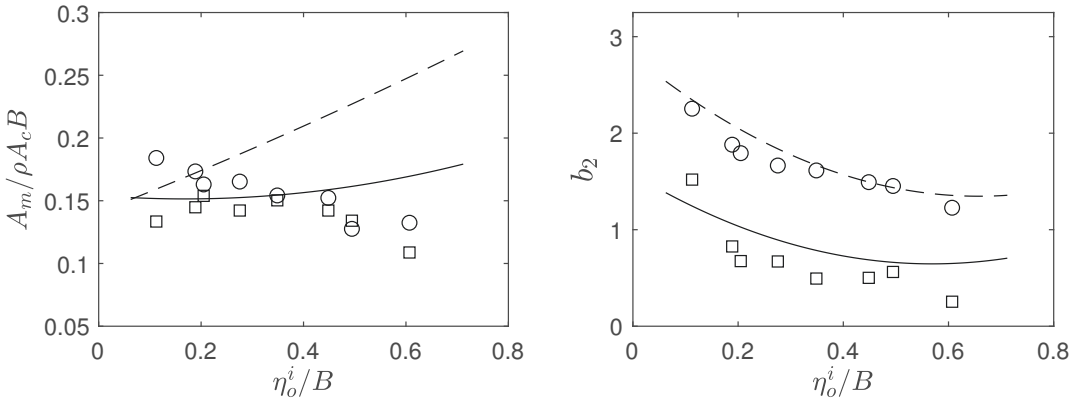

(a) (b)

Figure 6.20: Directionally dependent added-mass, $A_m/\rho A_c B$, and nonlinear damping coefficients, b_2, for an OWC with a SE mouth and $D/B = 0.435$, under regular wave conditions computed using the estimated wave-excitation force, F_{ext}, and compared with the forced oscillation coefficients for downward [$\circ$, – –] and upward displacements [$\square$, ——]; the 2^{nd}-order polynomial fitted lines corresponding to the forced oscillation coefficients.

To further investigate these results, the directionally invariant coefficients were also quantified. In addition, the coefficients were re-computed by adopting the Froude-Krylov force, F_{fk}, instead of the estimated wave-excitation force, F_{ext}. In adopting the F_{fk} force, nonlinearities associated with vortex motion were neglected. As in previous analysis, the time-histories of the F_{fk} force and the η^i elevation were substituted into the equation of motion. Figure 6.21(a) shows comparisons between the re-computed $A_m/\rho A_C B$ coefficient (presented by the symbols) and the forced oscillation coefficient (indicated by the line). Once again, large discrepancies arise, particularly at large η_o^i/B numbers. Conversely, Figure 6.21(b) confirms good agreement in respect of the b_2 coefficient at all η_o^i/B numbers, provided that nonlinearities were included in the wave-excitation forces.

The significance of these discrepancies is evaluated by comparing time-histories of the original and the re-simulated η^i elevations. Figure 6.22(a) shows that the

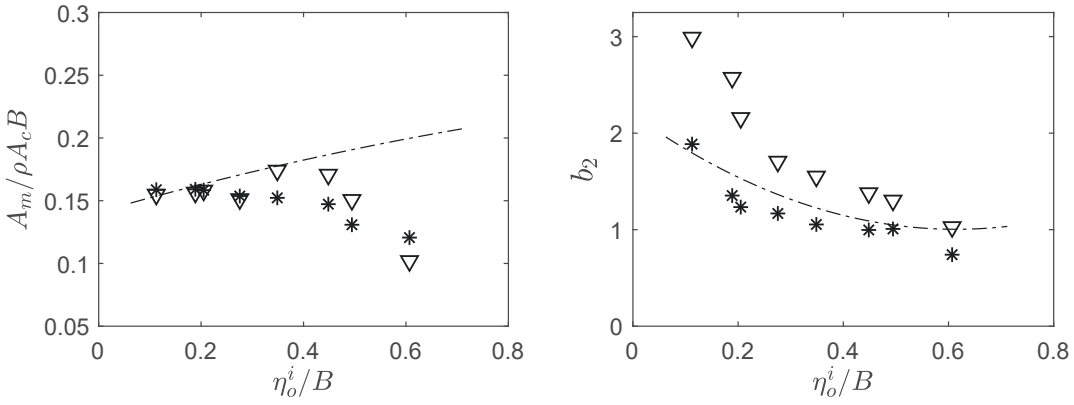

(A) (B)

Figure 6.21: Directionally invariant added-mass, $A_m/\rho A_C B$, and nonlinear damping coefficients, b_2, for an OWC with a SE mouth and $D/B = 0.435$ under the regular wave conditions computed using either the estimated wave-excitation force, F_{ext} [$*$], or the Froude-Krylov force, F_{fk} [$\triangledown$], and compared with the forced oscillation coefficients represented by the 2^{nd}-order polynomial lines [$-\cdot-$].

elevation driven by the linear wave with $A_o k = 0.03$ ($\eta_o^i/B = 0.1$) was accurately re-simulated using the forced oscillation coefficients and the F_{ext} force. Conversely, the re-simulated elevation corresponding to the steepest nonlinear wave with $A_o k = 0.3$ ($\eta_o^i/B = 0.6$), deviates from the original elevation (Figure 6.22(B)). Nevertheless, the extent of this difference is small, both in terms of the amplitude and phase. Certainly, it is much less significant than the deviation in the added-mass coefficient. The explanation for this lies in the fact that the nonlinear damping force is most important in determining the response under a resonant condition (Figure 6.15(B)).

Figure 6.22 also shows that neglecting the nonlinearities in the wave-excitation force causes discrepancies in the re-simulated elevations. This supports the earlier comparison of the b_2 coefficients on Figure 6.21(B). Taken as a whole, the forced oscillation coefficients may be applied to accurately predict the wave-induced response of a water column in a resonant state only if: (i) the b_2 coefficient is reliably predicted from the forced oscillation test and (ii) nonlinearities associated with vortices are included in the wave-excitation force.

Non-resonant excitation condition

Figure 6.23(A) concerns the hydrodynamic coefficients arising in a low-frequency excitation ($D/B = 0.15$). The re-computed $A_m/\rho A_c B$ coefficient is approximately half the forced oscillation coefficient for all η_o^i/B numbers. Conversely, the b_2 coefficient

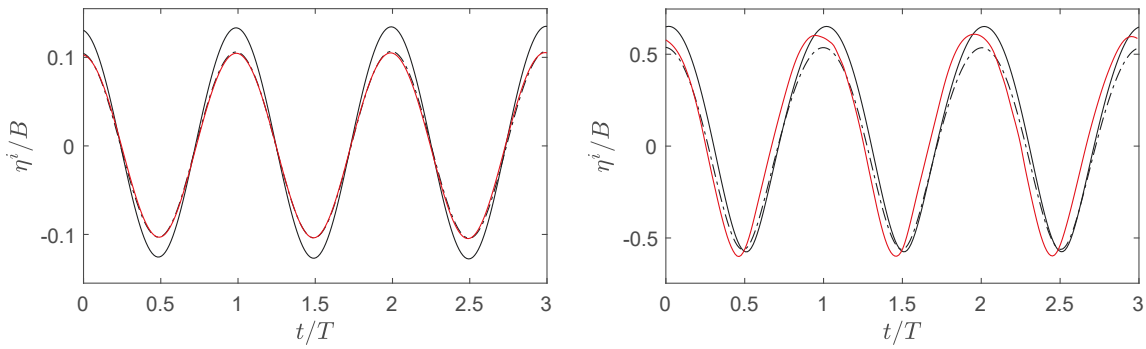

(A) (B)

Figure 6.22: Time-histories of the internal surface elevations, $\eta^i(t)$, within an OWC with a SE mouth and $D/B = 0.435$ re-simulated by adopting the forced oscillation coefficients and using either the estimated wave-excitation force, F_{ext} [— · —], or the Froude-Krylov force, F_{fk} [——], and comparisons with the original elevations [——], for: (A) $A_o k = 0.03$ and (B) $A_o k = 0.3$.

is shown to be in good agreement. Interestingly, nonlinearities in the wave-excitation force appear insignificant. Evidence of this is provided by the small difference between the coefficients re-computed using the estimated wave-excitation force, F_{ext}, and the Froude-Krylov force, F_{fk}.

Adopting these coefficients, the internal surface elevation was re-simulated using the F_{ext} force. Comparisons between the re-simulated and the original elevation presented in Figure 6.24(A) are in good agreement. This arises despite the poor description of the added mass, and the earlier evidence concerning the insignificance of vortex damping force (Figure 6.15(B)). Taken together, it appears that the hydrodynamic force under a low-frequency excitation is not that important. As a result, the implementation of forced oscillation coefficients in a low-frequency wave excitation is justified. Importantly, these comparisons also suggest that the nonlinearities in the wave-excitation force have a small part to play; the pressure field due to the incident wave being largely unaffected by the vortex motion at the bottom edge.

The description of the high-frequency excitation is very different. Figure 6.23(B) ($D/B = 1.25$) confirms that both $A_m/\rho A_c B$ and b_2 are poorly described at large η_o^i/B numbers. The discrepancies become even more significant when the nonlinearities in the wave-excitation forces are neglected. Furthermore, comparisons between the predicted elevation η^i/B given in Figure 6.24(B) reflect the poor description of the hdyrodynamic coefficients. Specifically, the elevation re-simulated using the F_{ext} force deviates more significantly as $A_o k$ increases. Moreover, the neglect of the force

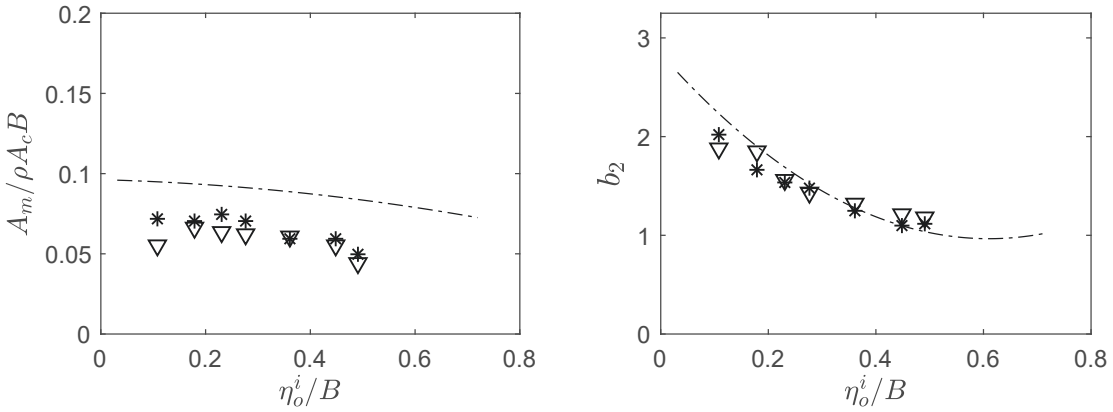

(A) $D/B = 0.15$

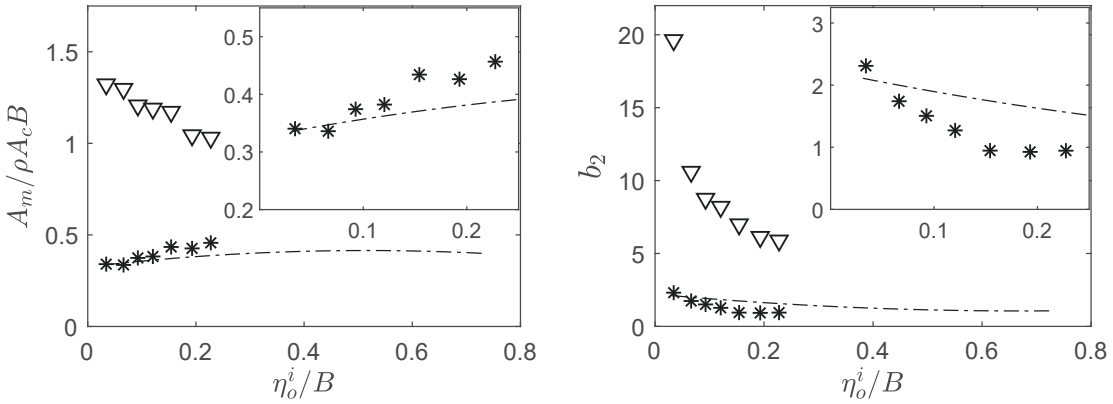

(B) $D/B = 1.25$

FIGURE 6.23: Directionally invariant added-mass, $A_m/\rho A_c B$, and nonlinear damping coefficients, b_2, for the OWCs with $D/B = 0.15$ and 1.25, computed by adopting either the estimated wave-excitation force, F_{ext} [$*$], or the Froude-Krylov force, F_{fk} [$\triangledown$], and comparisons with the forced oscillation coefficients, indicated by the 2^{nd}-order polynomial fitted lines [$—\cdot—$].

nonlinearities by adopting the F_{fk} force leads to a very poor description of the internal surface elevation. These results suggest that when modelling a high-frequency wave excitation, the forced oscillation coefficients are invalid and the nonlinearities in the wave-excitation force are extremely important.

Following on, the applicability of forced oscillation coefficients for an OWC with a fixed D/B ratio undergoing different wave-excitation conditions is investigated. Two cases of $\omega^2 B/g = 0.45$ and 1.25, with $D/B = 0.435$ are taken as representative examples. All computations implemented the F_{ext} force. The hydrodynamic coefficients, $A_m/\rho A_c B$ and b_2, for the low-frequency ($\omega^2 B/g = 0.45$) and high-frequency ($\omega^2 B/g = 1.25$) excitations are given on Table 6.5. Despite the difference in the

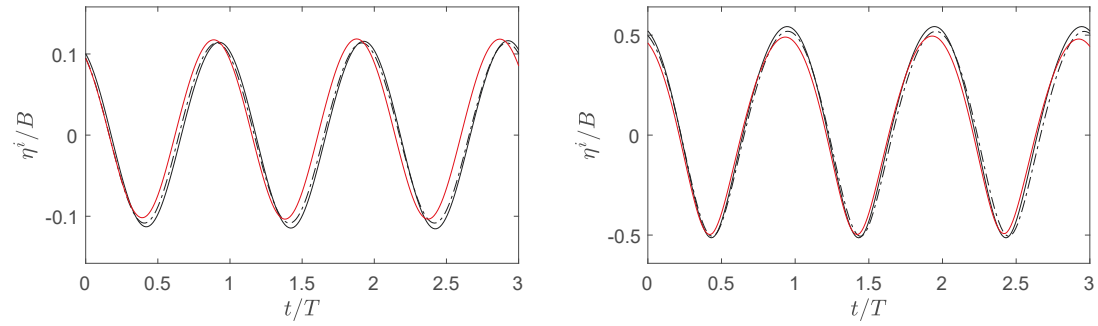

(A) $D/B = 0.15$

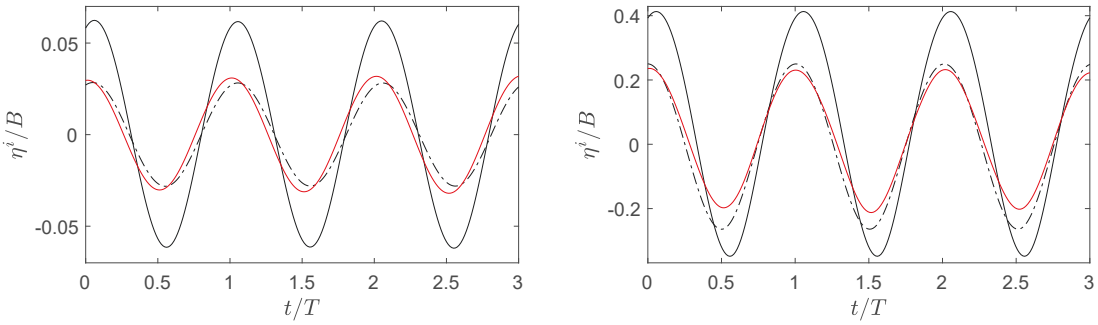

(B) $D/B = 1.25$

Figure 6.24: Time-histories of the internal surface elevations, $\eta^i(t)$, within an OWC with a SE mouth and for $D/B = 0.15$ and 1.25. In both cases, η^i was re-simulated by adopting the forced oscillation coefficients and using either the estimated wave-excitation force, F_{ext} [— · —], or the Froude-Krylov force F_{fk} [——]. Comparisons with the original surface elevations [——] are provided for two cases: $A_o k = 0.03$ (the first column) and $A_o k = 0.25$ (the second column).

low-frequency coefficients, good agreement between the re-simulated and the original elevation is observed in Figure 6.25(A). In contrast, the water surface elevation prediction for the high-frequency wave-excitation ($\omega^2 B/g = 1.25$) exhibits a discrepancy in the minimum elevation (Figure 6.25(B)). Clearly, these two contrasting results are consistent with the earlier cases involving different column diameters.

Table 6.5: Directionally invariant coefficients computed from RWTs and FWCTs for SE mouth at different frequencies

Frequency ($\omega^2 B/g$ or $\omega_f^2 B/g$)	Test	$A_m/\rho A_c B$	b_2
0.45	FWCT	0.17	1.70
	RWT	0.13	1.18
1.25	FWCT	0.14	2.5
	RWT	0.16	4.2

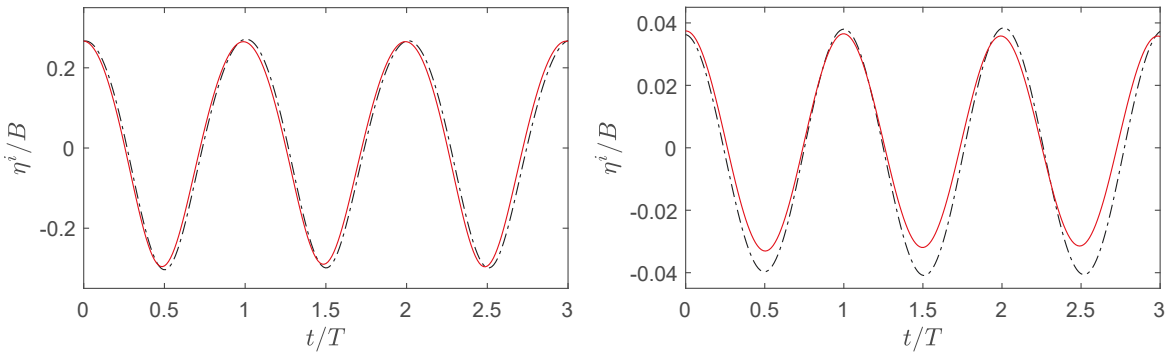

(A) $\omega^2 B/g = 0.45$ (B) $\omega^2 B/g = 1.25$

FIGURE 6.25: Time-histories of the internal surface elevations, $\eta^i(t)$, within an OWC with $D/B = 0.435$, re-simulated using the forced oscillation coefficients and the estimated wave-excitation force, F_{ext} [— · —], with comparisons to the original elevations [——]; two cases involving different wave frequencies, $\omega^2 B/g$.

Based upon these results, the applicability of forced oscillation coefficients to a wave-excitation problem and the validity of the linear superposition theory, depend on two issues:

(i) The theoretical *RAO* of the water column at a given wave frequency. When the *RAO* value exceeds one, the flow is dominated by the water column. Consequently, the similarity of the flow kinematics driven by the two different mechanisms is maintained.

(ii) The importance of the vortex damping force in the force balance. When this damping force is important under a wave excitation condition, but not comparable under a different (forced) excitation mechanism, the prediction of a wave-induced response using the forced oscillation coefficients will most likely be inaccurate.

6.7 Concluding remarks

This chapter has addressed the hydrodynamic coefficients for cylindrical OWCs. The vortex motion at the lowermost end has been confirmed as the primary source of the nonlinear damping coefficient, b_2, for an OWC with a SE mouth. This applies over a broad range of forcing amplitudes, η_o^i/B, and a practical range of forcing frequencies, ω_f. The present calculations have shown that the influence of cylinder aspect-ratio,

D/B, on b_2 is small; the coefficient converging to 1.0 at large η_o^i/B numbers and for all D/B ratios. In contrast, the variation of b_2 with mouth shape is evident. The smallest b_2 values for all cases arise in the absence of vortices.

The influence of the vortex motion also extends to the added-mass coefficient, $A_m/\rho A_c B$. For an OWC with a SE mouth, this coefficient is larger than the linear potential solution as η_o^i/B increases. This is consistent with the variation of the effective draft and the near-field radiated wave amplitude. Conversely, $A_m/\rho A_c B$ for an OWC with a BS mouth and $r_l = 0.5D$ is independent of the η_o^i/B number. Again, this is consistent with the constant radiated wave amplitude in the near-field.

Interestingly, the hydrodynamic coefficients for the SE mouth have small variations with the forcing frequency. This does not, however, indicate the relative importance of vortex damping on the response. Indeed, by considering the relative importance of the vortex damping force in a force balance, it was shown that irrespective of the excitation mechanism, the vortex induced damping is most important under a resonant or near-resonant condition, and is more important for a high-frequency excitation.

The appropriateness of linear superposition to solve a wave-excitation problem has also been evaluated. Under a high-frequency wave excitation, the theory is invalid; the prediction of the wave-induced response using forced oscillation coefficients generating a substantial error. Conversely, these coefficients give reasonably accurate predictions of the response in either a resonant state or under a low-frequency wave excitation. The former is explained by the dominance of the flow driven by the water column in comparison to the wave flow and the relative significance of the vortex damping force in the force balance. In the latter case, the explanation lies in the reduced importance of the hydrodynamic force in comparison to the incident wave force.

7
Conclusions

The principal aim of the present study was to advance our understanding of the dynamic response of the water column within a cylindrical OWC. The physical origins and the importance of the nonlinearities in both the forces and the response have been investigated. Additionally, the hydrodynamic coefficients for the OWC subjected to different excitation conditions have been evaluated. In undertaking these tasks, guidance is provided as to the appropriate time-domain modelling of an OWC. Key aspects of the study have included:

(A) The development of a viscous flow model of an OWC subject to varying excitation mechanisms.

(B) The validation of this model with comparisons to available laboratory data.

(C) The establishment of a wide range of test cases covering a variety of dimensions and mouth shapes operating in a range of flow conditions.

(D) The development of a linear analytical solver modelling a cylindrical OWC in three dimensions following the work of Evans & Porter (1997).

(E) Comparisons between (A) and (D) for the broad range of cases noted in (C), highlighting the origins and importance of the nonlinearities arising, both in the applied forcing and the water column response.

7.1 Principal findings

The principal findings of the present study are summarised as follows:

1. The LES classical Smagorinsky turbulence model was shown to be unsuitable for modelling the wall-bounded flow within an OWC. In contrast, the LES dynamic Smagorinsky turbulence model is preferable in all cases.

2. In the numerical modelling of a freely damped oscillation, good agreement was observed between all available laboratory data and the numerically predicted internal water surface elevation within an OWC. In achieving these results, it was also confirmed that continuously resolving the periodic boundary layer up to $y^+ = 1$ was less important than resolving the vertical grid size near the internal free-surface.

3. The numerical modelling of a forced water column oscillation was verified in terms of the air pressure above the water surface. Once again, good agreement was observed between existing laboratory data and the present numerical predictions. In these cases, resolving the vertical grid size is less important than the boundary layer, and setting the latter to $y^+ \leq 20$ is sufficient to obtain an accurate prediction of the air pressure.

4. Investigations of the rotational flow and the radiated wave fields generated in a Forced Water Column Test (FWCT) have confirmed the following descriptions:

   (a) Vortex circulation, Γ, and kinetic energy, Ek_v, have a nonlinear relationship with the forcing amplitude, η_o^i.

   (b) The vortex motion at the bottom mouth of an OWC influences the effective draft, B_e; both the vortex location and the effective draft increase with the forcing amplitude number, η_o^i/B.

   (c) The normalised circulation, Γ/UD, and the normalised locations, R_v/D and $R_v/|Z_v|$, of the vortex closest to the mouth, show small variations with the forcing frequency in the range of $0.2 \leq \omega_f^2 B/g \leq 1.4$. In contrast, both exhibit a dependence on the η_o^i/B number.

(d) The near-field radiated wave elevation close to an OWC with a sharp-edged (SE) mouth exhibits two distinct characteristics: both the amplitude and phase difference are progressively reduced. This contrasts with the far-field radiated wave elevation in which only its phase difference is progressively reduced.

(e) The two nonlinear characteristics (noted above) are much reduced in the near-field radiated wave elevation generated around an OWC with a bell-shaped (BS) mouth and a lip radius of $r_l = 0.5D$. Unlike the SE case, no vortex motion is generated near the bottom edge of this OWC. This is true for all η_o^i/B numbers considered.

5. The description noted above confirms that the two distinct characteristics of the near-field radiated wave elevation in the SE case are associated with the vortex formation and motion at the bottom edge. Furthermore, in respect of the progressively reduced amplitude, the vortex effect only influences the exponentially decaying (evanescent) modes of the radiated waves. As a result, the linear radiation theory is valid in the far field.

6. The increasing effective draft, B_e, with the η_o^i/B number is consistent with the increasing trend of the added-mass coefficient, $A_m/\rho A_c B$, for the SE mouth in a viscous flow. The progressive discrepancy in this coefficient when computed from the linear potential and the viscous flow solutions is caused by the vortex motion at the bottom mouth. Clearly, this discrepancy is consistent with the departures from linear potential theory when considering the near-field radiated wave elevation. The implication of this lies in the reduction of the undamped natural frequency. This may, in turn, change the excitation condition of the OWC from a low-frequency to a resonant excitation condition.

7. The nonlinear damping coefficient, b_2, for the SE case has an exponentially decaying trend with η_o^i/B; the coefficient being convergent to 1.0 at large η_o^i/B numbers. This convergence is valid in the cylinder aspect-ratio range of $0.15 \leq D/B \leq 1.25$ and the frequency range of $0.2 \leq \omega_f^2 B/g \leq 1.4$.

8. The exponential decay of the b_2 coefficient indicates that the vortex motion becomes less important as the η_o^i/B number increases. This is confirmed by

the relative values of the second-harmonic component, $F^{(2)}_{t,o}/F_{SO}$, of the air pressure in the SE case; the latter converging to those for the BS case at large η^i_o/B numbers.

9. When compared to the variation with the η^i_o/B number, the variation in both the $A_m/\rho A_c B$ and b_2 for the SE case with the forcing frequency ($\omega_f^2 B/g$) are small. This is supported by the earlier finding confirming very small changes in the normalised vortex properties. As a result, the hydrodynamic coefficients for an OWC with a SE mouth operating at an η^i_o/B number can be reliably computed across a broad frequency range.

10. The nonlinear characteristics of the forces experienced by an OWC incorporate both a force asymmetry associated with the zero-crossing period and a secondary loading cycle. The former arises in both irrotational and separated flow conditions, while the latter critically depends on the vortex shedding at the bottom edge. Furthermore, the substantially reduced secondary loading cycles in a force time-history at large response amplitudes support the earlier finding concerning the reduced importance of vortex shedding as the amplitude of the water column motion increases.

11. The depth-variation in the harmonic components of the normalised inline-pressures also supports the physical origins noted above. This variation specifically confirms that the free-surface nonlinearity arising from Type-2 scattered waves has a negligible effect on the wave-excitation force. Moreover, vortex shedding is the major source of the nonlinearities in this force, provided that the relative diameter, D/λ, lies outside the linear diffraction regime. The explanation for this rests upon the fact that the inline pressure associated with the water column oscillation is near zero at all depth locations.

12. The effect of vortex shedding on a wave-excitation force is most pronounced under resonant and high-frequency excitation conditions. As a result, the Froude-Krylov force associated with an incident wave cannot accurately represent the wave-excitation force under these two excitation conditions. The disagreement between the internal water surface elevations re-simulated by considering or neglecting the vortex shedding supports this conclusion.

13. The high-frequency effects associated with the Type-2 scattered waves is not apparent in the internal water surface elevation. This is consistent with the earlier finding concerning the significance of the free-surface nonlinearity. Interestingly, response asymmetry is identified as a nonlinear characteristic of the internal surface elevation. However, the instantaneously varying mass of the water column is responsible for this characteristic. Moreover, this effect becomes more evident as η_o^i/B increases.

14. Progressively decreasing RAO and progressively varying phase difference are the other nonlinear characteristics of the internal water surface elevation. Comparisons between the internal water surface elevations driven by forced air pressure oscillations and wave excitations have confirmed that these characteristics are physically caused by the increased nonlinear damping acting on the OWC. For the SE mouth, the vortex motion primarily drives this nonlinear damping. Overall, the effects of the vortex motion on the response of the water column, regardless of the excitation mechanism, are described as follows:

    (a) In a high-frequency excitation, the phase difference progressively decreases with the amplitude of forcing, either air pressure or incident wave. Conversely, the phase difference in a resonant case is relatively invariant, while in a low-frequency excitation it progressively increases.

    (b) The RAO of any excitation case gradually decreases as the amplitude of forcing increases, and is shown to be convergent at large amplitudes of forcing.

    (c) The vortex damping of the response of a water column is most pronounced under a resonant condition. Furthermore, this effect is more significant in the case of high-frequency than low-frequency excitations. The relative importance of the vortex damping in the force balance at different excitation frequencies supports this view.

15. In a separated flow condition, the linear superposition theory is valid for resonant and low-frequency wave-excitations. As a result, the associated forced oscillation coefficients are applicable to the prediction of the wave-induced responses of a water column in these conditions. In the absence of vortices, the theory is expected to be valid in all cases.

16. The reduction of the energy loss in a semi-circular (SC) case at the smallest amplitude of water column motion is estimated to be 20% of the energy loss for a SE case. A BS mouth is more effective in reducing the energy loss. For example, when $r_l = 0.11D$, the energy loss is approximately 50% of that in the SE case. With $r_l = 0.5D$, the energy loss is further reduced. The effectiveness of the SC mouth may be improved by increasing its curvature radius. However, to achieve this, the wall must be thickened. This may, in turn, increase the wave reflection and reduce the response amplitude of the water column, specifically in a high-frequency excitation condition.

17. This study has confirmed the nonlinear characteristics of the response of a water column and the excitation condition under which linear potential theory and linear superposition theory are valid in predicting the response. Given that the water column can be considered as a rigid body when $D/\lambda \leq 0.2$, these insights may be applied to any real wave energy converter that utilises a floating rigid body. In choosing the appropriate hydrodynamic coefficients, the dependence of these coefficients on the body motion instead of the amplitude of an incident wave should be considered; the former dependence having a physically grounded basis.

7.2 Recommendations for future work

1. The important role of the vortex motion in damping the response of an OWC and the inappropriateness of linear superposition theory under a high-frequency excitation has been described. However, there remains no clear definition of the lower boundary of the wave frequency corresponding to a high-frequency excitation for a given D/B ratio. An analysis that systematically quantifies the validity of using forced oscillation coefficients would be of substantial practical value.

2. The importance of nonlinearities in a wave-excitation force has been established. A force model that is more accurate than the Froude-Krylov force approximation is critically important if reliable time-domain modelling of an OWC is to be achieved.

3. The importance of vortex shedding and motion of the water column in producing nonlinearities in the air pressure has been confirmed. To evaluate the potential nonlinearities that may arise due to hydrodynamic-aerodynamic interactions, a PTO system should be incorporated into the OWC. In a FWCT, this system may be modelled as an orifice integrated into the moving piston (wall) placed above the internal free-surface of the OWC. Alternatively, an orifice may be integrated into the fixed upper wall of the OWC in a RWT. This is based upon the understanding that free-surface nonlinearity does not affect the motion and hence the air pressure.

4. The physical causes of any nonlinear response of a water column are vortex shedding and nonlinear inertial forcing. To understand any nonlinearities that may be provoked by a PTO system on the response, either a FAPT or a RWT may be explored. A numerical model of the former may consider an additional air chamber connected through an orifice to the air chamber located immediately above the internal free-surface. The prescribed air pressure is imposed in the additional air chamber.

5. Air compressibility may also affect the air pressure in a full-scale OWC. This has been suggested by Elhanafi et al. (2017c) who confirmed an insignificant change in the internal surface elevation, but a marked reduction in the air pressure and hence the hydrodynamic efficiency of a full-scale OWC. Given this view, future viscous flow modelling should incorporate air compressibility when investigating the nonlinear response and nonlinear air pressure at full scale.

6. The present study has been limited to regular wave cases. To advance the design of an actual OWC, realistic sea states must be incorporated. This must be included in both experimental and numerical viscous flow modelling, and should also address any scale effects.

7. Some of the findings reported in earlier studies of bottom-standing OWCs have been confirmed and explored in this thesis. It would be interesting to investigate whether the present findings are more generally applicable in a broader wave energy context. This includes the nonlinear response behaviour, the nonlinear wave-excitation and air forces, the variations of the hydrodynamic

coefficients and their applicability to wave-excitation problems. Specifically, the present effects should be considered in the context of an OWC integrated into a breakwater, a U-shaped OWC and the full range of floating OWCs.

References

Aalbers, A. (1984). The water motions in a moonpool. *Ocean Engineering*, *11*(6), 557 – 579. 55, 56

Abramowitz, M., & Stegun, I. (1972). *Handbook of mathematical functions with Formulae, Graphs and Mathematical Tables*. No. Tenth Printing in Applied Mathematics Series 55. National Bureau of Standards. 249

Ananthakrishnan, P. (1999). Radiation hydrodynamics of floating vertical cylinder in viscous fluid. *Journal of Engineering Mechanics*, *125*(7), 836–847. 105

Ananthakrishnan, P. (2015). Viscosity and nonlinearity effects on the forces and waves generated by a floating twin hull under heave oscillation. *Applied Ocean Research*, *51*, 138 – 152. 105

Aqua-RET (2008). Case study-european owc pilot plant pico/azores. 27

Ashlin, S. J., Sundar, V., & Sannasiraj, S. A. (2017). Pressures and forces on an oscillating water column - type wave energy caisson breakwater. *Journal of Waterway, Port, Coastal, and Ocean Engineering*, *143*(5). 217

Babarit, A., & Delhommeau, G. (2015). Theoretical and numerical aspects of the open source bem solver nemoh. In *In Proceedings of the 11th European Wave and Tidal Energy Conference*. 51

Babarit, A., Hals, J., Muliawan, M., Kurniawan, A., Moan, T., & Krokstad, J. (2012). Numerical benchmarking study of a selection of wave energy converters. *Renewable Energy*, *41*(0), 44 – 63. 30

Bai, W., & Eatock Taylor, R. (2006). Higher-order boundary element simulation of fully nonlinear wave radiation by oscillating vertical cylinders. *Applied Ocean Research*, *28*(4), 247–265. 51, 146

Bearman, P. W., Downie, M. J., Graham, J. M. R., & Obasaju, E. D. (1985). Forces on cylinders in viscous oscillatory flow at low keulegan-carpenter numbers. *Journal of Fluid Mechanics*, *154*, 337–356. 37, 40, 58, 112, 204

Bearman, P. W., Graham, J. M. R., Obasaju, E. D., & Drossopoulus, G. M. (1984). The influence of corner radius on the forces experienced by cylindrical bluff bodies in oscillatory flow. *Applied Ocean Research*, *6*, 83–89. 40

Boccotti, P. (2007). Caisson breakwaters embodying an owc with a small opening—part i: Theory. *Ocean Engineering*, *34*(5), 806 – 819. 27

Boccotti, P. (2012). Design of breakwater for conversion of wave energy into electrical energy. *Ocean Engineering*, *51*, 106 – 118. 27

Brito-Melo, A., Sarmento, A. J. N. A., Clément, A. H., & Delhommeau, G. (1999). A 3d boundary element code for the analysis of owc wave-power plants. vol. 1, (pp. 188–195). International Society of Offshore and Polar Engineers. 51

Bruggemann, M. (2017). *Floating body hydrodynamics: A load driven approach*. Ph.D. thesis, Imperial College London. 166, 216

CarbonBrief (2019). Analysis: Uk renewables generate more electricity than fossil fuels for first time. https://www.carbonbrief.org/. 28

Chakrabarti, S., & Cotter, D. (1984). Hydrodynamic coefficients of a mooring tower. *Journal of Energy Resources Technology*, *106*(2), 183–190. 193

Chakrabarti, S. K. (1980). In line forces on fixed vertical cylinder in waves. *Journal of Waterway, Port, Coastal, and Ocean Engineering*, *106*(WW2), 145–155. 193

Chakrabarti, S. K., Wolbert, A. L., & Tam, W. A. (1976). Wave forces on vertical circular cylinder. *Journal of The Waterways Harbors and Coastal Engineering Division*, *102*, 203–221. 29

Davidson, J., & Costello, R. (2020). Efficient nonlinear hydrodynamic models for wave energy converter design—a scoping study. *Journal of Marine Science and Engineering*, *8*(1). 51

De Moura, A., Carvalho, M., Patricioa, S., Nunes, N., & Soares, C. (2010). Airborne and underwater noise assessment at the pico owc wave power plant. In *International Conference on Ocean Energy*. 28

Delaure, Y., & Lewis, A. (2003). 3d hydrodynamic modelling of fixed oscillating water column wave power plant by a boundary element methods. *Ocean Engineering*, *30*(3), 309 – 330. 51

Demirdžić, I., & Perić, M. (1988). Space conservation law in finite volume calculations of fluid flow. *International Journal for Numerical Methods in Fluids*, *8*(9), 1037–1050. 267

Didden, N. (1979). On the formation of vortex rings: Rolling-up and production of circulation. *Zeitschrift für angewandte Mathematik und Physik ZAMP*, *30*(1), 101–116. 79, 80, 137

Elhanafi, A., A., F., Macfarlane, G., & Z., L. (2016). Numerical energy balance analysis for an onshore oscillating water column-wave energy converter. *Energy*, *116*, 539–557. 59

Elhanafi, A., Fleming, A., Macfarlane, G., & Leong, Z. (2017a). Numerical hydrodynamic analysis of an offshore stationary–floating oscillating water column–wave energy converter using cfd. *International Journal of Naval Architecture and Ocean Engineering*, *9*(1), 77 – 99. 59, 60, 61

Elhanafi, A., Fleming, A., Macfarlane, G., & Leong, Z. (2017b). Underwater geometrical impact on the hydrodynamic performance of an offshore oscillating water column–wave energy converter. *Renewable Energy*, *105*, 209 – 231. 60

Elhanafi, A., Macfarlane, G., Fleming, A., & Leong, Z. (2017c). Scaling and air compressibility effects on a three-dimensional offshore stationary owc wave energy converter. *Applied Energy*, *189*, 1–20. 233

Şentürk, U., & Özdamar, A. (2011). Modelling the interaction between water waves and the oscillating water column wave energy device. *Mathematical and Computational Applications*, *16*(3), 630–640. 59

Evans, D., & Porter, R. (1995). Hydrodynamic characteristics of an oscillating water column device. *Applied Ocean Research*, *17*(3), 155 – 164. 29, 36, 42, 58

Evans, D. V. (1982). Wave-power absorption by systems of oscillating surface pressure distributions. *Journal of Fluid Mechanics*, *114*, 481–499. 42

Evans, D. V., & Porter, R. (1997). Efficient calculation of hydrodynamic properties of owc-type devices. *Journal of Offshore Mechanics and Arctic Engineering*, *119*(4), 210–218. 23, 29, 36, 42, 45, 48, 105, 227, 261, 262

F. R. Menter, M. K., & Langtry, R. (2003). Ten years of industrial experience with the sst turbulence model. In *Turbulence, Heat and Mass Transfer 4*, (pp. 625–632). 265

Falcão, A. F. d. O. (2000). The shoreline owc wave power plant at the azores. 27

Falcão, A. F. d. O. (2010). Wave energy utilization: A review of the technologies. *Renewable and Sustainable Energy Reviews*, *14*(3), 899–918. 27, 28

Falnes, J., & McIver, P. (1985). Surface wave interactions with systems of oscillating bodies and pressure distributions. *Applied Ocean Research*, *7*(4), 225 – 234. 42

Faltinsen, O. M. (1999). *Sea loads on ships and offshore structures*. Cambridge University Press. 30

Faltinsen, O. M., Rognebakke, O. F., & Timokha, A. N. (2007). Two-dimensional resonant piston-like sloshing in a moonpool. *Journal of Fluid Mechanics*, *575*, 359–397. 105

Fenton, J. (1985). Fifth Order Stokes Theory for Steady Waves. *Journal of Waterway, Port, Coastal and Ocean Engineering*, *111*(2), 216–234. 65

Ferziger, J. H., & Peric, M. (2002). *Computational Methods for Fluid Dynamics*. Springer-Verlag Berlin Heidelberg. 95

Fung, D. P. K. (1998). Added Mass and Damping of Circular Moonpools. In *Proceedings of the 13th International Ocean and Polar Enginneering Conference*, (pp. 218–226). 87, 89, 90, 206

Germano, M., Piomelli, U., Moin, P., & Cabot, W. H. (1991). A dynamic subgrid scale eddy viscosity model. *Physics of Fluids A: Fluid Dynamics*, *3*(7), 1760–1765. 73, 264

Gharib, M., Rambod, E., & Shariff, K. (1998). A universal time scale for vortex ring formation. *Journal of Fluid Mechanics*, *360*, 121–140. 41, 116, 117, 121

Gomes, R., Henriques, J., Gato, L., & Falcão, A. (2012). Hydrodynamic optimization of an axisymmetric floating oscillating water column for wave energy conversion. *Renewable Energy*, *44*, 328 – 339. 61

Greenshields, C. (2015). *Open Foam: The open source CFD toolbox, version 2.4.0 edn, CFD Direct Ltd.*. CFD Direct Ltd. 68

Haller, G. (2005). An objective definition of a vortex. *Journal of Fluid Mechanics*, *525*, 1–26. 117

Hamel-Derouich, D. (1991). Wave forces on rectangular cylinders at low keulegan-carpenter numbers. In *Offshore Technology Conference*, (pp. 207–216). 40

He, F., Li, M., & Huang, Z. (2016). An experimental study of pile-supported owc-type breakwaters: Energy extraction and vortex-induced energy loss. *Energies*, *9*(7). 27

Heath, T., Whittaker, T., & Boake, C. B. (2001). The design, construction and operation of the limpet wave energy converter (islay, scotland)[land installed marine powered energy transformer. In *European wave energy conference*. 27

Heath, T. V. (2011). A review of oscillating water columns. *Philosophical Transactions of the Royal Society of London A: Mathematical, Physical and Engineering Sciences*, *370*(1959), 235–245. 26, 27, 28

Hettel, M., Wetzel, F., Habisreuther, P., & Bockhorn, H. (2007). Numerical verification of the similarity laws for the formation of laminar vortex rings. *Journal of Fluid Mechanics*, *590*, 35–60. 80, 145

Himeno, Y. (1981). Prediction of ship roll damping-state of the art. Tech. rep., Japan Shipbuilding Industry Foundation. 30

Hunt, J. C. R., Wray, A. A., & Moin, P. (1988). Eddies, streams, and convergence zones in turbulent flows. In *Studying Turbulence Using Numerical Simulation Databases, 2*. 80, 117

Issa, R. (1986). Solution of the implicitly discretised fluid flow equations by operator-splitting. *Journal of Computational Physics*, *62*(1), 40 – 65. 270

Iturrioz, A., Guanche, R., Armesto, J., Alves, M., Vidal, C., & Losada, I. (2014). Time-domain modeling of a fixed detached oscillating water column towards a floating multi-chamber device. *Ocean Engineering*, *76*, 65 – 74. 59

Iturrioz, A., Guanche, R., Lara, J., Vidal, C., & Losada, I. (2015). Validation of openfoam for oscillating water column three-dimensional modeling. *Ocean Engineering*, *107*, 222 – 236. 59, 60, 61

Jacobsen, N. G., Fuhrman, D. R., & Fredsøe, J. (2012). A wave generation toolbox for the open-source cfd library: Openfoam®. *International Journal for Numerical Methods in Fluids*, *70*(9), 1073–1088. 94

Jasak, H. (2009). *Dynamic mesh handling in OpenFOAM*. 267

Jeon, D., & Gharib, M. (2004). On the relationship between the vortex formation process and cylinder wake vortex patterns. *Journal of Fluid Mechanics*, *519*, 161–181. 116

Kamath, A., Bihs, H., & Øivind A. Arntsen (2015). Numerical investigations of the hydrodynamics of an oscillating water column device. *Ocean Engineering*, *102*, 40 – 50. 59, 60, 61

Kasiman, E. H. (2017). *Numerical Modelling of Wave Breaking and Wave-structure Interaction*. Ph.D. thesis, Imperial College London. 166, 167, 169, 170

Keulegan, G. H., & Carpenter, L. H. (1958). Forces on cylinders and plates in an oscillating fluid. *Journal of Research of the National Bureau of Standards*, *60*, 423–440. 29, 40

Knott, G., & Flower, J. (1980). Measurement of energy losses in oscillatory flow through a pipe exit. *Applied Ocean Research*, *2*(4), 155 – 164. 54, 55, 61, 62

Knott, G. F., & Flower, J. O. (1979). Wave-tank experiments on an immersed parallel-plate duct. *Journal of Fluid Mechanics*, *90*, 327–336. 53

Knott, G. F., & Mackley, M. R. (1980). On eddy motions near plates and ducts, induced by water waves and periodic flows. *Philosophical Transactions of the Royal Society of London A: Mathematical, Physical and Engineering Sciences*, *294*(1412), 599–623. 53, 54, 55, 61, 71, 74, 75, 76, 77, 79, 100

Koo, W., & Kim, M.-H. (2010). Nonlinear time-domain simulation of a land-based oscillating water column. *Journal of Waterway, Port, Coastal, and Ocean Engineering*, *136*(5), 276–285. 52

Koterayama, W., & Nakamura, M. (1988). Wave forces acting on a moving cylinder. *Journal of Offshore Mechanics and Arctic Engineering*, *110*(4), 315–319. 194

Krieg, M., & Mohseni, K. (2013). Modelling circulation, impulse and kinetic energy of starting jets with non-zero radial velocity. *Journal of Fluid Mechanics*, *719*, 488–526. 118, 124

Kristiansen, T., & Faltinsen, O. (2008). Application of a vortex tracking method to the piston-like behaviour in a semi-entrained vertical gap. *Applied Ocean Research*, *30*(1), 1 – 16. 105

Kristiansen, T., & Faltinsen, O. M. (2012). Gap resonance analyzed by a new domain-decomposition method combining potential and viscous flow {DRAFT}. *Applied Ocean Research*, *34*, 198 – 208. 105

Krueger, P. S., Dabiri, J. O., & Gharib, M. (2006). The formation number of vortex rings formed in uniform background co-flow. *Journal of Fluid Mechanics*, *556*, 147–166. 116, 117

Lawson, J. M., & Dawson, J. R. (2013). The formation of turbulent vortex rings by synthetic jets. *Physics of Fluids*, *25*(10), 105113. 80

Lee, C., & Cant, S. (2017). Assessment of les subgrid-scale models and investigation of hydrodynamic behaviour for an axisymmetrical bluff body flow. *Flow, Turbulence and Combustion*, *98*, 155–176. 75

Lee, C. H., & Newman, J. N. (1996). Wave interactions with an oscillating water column. In *International Offshore and Polar Engineering Conference*, vol. 1, (pp. 82–90). 51

Lilly, D. K. (1992). A proposed modification of the germano subgrid-scale closure method. *Physics of Fluids A: Fluid Dynamics*, *4*(3), 633–635. 265

Lin, C.-Y., & Huang, C.-J. (2004). Decomposition of incident and reflected higher harmonic waves using four wave gauges. *Coastal Engineering*, *51*(5–6), 395 – 406. 97, 98

Linton, C., & McIver, P. (2001). *Handbook of Mathematical Techniques for Wave/Structure Interaction*. Chapman & Hall/CRC. 251

Luo, Y., Nader, J.-R., Cooper, P., & Zhu, S.-P. (2014). Nonlinear 2d analysis of the efficiency of fixed oscillating water column wave energy converters. *Renewable Energy*, *64*, 255 – 265. 59

Masterton, S. (2007). *Nonlinear Wave-Structure Interaction: Scattering, Forcing and Dynamic Response*. Ph.D. thesis, Imperial College London. 165, 166, 167, 170

Mayer, S., Garapon, A., & Sørensen, L. S. (1998). A fractional step method for unsteady free-surface flow with applications to non-linear wave dynamics. *International Journal for Numerical Methods in Fluids*, *28*(2), 293–315. 94

Mehaute, B. (1976). *An Introduction to Hydrodynamics and Water Waves*. Springer-Verlag. 178

Mei, C. C. (1983). *The Applied Dynamics of Ocean Surface Waves*. Wiley Interscience, New York, NY. 49

Mohseni, K., & Gharib, M. (1998). A model for universal time scale of vortex ring formation. *Physics of Fluids*, *10*(10), 2436–2438. 125

Morison, J. R., Johnson, J. W., & Schaaf, S. A. (1950). The force exerted by surface waves on piles. *Petroleum Transactions AIME*, *189*, 149–157. 36

Morris-Thomas MT, I. R., & Thiagarajan, K. (2006). An investigation into the hydrodynamic efficiency of an oscillating water column. *Journal of Offshore Mechanics and Arctic Engineering*, *129*(4), 273–278. 57, 58, 59, 174, 204, 206

Nader, J.-R., Zhu, S. P., Cooper, P., & Stappenbelt, B. (2012). A finite-element study of the efficiency of arrays of oscillating water column wave energy converters. *Ocean Engineering*, *43*, 72–81. 51

Newman, J. N. (1974). Interaction of water waves with two closely spaced vertical obstacles. *Journal of Fluid Mechanics*, *66*, 97–106. 36

Ning, D.-Z., Shi, J., Zou, Q.-P., & Teng, B. (2015). Investigation of hydrodynamic performance of an owc (oscillating water column) wave energy device using a fully nonlinear hobem (higher-order boundary element method). *Energy*, *83*, 177 – 188. 52

Piomelli, U., Moin, P., & Ferziger, J. H. (1988). Model consistency in large eddy simulation of turbulent channel flows. *The Physics of Fluids*, *31*(7), 1884–1891. 75

Rodriguez, M. (2016). *The nonlinear wave loading and dynamic response of a freely-floating two-dimensional box*. Ph.D. thesis, Imperial College London. 166, 216

Sarmento, A. J. N. A. (1992). Wave flume experiments on two-dimensional oscillating water column wave energy devices. *Experiments in Fluids*, *12*(4), 286–292. 56, 57, 58, 60, 100

Sarmento, A. J. N. A., & Falcao, A. F. d. O. (1985). Wave generation by an oscillating surface-presure and its application in wave-energy extraction. *Journal of Fluid Mechanics*, *150*, 467–485. 57, 60

Sarpkaya, T. (1975). Forces on cylinders and spheres in a sinusoidally oscillating fluid. *Journal of Applied Mechanics*, *42*(1), 32–37. 29, 37, 38

Sarpkaya, T. (1977). *OTC-2533-MS*, chap. In - Line And Transverse Forces, On Cylinders In Oscillatory Flow At High Reynolds Numbers., (p. 200). Offshore Technology Conference. 29, 37, 39, 193

Sarpkaya, T. (1986). Forces on a circular cylinder in viscous oscillatory flow at low Keulegan-Carpenter numbers. *Journal of Fluid Mechanics*, *165*(61-71), 11–15. 37, 38, 39, 40

Smagorinsky, J. (1963). General circulation experiments with the primitive equations. *Mon. Wea. Rev.*, *91*(3), 99–164. 74, 264

Smith, P., & Stansby, P. (1991). Viscous oscillatory flows around cylindrical bodies at low keulegan-carpenter numbers using the vortex method. *Journal of Fluids and Structures*, *5*(4), 339 – 361. 112

Stansby, P. K., Bullock, G. N., & I, S. (1983). Quasi-2-d forces on a vertical cylinder in waves. *Journal of Waterway, Port, Coastal and Ocean Engineering*, *109*(1), 128–132. 193, 216

Stiassnie, M., Boguslavsky, I., & Naheer, E. (1986). Scattering and dissipation of surface wave by a bi-plate structure. *Applied Ocean Research*, *8*(1), 33 – 37. 101

Stiassnie, M., Naheer, E., & Boguslavsky, I. (1984). Energy losses due to vortex shedding from the lower edge of a vertical plate attacked by surface waves. *Proceedings of the Royal Society of London A: Mathematical, Physical and Engineering Sciences*, *396*(1810), 131–142. 98, 99, 216

Stokes, G. G. (1851). On the effect of the internal friction of fluids on the motion of pendulums. *Transactions of the Cambridge Philosophical Society*, *9*, 8–106. 38, 39

Swan, C., & Sheikh, R. (2015). The interaction between steep waves and a surface-piercing column. *Philosophical Transactions of the Royal Society A: Mathematical, Physical and Engineering Sciences*, *373*(2033), 20140114. 166

Sykes, R. K., Lewis, A. W., & Thomas, G. (2008). A numerical and physical comparison of a geometrically simple fixed and floating oscillating water column. (48234), 659–668. 56, 101, 102, 103

Takahasi, S., Nakada, H., Ohneda, H., & Shikamori, M. (1992). Wave power conversion by a prototype wave power extracting caisson in sakata port. In *Proceedings of the 23rd International Conference on Coastal Engineering*, (pp. 3440–3453). 27

Tanaka, N., Ikeda, Y., & Nishino, K. (1983). Hydrodynamic viscous force acting on oscillating cylinders with various shapes. Tech. rep., Department of Naval Architecture, University of Osaka Prefecture. 40, 205

Thiruvenkatasamy, K., & Neelamani, S. (1997). On the efficiency of wave energy caissons in array. *Applied Ocean Research*, *19*(1), 61 – 72. 27

Torre-Enciso, Y., Ortubia, I., Lopez de Aguileta, L., & Marques, J. (2009). Mutriku wave power plant: from the thinking out to the reality. In *Proceedings of the 8th European Wave and Tidal Energy Conference*. 27

Troesch, A. W., & Kim, S. K. (1991). Hydrodynamic forces acting on cylinders oscillating at small amplitudes. *Journal of Fluids and Structures*, *5*, 113–126. 40, 178

Tseng, R.-S., Wu, R.-H., & Huang, C.-C. (2000). Model study of a shoreline wave-power system. *Ocean Engineering*, *27*, 801–821. 27

UKERC (2019). Review of energy policy 2019. https://assets.publishing.service.gov.uk/government. 28

Vengatesan, V., Varyani, K., & Barltrop, N. (2000). An experimental investigation of hydrodynamic coefficients for a vertical truncated rectangular cylinder due to regular and random waves. *Ocean Engineering*, *27*(3), 291 – 313. 40

Walker, J. D. A., Smith, C. R., Cerra, A. W., & Doligalski, T. L. (1987). The impact of a vortex ring on a wall. *Journal of Fluid Mechanics*, *181*, 99–140. 122

WAMIT (2013). *WAMIT User Manual: Version 7.0*. WAMIT Inc, `www.wamit.com`. 47

Wang, H., & Falzarano, J. (2017). Energy balance analysis method in oscillating type wave converter. *Journal of Ocean Engineering and Marine Energy*, *3*(3), 193–208. 56

Wang, R.-Q., Ning, D.-Z., Zhang, C.-W., Zou, Q.-P., & Liu, Z. (2018). Nonlinear and viscous effects on the hydrodynamic performance of a fixed owc wave energy converter. *Coastal Engineering*, *131*, 42 – 50. 52

Wehausen, J. V. (1971). The motion of floating bodies. *Annual Review of Fluid Mechanics*, *3*(1), 237–268. 46

Yeung, R. W., & Jiang, Y. (2014). Shape effects on viscous damping and motion of heaving cylinders. *Journal of Offshore Mechanics and Arctic Engineering*, *136*(4), 041801–041801–9. 198

Zhang, Y., Zou, Q.-P., & Greaves, D. (2012). Air water two-phase flow modelling of hydrodynamic performance of an oscillating water column device. *Renewable Energy*, *41*, 159 – 170. 59, 61, 174, 199

Zhao, W., Frankel, S. H., & Mongeau, L. G. (2000). Effects of trailing jet instability on vortex ring formation. *Physics of Fluids*, *12*(3), 589–596. 121

Appendices

A
Radiation potential flow

A.1 The integral equation

α_0^R, β_0^R, α_n^R and β_n^R are determined by satisfying the continuity condition for the outward radial velocity at the outer radius, $U^R(z)$, over the gap length, L_g. This radial velocity is defined by:

$$\begin{aligned} U^R(z) &= \frac{\partial \phi^R}{\partial r}\Big|_{r=b}, \\ &= \alpha_0^R k H_0^{'}(kb)\,\psi_0(z) + \sum_{n=1}^{\infty} \alpha_n^R k_n K_0^{'}(k_n b)\,\psi_n(z), \\ &= \beta_0^R k J_0^{'}(kb)\,\psi_0(z) + \sum_{n=1}^{\infty} \beta_n^R k_n I_0^{'}(k_n b)\,\psi_n(z) = \sum_{n=0}^{\infty} U_n^R \psi_n(z), \end{aligned} \tag{A.1}$$

where $\psi_n(z) = N_n^{-1/2}\cos k_n(h+z)$ and $\psi_0(z) = N_0^{-1/2}\cosh k(h+z)$ are the depth-dependent eigenfunctions, with $N_n = \frac{1}{2}\left(1 + \frac{\sin 2k_n h}{2k_n h}\right)$ and $N_0 = \frac{1}{2}\left(1 + \frac{\sinh 2kh}{2kh}\right)$. Having implemented this condition and the orthogonality relation for the eigenfunctions, α_0^R, β_0^R, α_n^R and β_n^R may be related to the integral forms of the radial velocity.

$$\alpha_0^R k H_0^{'}(kb) = \beta_0^R k J_0^{'}(kb), \tag{A.2}$$

$$= \frac{1}{h}\int_{L_g} U^R(z)\,\psi_0(z)\,dz = U_0^R, \tag{A.3}$$

$$\alpha_n^R k_n K_0^{'}(k_n b) = \beta_n^R k_n I_0^{'}(k_n b), \tag{A.4}$$

$$= \frac{1}{h}\int_{L_g} U^R(z)\,\psi_n(z)\,dz = U_n^R. \tag{A.5}$$

Substituting Equations (A.2)-(A.5) into another continuity condition for the radiated velocity potential, $\phi^R(r,z)$, on the same surface generates

$$\begin{aligned}\alpha_0^R\left[H_0(kb) - \frac{H_0^{'}(kb)}{J_o^{'}(kb)}J_0(kb)\right]\psi_0(z) - K^{-1}\\ + \sum_{n=1}^{\infty} U_n^R\left[\frac{K_0(k_n b)}{k_n K_0^{'}(k_n b)} - \frac{I_0(k_n b)}{k_n I_o^{'}(k_n b)}\right]\psi_n(z) = 0.\end{aligned} \tag{A.6}$$

By employing the Wronskian identities for Bessel functions (Abramowitz & Stegun, 1972) and the derivatives of Bessel functions to simplify Equation (A.6), an integral equation with a kernel $L_0(z,l)$ can be expressed as

$$\int_{L_g} U^R(l)\,L_0(z,l)\,dl = -K^{-1} + \frac{2i\alpha_0^R}{\pi k b J_1(kb)}\psi_0(z), \tag{A.7}$$

$$L_0(z,l) = \sum_{n=1}^{\infty}\frac{\psi_n(z)\,\psi_n(l)}{k_n^2 h b I_1(k_n b)\,K_1(k_n b)}. \tag{A.8}$$

To solve this integral equation, velocity function, $u_i(z)$, that relates to the radial velocity U^R and satisfies Equation (A.7), is introduced as follows:

$$U^R(z) = -K^{-1}u_1(z) + \frac{2i\alpha_0^R}{\pi k b J_1(kb)}u_2(z), \tag{A.9}$$

$$\int_{L_g} u_i(z)\,L_0(z,l)\,dl = d_i(z),\ z \in L_g, \tag{A.10}$$

$$\text{where}\ \ d_1(z) = 1,\ \text{and}\ d_2(z) = \psi_0(z). \tag{A.11}$$

A.2 Galerkin approximation

In considering the solution of the integral equation, a 2x2 matrix $\boldsymbol{S}$ is defined by:

$$S_{ij} = \int_{L_g} u_i(z)\,d_j(z)\,dz. \tag{A.12}$$

Equations (A.10) and (A.12) can be re-written in an operator notation as follows:

$$\mathcal{L}_0 u_i = d_i, \text{ for } z \in L_g, \ i = 1, 2, \text{ with } d_1 = 1, \ d_2 = \psi_0, \tag{A.13}$$

$$(u_i, d_j) = S_{ij}. \tag{A.14}$$

The notation of $(.,.)$ means an inner product over the gap. The $u_i(z)$ is approximated by a series of products of a test function, $v(z)$, with a coefficient, a_n.

$$u_i(z) \simeq \tilde{u}_i(z) = \sum_{n=0}^{N} a_n^{(i)} v_n(z), i = 1, 2, \tag{A.15}$$

where the test function, $v_n(z)$, is chosen to represent the flow singularity near the sharp edge of an OWC. The velocity at a field point is assumed to be proportional to the square root of the distance from the field point to the sharp edge. In this case, a Chebychev polynomial, T_{2n}, establishes the function.

$$v_n(z) = \frac{2(-1)^n}{\pi\{(h-B)^2 - (h+z)^2\}^{1/2}} T_{2n}\left(\frac{h+z}{h-B}\right) \text{ for } -h < z < -B. \tag{A.16}$$

Substituting Equation (A.15) into Equation (A.13), multiplying the latter with $v_m(z)$, and integrating the product over L_g produces the following matrix.

$$\sum_{n=0}^{N} a_n^{(i)} L_{mn}^{(0)} = D_m^{(i)}, \ m = 0, 1, ..., N, \tag{A.17}$$

where $L_{mn}^{(0)} = (v_m, \mathcal{L}_0 v_n)$ and $D_m^{(i)} = (v_m, d_i)$. The matrix $\boldsymbol{S}$ is approximated by

$$\tilde{S}_{ij} = \sum_{n=0}^{N} a_n^{(i)} D_n^{(j)}, \tag{A.18}$$

and $\tilde{S} = D^T {L^{(0)}}^{-1} D$, where D is an $(N+1)\,x2$ matrix and $L^{(0)}$ is an $(N+1)$ x $(N+1)$ matrix. The elements of each matrix are defined in terms of Bessel functions.

$$D_m^{(1)} = \int \frac{2(-1)^m}{\pi\{(h-B)^2 - (h+z)^2\}^{1/2}} \ T_{2m}\left(\frac{h+z}{h-B}\right) dz, \tag{A.19}$$

$$D_m^{(2)} = (-1)^m N_0^{-1/2} I_{2m}\{k(h-B)\}, \tag{A.20}$$

$$L_{mn}^{(0)} = \sum_{s=1}^{\infty} \frac{J_{2m}\{k_s(h-B)\} J_{2n}\{k_s(h-B)\}}{N_s k_s h k_s b I_1(k_s b) K_1(k_s b)}. \tag{A.21}$$

To define the matrices defined above, three variables, N, M_1 and M_2, are considered. N determines the size of the matrices, D_{N+1x2} and $L_{N+1xN+1}$, while M_1 defines the number of standing wave modes and the number of the first terms in the infinite series of the matrix L and the radiated velocity potential ϕ^R. Furthermore, M_2 denotes the number of the remaining terms in the infinite series approximated by the asymptotic forms of the Bessel functions for large arguments.

A.3 Approximations to the infinite series

The asymptotic forms of the following Bessel functions for a large real argument as stated in Linton & McIver (2001) are given as follows:

$$I_m(x) \sim \sqrt{\frac{\pi}{2x}} e^x, \tag{A.22}$$

$$K_m(x) \sim \sqrt{\frac{\pi}{2x}} e^{-x}, \tag{A.23}$$

$$J_m(x) \sim \sqrt{\frac{2}{\pi x}} \cos(x - m\pi/2 - \pi/4), \tag{A.24}$$

$$H_m(x) \sim \sqrt{\frac{2}{\pi x}} \mathrm{e}^{i(x - m\pi/2 - \pi/4)}, \tag{A.25}$$

where a large $k_s h$ is approximated by $s\pi$ as $s \to \infty$. The constanta N_s in a depth-dependent eigenfunction is approximated by:

$$N_s = \frac{1}{2}\left(1 + \frac{\sin 2s\pi}{2s\pi}\right) \approx \frac{1}{2}. \tag{A.26}$$

The higher-mode terms in the infinite series of the matrix $L^{(0)}_{mn}$ (Equation (A.21)) are approximated by the asymptotic values given in Equations (A.22)-(A.24) as:

$$\sum_{s=M_1}^{M_2} \frac{J_{2m}\{k_s(h-B)\} J_{2n}\{k_s(h-B)\}}{N_s k_s h k_s b I_1(k_s b) K_1(k_s b)} = \sum_{s=M_1}^{M_2} \frac{4(-1)^{m+n}\left[1 + \sin(2\pi s(1-c_2))\right]}{\pi^4 s^2 (1-c_2)}, \tag{A.27}$$

where c_2 is the ratio of the draft, B, of the water column to the water depth, h.

Likewise, the asymptotic forms of the Bessel functions are implemented to estimate the contribution of the higher-mode terms in the infinite series of the radiated

velocity potential (Equation (2.17)). These higher-mode terms are approximated by:

$$\sum_{n=M_1}^{M_2} \alpha_n^R K_0\left(k_n r\right) \psi_n\left(z\right) = \sum_{n=M_1}^{M_2} \left(-1^{n+1}\right) \sqrt{\frac{4c_1 h}{\left(\pi n\right)^2 r}} e^{n\pi(c_1 - r/h)} \int_{L_g} U^R\left(z\right) \cos n\pi \left(1 - z/h\right) dz, \tag{A.28}$$

where c_1 is the ratio of the cylinder radius, b, to the water depth, h, and r the radial distance of a field point from the centre of the water column.

A.4 Quantification of the radiated velocity potential

The steps to quantify the radiated velocity potential are outlined as follows:

1. Determine the N, M_1 and M_2 variables.

2. Solve the dispersion equation to estimate the wave numbers of the progressive mode, k, and the standing modes, k_s, as many as M_1 modes.

3. Quantify the coefficients for the depth-dependent eigenfunctions corresponding to the progressive mode, N_0, and each standing wave mode, N_s .

4. Construct matrices D_{N+1x2} and $L_{N+1xN+1}$ using Equations (A.19)-(A.20) and (A.21), respectively. The remaining higher-mode terms in the infinite series of matrix L as approximated in Equation (A.27) are included.

5. Quantify matrices $a_n^{(i)}$ and $\tilde{S}_{2x2}$ using Equations (A.17) and (A.18), respectively

6. Quantify α_0^R coefficient of the progressive wave mode for $r \geq b$ using the elements of matrix $\tilde{S}$ as follows:

$$-\alpha_0^R khH_1\left(kb\right) = -K^{-1}S_{12} + \frac{2i\alpha_0^R S_{22}}{\pi kbJ_1\left(kb\right)}, \tag{A.29}$$

$$\alpha_0^R = \frac{K^{-1}\pi kbJ_1\left(kb\right)S_{12}}{\gamma H_1\left(kb\right) + 2iS_{22}}, \tag{A.30}$$

   where γ is defined as $\pi kbkhJ_1\left(kb\right)$.

7. Compute the velocity functions, $u_i\left(z\right)$, from Equation (A.15) to evaluate the radial velocity, $U^R\left(z\right)$, using Equation (A.9), and substitute this velocity into

Equations (A.4) and (A.5) to evaluate the coefficients of each exponentially decaying mode, α_n^R, for $r \geq b$ as follows:

$$\alpha_n^R = -\frac{\int_{L_g} U^R(z)\,\psi_n(z)\,dz}{k_n h K_1(k_n b)}. \tag{A.31}$$

8. Evaluate the radiated velocity potential, ϕ^R, for $r \geq b$, using Equation (2.17). The remaining higher-mode terms in the infinite series of the radiated velocity potential are approximated using Equation (A.28). Following on, check the convergence of this potential. If the convergence has not been achieved, increase the N value and repeat from step 1.

9. Determine the coefficients associated with the progressive and the exponentially decaying modes, β_0^R and β_n^R, for $r \leq b$ using Equations (A.2)-(A.5), respectively. Following on, approximate the higher-mode terms in the infinite series of the corresponding radiated potential velocity ϕ^R to compute this potential from Equation (2.18).

A.5 Convergence study

An OWC with a relative radius of $b/h = 0.035$ and relative water draft of $B/h = 0.11$ in a water depth of $h = 1.0$m was considered for a convergence study. The fequency was fixed at $\omega^2 B/g = 0.88$. The N and M_1 variables were varied, while the M_2 variable was set constant to 10000. In this study, N was given the value of $1, 5$, and 10, and M_1 was varied in the range of $10 \leq M_1 \leq 1000$.

Figure A.1 shows the radiated velocity potential computed at the external free-surface, ϕ_e^R, at various radial locations from the water column. When $N = 1$, the solutions never converge. In the cases of $N = 5$ and 10, ϕ_e^R converges as the number of standing wave modes, M_1, increases. The important criteria is to choose M_1 such that $M_1 \gg N$. Otherwise, the computation shows an instability or a sudden change in the radiated velocity potential. In Figure A.1, this instability is observed in the range of $M_1 \leq 25$ at all radial locations. Overall, with $N = 5$ and a minimum value of $M_1 = 100$, a convergent analytical solution is observed. Likewise, a convergence study of the radiated velocity potential computed at the internal free-surface, ϕ_i^R, was undertaken. The result is consistent with the convergence study for the ϕ_e^R.

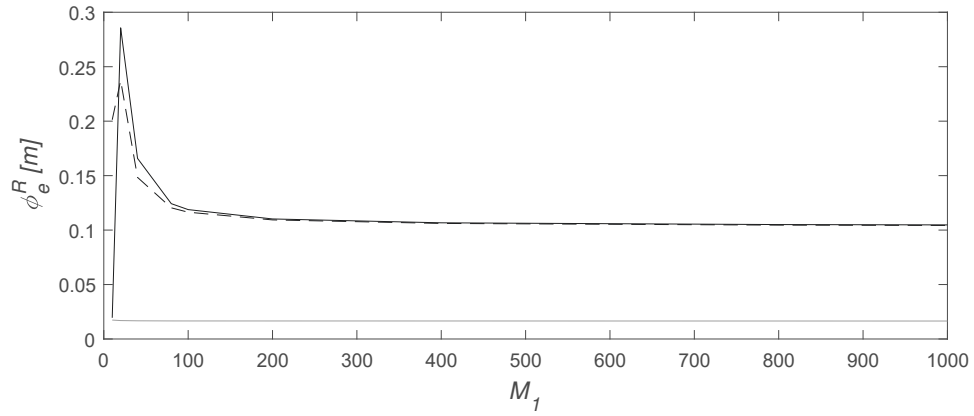

(A) ϕ_e^R at $r/b = 3$

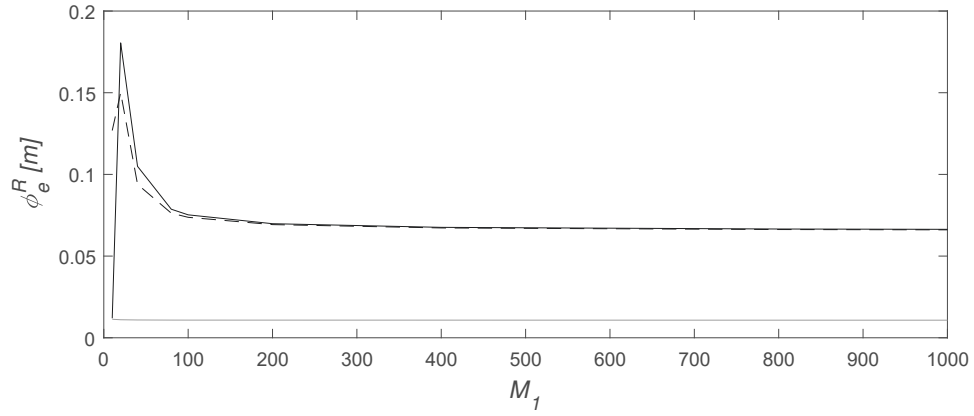

(B) ϕ_e^R at $r/b = 8$

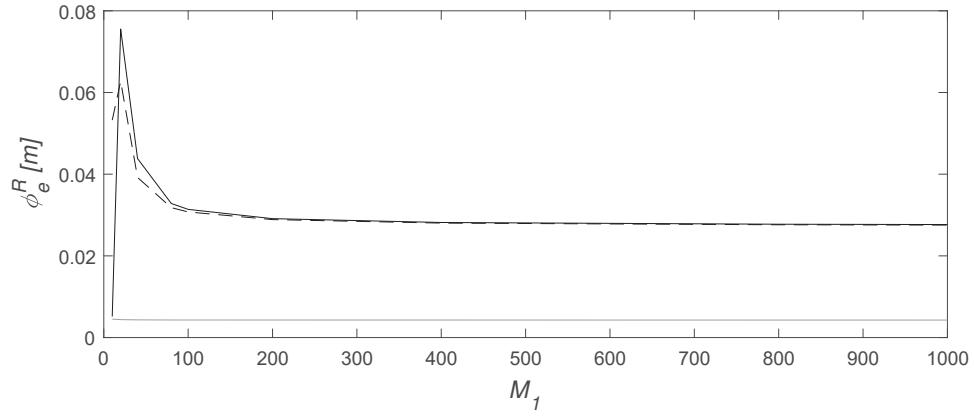

(C) ϕ_e^R at $r/b = 45$

Figure A.1: Radiated wave potentials computed at the external free-surface, ϕ_e^R, of an OWC with $b/h = 0.035$, $B/h = 0.11$ and $h = 1.0m$ when $\omega^2 B/g = 0.88$. M_2 was fixed at 10000, while N and M_1 were varied: $N = 1$ [——], 5 [— —], 10 [——].

B

Computations of radiated waves

B.1 Computation using radiated velocity potential

For the radiation potential flow generated by a cylindrical OWC, the free-surface elevation is expressed as $\eta(r,z,t) = \mathrm{Re}\left[\eta(r,z)\, e^{-i\omega t}\right]$ and the velocity potential as $\Phi(r,z,t) = \mathrm{Re}\left[\phi(r,z)\, e^{-i\omega t}\right]$. Given these expressions and the linearised dynamic free-surface boundary condition (Equation (2.7)), the two variables may be related in a time-independent function.

$$\eta^{i}(r) = -i\frac{\omega}{g}\phi(r,0) + \frac{P_o}{\rho g}, \text{ on } S_i, \tag{B.1}$$

$$\eta^{e}(r) = -i\frac{\omega}{g}\phi(r,0), \text{ on } S_e, \tag{B.2}$$

where η^i and η^e denote the internal and the external surface elevation, respectively. Both elevations are computed at the mean free-surface, $z = 0$. By substituting the velocity potential, defined as $\phi(r,z) = -i\omega\frac{P_o}{\rho g}\phi^R(r,z)$, into Equation (B.1), the amplitude of the radiated wave elevation at a radial location, $\eta_o^e(r)$, is given by:

$$\frac{\eta_o^e(r)}{\eta_o^i} = \frac{\mid \phi_e^R(r,0) \mid}{\mid \phi_i^R(0,0) - K^{-1} \mid}, \tag{B.3}$$

where $\phi_e^R(r,0)$ and $\phi_i^R(0,0)$ are the external and the internal radiated velocity potential, respectively. The latter may be evaluated at any radial location of $r \leq b$ due to the assumption of the uniform displacement of the water column.

B.2 Computation using radiation damping coefficient

Based upon the linear wave theory, the energy flux of a propagating wave per unit crest-width is given by:

$$P = \frac{1}{8}\rho g H^2 C_g, \tag{B.4}$$

where H is the wave height and C_g the group velocity defined as $C_g = nC = nL/T$. n is a constanta given by $n = \frac{1}{2}\left(1 + \frac{2kh}{sinh(2kh)}\right)$. For a wave that radiates due to an oscillating cylindrical body, the crest width of the radiated wave is $2\pi r$, and the energy flux of the wave is defined as follows:

$$P\left(r\right) = \frac{1}{2}\rho g \left[\eta_o^e\left(r\right)\right]^2 C_g 2\pi r. \tag{B.5}$$

Herein, the energy flux $P\left(r\right)$ is expressed as a function of radial distance from the oscillating body. By considering the radiated wave as a source of the damping force that acts on the body, the associated energy flux P_b can be given by:

$$P_b = \frac{1}{2}B_m U^2, \tag{B.6}$$

where B_m is the radiation damping coefficient. Herein, U is the velocity of the oscillating body and computed as the velocity of the internal surface elevation in the context of oscillating water column. This velocity U is simply defined as $\eta_o^i\omega$.

Since the energy is conserved, Equations (B.5) and (B.6) have to be equal. The normalised radiated wave amplitude, $\eta_o^e\left(r\right)/\eta_o^i$, is expressed as follows:

$$\frac{\eta_o^e\left(r\right)}{\eta_o^i} = \sqrt{\frac{2\pi}{\rho g n}\frac{B_m}{\lambda T r}}. \tag{B.7}$$

It should be noted that this computation of the radiated wave amplitude is only valid at a radial location sufficiently distant from the water column.

B.3 Comparisons of the computations with WAMIT

To validate the present linear analytical solver, the hydrodynamic coefficients and radiated wave profiles around a cylindrical OWC were evaluated and compared with

the numerical results obtained from WAMIT. A comparison of the added mass, A_m, shows small discrepancies in Figure B.1(A); the discrepancies estimated to be less than 3%. In respect of the radiation damping coefficient, B_m, good agreement is observed in Figure B.1(B).

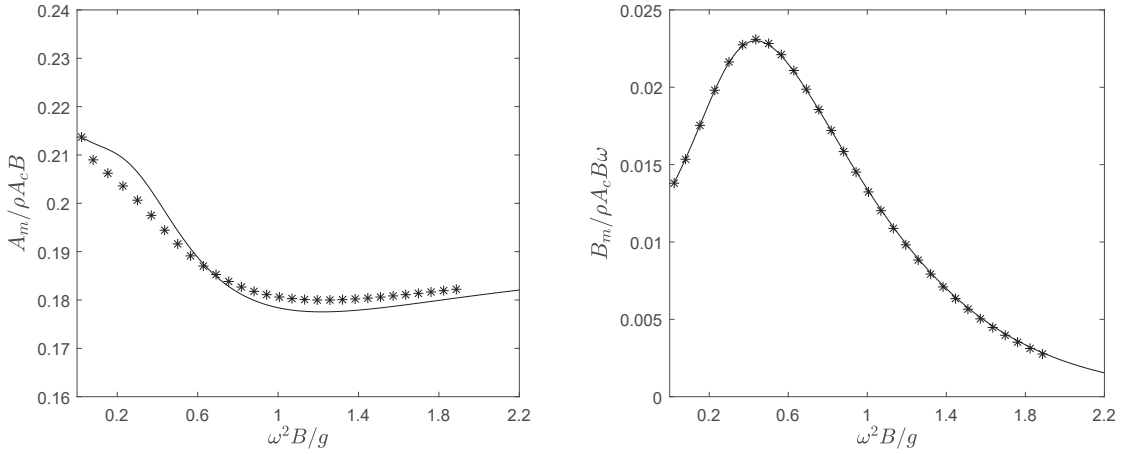

(A) (B)

Figure B.1: (A) Added-mass coefficient, $A_m/\rho A_c B$, and (B) radiation damping coefficient, B_m, computed from the linear analytical solver [——] and WAMIT simulation [$*$] for the OWC with $b/h = 0.035$, $B/h = 0.11$ and $h = 1.0$m.

Following on, the radiated wave profiles are compared in Figure B.2. The radiation damping coefficients computed from WAMIT were employed to estimate the radiated wave profiles generated at four different frequencies. These estimated profiles compare very well with the analytically predicted wave profiles, provided that the exponentially decaying modes of the radiated velocity potential are neglected in the analytical solutions. The comparison with the analytical solutions that consider the exponentially decaying modes, clearly shows that the largest deviations are observed in the fields near the OWC. These deviations in the near-fields confirm that the wave-radiation damping applied to an OWC is only associated with the progressive mode of the radiated wave, while the added mass is related to the exponentially decaying modes. Furthermore, Figure B.2 shows that the relative radial location, r/λ, where the influence of the exponentially decaying mode is negligble, increases with the frequency. The negligible influence is determined from the percentage of deviation being less than 0.5%. This analysis is useful to evaluate the radiated wave elevation in the field far from an OWC.

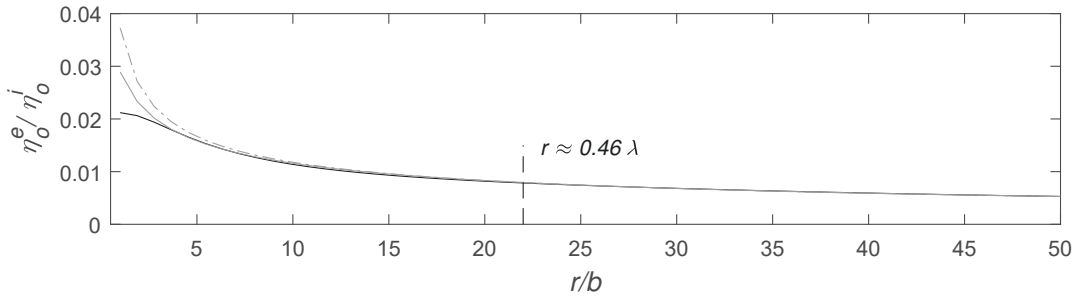

(A) $\omega^2 B/g = 0.44$

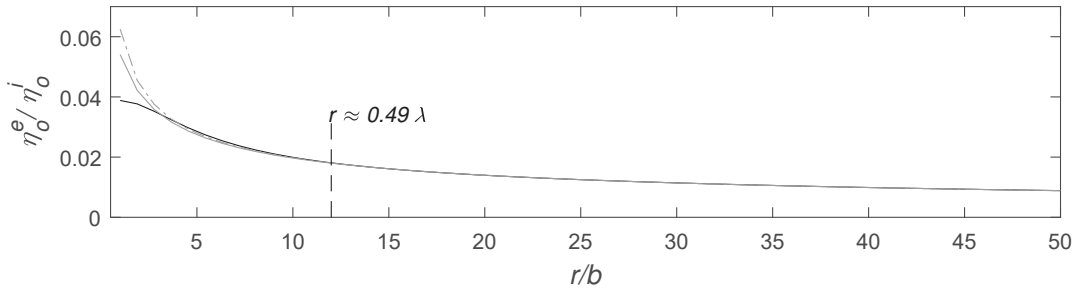

(B) $\omega^2 B/g = 0.88$

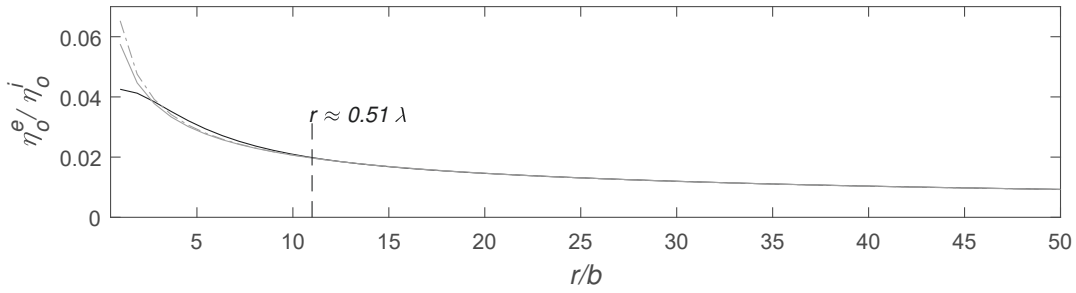

(C) $\omega^2 B/g = 1.00$

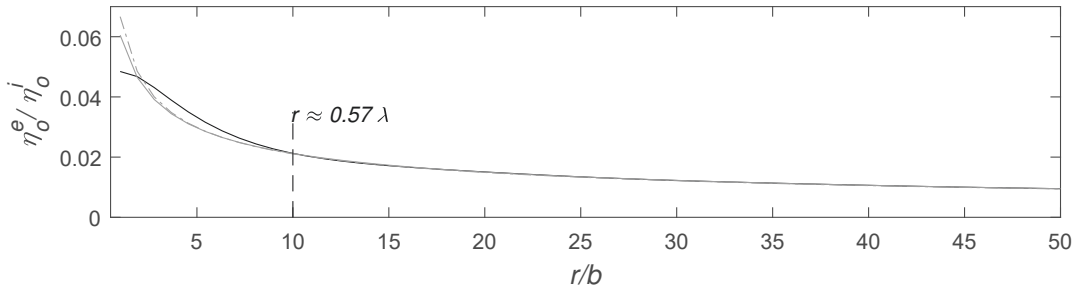

(D) $\omega^2 B/g = 1.26$

Figure B.2: Comparisons between the normalised radiated wave amplitude, η_o^e/η_o^i, for the OWC with $b/h = 0.035$, $B/h = 0.11$ and $h = 1.0$ m predicted using the radiation damping coefficient given from WAMIT [— · —] and computed from the linear analytical solution by considering [——] or neglecting [——] the exponentially decaying modes.

C
Scattering potential flow

C.1 The integral equation

$\alpha^S_{q,0}$, $\beta^S_{q,0}$, $\alpha^S_{q,n}$ and $\beta^S_{q,n}$ are determined by satisfying the continuity conditions for the radial velocity and the scattered potential at $r = b$, $U^S_q(z)$ and $\phi^S_q(z)$, over the gap length, L_g, for each azimuthal mode, q. The radial velocity is given by:

$$\begin{aligned} U^S_q(z) &= \frac{\partial \phi^S_q}{\partial r}\Big|_{r=b}, \\ &= \left(kJ'_q(kb) + \alpha^S_{q,0} kH'_q(kb)\right)\psi_0(z) + \sum_{n=1}^{\infty} \alpha^S_{q,n} k_n K'_q(k_n b)\,\psi_n(z), \\ &= \beta^S_{q,0} kJ'_q(kb)\,\psi_0(z) + \sum_{n=1}^{\infty} \beta^S_{q,n} k_n I'_q(k_n b)\,\psi_n(z) = \sum_{n=0}^{\infty} U^S_{q,n}\psi_n(z). \end{aligned} \tag{C.1}$$

By implementing the orthogonality relationship, Equation (C.1) can be expressed as

$$kJ'_q(kb) + \alpha^S_{q,0} kH'_q(kb) = \beta^S_{q,0} kJ'_q(kb), \tag{C.2}$$

$$= \frac{1}{h}\int_{L_g} U^S_q(z)\,\psi_0(z)\,dz = U^S_{q,0}, \tag{C.3}$$

$$\alpha^S_{q,n} k_n K'_q(k_n b) = \beta^S_{q,n} k_n I'_q(k_n b), \tag{C.4}$$

$$= \frac{1}{h}\int_{L_g} U^S_q(z)\,\psi_n(z)\,dz = U^S_{q,n}. \tag{C.5}$$

Equations (C.2)-(C.5) are combined with the continuity condition for the scattered potential. Having employed the Wronskian identities for Bessel functions, an equa-

tion that satisfies all the matching conditions can be expressed as follows:

$$\left(J_q(kb)+\alpha_{q,0}^S H_q(kb)-\beta_{q,0}^S J_q(kb)\right)\psi_0(z)+\sum_{n=1}^{\infty}\left(\alpha_{q,n}^S K_q(k_nb)-\beta_{q,n}^S I_q(k_nb)\right)\psi_n(z)$$
$$=\frac{-2i\alpha_{q,0}^S}{\pi kbJ_q'(kb)}\psi_0(z)+\sum_{n=1}^{\infty}\frac{U_{q,n}^S}{k_n^2bK_q'(k_nb)\,I_q'(k_nb)}\psi_n(z)=0 \tag{C.6}$$

Substituting the definition of $U_{q,n}^S$ into Equation (C.6) produces the integral equation for the scattering potential flow given by:

$$\int_{L_g}U_q^S(l)\,L_q(z,l)\,dl=\frac{-2i\alpha_{q,0}^S}{\pi kbJ_q'(kb)}\psi_0(z),\ z\in L_g \tag{C.7}$$

$$L_q(z,l)=-\sum_{n=1}^{\infty}\frac{\psi_n(z)\,\psi_n(l)}{k_n^2hbI_q'(k_nb)\,K_q'(k_nb)}. \tag{C.8}$$

In solving this integral equation, a function $u_q(l)$ that satisfies Equations (C.7)-(C.8) and has the following relationship is employed.

$$\int_{L_g}u_q^S(l)\,L_q(z,l)\,dl=\psi_0(z),z\in L_g \tag{C.9}$$

$$\text{where}\ \ U_q^S(l)=\frac{-2i\alpha_{q,0}^S}{\pi kbJ_q'(kb)}u_q^S(l). \tag{C.10}$$

By substituting Equation (C.10) into (C.2), the $\alpha_{q,0}^S$ coefficient can be computed as:

$$\alpha_{q,0}^S=\frac{-\gamma_qJ_q'(kb)}{\gamma_qH_q'(kb)+2iA_q^s},\ \text{where}\ \ \gamma_q=\pi kbkhJ_q'(kb), \tag{C.11}$$

$$\text{and}\quad A_q^S=\int_{L_g}u_q^S(z)\,\psi_0(z)\,dz. \tag{C.12}$$

C.2 Galerkin approximation

Equations (C.9) and (C.12) may be expressed in an operator notation as follows:

$$\mathcal{L}_qu_q^S=\psi_0,\ z\in L_g \tag{C.13}$$

$$\left(u_q^S,\psi_0\right)=A_q^S. \tag{C.14}$$

The function, $u_q^S(z)$, is approximated by a series of products of a test function, $v_n(z)$, with a coefficient, b_n. Again, the test function, $v_n(z)$, is expressed in terms of Chebychev polynomial and given a square root singularity factor (see Equation A.16).

$$u_q^S(z) \simeq \tilde{u}_q^S(z) = \sum_{n=0}^{N} b_n^{(q)} v_n(z). \tag{C.15}$$

A_q^S defined in Equation (C.14), is approximated by $\tilde{A}_q^S$ that is computed as

$$\tilde{A}_q^S(z) = F^T L^{(q)^{-1}} F, \tag{C.16}$$

$$\text{where} \quad F_{m0} = (-1)^m N_0^{-1/2} I_{2m}\{k(h-B)\}, \tag{C.17}$$

$$\text{and} \quad L_{mn}^{(q)} = -\sum_{s=1}^{\infty} \frac{J_{2m}\{k_s(h-B)\} J_{2n}\{k_s(h-B)\}}{N_s k_s h k_s b I_q'(k_s b) K_q'(k_s b)}. \tag{C.18}$$

F is an $(N+1)$ vector and $L_{mn}^{(q)}$ is an $(N+1)$ x $(N+1)$ matrix. The higher-mode terms in the infinite series seen from Equation (C.18), may be approximated in a similar way as for the radiation potential flow problem. The asymptotic forms of the Bessel functions for large real arguments given in Equations (A.22)-(A.25) can be employed.

C.3 Code verification

The response amplitude operator (RAO) for an OWC and the phase of this response θ_S were computed from the present linear analytical solver and WAMIT simulations. Direct comparisons of the RAO and θ_S are provided in Figure C.1 to verifiy the present linear analytical solver. The dimensions of the OWC for this comparison follows those described in Figure B.1, that shows the comparisons between the hydrodynamic coefficients computed from the WAMIT simulations and the present linear analytical solver. Figure C.1 shows that the RAO and θ_S have very good agreement. This proves that the present solver is capable of solving the boundary-value problem arising from the wave interaction with a thin-walled OWC in a linear potential flow.

Following on, the solutions available from Evans & Porter (1997) were reproduced using the present linear analytical solver. Direct comparisons are provided in Figure C.2. These comparisons involve OWCs with varying radius, b, in a constant water

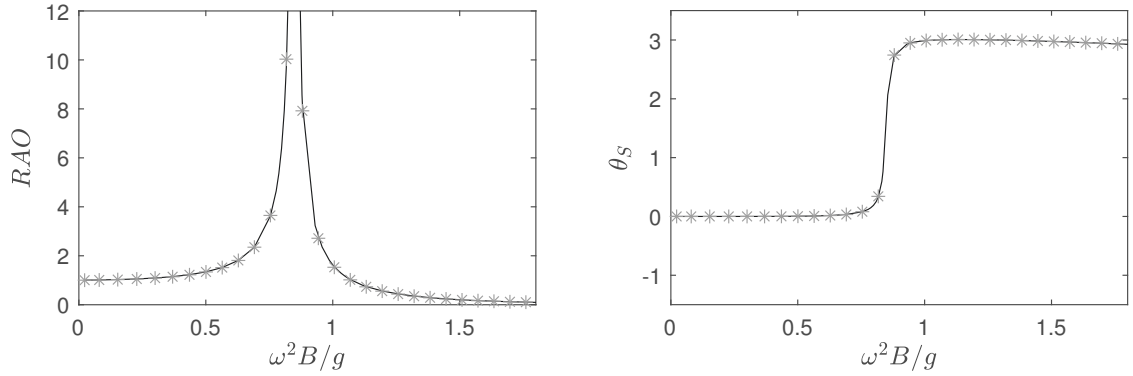

(A) (B)

Figure C.1: Comparisons of (A) *RAO* and (B) phase of the response θ_S computed from the linear analytical solver [——] and WAMIT simulations [$*$] for an OWC with a relative radius of $b/h = 0.035$, relative draft of $B/h = 0.11$ and water depth of $h = 1.0$m and at varying incident wave frequencies ω.

depth, h, and varying incident wave frequencies, ω. The dimensions of these OWCs are identical to those of which the hydrodynamic coefficients are presented earlier in Figure 2.4. Good agreement of the *RAO* values and the phases confirm the accurate implementation of the present linear analytical solution. Furthermore, Figure C.2 shows that the peak frequency at which the peak response occurs, shifts to a lower frequency as the radius increases. This results from the increased water column mass, that in turn reduces the undamped natural frequency from the piston natural frequency; the latter having $\omega^2 B/g = 1$.

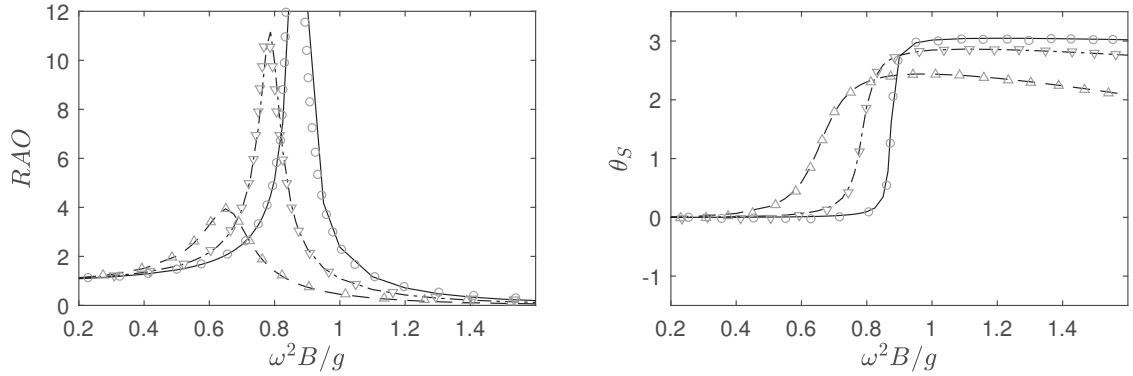

(A) (B)

Figure C.2: (A) *RAO* and (B) phase of the response θ_S computed from the present linear analytical solver for OWCs with varying radius of $b/h = \frac{1}{8}$ [——], $\frac{1}{4}$ [— · —] and $\frac{1}{2}$ [— —] and varying incident wave frequencies ω are compared with Evans & Porter (1997)'s calculations: $b/h = \frac{1}{8}$ [$\circ$], $\frac{1}{4}$ [$\triangledown$] and $\frac{1}{2}$[$\triangle$].

D
Finite volume method

D.1 Governing equations

OpenFOAM uses a Finite Volume Method (FVM) to numerically model a flow. In this method, the computational domain of a numerical model is discretised into a finite number of collocated-based control volumes (CVs). As such, the variable fields are allocated at the central point of the CV. The mass and momentum conservation equations are implemented by integrating these equations over each CV. To capture rapid fluctuations and mixing process that occur in the flow, a large eddy simulation or a Reynolds-averaged Navier-Stokes approach may be adopted in the numerical model.

D.1.1 Large eddy simulation (LES) principle

In a LES, the flow field is spatially filtered and solved directly. For the velocity field, the filtered velocity is expressed as follows:

$$\overline{\boldsymbol{u}}(\boldsymbol{x}) = \int \boldsymbol{u}(\boldsymbol{x}')G(\boldsymbol{x},\boldsymbol{x}')d\boldsymbol{x}', \tag{D.1}$$

$$\text{where} \quad G(\boldsymbol{x},\boldsymbol{x}') = \begin{cases} \frac{1}{V}, \text{ if } \boldsymbol{x}' \in V \\ 0 \text{ otherwise.} \end{cases} \tag{D.2}$$

Herein, $G(\boldsymbol{x}, \boldsymbol{x}')$, the spatial filter kernel, is defined as a simple box-hat filter, and V is the volume of the CV.

The filtered mass and momentum conservation equations can be expressed as follows:

$$\boldsymbol{\nabla} \cdot (\overline{\boldsymbol{u}} - \overline{\boldsymbol{u_g}}) = 0, \tag{D.3a}$$

$$\frac{\partial}{\partial t}\overline{\boldsymbol{u}} + \boldsymbol{\nabla} \cdot (\overline{\boldsymbol{u}} - \overline{\boldsymbol{u_g}})\ \overline{\boldsymbol{u}} = -\frac{1}{\rho}\boldsymbol{\nabla}\overline{p} + \boldsymbol{\nabla} \cdot \nu(\nabla\overline{\boldsymbol{u}} + \nabla\overline{\boldsymbol{u}}^T) + \boldsymbol{\nabla} \cdot \boldsymbol{\tau^s} + \boldsymbol{g}, \tag{D.3b}$$

where $\boldsymbol{u_g}$ denotes the velocity of grid for a dynamic mesh problem and has a zero value in a static mesh. Furthermore, $\boldsymbol{\tau^s}$ represents the subgrid scale (SGS) stress that has to be modelled to solve the closure problem arising from Equations (D.3a) and (D.3b). Following the classical Smagorinsky model (Smagorinsky, 1963), an eddy viscosity model has been adopted in the present study. This model assumes that the SGS stress results in increased transport and dissipation in the flow and thus this stress is related to the strain rate of the large (or resolved) scale field.

$$\boldsymbol{\tau^s} = -\nu_t(\nabla\overline{\boldsymbol{u}} + \nabla\overline{\boldsymbol{u}}^T) = -2\nu_t\overline{\boldsymbol{S}}, \tag{D.4}$$

where K denotes the SGS kinetic energy. ν_t, the eddy viscosity, and $\overline{\boldsymbol{S}}$, the large-scale strain rate, are repectively defined as:

$$\nu_t = C_s\Delta^2|\overline{\boldsymbol{S}}|, \tag{D.5a}$$

$$\overline{\boldsymbol{S}} = \frac{1}{2}(\nabla\overline{\boldsymbol{u}} + \nabla\overline{\boldsymbol{u}}^T), \tag{D.5b}$$

$$\text{where } |\overline{\boldsymbol{S}}| = \sqrt{2\overline{\boldsymbol{S}}\,\overline{\boldsymbol{S}}}. \tag{D.5c}$$

Δ given in Equation (D.5a) is the filter length scale and defined by:

$$\Delta = \sqrt[3]{V}. \tag{D.6}$$

Furthermore, C_s in Equation (D.5a) is the Smagorinsky coefficient determined as an a priori input in the classical Smagorinsky model.

In the dynamic Smagorinsky model proposed in Germano et al. (1991), C_s is

estimated at every computational time step. This model assumes that the interaction between the SGS field and the smallest resolved scale field is similar to the interaction between the latter and the larger resolved scale field. A second filtering of the formerly filtered equations of motion is thus undertaken. The second filtered equations can be expressed as follows:

$$\frac{\partial}{\partial t}\widetilde{\overline{\boldsymbol{u}}} + \boldsymbol{\nabla} \cdot \left(\widetilde{\overline{\boldsymbol{u}}} - \widetilde{\overline{\boldsymbol{u_g}}}\right) \widetilde{\overline{\boldsymbol{u}}} = -\frac{1}{\rho}\boldsymbol{\nabla}\widetilde{\overline{p}} + \boldsymbol{\nabla} \cdot \nu(\nabla\widetilde{\overline{\boldsymbol{u}}} + \nabla\widetilde{\overline{\boldsymbol{u}}}^T) + \boldsymbol{\nabla} \cdot \boldsymbol{T^s} + \boldsymbol{g}, \tag{D.7a}$$

where the SGS stress is now

$$\boldsymbol{T^s} = -2\nu_t\widetilde{\overline{\boldsymbol{S}}} \tag{D.8}$$

$$\text{where} \quad \nu_t = C_s\widetilde{\Delta}^2|\widetilde{\overline{\boldsymbol{S}}}| \tag{D.9}$$

$$\text{and} \quad \widetilde{\overline{\boldsymbol{S}}} = \frac{1}{2}(\nabla\widetilde{\overline{\boldsymbol{u}}} + \nabla\widetilde{\overline{\boldsymbol{u}}}^T) \tag{D.10}$$

$\widetilde{\Delta}$ is the filter length scale defined as $\widetilde{\Delta} = 2\Delta$ in the second filtering. The resolved scale stress is given by

$$\boldsymbol{L} = \boldsymbol{T^s} - \widetilde{\overline{\boldsymbol{\tau}^s}} \tag{D.11}$$

$$= 2C_s\boldsymbol{M} \tag{D.12}$$

$$\text{where} \quad \boldsymbol{M} = \Delta^2\left(\widetilde{|\overline{\boldsymbol{S}}|\overline{\boldsymbol{S}}} - 4|\widetilde{\overline{\boldsymbol{S}}}|\widetilde{\overline{\boldsymbol{S}}}\right). \tag{D.13}$$

Lilly (1992) implemented the least-squares method to estimate C_s and derive the following expression.

$$C_s = \frac{1}{2}\frac{\boldsymbol{LM}}{\boldsymbol{LM}}. \tag{D.14}$$

D.1.2 Reynolds-averaged Navier-Stokes (RANS) principle

In a RANS model, the variable fields are time averaged over a time interval larger than the typical time scale of the fluctuations. This averaging also introduces an additional term referred to as the Reynolds stress in the time-averaged momentum conservation equations to approximate the nonlinear convective flux.

The present study considers the k-ω SST model proposed by F. R. Menter &

Langtry (2003). The superiority of this RANS model over the k-ϵ and the k-ω models lies in its capability to predict separated flows near a wall and free shear flows at the locations far from the wall. By using blending functions, the k-ω SST model switches to the k-ϵ model for the flow far from any wall, and adopts the k-ω model inside a boundary layer at which the flow may separate.

The time-averaged mass and momentum conservation equations and the transport equations of the turbulent kinetic energy k and the turbulence specific dissipation rate ω are expressed as follows:

$$\boldsymbol{\nabla} \cdot (\overline{\boldsymbol{u}} - \overline{\boldsymbol{u_g}}) = 0, \tag{D.15a}$$

$$\frac{\partial}{\partial t}\overline{\boldsymbol{u}} + \boldsymbol{\nabla} \cdot (\overline{\boldsymbol{u}} - \overline{\boldsymbol{u_g}})\ \overline{\boldsymbol{u}} = -\frac{1}{\rho}\boldsymbol{\nabla}\overline{p} + \boldsymbol{\nabla} \cdot \nu(\nabla\overline{\boldsymbol{u}} + \nabla\overline{\boldsymbol{u}}^T) + \boldsymbol{\nabla} \cdot \boldsymbol{\tau^R} + \boldsymbol{g}\, dV, \tag{D.15b}$$

$$\frac{\partial}{\partial t}\int_V k + (\boldsymbol{\nabla} \cdot \overline{\boldsymbol{u}})k = \boldsymbol{\nabla} \cdot (\nu + \sigma_k\nu_t)\boldsymbol{\nabla}k + \frac{1}{\rho}\tilde{P}_k - \beta^* k\omega, \tag{D.15c}$$

$$\frac{\partial}{\partial t}\omega + (\boldsymbol{\nabla} \cdot \overline{\boldsymbol{u}})\omega = \boldsymbol{\nabla} \cdot (\nu + \sigma_{\omega 1}\nu_t)\boldsymbol{\nabla}\omega + \alpha^*|\overline{\boldsymbol{S}}|^2 - \beta\omega^2 + 2\,(1 - F_1)\,\sigma_{\omega 2}\frac{1}{\omega}\boldsymbol{\nabla}k\boldsymbol{\nabla}\omega. \tag{D.15d}$$

$\boldsymbol{\tau^R}$ of Equation (D.15b) is the Reynolds stress and defined as

$$\boldsymbol{\tau^R} = -\nu_t(\nabla\overline{\boldsymbol{u}} + \nabla\overline{\boldsymbol{u}}^T) = -2\nu_t\overline{\boldsymbol{S}}, \tag{D.16a}$$

$$\text{where}\quad \nu_t = \frac{a_1 k}{\max\left(a_1\omega, |\overline{\boldsymbol{S}}|F_2\right)}. \tag{D.16b}$$

ν_t denotes the eddy viscosity with the coefficient of $a_1 = 0.31$ and the modulus of the mean strain rate given by $|\overline{\boldsymbol{S}}| = \sqrt{2\overline{\boldsymbol{S}}\,\overline{\boldsymbol{S}}}$. Furthermore, the term $\tilde{P}_k$ is a limiting function given by:

$$\tilde{P}_k = \min\left(P_k, 10\beta^* k\omega\right), \tag{D.17a}$$

$$\text{where}\quad P_k = -2\nu_t\nabla\overline{\boldsymbol{u}}\overline{\boldsymbol{S}}. \tag{D.17b}$$

It should be noted that the notations of k and ω used in this appendix have different definitions from those described in the chapters of this thesis.

α^* of Equation (D.15d) is computed as $\alpha^* = \alpha_1 F_1 + \alpha_2\,(1 - F_1)$, and the closure

coefficients are given by $\sigma_{k1} = 0.85$, $\sigma_{k2} = 1.0$, $\sigma_{\omega 1} = 0.5$, $\sigma_{\omega 2} = 0.856$, $\alpha_1 = 5/9$, $\alpha_2 = 0.44$, $\beta_1 = 0.075$, $\beta_2 = 0.0828$ and $\beta^* = 0.09$. Furthermore, F_1 and F_2 are the blending functions, which are respectively defined by:

$$F_1 = \tanh\left[\left[\min\left(\max\left(\frac{\sqrt{k}}{\beta^*\omega n_w}, \frac{500\nu}{n_w^2\omega}\right), \frac{4\rho\sigma_{\omega 2}k}{CD_{kw}n_w^2}\right)\right]^4\right], \tag{D.18a}$$

$$F_2 = \tanh\left[\left[\max\left(\frac{2\sqrt{k}}{\beta^*\omega n_w}, \frac{500\nu}{n_w^2\omega}\right)\right]^2\right], \tag{D.18b}$$

$$\text{where} \quad CD_{kw} = \max\left(2\rho\sigma_{\omega 2}\frac{1}{\omega}\boldsymbol{\nabla}k\boldsymbol{\nabla}\omega, 10^{-10}\right), \tag{D.18c}$$

and n_w is the distance to the nearest wall.

D.1.3 Additional equations

For capturing the free surface in a computational domain, a Volume of Fluid (VOF) method is applied. A scalar quantity α is introduced to represent the amount of fluid contained in a CV. For a two phase problem considering air and water, $\alpha = 1$ if the CV is fully filled with water and 0 if empty. The free surface is identified when $0 < \alpha < 1$. The scalar quantity is computed in the numerical model by satisfying the transport equation of α given by:

$$\frac{\partial\alpha}{\partial t} + \boldsymbol{\nabla} \cdot (\overline{\boldsymbol{u}} - \overline{\boldsymbol{u_g}})\,\alpha + \boldsymbol{\nabla} \cdot \boldsymbol{u_r}\alpha\,(1-\alpha) = 0, \tag{D.19}$$

where u_r is the compression velocity used to limit the smearing of the interface and maintain this interface sharp.

For a dynamic mesh, the space conservation law (SCL) must be satisfied (Demirdžić & Perić, 1988, Jasak, 2009). The SCL defines the relationship between the velocity of the moving surface of a CV and the rate of change of the volume V. In a volume integral, this SCL can be expressed as follows:

$$\frac{\partial}{\partial t}\int_V dV - \int_V \boldsymbol{\nabla} \cdot \overline{\boldsymbol{u_g}}\, dV = 0 \tag{D.20}$$

D.2 Discretisation practises

The generic transport equation for a scalar quantity φ is expressed as follows:

$$\frac{\partial}{\partial t}\int_V \varphi\, dV + \int_V \boldsymbol{\nabla}\cdot\left(\boldsymbol{u}-\boldsymbol{u_g}\right)\varphi\, dV - \int_V \boldsymbol{\nabla}\cdot\left(\Gamma_\varphi \boldsymbol{\nabla}\varphi\right) dV = \int_V S_\varphi \varphi\, dV. \quad \text{(D.21)}$$

The first term of Equation (D.21) is referred to as temporal flux, the second term convective flux, the third term diffusive flux and the last is referred to as source flux. The discretisation of each term will be described in the sections that follow.

D.2.1 Temporal discretisation

For the temporal discretisation, various time-advancing schemes have been implemented within the present study. An investigation of the accuracy of these schemes is provided in Section 3.4.1. In the scheme of the first-order implicit Euler, the temporal flux in a discretised form is given from:

$$\frac{\partial}{\partial t}\int_V \varphi\, dV = \frac{\varphi^{t+\Delta t}-\varphi^t}{\Delta t}\, V. \quad \text{(D.22)}$$

The volume integral in this flux has been aproximated using the mid-point rule. Furthermore, the terms in the convective and diffusive fluxes are treated implicitly and thus expressed in terms of the scalar quantity at the current time step, $\varphi^{t+\Delta t}$.

D.2.2 Spatial Discretisation

For the convective flux, the volume integral is transformed into a surface integral using the Gauss divergence theorem. The approximation to this surface integral again uses the mid-point rule. The spatial discretisation is given as follows:

$$\int_V \boldsymbol{\nabla}\cdot\left(\boldsymbol{u}-\boldsymbol{u_g}\right)\varphi\, dV = \int_{\partial A}\left(\boldsymbol{u}-\boldsymbol{u_g}\right)\varphi\cdot d\boldsymbol{A} = \sum_f \left[\boldsymbol{A_f}\cdot\left(\boldsymbol{u}-\boldsymbol{u_g}\right)^{m-1}\right]\varphi_f^m. \quad \text{(D.23)}$$

Since the convective flux is a nonlinear term, a blending scheme that maintains both numerical accuracy and stability is adopted to interpolate the scalar quantity at every surface of a CV, φ_f, with $\boldsymbol{A_f}$ being the normal surface vector. To linearise this

term, the mass flux in Equation (D.23) is predicted using the velocity field computed from the previous iteration, $\overline{\boldsymbol{u}}^{m-1}$.

Likewise, the volume integral corresponding to the diffusive flux in Equation (D.21) is transformed into a surface integral. The discretisation is thus expressed as:

$$\int_V \boldsymbol{\nabla} \cdot (\Gamma_\varphi \boldsymbol{\nabla}\varphi) = \sum_f \Gamma_\varphi (\boldsymbol{A_f} \cdot \boldsymbol{\nabla}\varphi_f), \tag{D.24}$$

$$\text{where } \boldsymbol{A_f} \cdot \boldsymbol{\nabla}\varphi_f = |\boldsymbol{A_f}| \frac{\varphi_N^m - \varphi_P^m}{|\boldsymbol{d}|} + [|\boldsymbol{A_f}| \boldsymbol{\nabla}\varphi_f \cdot (\boldsymbol{n} - \boldsymbol{i_d})]^{m-1}. \tag{D.25}$$

The first term in Equation (D.25) is the approximation to the surface integration applied to a purely orthogonal CV, while the second term is a corrector associated with non-orthogonality of the CV. $|\boldsymbol{d}|$ of the first term denotes the distance between the centres of two adjacent CVs. In the second term, $\boldsymbol{\nabla}\varphi_f$ indicates the gradient of the scalar quantity interpolated at the surface and $\boldsymbol{n} - \boldsymbol{i_d}$ the difference between the vector normal to this surface and the vector parallel to the line connecting the two centres. Furthermore, this second term requires data computed from the previous iteration and is thus merged into the source flux of Equation (D.21).

To approximate $\nabla\varphi_f$, the Gauss' theorem is implemented and the value of φ_f at each surface of the CV is averaged as follows:

$$\boldsymbol{\nabla}\varphi = \frac{\int_V \boldsymbol{\nabla}\varphi}{V} = \frac{\sum_f \mathrm{A}_f \cdot \varphi}{V}. \tag{D.26}$$

This approximation is also applied to quantify the pressure gradient, which is computed using data of previous iteration. The pressure gradient, together with the volume integral corresponding to the body force term, contribute the source flux in Equation (D.21).

D.3 Pressure-velocity coupling: PISO algorithm

The implementation of the discretisation practises for all CVs in a computational domain generates a set of equations that can be expressed in a matrix form:

$$a_P u_P + \sum_N a_N u_N = \boldsymbol{Q}, \tag{D.27}$$

where a_p is the matrix coefficient for the velocity at the centre of a CV, a_N the matrix coefficient derived from the neighbouring CVs and $\boldsymbol{Q}$ is the vector corresponding to the source term noted earlier. In the present study, an iterative solver appropriate to an asymmetric system is adopted to solve this matrix equation.

By solving Equation (D.27) using the iterative solver, the provisional values of the velocity field can be computed. To satisfy the continuity equation, these provisional velocities have to be corrected by coupling the pressure and velocity variables. A segregated approach based upon PISO (Issa, 1986) is adopted to solve the governing equations within the present study. This approach substitutes pressure correction $p^{'}$ and velocity correction $u^{'}$ into the momentum conservation equation and the continuity equation. A pressure correction equation for each CV can thus be expressed as follows:

$$\frac{1}{a_P}\nabla^2 p_P^{'} = \nabla u_P + \nabla \widehat{u}_P^{'}, \tag{D.28}$$

$$\text{where} \quad \widehat{u}_P^{'} = -\frac{\sum_N a_N u_N^{'}}{a_P}. \tag{D.29}$$

The pressure correction $p^{'}$ can be computed using Equation (D.28) with $\overline{u}$ denoting the provisonal velocity. For this first correction, $\widehat{u}_P^{'}$ is neglected as it is unknown. The first velocity correction $u^{'}$ is then predicted using the following relationship:

$$u_P^{'} = -\frac{1}{a_P}\nabla p_P^{'} \tag{D.30}$$

A second pressure and velocity correction may be computed as:

$$\frac{1}{a_P}\nabla^2 p_P^{''} = \nabla \widehat{u}_P^{'}, \tag{D.31}$$

$$u_P^{''} = \widehat{u}_P^{'} - \frac{1}{a_P}\nabla p_P^{''}. \tag{D.32}$$

Further corrector steps can be undertaken in the same way. In the present study, the number of correctors is generally set to three. Having solved the pressure correction equation, the momentum conservation equation is again solved as described earlier and iteratively until a pre-determined tolerance is reached.